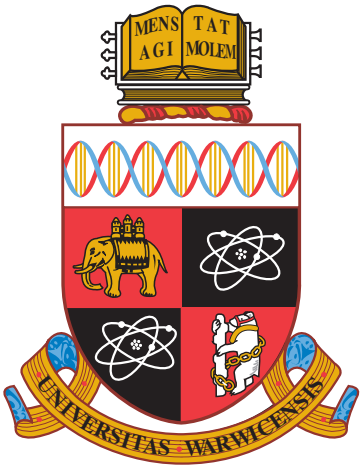

Experimental Studies of Noncentrosymmetric Superconductors

by

Daniel Alexander Mayoh

Thesis

Submitted to the University of Warwick

for the degree of

Doctor of Philosophy in Physics

Department of Physics

July 2019

THE UNIVERSITY OF WARWICK

Contents

List of Tables

List of Figures

Acknowledgments

A PhD has been a large and some times daunting task. While the work I am presenting in this thesis is my own, it would not have been possible without the help of others.

I would first like to thank my supervisors Martin Lees and Geetha Balakrishnan without whom none of this would have been possible. They have provide a constant source of guidance and support throughout my PhD. In particular I am incredibly thankful to you for giving me the opportunity to spend a month living and working at Hiroshima University in Japan. I would also like to extend this thanks to Prof. Takabatake who took time to welcome me into his research group at Hiroshima University and to share his expertise in crystal growth with me. Many thanks go to Patrick Ruddy and Ali Julian for their glass blowing skills and technical support throughout the last four years. Thank you to Kathrin and Matt for their help with the high-field measurements, Steve York for performing EDAX measurements and to Monica for invaluable support with sample preparation and crystal growth. I would also like to thank all the instruments scientist I have worked with; Adrian Hillier, Pabitra Biswas and Ivan de Silva. I don't think I will ever forget the beamtime I spent running around Harwell campus during the 'Beast from the East 2018' at 3 am trying to persuade the dilution fridge to re-condense. Thank you to all of the superconductivity and magnetism group and a special mention to Will, Talha, Ray, Beth and everyone else that has spent time in the 220 office. You have made the last four years an absolute joy!

I would like to thank Joe, Richard, Becca, Connor, Cayo and the Pathfinder crew for keeping me sane with pub trips and allowing me to inflict many board game

nights upon them.

I am very grateful to my Mum, Linda, and the rest of my family for their continuous support especially during the final year with my battle between my thesis and health problems. Finally, this would not have been possible without the continuous encouragement of my girlfriend, Becky, who has been incredibly patient, understanding and supportive throughout the entire roller-coaster ride that has been this PhD.

Declarations

This thesis is submitted to the University of Warwick in support of my application for the degree of Doctor of Philosophy. It has been composed by myself and has not been submitted in any previous application for any degree. The work presented (including data generated and data analysis) was carried out by the author except in the case outline below.

The polycrystalline samples of La_7Pd_3, Re_6Zr, $TaRh_2B_2$ and $NbRh_2B_2$ were produced exclusively by myself. The single crystal samples of La_7Ir_3 were produced by myself, under the guidance of Prof. Takabatake. EDAX measurements of La_7Ir_3 were performed by Steve York at the University of Warwick. High field resistivity measurements of $TaRh_2B_2$ and $NbRh_2B_2$ were performed with Dr Kathrin Götze and Matthew Pearce at the University of Warwick. Physical property and magnetic property measurements were performed by myself at the University of Warwick under the supervision of Dr Martin Lees. Neutron scattering and muon spin relaxation/rotation measurements were performed at ISIS neutron spallation source, UK. For all experiments I was the leading member of the experimental team. The data collected at central facilities was analysed by myself under the guidance of Dr Adrian Hillier and Dr Ivan de Silva.

Parts of the work described in this thesis have been published in the following articles:

- **D. A. Mayoh**, J. A. T. Barker, R. P. Singh, G. Balakrishnan, D. Mck. Paul and M. R. Lees, *Superconducting and normal-state properties of the noncentrosymmetric superconductor Re_6Zr*, Physical Review B **96**, 064621 (2017).

- **D. A. Mayoh**, A. D. Hillier, K. Götze, D. Mck. Paul, G. Balakrishnan, and M. R. Lees, *Multigap superconductivity in chiral noncentrosymmetric* $TaRh_2B_2$, Physical Review B **98**, 014502 (2018).

- **D. A. Mayoh**, M. J. Pearce, K. Götze, A. D. Hillier, G. Balakrishnan, and M. R. Lees, *Superconductivity and the upper critical field in the chiral noncentrosymmetric superconductor* $NbRh_2B_2$, Journal of Physics: Condensed Matter 31 465601 (2019).

- **D. A. Mayoh**, A. D. Hillier, G. Balakrishnan, and M. R. Lees, *Detection of time-reversal symmetry breaking and nodeless superconductivity in* La_7Pd_3, *Manuscript under preparation* (2019).

- **D. A. Mayoh**, A. D. Hillier, T. Takabatake, G. Balakrishnan, and M. R. Lees, *Growth and characterisation of monocrystalline* La_7Ir_3, *Manuscript under preparation* (2019).

Parts of the work described in this thesis have also been presented at the following meetings:

- *Detecting unconventional superconductivity using muons*, UK Neutron and Muon Science and User Meeting, Warwick, UK, April 2019 - **Talk**.

- *Superconductivity and the upper critical field in the chiral noncentrosymmetric superconductor* $NbRh_2B_2$, UK Neutron and Muon Science and User Meeting, Warwick, UK, April 2019 - **Poster**.

- *Unconventional superconductivity in noncentrosymmetric compounds*, Public Seminar, Paul Scherrer Institut, Switzerland, March 2019 - **Talk**.

- *Multigap superconductivity in chiral noncentrosymmetric* $TaRh_2B_2$, Muon User Meeting 2018, Abingdon, UK, June 2018 - **Talk**.

- $TaRh_2B_2$*: A new family of chiral noncentrosymmetric superconductors*, UK Neutron and Muon Science and User Meeting, Warwick, UK, April 2018 - **Poster**.

- *Unconventional superconductivity of the noncentrosymmetric superconductor* La_7Ir_3, American Physical Society March Meeting, Los Angeles, USA, March 2018 - **Talk & Poster**.

- *Superconducting and normal-state properties of the noncentrosymmetric superconductor* Re_6Zr, Strongly Correlated Electron Systems 2017, Prague, Czech Republic, July 2017 - **Poster**.

- *Superconducting and normal-state properties of the noncentrosymmetric superconductor* Re_6Zr, Frontiers of Condensed Matter, Bristol, UK January 2017 - **Poster**.

Abstract

Noncentrosymmetric (NCS) superconductors lack a centre of inversion symmetry. This along with antisymmetric spin orbit coupling can result in an admixture of singlet and triplet pairing in the superconducting state. This admixture can give rise to several unconventional superconducting behaviours such as exotic superconducting gap functions, upper critical fields that violate the Pauli limiting field and time-reversal symmetry breaking among others. In this thesis, the NCS superconductors Re_6Zr, La_7Pd_3, La_7Ir_3, $TaRh_2B_2$ and $NbRh_2B_2$ have been studied using a combination of low-temperature magnetisation, heat capacity, resistivity and muon spin spectroscopy techniques (μSR).

High quality single crystal and polycrystalline samples have been prepared by a variety of synthesis techniques. Polycrystalline samples of Re_6Zr and La_7Pd_3 were prepared by arc melting. Polycrystalline samples of $NbRh_2B_2$ and $TaRh_2B_2$ have been synthesised by solid state reaction. Single crystal samples of La_7Ir_3 have been prepared using the Czochralski process.

The superconducting and normal-state properties of the cubic NCS superconductor Re_6Zr with $T_c = 6.75(5)$ K have been investigated. The properties of Re_6Zr are observed to be dominated by the effects of disorder with electrical resistivity measurements indicating poor metallic behaviour. Heat capacity measurements of Re_6Zr indicate that the superconducting gap is isotropic and s-wave in nature with enhanced electron-phonon coupling.

La_7Pd_3 and La_7Ir_3 are hexagonal NCS superconductors with T_c of 1.46(5) and 2.41(5) K respectively. Magnetisation, resistivity, heat capacity and transverse-field μSR measurements of polycrystalline La_7Pd_3 reveal that it is a fully gapped s-wave superconductor. However, zero-field μSR measurements indicate that time-reversal symmetry is broken in the superconducting state. La_7Ir_3 single crystals have been synthesised and characterised to look for evidence of anisotropy in the superfluid density to explain the observation of time-reversal symmetry breaking in polycrystalline samples.

$TaRh_2B_2$ and $NbRh_2B_2$ are isostructural chiral NCS superconductors with a T_c of 6.05(5) and 7.58(5) K respectively. Both compounds have upper critical fields that violate the Pauli limiting field which can not be modelled by the Werthamer-Helfand-Hohenberg model. Evidence for multigap superconductivity has been found in heat capacity and μSR measurements performed on $TaRh_2B_2$ and $NbRh_2B_2$.

Chapter 1

Introduction and Historical Overview of Unconventional Superconductivity

1.1 The Discovery of Conventional Superconductivity

At the beginning of the 20th century Dutch physicist, Heike Kamerlingh Onnes, discovered that when mercury is cooled down below 4.2 K the resistivity drops to zero. This original phenomena was named by Onnes as "supraconductivity" which is now better known as superconductivity [15]. A few years later it was discovered that resistivity could be restored by applying a sufficiently large magnetic field or current. In the following years several other metals were reported to exhibit the same behaviour such as lead ($T_c = 7.2$ K) and with the highest superconducting transition temperature being reported in Niobium at $T_c = 9.2$ K. The next big step in the story of superconductivity was taken in 1933 when Franz Walther Meissner and Robert Ochsenfeld noticed that when a superconducting material was cooled below its transition temperature they observed perfect diamagnetism where the magnetic flux is expelled from the interior of sample [16]. A year later Fritz and Heinz London came up with the first phenomenological theory for superconductivity in which they proposed a simple two fluid model. In this theory they explained the Meissner effect and predicted one of the key characteristic properties of superconductors known as the penetration depth λ [17]. Then in 1950 Vitaly Ginzburg and Lev Landau devised the macroscopic theory of superconductivity which uses Landau's theory of second-order phase transitions [18]. Although a phenomenological model, it has proved to be a powerful tool in understanding superconductivity.

Seven years later two more major steps forward in understanding superconductors occurred. The first came from Alex Abriskosov who when applying external magnetic fields determined there are two categories of superconductors: Type I where all the magnetic flux is expelled from the superconductor below its critical temperature and Type II where in large external fields the superconductor is partially penetrated by the magnetic flux [19]. The second step, and potentially the largest in the history of superconductors so far, was the proposal of a complete microscopic theory of superconductors put forward by John Bardeen, Leon Cooper and Robert Schrieffer. This theory now known as BCS theory suggested that below the critical temperature of a superconductor an attractive interaction forms between electrons close to the Fermi surface which is mediated by phonons [20]. The electrons in fact form pairs known as Cooper pairs that have opposite momentum and spin. The BCS theory for superconductivity has been so successful that it forms the basis of present understanding of conventional superconductivity and forms a reference theory for more unconventional superconductivity as shall be discussed in this thesis. Until this point Matthias' rules had been used to empirically explain the variation in critical temperatures as well as excluding the possibility of superconductivity existing in non-metallic systems and rare earths with unpaired electrons, and co-existing with ferromagnetism, anti-ferromagnetism [21, 22]. However, BCS theory was able to qualitatively explain many of these rules. The crystal structure of superconductors had never been thought of as one of the key components in determining the properties of superconductors. In the years to come crystal structure would be found to indeed play a vital role.

1.2 The Road to Unconventional Superconductivity

Having given an overview of the experimental and theoretical progression of "conventional" superconductivity we now discuss "unconventional" superconductivity. In this thesis we will define a superconductor to be classed as unconventional if the pairing mechanism from which Cooper pairs form deviates from that of the BCS description.

1.2.1 Superfluid ^{3}He

While BCS theory proved to be a excellent theory for explaining and understanding the behaviour of conventional superconductors it was found that it could be applied to a multitude of interesting systems. The story leading to the discovery of unconventional superconductivity in heavy fermion materials starts with superfluid

^{3}He. At the time it was understood that ^{4}He undergoes Bose condensation at low-temperatures when it enters its superfluid phase however it was not clear whether ^{3}He had a superfluid phase. ^{3}He is a fermion so to condense would need a pairing mechanism, since ^{3}He has a large hard core repulsion from the filled electron shell it was speculated that a d-wave ordering parameter would allow sufficient nodes to allow an attractive van der Waals tail to pair the fermions [23]. Hence it came as rather a surprise to researchers when superfluid ^{3}He was discovered [24] and even more so when it was found to have p-wave superfluidity [25]. Further investigations into the superfluid phase of ^{3}He revealed two distinct phases: a B phase where the pairing states form in a sphere i.e. $k_{\mathrm{x}}\hat{x} + k_{\mathrm{y}}\hat{y} + k_z\hat{z}$ where $\hat{x}$ for example is the projection of the Cooper pairs spin, indicating that the energy gap is isotropic [26]. In the A phase, however, the pairing state has the form $(k_{\mathrm{x}} + \imath k_{\mathrm{y}})\,\hat{z}$ which has nodes in the Fermi surface giving an anisotropic energy gap [27]. For condensed matter physicists ^{3}He provided a simple system to investigate. Its parabolic dispersion with weak spin-orbit interactions along with its normal-state parameter are well known from experiments and easily described by simple Legendre polynomials [28, 29]. The complexity in this system comes when looking at the contributions to the pairing interactions; it turns out that everything contributes to the pairing including spin, density and current fluctuations [30]. The investigations into these complexities laid the vital ground work for the subsequent exploration of unconventional superconductors.

1.2.2 Heavy Fermion Superconductors

There was a staggered start to the discovery of heavy fermion superconductors. At the time there was general consensus that magnetism and superconductivity could not co-exist in a system [31, 32], although there were researchers who were not captivated by the BCS theory, such as Matthias, that believed this was not the case [33]. Superconductivity had been found in several uranium compounds such at U_2PtC_2 [33] and UBe_{13} [34] although it was thought that the superconductivity was due to filaments of α-U (a conventional superconductor). The first conclusive proof of heavy fermion superconductivity came in 1979 with the discovery of superconductivity below 0.5 K in $CeCu_2Si_2$ [35]. The two key properties of $CeCu_2Si_2$ are the enhanced electronic coefficient of the specific heat which is a 1000 times that of copper ($\approx$ 1 J/mol K^2) and the jump in specific heat that is enhanced by a similar factor. The enhancement to electronic contribution to the specific heat can be explained as the result of the Kondo interaction due to the hybridisation of the f electrons with the conduction band. The enhanced superconducting transi-

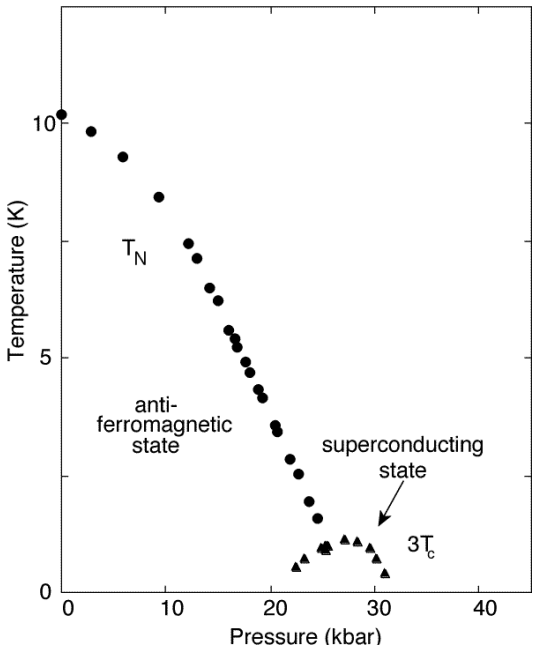

Figure 1.1: Phase diagram of $CePd_2Si_2$ versus pressure. As the pressure is increased the antiferromagnetic phase is suppressed until the appearance of a superconducting dome at 20 kbar. Adapted from Ref. [1].

tion indicates that the Cooper pairs are formed of electrons within these "heavy" hybridised bands. It was seen that the superconductivity in this system could be easily suppressed by adding non-magnetic impurities. When considered together these phenomena indicate that the quasiparticles in $CeCu_2Si_2$ are strongly interacting. The properties of $CeCu_2Si_2$ were observed to be highly sample dependent with some showing antiferromagnetic behaviour and other showing superconductivity [36]. In some cases both were seen. Closer inspection of $CeCu_2Si_2$ using muon spin resonance measurements reveals the lack of microscopic coexistence of both antiferromagnetism and superconductivity [37].

Soon after $CeCu_2Si_2$ more heavy fermion materials were discovered such UPt_3 [38] along with the (re)discovery of UBe_{13} [39] and U_2PtC_2 [40]. Many of the properties of UPt_3 were seen to be reminiscent of ^{3}He encouraging many theorists to transfer the theories from ^{3}He to UPt_3. Researchers soon realised this would lead to a *d*-wave singlet pairing rather than *p*-wave triplet pairing. The question then quickly turned to whether magnetic correlations are responsible for superconductivity in heavy fermion systems? A clearer picture started to emerge with the discovery of $CeIn_3$ and $CePd_2Si_2$ whose antiferromagnetic phase is found to be suppressed with increasing pressure [1]. A quantum critical point was found when the

antiferromagnetic order was suppressed to zero and a superconducting 'dome' appears. This was taken as evidence for the attractive interaction between Cooper pair electrons in these systems to be mediated by magnetic interactions rather than phonon. The same behaviour was seen in CeXIn$_5$ where X is a transition metal with one slight difference that the superconducting phase overlaps with the antiferromagnetic phase [41, 42].

1.2.3 High-temperature Cuprate Superconductors

Up until 1986 the superconductor with the highest critical field discovered was Nb_3Ge with $T_c = 23$ K [43]. At this time reports started to appear of materials with superconductivity with many turning out to be false. This lead to Bednorz-Muller's paper on superconductivity in Ba doped La_2CuO_4 [44] to go largely unnoticed. When superconductivity was then verified by Tanake's group six months later this opened the way to the high temperatures cuprate superconductors. Many of these superconductors had much higher critical temperatures than any other material with $YBa_2Cu_3O_{7-x}$ having a $T_c = 93$ K [45] and Hg-Ba-Ca-Cu-O with a $T_c = 164$ K under pressure [46]. The discovery of the cuprate superconductors came as much of a surprise to the superconductor community as they clearly violate many of Matthais rules being quasi-2D doped insulating oxides materials. A comparison of the phase diagram of a cuprate superconductor highlights the similarities to the heavy fermion materials with a antiferromagnetic phase being present at low hole doping that is gradually suppressed with increased hole doping before a superconducting 'dome' appears, as can be seen in Fig. 1.2. Analysis of the superconducting gap in cuprates has revealed they host an anisotropic d-wave ordering parameter which is highly contrasting to BCS theory that would predict a isotropic s-wave state [47].

1.2.4 Organic Superconductors

It had been speculated that superconductivity could exist in organic compounds [48] but it was not until 1980 the first confirmation of superconductivity in quasi-1D Bechgaard salt was reported by Denis Jerome's group [49]. One example of a quasi-1D organic superconductor is $(TMTSF)_2PF_6$ which was seen to have a spin density wave at ambient pressures but develop superconductivity as pressure is applied. These materials are of particular interest due to the tendency to exhibit anomalously large upper critical fields far above the Pauli limit, this behaviour is seen as indicative of triplet pairing [50]. While Buckminsterfullerene (C_{60} also known as Buckyballs) were largely regarded as strong-coupling BCS superconductors. Recent work on the

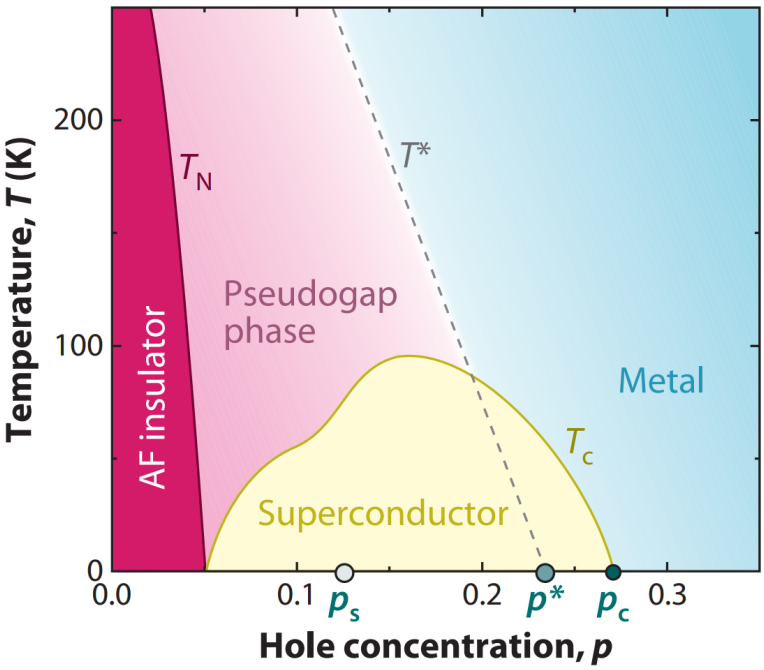

Figure 1.2: Schematic phase diagram as function of hole doping in a cuprate superconductor. As the concentration of hole doping increases the antiferromagnetic phase is suppressed. If hole doping is increased further a superconducting dome appears. Figure taken from Ref. [2].

caesium variant indicates a superconducting diagram much like the heavy fermion and cuprate superconductors [51] where superconductivity emerges under pressure from an insulating antiferromagnetic phase.

1.2.5 Iron Pnictide Superconductors

More recently in 2008 came the first report of superconductivity in the iron arsenide compound $LaO_{1-x}F_xFeAs$ [52]. The most studied class of the iron pnictide compounds have a 122 structure which is same structure of $CeCu_2Si_2$, a heavy fermion superconductor. The similarities between the iron pnictides and other unconventional superconductors does not stop there, like the cuprates the undoped variant of a compound is seen to be a commensurate antiferromagnet but upon doping a superconducting dome opens. An example of a phase diagram for an iron pnictide superconductor can be seen in Fig. 1.3. There are some differences, the first being that iron pnictides generally are metallic with a Dirac-like dispersion [53]. They have also been found to exhibit a full energy gap with weak anisotropy which can be seen in directional dependence of the upper critical field [54, 55]. Studies have

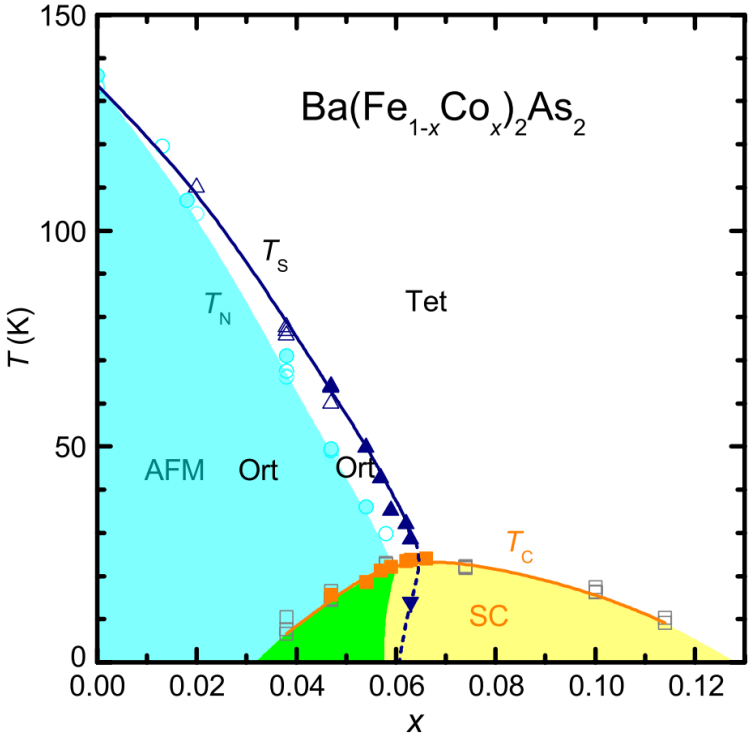

Figure 1.3: Phase diagram as function of Co doping in $Ba(Fe_{1-x}Co_x)_2As_2$. As the concentration of Co increases the antiferromagnetic phase is suppressed and a superconducting dome comes up to meet it at $x \approx 0.06$. Figure taken from Ref. [3]

ruled out the possibility of a phonon mediated pairing mechanism likely indicating that the pairing involves antiferromagnetic spin fluctuations although this far from being conclusively proved [56].

In the above section we have discussed many unconventional superconductors but one key feature that they all contain is that their crystal structures are all centrosymmetric. For the rest of this thesis the discussion will be centred around superconductors that lack a centre of inversion in their crystal structure. In centrosymmetric compounds the inversion symmetry of the compounds means that parity is a good quantum number. For superconducting systems this implies that the Cooper pairs must form in either a spin singlet or triplet configuration. In the case where a compound is noncentrosymmetric (NCS) and has a finite antisymmetric spin-orbit coupling (ASOC) parity is no longer a good quantum number. The superconducting state in these compounds can no longer be classified as either spin singlet or triplet but rather an admixture of the two.

The discovery of superconductivity in noncentrosymmetric compounds was in 1960 however the importance of this was not highlighted by the author [57, 58].

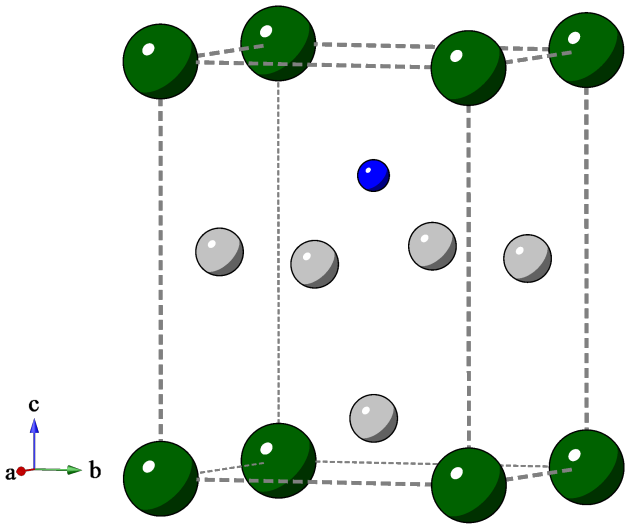

Figure 1.4: Crystal structure of the heavy fermion noncentrosymmetric $CePt_3Si$. The Ce atoms are show in green, Pt atoms shown in grey and the Si atom shown in blue. The absence of inversion symmetry is easily observable in this structure.

The discovery of superconductivity in $CePt_3Si$ triggered an intensive experimental and theoretical response from the superconductivity research community [59, 60]. In the next section, noncentrosymmetric heavy fermion superconductors shall be highlighted. Due to difficulties in separating the heavy fermion behaviour from that of noncentrosymmetric superconductivity weakly correlated noncentrosymmetric systems are then discussed.

1.3 Heavy Fermion Noncentrosymmetric Superconductors

1.3.1 Superconductivity in $CePt_3Si$

The first reported heavy fermion noncentrosymmetric compound was $CePt_3Si$ which crystallises in the tetragonal crystal structure (space group $P4mm$) [61, 62] as shown in Fig. 1.4. $CePt_3Si$ orders antiferromagnetically below 2.25 K [63] and is the seen to have a superconducting transition below 0.75 K in polycrystalline samples. Evidence for heavy fermion behaviour in $CePt_3Si$ is seen in the Kondo interaction causing a substantial enhancement to the Sommerfled coefficient with $\gamma_n \approx 400$ mJ/mol K^2 and a measured ordered moment 0.16 μ_B/Ce which is much smaller than the expected 0.65 μ_B/Ce predicted by the crystal electric field scheme [63, 64]. μSR measurements have shown the coexistence of both long-range magnetic ordering

and superconductivity [65]. If the superconducting gap structure is isotropic a BCS exponential temperature dependence is expected. If instead nodes exist in the superconducting gap structure this gives rise to power law behaviour in the low-temperature dependence of superconducting properties. A line nodal structure to the superconducting gap has been detected in specific heat, penetration depth and thermal conductivity due to the power law dependence of the low-temperature superconducting properties in $CePt_3Si$ [66, 67, 68].

Several unconventional properties of the superconducting state have been reported in $CePt_3Si$ which has stimulated much of the theoretical and experimental research in this class of materials. The first of the unconventional properties of $CePt_3Si$ is the anomalously large width of the superconducting transition. The upper critical field for $CePt_3Si$ has also been reported to exceed the Pauli limit of $\mu_0 H_{\rm p} = 1.4$ T with $\mu_0 H_{\rm c2} = 5$ T [61]. This Pauli limit violation is normally taken as evidence of spin triplet superconductivity. Other anomalous behaviour includes nuclear magnetic resonance (NMR) experiments reporting that the electronic-spin paramagnetic susceptibility $\chi_{\rm s}$ remains constant across all orientations of the crystal [69].

1.3.2 CeTX_3 Family

After the first reports of noncentrosymmetric superconductivity in $CePt_3Si$ it was soon discovered by Kimura that $CeRhSi_3$ is a superconductor under pressure [70]. $CeRhSi_3$ crystallises in the $BaNiSi_3$-type tetragonal structure with noncentrosymmetric space group $I4mm$. At ambient pressure $CeRhSi_3$ is seen to order antiferromagnetically with $T_{\rm N} = 1.6$ K. Kondo interactions class $CeRhSi_3$ as a heavy fermion superconductor as is seen in the enhancement to the Sommerfeld coefficient $\gamma_{\rm N} = 110$ mJ/mol K^2 [71]. Much like the centrosymmetric heavy fermion superconductors as the pressure is increased $T_{\rm N}$ is seen to increase to a maxima at 9 kbar before being suppressed and eventually connecting with a superconducting dome. The superconducting transition temperature is seen to increase with increasing pressure up to a plateau at 30 kbar where $T_{\rm c} = 1.05$ K. The upper critical field of $CeRhSi_3$ is much larger than the Pauli limiting field with $\mu_0 H_{\rm c2} = 16$ T reported at $p = 26$ kbar [72]. Again this extraordinarily larger upper critical field is taken as evidence for spin triplet superconductivity.

Several other members of the CeTX_3 family, where T = transition metal and X = Si or Ge, crystallise in the $BaNiSi_3$-type tetragonal structure with space group $I4mm$ which lacks mirror symmetry along the c-axis. Of these only a few have been reported to show superconductivity under pressure: $CeRhSi_3$ (as discussed

above), $CeIrSi_3$ at $p > 18$ kbar [73], $CeCoGe_3$ at $p > 43$ kbar [74] and $CeIrGe_3$ at $p > 200$ kbar [75].

$CeIrSi_3$ is isotructural to $CeRhSi_3$ so it is expected that the compounds will exhibit similar superconducting and normal state behaviours. $CeIrSi_3$ is reported to have a higher ordering temperature $T_N = 5$ K and a higher pressure necessary for superconductivity. As pressure is increased T_N is suppressed with superconductivity appearing at 18 kbar where is reaches its maximum transition temperature at 25 kbar [73]. Heat capacity measurements performed under pressure show a very sharp superconducting transition with $\Delta C/\gamma_c T = 5.7$ which is much larger than the BCS value of 1.43. This indicates strong coupling within the superconductor and could go some way to explain the anomalously large upper critical field [76]. It is worth noting that is one of the largest values of $\Delta C/\gamma_c T$ reported in any superconductor.

$CeCoGe_3$ while isotructural to $CeIrSi_3$ and $CeRhSi_3$ presents a rather different set of behaviours. $CeCoGe_3$ has a higher antiferromagnetic ordering temperature $T_{N1} = 21$ K than the previous compounds. Unlike the other compounds it has been reported to have two more antiferromagnetic transitions. Under applied pressure the antiferromagnetic phase is suppressed before superconductivity is detected between 54 and 75 kbar with a maximum $T_c = 0.69$ K. The Kondo interaction is also seen to be diminished due to a small enhancement in the Sommerfeld coefficient $\gamma_n = 49$ mJ/mol K^2 [75, 77].

Many other compounds have been reported on in the $CeTX_3$ family with $CeRhGe_3$ [71], $CePtSi_3$ [78] and $CePdSi_3$ [79] boasting antiferromagnetic ordering at ambient pressures. No superconductivity has presently been found in these compounds under pressure. In $CeRuSi_3$, $CeOsSi_3$ and $CeCoSi_3$ no magnetic ordering or superconductivity has been observed [78].

Heavy fermion noncentrosymmetric superconductors have proved to be a bountiful resource for investigating the effects of strong correlations and the potential for singlet-triplet mixing. They have provided many challenges to the research community. Most notably there are few discovered heavy fermion superconductors with only $CePt_3Si$, $CeTX_3$ and UIr [80] having been reported. From an experimental stand point only $CePt_3Si$ is a superconductor at ambient pressure, this necessitates the use of pressure to access the superconducting regime which complicates most experimental measurement techniques. From a theoretical stand point it has proved challenging to isolate the behaviours caused by strong correlations and those caused by singlet triplet mixing. Many of the results for $CePt_3Si$ take as evidence for pair mixing can be explained through other means. For example; the

line nodal order parameter can be explained by magnetic ordering in $CePt_3Si$ while the constant spin susceptibility in all crystal directions can be explained by strong correlations [81, 82]. Research has now turned to investigate the superconducting properties of noncentrosymmetric systems which lack strong correlations.

1.4 Weakly Correlated Noncentrosymmetric Superconductors

Recently experimental and theoretical investigations have taken place into noncentrosymmetric superconductors without f or d electrons. A large number of noncentrosymmetric superconductors without strongly correlated electrons have been reported. A number of these compounds will discussed in this section with priority given to those with chiral noncentrosymmetric structures and those where time-reversal symmetry breaking has been reported.

1.4.1 Nodal Versus Nodeless Superconductivity in Li_2-$(Pd_{1-x}Pt_x)_3B$

Due to the highly tunable nature of the spin-orbit coupling parameter $Li_2(Pd_{1-x}Pt_x)_3B$ is one of the most interesting examples of noncentrosymmetric superconductors with weak correlations [83, 84, 60]. By doping from Pd to Pt the ASOC is increased due to the replacing 4d electrons with 5d electrons. $Li_2\,(Pd_{1-x}Pt_x)_3B$ crystallises in a cubic antiperovskite structure with the space group $P4_332$. This space group is both noncentrosymmetric and chiral. Superconductivity is observed across all doping concentrations in $Li_2\,(Pd_{1-x}Pt_x)_3B$ with Li_2Pd_3B and Li_2Pt_3B having superconducting transitions at 7 and 2.2 K respectively. The small magnitude of the Sommerfeld coefficient with $\gamma_N \approx 7{-}9$ mJ/mol K^2 provides confirmation of the weak correlations in $Li_2\,(Pd_{1-x}Pt_x)_3B$ [85]. Evidence of the effects of ASOC on the superconducting state in $Li_2\,(Pd_{1-x}Pt_x)_3B$ has been seen in both thermodynamic and NMR measurements where Li_2Pd_3B is reported to have fully gapped s-wave superconductivity [86, 87]. However, in Li_2Pt_3B these measurements have indicated a line nodal structure to the superconducting gap. Penetration depth measurements have also observed the same behaviour, with a exponential temperature dependence in Li_2Pd_3B and a linear temperature dependence in Li_2Pt_3B, as shown in Fig. 1.5 [4]. The penetration depth data has been modelled using a two-gap function which allows for the coexistence of spin singlet and triplet pairing. Using this model it was found that by doping from the Pd to Pt the triplet component is increased. While this is taken as strong evidence from singlet-triplet

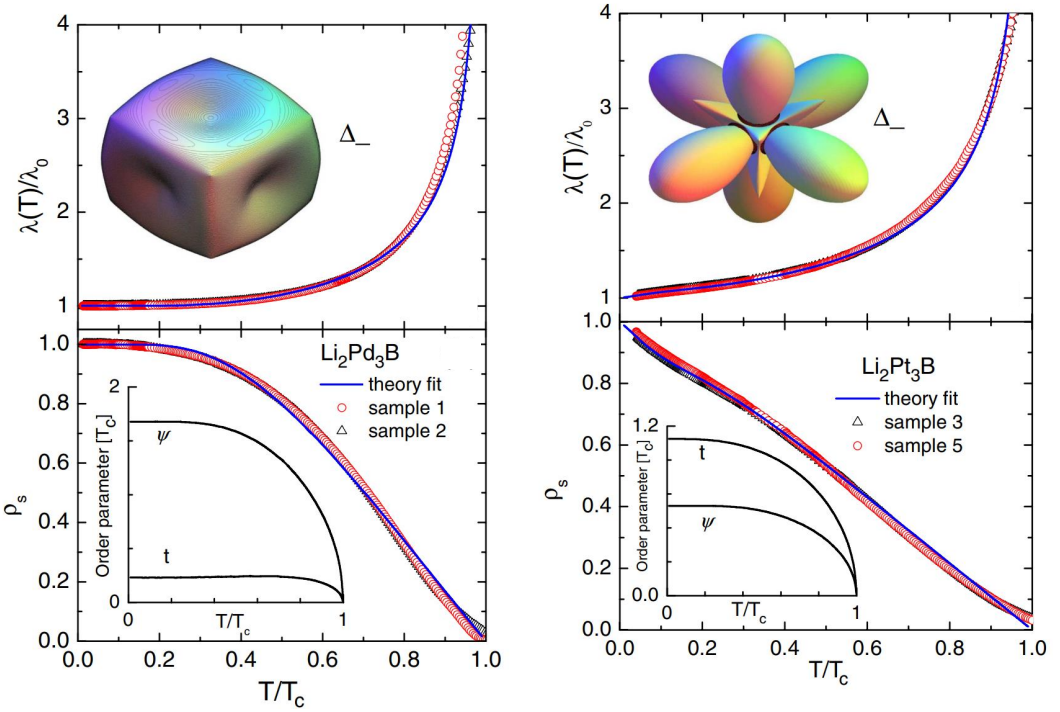

Figure 1.5: Normalised temperature dependence of the normalised penetration depth and superfluid density in Li_2Pd_3B (left) and Li_2Pt_3B (right). The blue lines indicate a fit to the data using a model of mixed singlet-triplet pairing. The near linear superfluid density in Li_2Pt_3B is evidence of line nodes in the superconducting gap. The curved behaviour of the superfluid density in Li_2Pd_3B indicates an anisotropic s-wave gap. Adapted from Ref. [4].

mixing other explanations have been offered for this behaviour. Electronic band calculations have seen that when bands cross the Fermi level they have an enhanced d-wave characteristic and show significant nesting. This would suggest that the gap structure can be explained as $s_{\pm}$ state with accidental nodes [88]. Mo_3Al_2C also crystallises in the cubic antiperovskite structure with the space group $P4_332$ which as previously mentioned is also chiral as well as noncentrosymmetric [89].

1.4.2 Line Nodal Superconductivity in Mo_3Al_2C

Mo_3Al_2C has a superconducting transition at $T_c = 9.05$ K. Evidence for unconventional superconducting behaviour is present in specific heat capacity measurements showing a clear deviation from the exponential temperature dependence of a BCS superconductor and rather shows a line nodal gap [90]. Enhancement to the superconducting transition temperature under pressure suggests the presence of

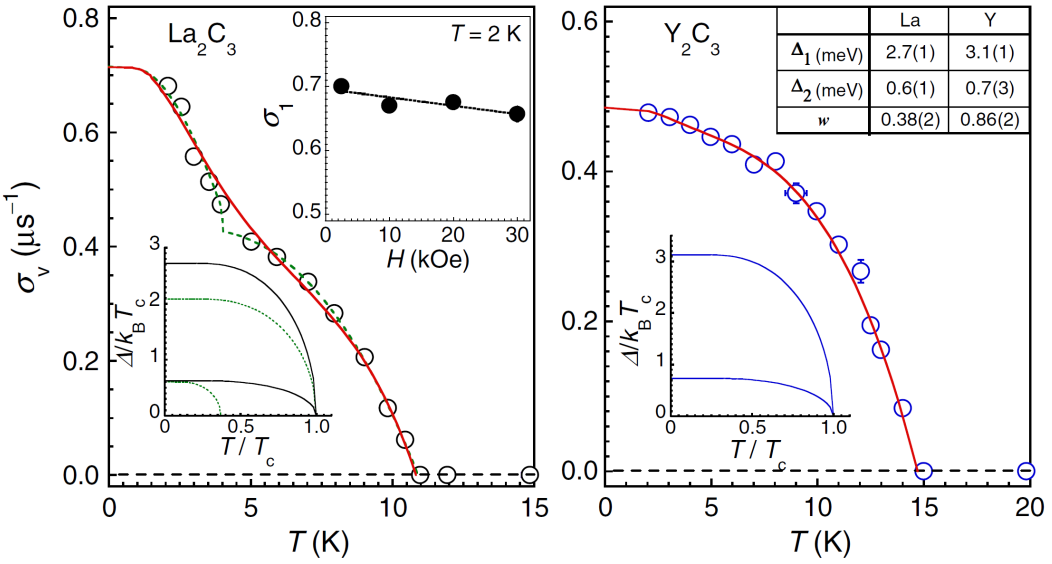

Figure 1.6: Muon spin relaxation rate of La_2C_3 (left) and Y_2C_3 (right) as a function of temperature. The red line shows the fit to the data using a two-gap model. Insets show the size of the two superconducting gaps for each compound. Adapted from Ref. [5]

singlet-triplet mixing [91].

1.4.3 Multigap Superconductivity in Y_2C_3 and La_2C_3

Nodal structures in the superconducting gap are highly sought after for proof of singlet-triplet mixing but they are not the only available superconducting gap configuration to allow for an admixture to form. Two-band fully gapped structures are also anticipated to host singlet-triplet mixing if these gaps are anisotropic. One example of a weakly correlated noncentrosymmetric superconductors that may contain two-gap superconducting band structures are Y_2C_3 [92] and La_2C_3 [93]. This pair of superconductors crystallise in a body-centred noncentrosymmetric structure with space group $I\bar{4}3d$. Y_2C_3 has a superconducting transition at $T_c = 18$ K [94, 95] and La_2C_3 has a superconducting transition at $T_c = 13.2$ K [93] however, T_c is highly sample dependent. Penetration depth measurements on Y_2C_3 show a linear temperature dependence which indicates line nodes in the superconducting gap [96], unfortunately no other technique has been able to replicate this result. Thermodynamic, μSR and NMR measurements show a fully gapped s-wave superconductor [97, 98]. μSR and NMR measurements can also be modelled using a two-gap model with one large superconducting gap dominating with a small contribution provided by a much

smaller gap [5] as shown in Fig. 1.6. Tunnel diode oscillation (TDO) measurements of the penetration depth can be modelled with a two-gap structure but below 10% of T_c a noticeable difference can be seen between the two gap and the line nodal models with the line nodal being the best fit to the experimental data. It is worth noting that TDO measurements have been performed down to 90 mK while other techniques have only measured down to 1.8 K. The upper critical field of Y_2C_3 $\mu_0 H_{c2} \approx 28$ T is seen to slightly exceed the weak coupling Pauli limit [96, 99]. This is normally taken as an indication of triplet pairing in a superconductor. There are several other reasons for this slight enhancement to the upper critical field that do not require singlet-triplet mixing. La_2C_3 plays host to two-gap superconductivity which has been confirmed by μSR [5, 100] and photoemission spectroscopy [101]. Heat capacity measurements performed on La_2C_3 suggests the superconductivity is dominated by a single gap s-wave model with strong electron-phonon coupling [102].

1.4.4 Coexistence of Magnetism and the Superconducting State

The observation of time-reversal symmetry breaking in noncentrosymmetric superconductors has intrigued both the experimental and theoretical research community. Time-reversal symmetry breaking (TRSB) in noncentrosymmetric superconductors is often taken as evidence of unconventional superconductivity since certain triplet states will break time-reversal symmetry [103]. $LaNiC_2$ was the first noncentrosymmetric compound where the observation of time-reversal symmetry breaking was reported [104]. $LaNiC_2$ crystallises in the noncentrosymmetric orthorhombic $CeNiC_2$ structure with space group $Amm2$ [105]. There has been some controversy from heat capacity measurements, the first report showed a T^3 temperature dependence to the heat capacity [105], this has since been found to be incorrect. With more modern instrumentation a exponential BCS temperature dependence has now been reported [106, 107]. Magnetic penetration depths measurements have also proved to be similarly convoluted with both point node [108] and two gap s-wave structures being reported [107]. The discrepancy seen in penetration depth measurements has found to be due to magnetic impurities. μSR measurements have observed time-reversal symmetry breaking in $LaNiC_2$ [104]. Symmetry analysis on the crystal structure of $LaNiC_2$ reveals there are three possible non-unitary states though in the presence of spin-orbit coupling these three states are disallowed [109]. The detection of time-reversal symmetry breaking in the centrosymmetric $LaNiGa_2$ highlights that the observed behaviour behind the superconducting state in $LaNiC_2$ can not be attributed to the noncentrosymmetric structure [110].

Recently a large body of experimental work has been published on the Re-

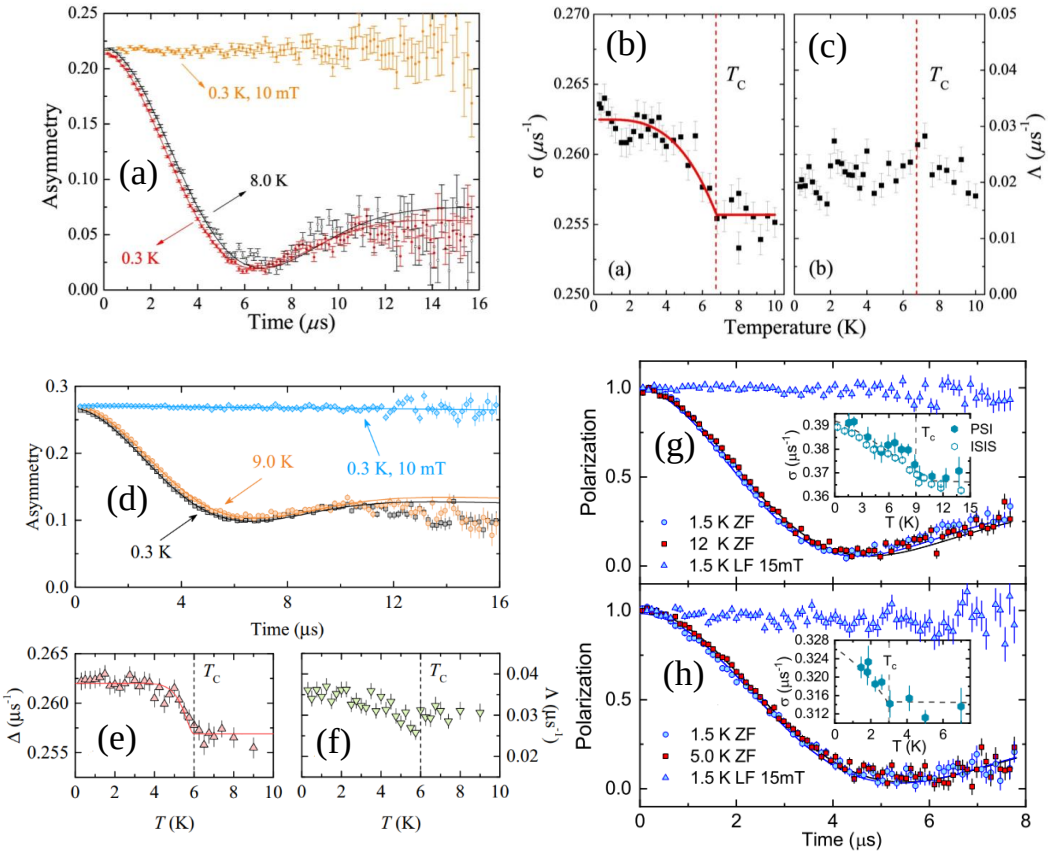

Figure 1.7: (a) Zero-field μSR measurements of Re_6Zr collected at 0.3 (red) and 8.0 K (black) where a faster decay in the asymmetry is observed below T_c. (b) The temperature dependence of Kubo-Toyabe relaxation rate σ where there is a clear increase at T_c and (c) the exponential relaxation rate Λ which remains constant. (d) Zero-field μSR measurements of Re_6Hf collected at 0.3 (black) and 9.0 K (orange) where a faster decay in the asymmetry is observed below T_c. (e) The temperature dependence of Kubo-Toyabe relaxation rate Δ where there is a clear increase at T_c and (f) the exponential relaxation rate Λ which remains constant. (g) Zero-field μSR time spectra for $Re_{0.82}Nb_{0.18}$ above (red) and below (blue) the superconducting transition. The inset shows the temperature dependence of the Kubo-Toyabe relaxation rate σ where there is a clear increase at T_c from measurements done at ISIS and PSI. (h) Zero-field μSR time spectra for pure rhenium above (red) and below (blue) the superconducting transition. The inset shows the temperature dependence of the Kubo-Toyabe relaxation rate σ where there is a clear increase at T_c. Figures (a, b, c) taken from Ref. [6], (d, e, f) taken from Ref. [7] and (g, h) taken from Ref. [8]

based α-Mn noncentrosymmetric compounds. In this thesis the superconducting and normal state properties of Re_6Zr will be discussed. It is worth summarising the

findings of these recent reports in this section. Re-based α-Mn noncentrosymmetric compounds crystallise in the cubic noncentrosymmetric space group $I\bar{4}3m$ [57]. These compounds have a particularly large unit cell with 58 atoms occupying 4 sites. Re_6Zr [6, 111, 112], Re_6Hf [113, 114, 7], Re_6Ti [115], $Re_{24}Ti_5$ [116, 117], Re_3Ta [118], Re_3W [119, 120, 121] and $Re_{1-x}Nb_x$ [122, 123] are all bulk superconductors with full gapped s-wave superconductivity measured by heat capacity and penetration depth. NMR measurements have also confirmed the isotropic s-wave nature of the superconductivity in Re_6Zr. As a result of time-reversal symmetry breaking spontaneous magnetic moments are expect to arise below T_c which can be detected using μSR. Re_6Zr [6], Re_6Hf [7], Re_6Ti [115], $Re_{0.82}Nb_{0.18}$ [8] and $Re_{24}Ti_5$ [117], have been observed to break time-reversal symmetry as shown in Fig. 1.7. Very recently a paper has been published showing that pure Re is observed to break time-reversal symmetry below its T_c suggesting that the origin of this behaviour is not due to broken inversion symmetry but rather due to the inherent large spin-orbit coupling strength of Re [8]. No time-reversal symmetry breaking has been observed in Re_3Ta and Re_3W.

La_7Ir_3 a hexagonal noncentrosymmetric compound (space group $P6_3mc$) has also been reported to break time-reversal symmetry breaking and to have fully gapped s-wave superconductivity [124, 125]. The superconducting and normal state properties of polycrystalline La_7Ir_3 shall be discussed later in this thesis along with the synthesis and characterisation of single crystals of La_7Ir_3.

The multitude of experimental phenomena presented above gives an indication of the large range of exotic superconducting properties noncentrosymmetric superconductors can exhibit. The results discussed above are summarised in Table 1.1 along with other noncentrosymmetric compounds that have not been discussed here. It is clear that there is a need for high quality single crystals, more experimental data on existing compounds and the discovery of new noncentrosymmetric compounds with interesting superconducting properties to gain further understanding into the role crystal structure plays on the superconducting state in these systems.

1.5 Thesis Overview

In this thesis experimental data from several weakly correlated noncentrosymmetric systems will be presented and discussed. Below is summary of upcoming chapters and their contents:

- **Chapter 2, Theory of Superconductivity**

In this chapter a brief discussion of the theoretical background of superconductivity will take place. The chapter begins by examining the London model for superconductivity before discussing the Ginzburg-Landau theory of superconductivity along with BCS theory.

- **Chapter 3, Experimental Details**

  In this chapter the experimental techniques that have been utilised to grow and characterise the materials present in this thesis are discussed in detail.

- **Chapter 4, Superconducting and Normal-State Properties of Cubic Noncentrosymmetric Re_6Zr**

  The normal-state and superconducting properties of Re_6Zr are presented in this chapter along with neutron diffraction measurements. We compare our results with the discovery of time-reversal symmetry breaking in pure centrosymmetric rhenium.

- **Chapter 5, Hexagonal Noncentrosymmetric Superconductors La_7Pd_3 and La_7Ir_3**

  This chapter begins by discussing the superconducting properties of La_7Pd_3 along with the detection of time-reversal symmetry breaking in this system. Finally we discuss the single crystal growth and characterisation of La_7Ir_3. We compare these results with other members of La_7X family of superconductors.

- **Chapter 6, Chiral Noncentrosymmetric Superconductors $TaRh_2B_2$ and $NbRh_2B_2$**

  $TaRh_2B_2$ and $NbRh_2B_2$ are new chiral noncentrosymmetric superconductors previously reported to violate the Pauli limiting field. In this chapter, the superconducting properties of $TaRh_2B_2$ and $NbRh_2B_2$ are characterised using magnetisation, resistivity, heat capacity and muon spin resonance techniques. Using these techniques the superconducting order parameter within these compounds is investigated.

- **Chapter 7, Summary and Conclusions**

  A summary of the key results and outcomes as well as a discussion on the remaining challenges.

Table 1.1: Normal-state and superconducting properties of some noncentrosymmetric superconductors discussed in chapter 1. The superconducting gap is indicated by F for fully gapped, PN for point nodes, LN for line nodal, U for unknown and 2 for indicating if two gaps are present.

Compound	Space Group	T_c (K)	γ_N (mJ/mol K^2)	$\mu_0 H_{c2}$ (T)	Superconducting Gap	TRSB
$CePt_3Si$	$P4mm$	0.75	390	3.2	LN	N
$CeRhSi_3$	$I4mm$	1.05	120	30	U	N
$CeIrSi_3$	$I4mm$	1.6	125	45	LN	N
$CeCoGe_3$	$I4mm$	0.64	32	20	U	N
UIr	$P2_1$	0.13	49	0.026	U	N
Li_2Pd_3B	$P4_332$	8	9	5	F2	N
Li_2Pt_3B	$P4_332$	2.8	7	2	LN	N
Mo_3Al_2C	$P4_132$	9	17.8	15	PN	N
Y_2C_3	$I\bar{4}3d$	18	6.3	30	LN/F2	N
La_2C_3	$I\bar{4}3d$	13	10.6	19	F2	N
BiPd	$P2_1$	3.8	4	0.8	F2	N
$LaNiC_2$	$Amm2$	2.7	7.7	0.5	F2	Y
Re_6Hf	$I\bar{4}3m$	5.96	27.2	12.2	F	Y
Re_3W	$I\bar{4}3m$	7.8	15.9	12.5	F	N
$Re_{24}Ti_5$	$I\bar{4}3m$	5.8	111.8	10.75	F	Y
La_7Ir_3	$P6_3mc$	2.25	47	2	F	Y

Chapter 2

Theory of Superconductivity

2.1 Introduction

When a material known as a superconductor is cooled below its transition temperature, T_c, it exhibits two distinctive experimental properties: 1) zero electrical resistance [15] and 2) perfect diamagnetism [16]. Diamagnetism is a behaviour of a material to weakly oppose an applied magnetic field. Superconductors exhibit perfect diamagnetism when cooled below T_c in a low applied field, the field is unable to penetrate the material beyond the surface and all magnetic flux is expelled from the bulk of the material. This behaviour is called the Meissner-Ochsenfeld effect and it is the ultimate test of if a material is truly a superconductor. It is important to note that the Meissner-Ochsenfeld effect does not come about as a result of the material have zero electrical resistance. If zero electrical resistance was the cause of this behaviour when a superconductor is cooled in an applied field, when the applied field is then removed below the T_c eddy currents would persist and persevere the trapped field in the interior of the superconductor. Expulsion of the magnetic flux implies that the superconducting state is a true thermodynamic equilibrium state.

2.2 Elementary Phenomenological Theory

This section will outline some of the early attempts to phenomenologically explain the key experimental behaviours of superconductors. The key ideas and results of each of these theories will be highlighted.

2.2.1 London Theory

The first attempt to explain Meissner-Ochsenfeld effect was with the London model. The London model tried to reconcile Maxwell's equations for electrodynamics with a two fluid model for the superconducting state. The two fluids in question are normal-state electrons n mixed with a fraction of anomalous superconducting electrons n_{s}. The model was incredibly successful in describing the two key properties of superconductors. Although a phenomenological model the electrodynamic properties are captured by the two London equations [126]

$$\frac{\partial \mathbf{J}_{\mathrm{s}}}{\partial t} = \frac{n_{\mathrm{s}} e^2}{m_{\mathrm{e}}} \mathbf{E}, \tag{2.1}$$

$$\nabla \times \mathbf{J}_{\mathrm{s}} = \frac{n_{\mathrm{s}} e^2}{m_{\mathrm{e}}} \mathbf{B}, \tag{2.2}$$

where $\mathbf{B}$ and $\mathbf{E}$ are the magnetic flux density and the electric field respectively, m_{e} is the mass of an electron, n_{s} is the number density of superconducting electrons and $\mathbf{J}_{\mathrm{s}}$ is the supercurrent density. Equation (2.1) describes the phenomenon of zero electric resistance since any field applied to the superconducting electrons will accelerate them rather than apply a sustained velocity against the resistance as described in Ohm's law. When Eq. (2.2) is applied to Ampere's law the follow result is found

$$\nabla^2 \mathbf{B} = \frac{\mathbf{B}}{\lambda_{\mathrm{L}}^2}, \tag{2.3}$$

where the λ_{L} is the London penetration depth, an intrinsic property of the superconducting materials and describes the penetration of the magnetic field into the superconductor in the superconducting state which is given by

$$\lambda_{\mathrm{L}} = \sqrt{\frac{m_{\mathrm{e}} c^2}{4\pi n_{\mathrm{s}} e^2}}. \tag{2.4}$$

Now consider the case of a constant magnetic field $\mathbf{B}$ applied to an infinite superconducting slab the field distribution in the x direction is given by

$$\mathbf{B}_{\mathrm{x}} = -\lambda_{\mathrm{L}}^2 \frac{d^2 \mathbf{B}_{\mathrm{x}}}{d\mathrm{x}^2}, \tag{2.5}$$

one solution to this differential equation is

$$\mathbf{B}_{\mathrm{x}}(\mathrm{x}) = \mathbf{B}_{\mathrm{x}}(0) \exp\left(\frac{-\mathrm{x}}{\lambda_{\mathrm{L}}}\right), \tag{2.6}$$

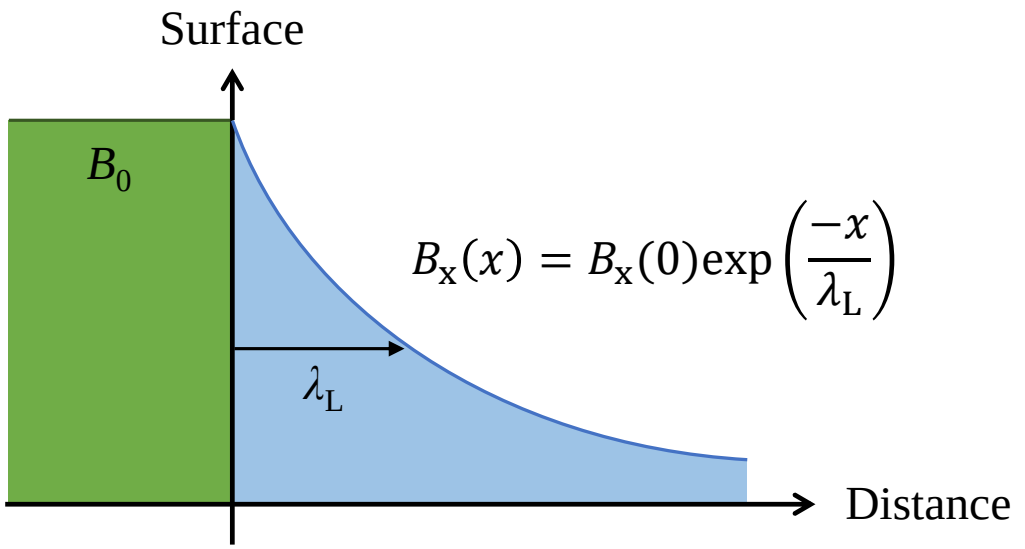

Figure 2.1: Schematic of the Meissner effect from the London interpretation of superconductivity. The magnetic field is screened exponentially from the interior of the slab with a penetration depth λ_L.

which describes the Meissner-Ochsenfeld effect where the applied magnetic field is screened exponentially from the interior of the slab with a penetration depth λ_L as shown in Fig. 2.1. One restriction of the London equations is that they have no temperature dependence for the magnetic penetration depth which did not match observed behaviour. By using the temperature dependence for the number density of superconducting electrons n_s proposed by Gorter-Casimir [127] the London penetration depth can given by

$$\lambda(T) = \frac{\lambda(0)}{\sqrt{\left[1 - \left(\frac{T}{T_c}\right)^4\right]}}. \tag{2.7}$$

From Eq. (2.7) it can be seen that as the temperature increases towards the transition temperature the penetration depth trends to infinity.

2.2.2 Landau Theory of Second Order Phase Transitions

The limitations of the London model are very clear; the London equations no longer hold when the number density of the superconducting electrons n_s varies. It is also desirable to have a more general framework through which n_s can be related to external parameters such as the applied field or the current. A better under-

standing of superconductivity can be gained by considering the thermodynamics of the superconducting phase transition. The Ginzburg-Landau theory use Landau's general theory of second order phase transitions to describe the change from an disordered to an ordered state. A example of a second order phase transition that can be modelled by Landau's theory is that of a transition from a ferromagnetic to paramagnetic phase. Here a spontaneous magnetisation M is seen below a critical temperature T_c and vanishes above T_c. A minimum in the Helmholtz free energy F must occur at the T_c with the conditions: For $T > T_c$, $M = 0$ and $T < T_c$, $M \neq 0$. For a second order phase transition the Helmholtz free energy F is expressed as:

$$F(T, M) = F(T, 0) + a(T - T_c) M^2 + bM^4 + c|\nabla M|^2, \tag{2.8}$$

where it is assumed that a and $b > 0$. It can be seen that if $T > T_c$, F is minimised only for $M = 0$ but for $T < T_c$ there is a non-zero solution:

$$M^2 = \frac{b(T_c - T)}{2b}. \tag{2.9}$$

This solution shows M grows perpetually from zero when cooled below the transition temperature. If Eq. (2.8) is differentiated it remains continuous at the phase transition, however, if Eq. (2.8) is differentiated twice a discontinuity arises at the phase transition. A discontinuity will therefore be seen in parameters that are dependent on the second derivative of the free energy, for example, the anomaly in the specific heat of the superconducting transition.

2.2.3 Ginzburg-Landau Theory of Superconductivity

In the Ginzburg-Landau theory of superconductivity instead of using spontaneous magnetisation M as discussed above, Ginzburg and Landau postulated that an order parameter $\psi(\mathbf{r})$ can be used to explain the superconducting transition. The wavefunction for this order parameter is defined as

$$\psi(\mathbf{r}) = |\psi(\mathbf{r})| \exp^{i\varphi(\mathbf{r})}, \tag{2.10}$$

which has the following properties: 1) $|\psi * \psi|$ is interpreted as the number of superconducting electrons at point $\mathbf{r}$, 2) $\varphi(\mathbf{r})$ is related to the supercurrent, and 3) $\psi \neq 0$ below T_c and $\psi = 0$ above T_c. Using Landau's theory of second order phase transitions Ginzburg and Landau have defined the Helmholtz free energy with the following form

$$F_{\mathrm{s}} = F_{\mathrm{n}} + \alpha|\psi|^2 + \frac{\beta}{2}|\psi|^4 + \frac{\hbar}{2m}\left(\nabla|\psi|\right)^2 + \frac{1}{2}|\psi|^2 m\mathbf{v}_{\mathrm{s}}^2 + \frac{\left(\mathbf{B}-\mathbf{B}_{\mathrm{app}}\right)^2}{2\mu_0}, \tag{2.11}$$

where $\mathbf{v}_{\mathrm{s}}$ is the superfluid velocity

$$\mathbf{v}_{\mathrm{s}} = \frac{1}{m}\left(\hbar\nabla\varphi - 2e\mathbf{A}\right). \tag{2.12}$$

Here F_{s} is the superconducting state free energy density, F_{n} is the normal-state free energy density, $\mathbf{B}$ is the total magnetic field, $\mathbf{B}_{\mathrm{app}}$ is the contribution from the external magnetic field and $\mathbf{A}$ is the magnetic vector potential. The usefulness of these Ginzburg-Landau equations quickly becomes apparent when you assume a homogeneous distribution. In this case the gradient terms equal zero and a minimised solution can be found in a similar manner to Eq. (2.9). It can be seen that there is a critical field above which the free energy of the Meissner state ($B = 0$) is greater than the free energy of the normal-state implying there is a phase transition at a critical field known as the thermodynamic critical field B_{c}. Phenomenologically it was found that B_{c} follows a parabolic temperature dependence given by [128]:

$$B_{\mathrm{c}}\left(T\right) = B_{\mathrm{c}}\left(0\right)\left[1 - \left(\frac{T}{T_{\mathrm{c}}}\right)^2\right]. \tag{2.13}$$

The magnetic phase diagram for Eq. (2.13) is drawn in Fig. 2.2. Superconductors that follow this behaviour are categorised as type-I superconductors. However, it was found that samples existed that could maintain the superconducting state well above B_{c}. These materials are categorised as type-II superconductors where above a lower critical field B_{c1}, the superconductor enters a mixed state where magnetic flux can penetrate through the superconductor. It was later predicted by Abrikosov that the magnetic field penetration must be in the form of magnetic vortices containing exactly one magnetic flux quantum of magnitude [19]:

$$\Phi_0 = \frac{h}{2e} = 2.07 \times 10^{-15}\mathrm{Wb}. \tag{2.14}$$

There is then a further upper critical field B_{c2} where the material returns to the normal-state. The magnetic phase diagram for a type-II superconductor can be seen in Fig. 2.3.

The Ginzburg-Landau theory gives rise to two important characteristic length scales for superconductors. The first of these length scales is the effective penetration depth λ_{GL} which is proportional to the London penetration depth. The second

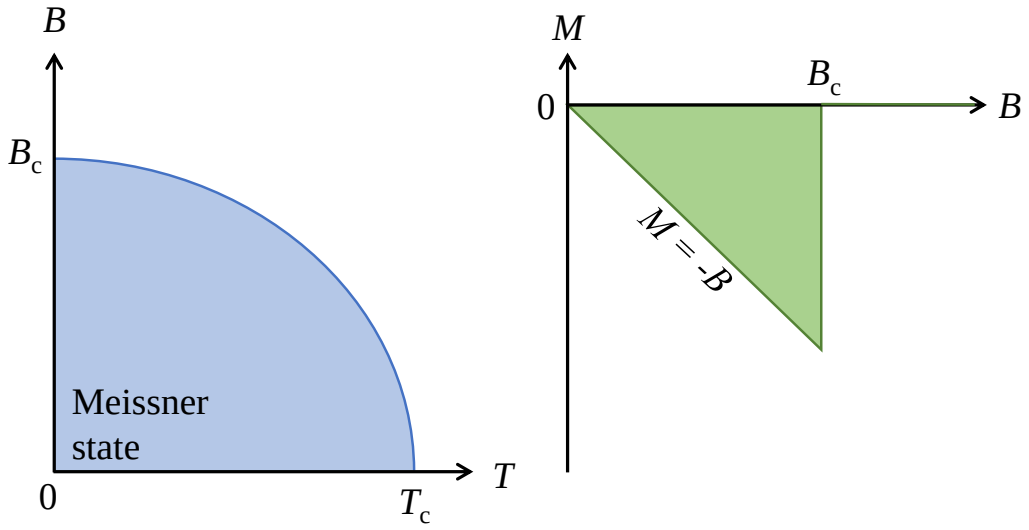

Figure 2.2: The left hand panel shows a schematic magnetic phase diagram for a type-I superconductor showing the Meissner state. The right hand panel shows a schematic of the magnetisation versus field for a type-I superconductor. The magnetisation has a gradient of -1 indicating complete flux expulsion up to the critical field at which point superconductivity is destroyed.

characteristic length scale is the Ginzburg-Landau coherence length ξ_{GL} which measures the distance over which the superconducting order parameter establishes itself (i.e. ψ rises from zero to its maximum over a distance ξ_{GL}). Both λ_{GL} and ξ_{GL} can determined experimentally from critical field measurements using the following relations

$$B_{\mathrm{c2}}^{\mathrm{orb}} = \frac{\Phi_0}{2\pi\xi_{\mathrm{GL}}^2}, \tag{2.15}$$

$$B_{\mathrm{c1}} = \frac{\Phi_0}{4\pi\lambda_{\mathrm{GL}}^2}\ln\kappa, \tag{2.16}$$

where B_{c2} and B_{c1} can be determined from magnetisation, resistivity and heat capacity measurements. Here, κ is the ratio of the two parameters giving the Ginzburg-Landau parameter

$$\kappa = \frac{\lambda_{\mathrm{GL}}}{\xi_{\mathrm{GL}}}. \tag{2.17}$$

The thermodynamic critical field can also be related to the two length scales by the following equation

$$B_{\mathrm{c}} = \frac{\Phi_0}{2\sqrt{2}\pi\lambda_{\mathrm{GL}}\xi_{\mathrm{GL}}}. \tag{2.18}$$

An important result can be found by relating $B_{\mathrm{c2}}^{\mathrm{orb}}$ and B_{c} by combining Eqs. (2.15)

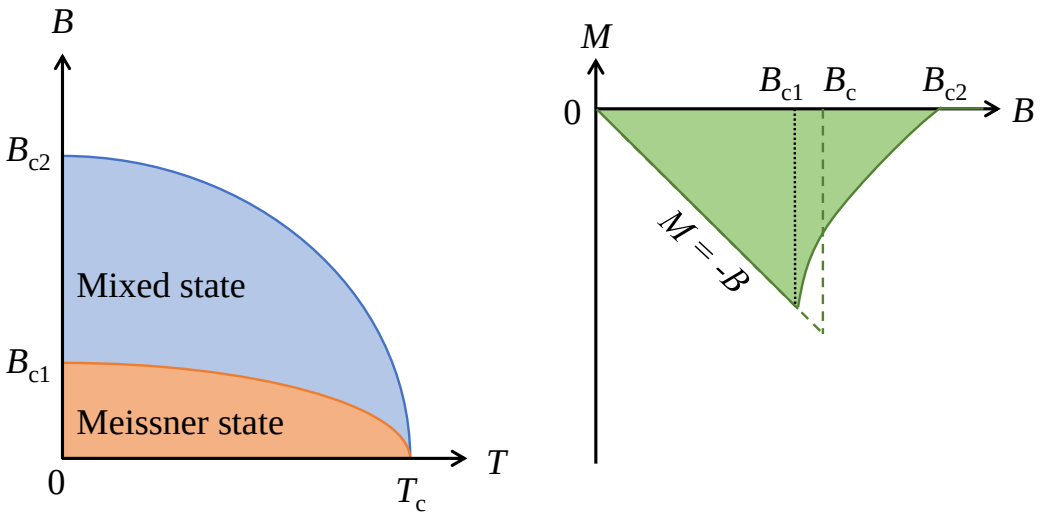

Figure 2.3: The left hand panel shows a schematic magnetic phase diagram for a type-II superconductor showing the upper and lower critical fields. The right hand panel shows a schematic of a typical magnetisation versus field for a type-II superconductor. Initially the magnetisation has a gradient of -1 indicating complete flux expulsion up to the lower critical field. Above this point the magnetic field penetrates into the superconductor forming the mixed state until the superconductivity is destroyed at the upper critical field.

and (2.18) to give

$$B_{c2} = \kappa\sqrt{2}B_c. \tag{2.19}$$

From this we can see that the two types of superconductivity. When $\kappa > 1/\sqrt{2}$ this implies that $B_{c2} > B_c$, therefore superconductivity can exist above B_c by the creation of a mixed state which would classify the superconductor as type-II. In the case where $\kappa < 1/\sqrt{2}$ then $B_{c2} < B_c$ which implies that the superconductivity is destroyed above the B_c which would classify the superconductor as type-I. The Ginzburg Landau parameter provides a useful way to classify superconductors using their characteristic length scales.

Numerical calculations in Ginzburg and Landau's original paper showed the surface energies of the interfaces between the normal and the superconducting state are positive if $\kappa < 1/\sqrt{2}$ and are negative if $\kappa > 1/\sqrt{2}$. They recognised that an intermediate state would be formed in a type-I superconductor with a non-zero demagnetisation factor though failed to realise any other distinctions between the positive and negative surface energies. In 1957 Abrikosov found that upon further inspection that a negative surface energy allows for nucleation of normal-state regions within the superconducting state. Abrikosov predicted that these

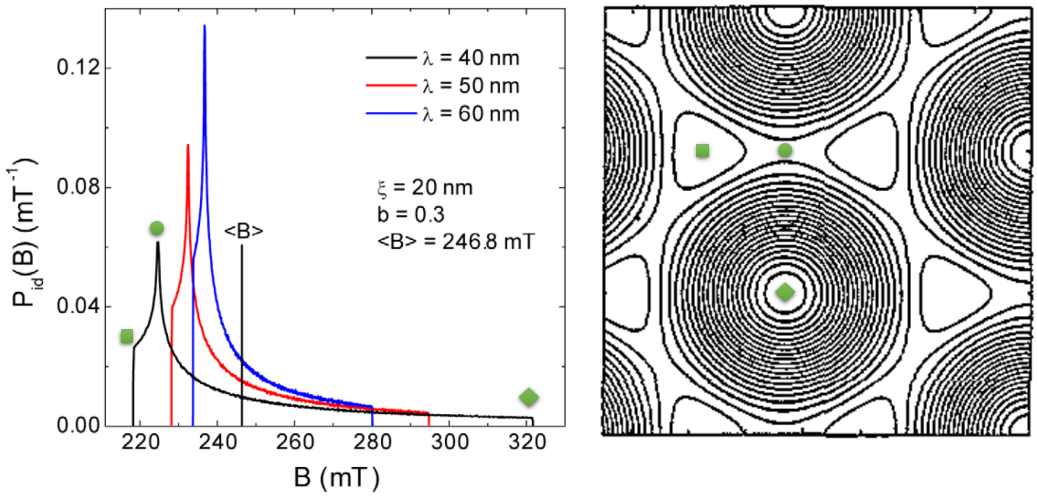

Figure 2.4: Left panel shows the local magnetic field distribution for a type-II superconductor in the mixed state with three different penetration depths. Adapted from Ref. [9]. Right panel shows the spatial magnetic field distribution for an hexagonal flux line lattice shown in a contour plot. Adapted from Ref. [10]

normal-state regions would be formed of magnetic vortices containing exactly one magnetic flux quantum. Each of these magnetic vortices is constructed of a normal core surrounded by a swirling supercurrent which screens the magnetic field from the superconducting region. It was further shown by Abrikosov that the magnetic vortices must form in a square lattice configuration due to the mutual repulsion of the vortices, these lattice configurations are known as the flux-line lattice. Later it was shown that the lowest energy state for a flux-line lattice is in a hexagonal configuration rather than a square [129].

By numerically solving the Ginzburg-Landau equations the magnetic field profile and probability distribution can be obtained as shown in Fig. 2.4. The probability distribution in Fig. 2.4 has a broad distribution with a peak in the in the probability which corresponds to a saddlepoint in the magnetic field profile. The maximum and minimum represent the vortex cores and the point which is equidistant between the cores respectively. Fig. 2.4 also shows that as the magnetic penetration depth increases the peak probability moves closer to the average field $\langle B \rangle$ and the overall distribution narrows.

2.3 Microscopic Theory of Superconductivity

2.3.1 Bardeen, Cooper and Schrieffer Model

The microscopic theory of superconductivity known as BCS theory showed in brief that electrons within a superconductor form pairs known as Cooper pairs. The electrons pair up due to an attractive interaction arising from their interaction with the lattice. The electron-phonon interactions allow for the pairs of electrons to have a bosonic like nature where they can condense into a quantum ground state and no longer interact with other electrons. The s-wave pairing symmetry is the simplest form which is where the Cooper pairs form spin-singlets with zero orbital angular momentum. A detailed summary of the BCS theory can be found in Refs. [20, 130, 131]. For this thesis it is worth summarising some important results of the BCS theory. The ground state wave function for Cooper pairs in the s-wave state from BCS theory is given by

$$|\Psi_{\mathrm{BCS}}\rangle = \prod_{k} \left(u_k^* + v_k^* c_{k\uparrow}^\dagger c_{-k\downarrow}^\dagger\right)|0\rangle, \tag{2.20}$$

where $|0\rangle$ is the vacuum state, u_k^* and v_k^* are complex wavefunctions where $|u_k|^2 + |v_k|^2 = 1$. $c_{k\uparrow}^\dagger$ and $c_{-k\downarrow}^\dagger$ represent the electron pair creation operators with crystal momenta k and $-k$. The lowest energy configuration for the wave function is spatially symmetric, isotropic interaction. To ensure that the overall pair wave function is antisymmetric it is required that the electron pair have opposite spins. The reduced Hamiltonian for the Cooper pair can then be given by summing the energy band dispersion $\epsilon_k = \left(\frac{\hbar^2 k}{2m} - \mu\right)$ with chemical potential μ with the sum of the attractive interaction between the electron pairs $V_{k,k'}$. This gives the following Hamiltonian

$$H = \sum_{k,\sigma=\uparrow\downarrow} \epsilon_k c_{k\sigma}^\dagger c_{-k\sigma}^\dagger + \frac{1}{2}\sum_{k,k'} c_{k\uparrow}^\dagger c_{-k\downarrow}^\dagger V_{k,k'} c_{k'\uparrow}^\dagger c_{-k'\downarrow}^\dagger. \tag{2.21}$$

By minimising the expectation value of the sum by equating it to zero the ground state of the system can be found. This minimisation gives the quasiparticle excitation energy

$$E_{\mathrm{k}} = \sqrt{\epsilon_{\mathrm{k}}^2 + \Delta_{\mathrm{k}}^2}, \tag{2.22}$$

where Δ_k is the gap energy of the excitation spectrum or rather the energy required to break up the pair electrons. At $T = 0$ the magnitude of the superconducting gap

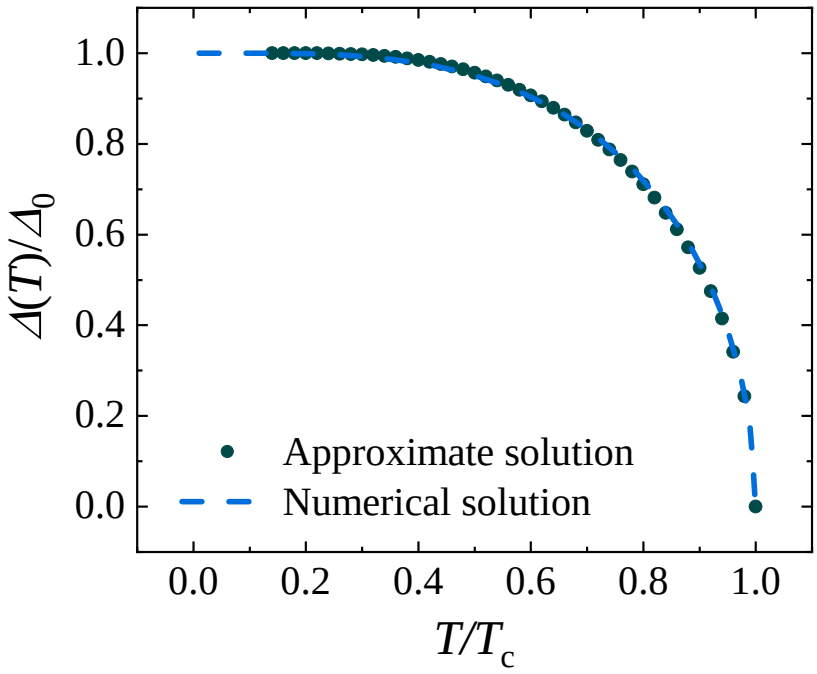

Figure 2.5: Normalised temperature dependence of the BCS energy gap from the numerical [11] (dark green circles) and the approximate solution [12] (blue dashed line) showing strong agreement between the two calculations.

is given by

$$\Delta_0 = 1.764 k_\mathrm{B} T_\mathrm{c} \tag{2.23}$$

where k_B is the Boltzmann constant. However at $T \neq 0$ an analytical solution can not be found, it is instead necessary to calculate $\Delta(T)$ numerically [11] or with the approximation [12]

$$\Delta = 1.764 k_\mathrm{B} T_\mathrm{c} \tanh\left(1.82\left[\left(\frac{T_\mathrm{c}}{T} - 1\right)\right]^{0.51}\right). \tag{2.24}$$

As shown in Fig. 2.5 the approximation and the numerical solution have good agreement.

2.3.2 Multiband and Unconventional Superconductivity

The underlying assumption of BCS theory of superconductivity is that all the electrons on the isotropic Fermi surface contribute equally to the pairing interaction giving a single gap energy. Typical band structures are never normally that simple with multiple bands lying close to the Fermi surface with different electron masses

depending on the electron dispersion energies. For superconductors with multiple bands lying close to the Fermi surface this can lead to different electron-phonon coupling strengths therefore giving difference gap energies. Multiband superconductivity was proposed in the 1950s [132] and has been found to be successful in explaining much of the physics in MgB_2 [133, 134] and the Iron-pnictide superconductors [135, 136].

The two-band model is dependent upon the strength of the inter and intraband coupling with three different scenarios arising. In the case of weak interband coupling the superconductor will have two separate distinct transition temperatures for the two separate bands. In the case of strong interband coupling both superconducting transitions occur at the same temperature but still have different gap energies. For intermediate interband coupling the superconducting transition still occur at the same temperature but the full opening of the superconducting gap will be suppressed to temperatures lower than the onset transition temperature.

So far we have only discussed the case of an isotropic s-wave superconducting state which has even parity ($l = 0$) ensuring a spin singlet state. It is however possible for $l = 0, 1, 2...$ and not require the electron-phonon interaction. In these cases other pairing mechanisms are at play however the details of these other mechanisms will not be discussed in this thesis, further details can be found in Ref. [137]. When $l = 1$ the Cooper pairs form with odd parity so have a spin-triplet configuration, these are known as p-wave superconductors. Here there is possibility of the Cooper pairs forming with different possible spin configurations that are parallel to each other. Therefore the triplet pairing state is described by the vector $\vec{d} = \frac{1}{2}\left(\Delta^{--} - \Delta^{++}, -\mathrm{i}\left(\Delta^{--} + \Delta^{++}\right), \Delta^{+-} - \Delta^{-+}\right)$ where the pseudospins are denoted by $+$ and $-$ and the gap energy is given by $|\vec{d}|^2$ [138, 139, 140]. The superconducting gap is no longer required to be strictly isotropic with the potential for zero points along the Fermi surface. These zeros can form as either point or line node depending upon $\vec{d}$. It is also possible for non-unitary triplet states to form with partial polarisation of the Cooper pairs, this can lead to time-reversal symmetry breaking. When $l = 2$ this results in higher ordered angular momenta singlet states as $l = 2$ has even parity. Superconductors with $l = 2$ are known as d-wave superconductors.

2.3.3 Noncentrosymmetric Superconductivity

So far we have only discussed the case of centrosymmetric superconductors where the overall wave function is required to be antisymmetric under particle interaction. This has then required that the orbital part of the wave function be either odd or

even parity (either singlet or triplet pairing). Noncentrosymmetric superconductors lack a centre of inversion symmetry, what this means for the superconducting wave function is that parity is no longer a good quantum number [60]. A Rashba-type antisymmetric spin-orbit coupling (ASOC) is allowed lifting the degeneracy of the Fermi surface. The Hamiltonian of the ASOC has the form $\alpha \mathbf{g}_{\mathrm{k}} \cdot \mathbf{S}$ where α is the strength of the ASOC and $\mathbf{g}_{\mathrm{k}}$ is a vector dependent upon the crystal and electronic structure of the compound. Cooper pairs now no longer form as purely singlet or triplet pairs but rather an admixture of the two [141, 142]. The superconducting gap $\hat{\Delta}$ can described by the following matrices which takes in account an s-wave component and a d-vector that describes the triplet order parameter [143, 140]

$$\hat{\Delta} = \begin{pmatrix} \Delta^{++} & \Delta^{+-} \\ \Delta^{-+} & \Delta^{--} \end{pmatrix} = \begin{pmatrix} -d_{\mathrm{x}} + \mathrm{i}d_{\mathrm{y}} & d_{\mathrm{z}} + \Delta_{\mathrm{s}} \\ d_{\mathrm{z}} - \Delta_{\mathrm{s}} & d_{\mathrm{x}} - \mathrm{i}d_{\mathrm{y}} \end{pmatrix} \tag{2.25a}$$

where the s-wave term is given by

$$\Delta_{\mathrm{s}} = \frac{1}{2}\left(\Delta^{+-} - \Delta^{-+}\right), \tag{2.25b}$$

and where the d-vector that describes the triplet order parameter is given by

$$\vec{d} = \frac{1}{2}\left(\Delta^{--} - \Delta^{++}, -\mathrm{i}\left(\Delta^{--} + \Delta^{++}\right), \Delta^{+-} - \Delta^{-+}\right). \tag{2.25c}$$

Here it can be seen that the singlet case corresponds to $\vec{d} = 0$ and the triplet case corresponds to $\Delta_{\mathrm{s}} = 0$. It can be seen that the gap for an admixture of triplet and singlet superconductors results from the sum of the two components. An interesting result can be seen when the triplet term is small. This will result in a nodeless near isotropic gap making it experimentally difficult to distinguish from a centrosymmetric *s*-wave superconductor.

2.4 The Clean and Dirty Limit

In most materials there is a level of intrinsic disorder from impurities and structural inhomogeneities. In superconductors in the normal-state this will lead to changes in the scattering rate. The ratio of the scattering rate $1/\tau$ compared to the superconducting gap indicates whether the superconductor is in the clean or dirty regime. If a superconductor is in the clean regime then $1/\tau << 2\Delta$ and if a superconductor is in the dirty regime then $1/\tau \geq 2\Delta$. Therefore as the scattering rate increases the system becomes increasingly disordered. The clean and dirty limit are more commonly

expressed as the ratio of the scattering length l_e and the BCS coherence length ξ_0 which denotes the spatial extent of the Cooper pair inside the superconductor. The BCS coherence length is given by [144]

$$\xi_0 = \frac{\hbar \nu_F}{\pi \Delta}, \tag{2.26}$$

where ν_F is the Fermi velocity. The clean limit can be expressed as $\xi_0/l_e << 1$ and the dirty limit as $\xi_0/l_e >> 1$. Many superconducting parameters will be affected by disorder for example the Ginzburg-Landau coherence length $\xi_{GL}(T)$ is reduced in the dirty limit

$$\xi_{GL}(T) = 0.85\sqrt{\xi_0 l_e}\left(\frac{T_c}{T_c - T}\right)^{1/2}. \tag{2.27}$$

Whereas in the clean limit the scattering is assumed to be negligible

$$\xi_{GL}(T) = 0.74\xi_0\left(\frac{T_c}{T_c - T}\right)^{1/2}. \tag{2.28}$$

The Ginzburg-Landau penetration depth $\lambda_{GL}(T)$ is seen to be similarly affected by the scattering length where in the clean limit

$$\lambda(T) = \frac{\lambda_L}{\sqrt{2}}\left(\frac{T_c}{T_c - T}\right)^{1/2}. \tag{2.29}$$

However, increased scattering of the electrons leads to a lowering of the superfluid density. Hence the penetration depth increases in the dirty limit due to less effective screening of the magnetic fields

$$\lambda(T) = 0.64\lambda_L\sqrt{\frac{\xi_0}{l_e}}\left(\frac{T_c}{T_c - T}\right)^{1/2}. \tag{2.30}$$

The details of other superconducting parameters in the clean and dirty limit will be discussed when required in later chapters of this thesis.

2.5 Pair-Breaking Mechanisms

For type-II superconductors there are two possible mechanisms for destroying the superconducting state. The first pair breaking mechanism is known as the orbital critical field, $\mu_0 H_{c2}^{orb}$ [see Eq. (2.15)]. Here as the field increases more normal-state vortex cores will be generated eventually the intervortex spacing decreases to a point where the vortices begin to overlap. Once this happens the superconductivity is

destroyed. The second mechanism is due to a paramagnetic limiting effect otherwise know as the Pauli limiting field. When a magnetic field is applied to a band of electrons a splitting into spin up and spin down bands is observed i.e. the Zeeman effect. By equating the superconducting condensate energy with the Zeeman energy the Pauli paramagnetic limit can be seen to be

$$\mu_0 H_{c2}^{\mathrm{P}} = \frac{\sqrt{2}\Delta_0}{g\mu_{\mathrm{B}}\sqrt{(1-\chi_{\mathrm{s}}/\chi_{\mathrm{n}})}}, \tag{2.31}$$

where $g = 2$ for free electrons, χ_{s} and χ_{n} are the spin susceptibilities of the superconducting and normal-state respectively. The Clogston-Chandrasekhar limit can be found for an s-wave superconducting state since $\chi_{\mathrm{s}} = 0$ giving

$$\mu_0 H_{c2}^{P} = 1.86 T_{\mathrm{c}}. \tag{2.32}$$

In the case of triplet pairing however, $\chi_{\mathrm{s}} = \chi_{\mathrm{n}}$ and therefore no Pauli limit exists.

The Werthamer, Helfand, Hohenberg model (WHH) theory of single-band, dirty limit superconductors can be used to model the upper critical field taking into account orbital and Pauli paramagnetic pair breaking effects. The WHH model will be discussed in more detail in Chapter 4.

Chapter 3

Experimental Details

3.1 Sample Preparation

3.1.1 Polycrystalline Growth

Arc Melting

Polycrystalline samples of Re_6Zr, La_7Ir_3 and La_7Pd_3 were produced by arc melting using a tri-arc furnace. Stoichiometric amounts of the constituent materials are placed onto a water-cooled copper hearth in the sample chamber. A rotary pump is then used to evacuate the chamber before being flushed with argon gas, this process is repeated at least three times. The materials are melted by generating a high current arc between the tip of a tungsten electrode and the copper hearth. To ensure sample homogeneity the samples are flipped and remelted several times. The samples are then annealed by sealing the as-cast samples in an evacuated quartz tubes and placing the tube in a box furnace for two weeks at a temperature determined by the phase diagram of the material.

Solid State Reaction

Polycrystalline samples of $TaRh_2B_2$ and $NbRh_2B_2$ were produced by solid state reaction method. In this method, powders of the constituent materials are mixed and ground together before being pressed into a pellet. The pellet is wrapped in tantalum foil and placed on an alumina boat. The samples are then placed into a high vacuum furnace. The high vacuum furnace consists of an alumina tube that can be sealed at either end, One end is typically attached to diffusion pump that is backed by a rotary pump to achieve a vacuum of 10^6 mbar.

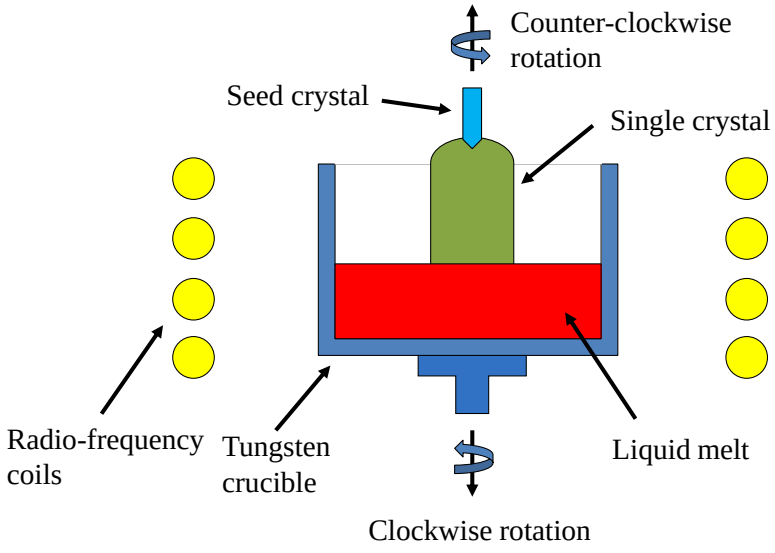

Figure 3.1: Schematic diagram of the RF furnace used to perform single crystal growth.

3.1.2 Single Crystal Growth

Single crystals are required to thoroughly understand the role of crystal structure on the properties of noncentrosymmetric compounds. In the case of polycrystalline samples the disordered nature of the crystal domains can dominate the properties, in particular they make it very difficult to detect if there are any anisotropic behaviour due to random orientation of the domains. We have used Czochralski process to grow single crystals.

The Czochralski Process

Single crystals of La_7Ir_3 where produced by the Czochralski process using a radio frequency (RF) furnace as shown in Fig. 3.1 [145]. Polycrystalline La_7Ir_3 was placed in a tungsten crucible which is inserted into a quartz tube that is evacuated and flushed with argon gas. The tungsten crucible and sample is then heated using a radio-frequency furnace. The sample was heated to very close to its melting point such that a skin can be seen to be forming over the melt. At this point a seed rod,

consisting of either a pointed tungsten rod or a single crystal attached to a tungsten rod, is lowered just below the surface of the melt. The tungsten crucible and sample are then rotated in a clockwise direction while the seed rod is rotated in the opposite direction. After 10 minutes the the seed rod is then raised at 10 mm/hr as the single crystal is pulled from the liquid melt.

3.2 Powder X-ray Diffraction

When a wave scatters off a grating constructive interference can be seen at certain angles producing a diffraction pattern. If the scatterers are planes of atoms these act like a grating as well, however, the distance between the atoms determines the wavelength of radiation required. The spacing between the atoms will be of the order of angstroms so the required wavelength of radiation is in the x-ray regime. Unlike a grating, crystals have many periodic three dimensional planes so the angle of diffraction will be related to the overall structure of the crystal. X-ray diffraction is a powerful tool to measure the structure of materials, Max von Laue first described diffraction patterns of crystal using three vector dot products. A much simpler model was proposed by William Henry Bragg which uses three crystallographic planes as shown in Fig. 3.2. In the Bragg model the incident x-rays are reflected by each of the crystallographic planes. When the incident x-ray is reflected off the second and third plane it can be seen in Fig. 3.2 that they are required to travel a further distance equal to ABC for the second plane. This implies that the phase will shift with respect to the first wave giving rise to either constructive or destructive interference. For constructive interference to be observed it is required that the distance ABC is exactly an integer number of wavelengths $n\lambda$. This now allows us to derive the Bragg law since

$$\mathrm{AB} = d_{\mathrm{hkl}} \sin\theta, \tag{3.1}$$

and when diffraction occurs $\mathrm{AB} = \lambda/2$

$$\lambda = 2d_{\mathrm{hkl}} \sin\theta. \tag{3.2}$$

The Bragg's law underpins all scattering techniques and shows that from a x-ray diffraction pattern the inter-plane spacing of the crystallographic structure can be calculated. In the Laue description of x-ray diffraction we can define the following wave vectors for the incoming and scattered x-rays as $\mathbf{k}_{\mathrm{i}}$ and $\mathbf{k}_{\mathrm{f}}$. For elastic scattering to occur the following must be true $\mathbf{k}_{\mathrm{i}} = \mathbf{k}_{\mathrm{f}} = 2\pi/\lambda$. Constructive interference of

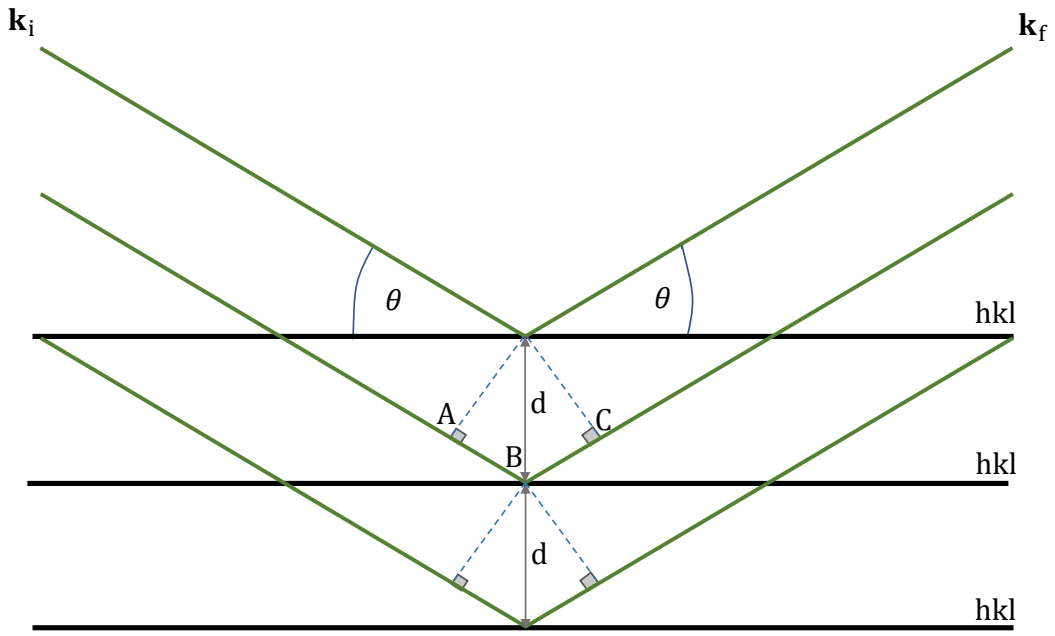

Figure 3.2: The diffraction process as described by Bragg's scattering model for uniformly spaced planes of atoms.

the wave vectors is necessary to observe diffraction is give the following relation

$$\mathbf{q} = \mathbf{k}_i - \mathbf{k}_f = \mathbf{G} \tag{3.3}$$

where $\mathbf{q}$ is the scattering vector and $\mathbf{G}$ is the reciprocal lattice vector. The real space lattice can be found by taking the Fourier transform of the reciprocal space lattice. This means that by mapping out the positions and intensities of the reciprocal space lattice the orientation and structure of the real space lattice can be obtained. By using a Ewald sphere the conditions for diffraction can be more readily seen as shown in Fig. 3.3. An Ewald sphere can be constructed by considering the wave vectors $\mathbf{k}_i$ and $\mathbf{k}_f$ both originating from the same point with a length equal to $2\pi/\lambda$. All possible configurations of $\mathbf{k}_i$ and $\mathbf{k}_f$ will form a three dimensional Ewald sphere. However, diffraction is only observed when the reciprocal lattice points intersect with the Ewald sphere. A more detailed theory of x-ray scattering can be found in Ref. [146]

Powder x-ray diffraction patterns were captured using a PANalytical X'Pert PRO multi-purpose X-ray diffractometer (MPD) and a Bruker D5005 diffractometer. The Panalytical X'Pert Pro MPD is equipped with a Johansson monochromator giving a very high-resolution source of pure Cu $K_{\alpha 1}$ radiation. The Bruker D5005

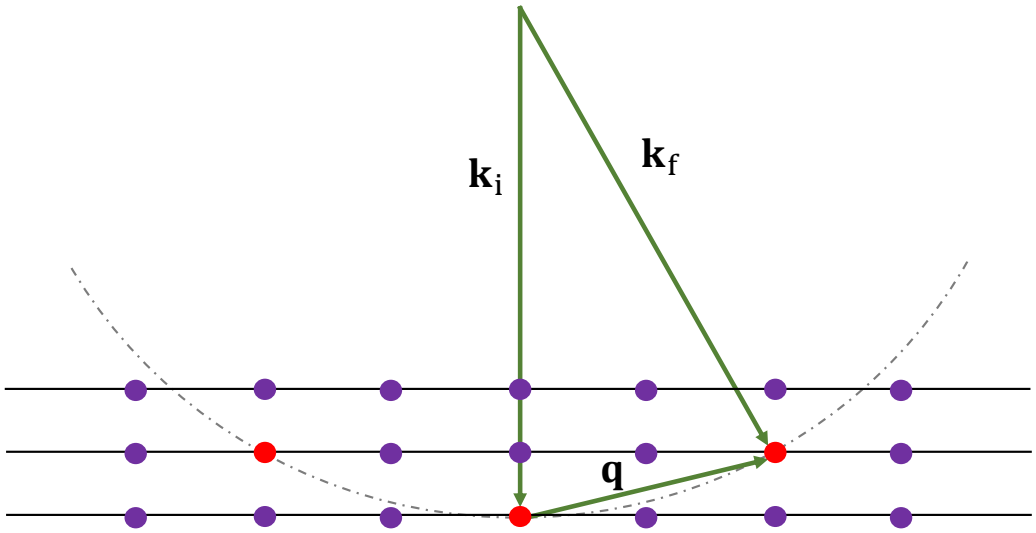

Figure 3.3: The diffraction process in reciprocal space where a plane of atoms are denoted by a single point (purple spheres). When the diffraction condition is met an Ewald sphere can be constructed shown by the dot-dashed line.

is a general purpose diffractometer equipped with Cu K_α sources and set up in the Bragg-Brentano geometry where the detector is moved across a variety of scattering angles 2θ and the scattering intensity is measured at each of these points. The diffraction pattern consists of intensity as a function of scattering angle which can then be fit using methods such Rietveld refinement. These structural refinement methods allow for the theoretical diffraction pattern to be fit using variables such as the lattice parameters, atomic positions and site occupancies [147].

3.3 Laue Diffraction

In order to orientate single crystal samples back-reflection Laue diffraction was used. This method involves backscattering a beam of polychromatic x-rays sent from the centre of a scintillator screen off a single crystal sample. When the x-rays backscatter off the sample an image of the reciprocal space lattice can be obtained. The images are captured using a Photonic Science charge-coupled device (CCD). To allow for easy orientation of the single crystal the samples are mounted on a triple axis goniometer. A full description of this technique can be found in Ref. [148]

3.4 Energy Dispersive X-ray Spectroscopy

Energy dispersive x-rays spectroscopy (EDX) is a technique used to determine the stoichiometry of a material. EDX uses a scanning electron microscope (SEM) with x-rays to excite electrons in the inner shell of the atom to higher energy outer shells. An electron then decays from a higher energy outer shell back into the inner shell. These decays emit x-rays with energies corresponding to the difference between the two energy levels. The decay energy is unique to the atom's electron configuration so can be used to identify the elemental composition of a sample. More details about the EDX technique can be found in Ref. [149].

3.5 Magnetisation

DC Susceptibility

Bulk magnetisation measurements were performed using a Quantum Design Magnetic Properties Measurement System (MPMS). The magnetometer consists of a set of superconducting coils arranged in a second-order gradiometer configuration connected to a superconducting quantum interference device (SQUID), as shown in Figure 3.4. A small heater is used to drive the superconducting coil and SQUID into the normal-state to quench any persistent supercurrents. Measurements can be performed at temperatures from 1.8 to 400 K and in applied magnetic fields up 7 T. The sample is mounted in non-magnetic straw which is attached to a sample rod. This is then inserted vertically through the pick up coils inducing supercurrents. The sample is scanned across a 4 cm length where the system takes 32 measurements. The induced current at each of these 32 points is converted to a extremely accurate voltage by the SQUID. The measured voltages are then fit with a model of a dipole field. To obtain the magnetic susceptibility of an unknown sample the system is first calibrated with a sample of well known magnetic susceptibility, usually Palladium. A full description of the operation of MPMS can be found in Ref. [150].

For superconductors the DC magnetic susceptibility is measured in two modes, zero-field-cooled warming (ZFCW) and field-cooled-cooling (FCC). In ZFCW the sample is cooled in zero-field before a magnetic field is applied. This allows for maximum field exclusion from the superconducting sample leading to a measurement of the full Meissner fraction. In FCC mode a field is applied at temperatures above the superconducting transition temperature and then cooled, this allows for maximum field penetration but is the excluded on cooling through T_c.

In low magnetic fields it is necessary to take into account the shape of the

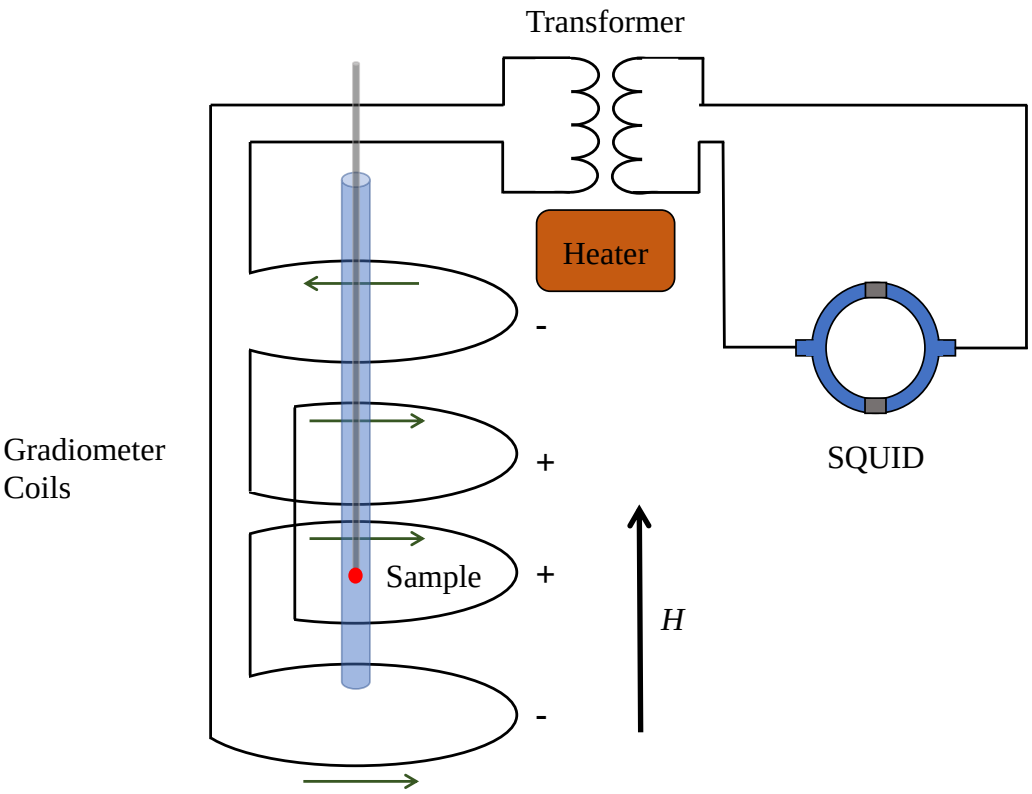

Figure 3.4: Schematic diagram of the second-order gradiometer for the MPMS SQUID magnetometer. The sample is vertically scanned through the second-order gradiometer coils inducing a current in the superconducting wires. This induced current is then converted to a voltage and detected very accurately by the SQUID sensor. A magnetic field can be applied along the axis of the gradiometer coils. A small heater can be used to quench the superconducting wires and SQUID to remove any persistent supercurrents trapped in the circuit.

sample for demagnetisation effects. Unless otherwise stated the sample was orientated in the field to minimise the effects of demagnetisation. All calculations of the magnetic susceptibility include a demagnetisation factor which has been calculated using Ref. [151].

Using an iQuantum ^{3}He insert bulk magnetisation measurements can be performed down to 0.5 K. The sample is placed inside a sealed pipe which is vertically inserted into the sample space. ^{3}He is then condensed inside the pipe allowing the system to cool to 0.5 K. The system operates in "one-shot" mode meaning that only ZFCW and field-cooled-warming measurements can be performed. Measurements as a function of field can be made by holding the sample at a fixed temperature but once the liquid ^{3}He is evaporated temperatures become unstable and the ^{3}He gas

then needs to be recondensed for further measurements.

AC Susceptibility

AC susceptibility measurements where performed using the AC susceptibility option in the Quantum Design MPMS. In AC magnetisation measurements a small AC drive magnetic field is applied on top of any DC field, causing a time-dependent response in the sample. These responses induce supercurrents in the detection coils. The detection circuit is configured to detect a narrow band of frequencies at the fundamental frequency of the driving AC field. AC magnetisation yields two quantities, χ' and χ'' which are the in-phase and out-of-phase component respectively. While χ' closely follows the response of the DC magnetisation χ'' gives a indication of energy losses in the system. A full description of the operation of the AC susceptibility option for the Quantum Design MPMS can be found in Ref. [150].

Vibrating Sample Magnetometer

Bulk magnetisation measurements as function of field where performed using an Oxford Instruments Vibrating Sample Magnetometer (VSM). Samples are mounted vertically on a PEEK sample holder attached to a carbon-fibre sample stick which is oscillated at a typical frequency of 55 Hz between two pick up coils. The induced voltage in the coils due to the oscillation of the sample is measured by a lock-in amplifier. Measurements where performed in fields up to 12 T and in temperatures between 1.4 and 300 K. One of the advantages of using a VSM is that the magnetic field does not need to be stabilised between measurements unlike in a SQUID magnetometer. This means that the flux dynamics of the systems can be more easily observed when measuring the magnetisation as a function of field.

Pressure Cell

Magnetisation measurements as a function of pressure were performed using an easyLab Mcell-10 hydrostatic pressure cell which can apply pressure up to 10 kbar. Figure 3.5 shows a schematic diagram of the pressure cell which is designed for use in a Quantum Design MPMS. The hydrostatic pressure is transmitted to the sample via Daphne oil which is used to fill a PTFE capsule. Copper gaskets are inserted on either side of the sealed PTFE capsule to form a loose seal inside the cell body. The pressure is applied by the PTFE capsule through the ceramic piston and caps by applying pressure using a hydrostatic pump. The pressure is then maintained by tightening the upper locking nut. To measure the internal pressure of the cell in

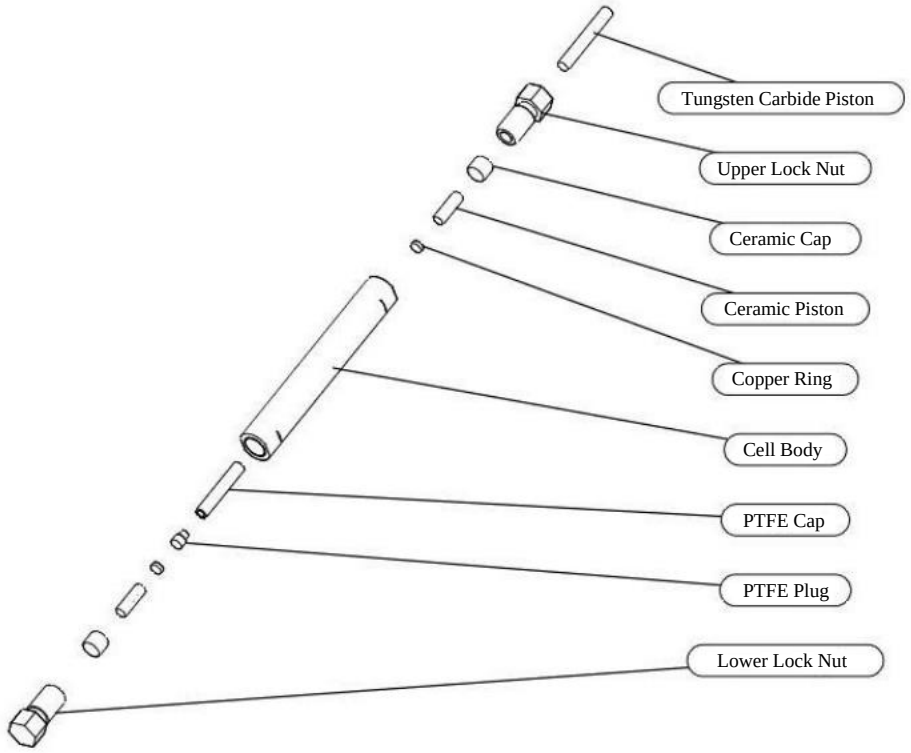

Figure 3.5: Schematic diagram of the exploded view of easyLab Mcell-10 hydrostatic pressure cell.

situ a small piece of Sn, which servers as a manometer, is inserted into the PTFE capsule along with the sample.

3.6 Resistivity

A Quantum Design Physical Properties Measurement System (PPMS) was used to measure the resistivity. Measurements were performed in applied fields up to 9 T and in temperatures from 300 to 1.8 K or down to 0.4 K using a ^{3}He insert. Samples were cut into bars with a well defined cross-sectional area and four silver wires of 0.05 mm diameter were attached using DuPont 4929N silver paste. The wires are set up in the four-probe geometry which requires two outer wires to supply current and two inner wires separated by length l to measure the potential difference as seen in Fig. 3.6. The resistivity can then be calculated by

$$\rho = \frac{RA}{l}, \tag{3.4}$$

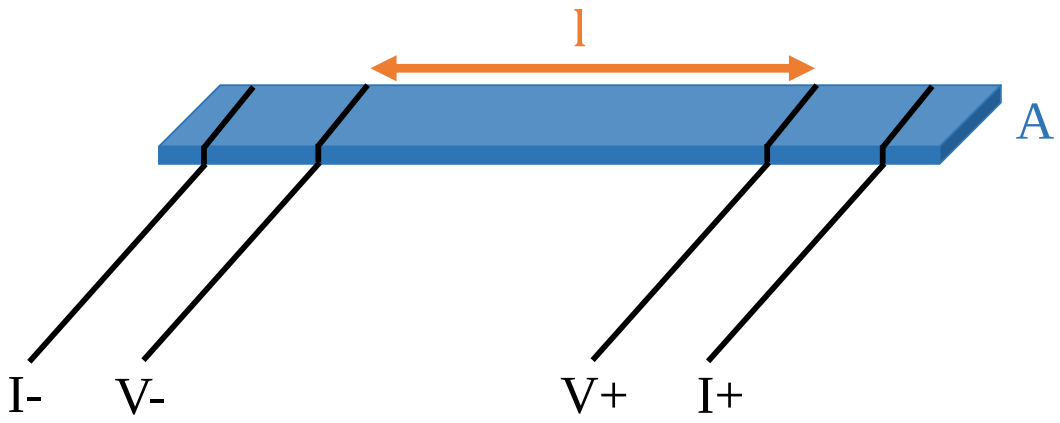

Figure 3.6: Schematic diagram of how the contacts are laid out for a four probe resistivity measurement, where l is the distance between the two voltage contacts.

where A is the cross-sectional area of the sample and R is the sample electrical resistance. By using this method the contact resistance can be neglected due to the voltage leads drawing little current which allows for an accurate measurement of the voltage.

3.7 Specific Heat

A Quantum Design PPMS was used to perform specific heat measurements between 1.8 and 400 K in applied field up to 9 T. A ^{3}He insert was used to attain temperatures down to 400 mK and a dilution refrigerator insert was used to measure down to 50 mK. Samples are mounted on a sapphire platform using Apiezon N grease and to ensure good thermal contact the face of the sample in contact with the platform is polished. The sample stage is suspended by wires attached to a copper heat sink held at a constant temperature. The wires provide connections for the heater and thermometer that are attached to the bottom of the platform while also providing thermal link between the isolated stage and heat sink.

The heat flow diagram of the heat capacity puck is shown in Fig. 3.7. Here the sample heat capacity is denoted by C_s and the combined platform, thermometer, heater and grease heat capacity is denoted by C_a. There are also two thermal conductivity parameters K_1 and K_2 which represent the conductivity between the platform and the heat sink, and the platform and the sample respectively. The sample, platform and heat sink have temperatures T_s, T_p and T_0. Specific heat measurements are performed by switching on the platform heater to warm the the sample and platform. Here the heater provides power P to the platform assem-

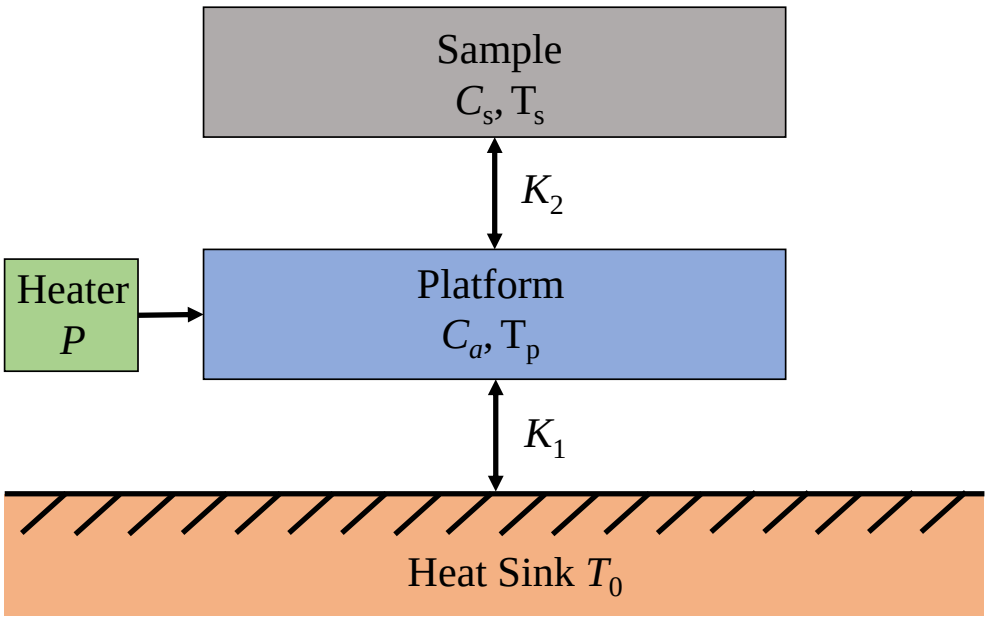

Figure 3.7: Heat flow diagram of the heat capacity puck. The platform is heated by the attached heater while the temperature of the platform is measured. The sample should be strongly thermally coupled to the platform ($K_2 >> K_1$) ensuring $T_s \approx T_p$.

bly such that the temperature rises by $\Delta T = P/K_1$. The following heat balance equation is obtained when it is assumed that sample and the platform are strongly coupled so that $T_p \simeq T_s$ [152]:

$$P = (C_a + C_s)\frac{dT_p}{dt} + K_1 (T_p - T_0). \tag{3.5}$$

After some period of time the the heater is switched off so that the sample and platform relax back to the thermal bath temperature. The platform cools with an exponential relaxation given by

$$T_p(t) = T_0 + \Delta T \exp(-t/\tau) \tag{3.6}$$

where the time constant is given by

$$\tau = \frac{(C_s + C_a)}{K_1}. \tag{3.7}$$

By performing an initial addendum measurement of C_a the sample heat capacity

can then be measured and quantified using the method described above. However, in reality there is imperfect thermal contact between the sample and the platform so the assumption that $T_{\mathrm{p}} \simeq T_{\mathrm{s}}$ no longer holds. For real systems it is then necessary to use two exponential functions to model the thermal relaxation:

$$T_{\mathrm{p}}(t) = T_0 + A\exp(-t/\tau_1) + B\exp(-t/\tau_2) \tag{3.8}$$

This is known as the two-tau model. In this model one relaxation is much faster than the other. The fast relaxation is observed as the sample and platform reach equilibrium. While the slower relaxation results from the sample/platform cooling back to the temperature of the heat sink. A full description of how specific heat measurements are performed on a Quantum Design PPMS can be found in Refs. [153].

3.8 Neutron Scattering

3.8.1 Neutron Production

There are two methods of neutron production employed for neutron diffraction experiments: spallation and a nuclear reactor. In this thesis neutron diffraction and muon spectroscopy experiments were performed using the ISIS neutron spallation source at the Rutherford Appleton Laboratory so spallation will be the only technique discussed.

The first step to produce neutrons at ISIS is to generate hydrogen ions using a H^- source where an arc is generated using a 50 A current source to make a plasma. The H^- ions are accelerated to 35 keV on leaving the source. The H^- are then accelerated using radio frequency quadrupole accelerators from 35 to 665 keV and grouped into 1 ns long bunches at a frequency of 202.5 MHz. The H^- are then accelerated further to 70 MeV using a four-section drift tube linear accelerator. Before entering the synchrotron the H^- are stripped of the electrons by a thin alumina foil. The protons are accelerated and focused around the synchrotron ring by bending and focusing magnets and radio frequency electric field accelerators. After 10,000 revolutions the protons now have an energy of 800 MeV and have been collected into two bunches of protons. Once the protons have reached the correct energy they are then extracted from the synchrotron using a kicker. The protons are then directed to a tungsten target to produce neutrons by spallation. When the proton bunches bombard the tungsten target neutrons are produced at an approximate ratio of 15 - 20 neutrons per proton which implies the total number of neutrons generated per

pulse is approximately 4×10^{14}. The neutrons created in this process have similar energies to the protons used to generate them. It is therefore necessary to slow the neutrons down using a moderator that consists of liquid hydrogen (20 K), methane (100 K) and water (290 K) which bring the energy of the neutrons down to meV. Spallation neutron production allows for a high intensity of neutrons with minimal heat production at the target. The layout of the H^- source, linear accelerator, synchrotron and target station at the ISIS neutron spallation source is shown in Fig. 3.8 [13].

3.8.2 Neutron Diffraction

Neutrons are an excellent tool for studying the bulk crystal and magnetic structures of materials. The versatility of neutrons stems from being highly penetrative and their inherent spin-$\frac{1}{2}$. Thermal neutrons that have a wavelength $\lambda \approx 2 \times 10^{-10}$ m are scattered by a point-like strong interaction with the nucleus which has an interaction length $\approx 10^{-14}$ m. For neutrons this means they are scattered almost isotropically from the atomic nuclei unlike x-ray scattering where the scattering is determined by the charge density of the Fermi-sea. For neutrons the bound scattering length b is both independent of incident angle and wavelength [154] and describes the the interaction of a neutron with the entire atom which also includes contributions from various electromagnetic interactions. The value of b is not well understood but originates from a combination of the orientation of the nuclei's spin and the make up of the nucleus which makes it highly isotope dependent. If b is plotted as function of atomic mass no clear trend can be seen, this provides clear advantage for neutron over x-ray scattering [155]. For x-rays the scattering intensities are highly dependent on the atomic number Z of the elements being measured where heavy elements will provide strong scattering intensities and lighter elements will have weaker scattering intensities thus making lighter elements more difficult to identify. Similarly elements with Z that are in close proximity will produce very similar x-ray scattering intensities making it difficult to distinguish between them. Since b is so different from element to element and isotope to isotope for neutron scattering this proves not to be a problem. There are several disadvantages to neutron scattering, the first being that most elements also have an absorption cross section as well as a scattering cross section, and for some elements such as the most abundant isotope of gadolinium this is particularly problematic as absorption dominates over scattering. It is therefore necessary to use an isotope with a lower absorption cross section. Another disadvantage of neutron scattering is the requirement of either a nuclear reactor or a spallation source which presents a host of resource and safety

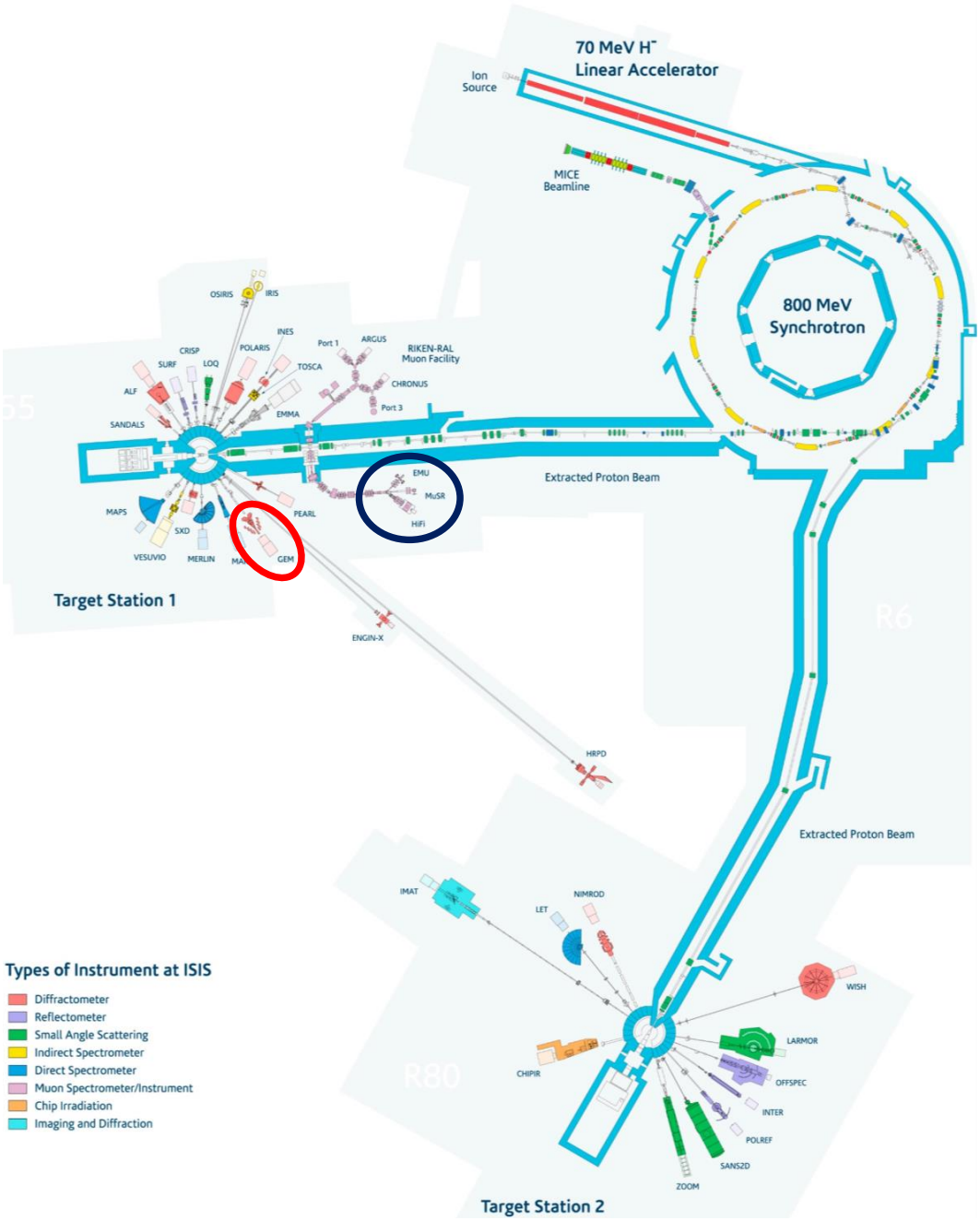

Figure 3.8: Schematic layout of the ISIS spallation neutron and muon source showing the approximate locations of all the end stations. The GEM diffractometer is highlighted by a red circle and the μSR end stations are highlighted by a blue circle. Taken from [13].

complications.

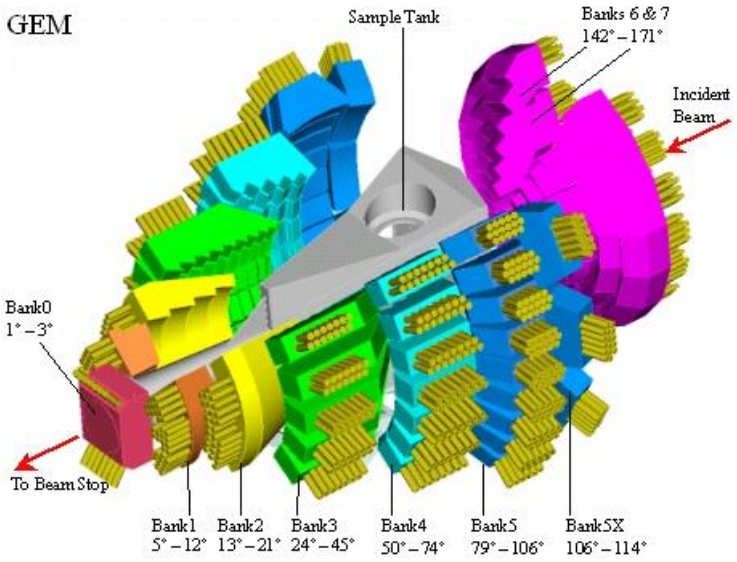

Figure 3.9: Schematic of the GEM diffractometer showing the position of the detector banks around the central sample tank. Adapted from Ref. [14]

3.8.3 GEM Diffractometer

Powder neutron diffraction experiments were performed using the General Materials (GEM) diffractometer at ISIS. The high intensity and high resolution of the GEM diffractometer allows for the study of crystal and magnetic structure materials as well as the study of structure of disordered materials such as liquids and glasses. The diffractometer consists of 6 banks of detectors that are arranged at fixed positions at a range of scattering angles from 1.1 to 169.3 ^{o} around an evacuated sample tank as seen in Fig. 3.9. The arrangement of the detectors in this way means that bank 1 provides largest d spacing at the cost of resolution while bank 6 provides the highest resolution but at the cost of d space. The incident flight path for GEM is 17 metres and a neutron wavelength of ~ 0.3 nm is produced by a series of choppers [14].

3.9 Muon Spectroscopy

Muon spin relaxation and rotation, collectively know as μSR, is a technique used to probe the magnetic distribution of the vortex lattice inside a superconductor by implanting positive muons and measuring the directional dependence of the emitted positrons. Muons are a second generation lepton with spin-$\frac{1}{2}$ that are 207 m_{e}. Positive muons are used to measure condensed matter systems since they behave like light protons rather than heavy electrons in the negative muons case. When

negative muons are implanted into the sample the muon will implant close to the nucleus of the atom and will be captured by the nuclei giving a material dependent life-time. However, when positive muons are implanted they stop in the interstitial sites of the crystal structure so will be susceptible to the physics of the surrounding electrons and will decay after a well-defined lifetime of 2.2 μs that is independent of the material. The vital property of muons that make them so interesting for studying condensed matter systems is their non-zero spin that makes them susceptible to the local magnetic environment. The spin of the muon will precess in a magnetic field with a well defined gyromagnetic ration of $\gamma_\mu/2\pi = 135.5$ MHz T^{-1}.

The muon spectroscopy data presented in this thesis was taken at the MuSR instrument at the ISIS pulsed neutron spallation source. The production of muons at this facility makes use of the proton beam used to generated neutrons. For muon production a graphite target is placed in the proton beam and absorbs about 5% of the beam's power. At the graphite target high energy protons collide into carbon atoms to produce a zoo of pions. To ensure the production of μ^+ we need positive pions, π^+, which are produced through several decays channels [156]

$$p + p \rightarrow \pi^+ + p + n, \tag{3.9a}$$

$$p + n \rightarrow \pi^+ + n + n, \tag{3.9b}$$

as well as other less common decay channels. Pions are highly unstable and decay into two bodies

$$\pi^+ \rightarrow \mu^+ + \nu_\mu, \tag{3.10}$$

where ν_μ is muon-neutrino. Conservation of momentum for a two body decay dictates that the muon and neutrino need to have equal and opposite momentum. Similarly conservation of angular momentum requires that the muon and the neutrino spins are anti-parallel as the the π^+ is a spin zero boson. For neutrinos the spin and momentum vector will always be anti-parallel; this is due to parity violation in the weak interaction. It therefore follows that the muon will have its spin and momentum vector similarly anti-parallel. A beam of 100% spin polarised muons can be ensured by selecting the π^+ that are at rest in the surface of the graphite target [103]. The muon is then guided and focused on to the sample by a series of quadrupole magnets. These magnets also help clean the beam of muons removing any other products from the pion production. When the muon is implanted into the sample it quickly comes to rest dues to interactions with the surrounding electronic environment in the crystal structure of the sample. Muons have a half-life of 2.2 μs

which allows for the spin of the sample to detect and precess in the local magnetic environment. When the muon decays it emits a positron e^+ and two neutrinos:

$$\mu^+ \rightarrow e^+ + \nu_e + \bar{\nu}_\mu. \tag{3.11}$$

When the positron is emitted during the decay it can then be detected using scintillation detectors. Again this decay involves the weak interaction meaning parity violation dictates that the positron is preferentially emitted along the spin vector direction. The angular dependence of the positron emission is given by

$$N(\theta) \propto 1 + A\cos(\theta), \tag{3.12}$$

where A is the strength of the asymmetry and θ is the angle between the muon spin vector and the direction of the positron emission. The strength of the asymmetry is dependent upon the energy of the emitted positron with low energy positrons having zero asymmetry ($A = 0$) and high energy positrons having ($A = 1$). When integrated over all energies an asymmetry of ($A = 1/3$) is found. In this thesis two different muon spectroscopy techniques were utilised, transverse-field muon spin rotation (TF-μSR) and longitudinal muon spin relaxation (LF-μSR). The MuSR instrument at ISIS was used for all the experiments described in this thesis as both of these techniques are available [157]. We will now briefly discuss the two experimental configurations. A full description of μSR techniques can be found in Refs. [158, 156, 159, 103, 157].

3.9.1 Transverse-field Muon Spin Rotation

In the TF-μSR configuration the external magnetic field is applied perpendicular to the direction of the muon spin vector as shown in Fig. 3.11. The spin of a muon in the presence of magnetic fields will begin to precess with the angular frequency $\omega_\mu = \gamma_\mu B$, where $\gamma_\mu/2\pi = 135.5$ MHz/T is the gyromagnetic ratio for the muon. It therefore follows that this technique is sensitive to the internal magnetic field distribution of the sample. For type-II superconductors the flux line lattice leads to a variation in the internal field inside the superconductors so that a muons that stop at a vortex site will see a larger magnetic field than if the muon stopped in between the vortices. The variation in the magnetic field due to the flux line lattice implies that the muons stopping at different sites will precess at different frequencies leading to a damping of the oscillatory signal. The magnetic penetration of a superconductor can then be measured from the size of the damping of the oscillatory signal [159]. For a large magnetic penetration depth the field variation inside the superconductor

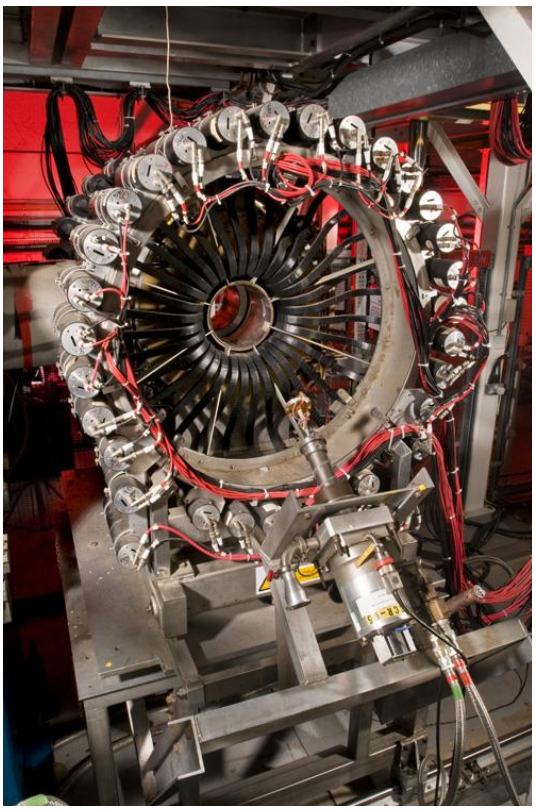

Figure 3.10: An image of the muSR spectrometer at ISIS with the detectors in the transverse-field configuration.

is small so a small damping of the oscillatory signal is seen. Where as for a small magnetic penetration depth the field variation is large so a large damping is seen.

3.9.2 Longitudinal-Field Muon Spin Relaxation

In the LF-μSR the external magnetic field is applied parallel to the spin vector of the muon as shown in Fig. 3.11. This magnetic field configuration can be used to measure the time evolution of the muon spin polarisation along its original direction. In the longitudinal field configuration the positrons are detected in either a forward (F) or backward (B) detector as shown in Fig. 3.11. The number of positrons $N_{\mathrm{F,B}}(t)$ detected in the F and B is given by

$$N_{\mathrm{F,B}}(t) = N_{\mathrm{F,B}}(0) \exp\left(\frac{-t}{\tau_\mu}\right) \left[1 \pm A_0 G_z\left(t\right)\right], \tag{3.13}$$

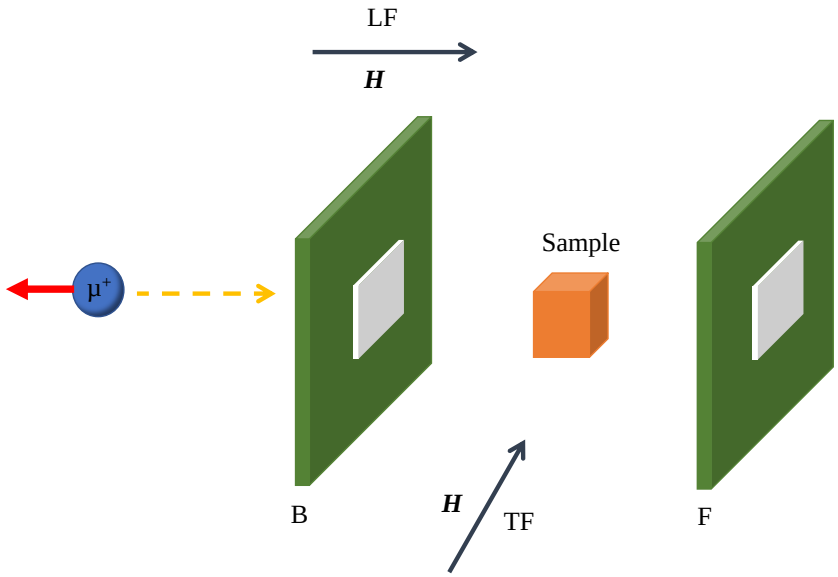

Figure 3.11: A schematic of a μSR spectrometer. Two detectors are shown in green in the forward (F) and backward (B) positions. The grey arrows show the two possible field directions for the transverse-field and the longitudinal-field. For the muon the yellow dashed arrow indicates the momentum vector with the spin aligned anti-parallel (red arrow).

where G_z is the time evolution of the muon polarisation along the z-axis and A_0 is the initial asymmetry. The experimental asymmetry $A(t)$ is then given by

$$A(t) = A_0 G_z(t) = \frac{N_\mathrm{B} - \alpha N_\mathrm{F}}{N_\mathrm{B} + \alpha N_\mathrm{F}}, \tag{3.14}$$

where α is a measure of the efficiency of the F and B detectors which is sample and environment dependent.

By using the zero-field configuration the muons can be used to measure very weak internal magnetic fields inside the sample. For superconducting systems this can result in the detection of time-reversal symmetry breaking or magnetic impurities in the sample. Zero-field μSR can be used to look for small internal magnetic fields that result from ordering of magnetic moments or from randomly orientated moments that are static or quasi-static in the lifetime of the muon. Zero-field μSR allows for a much more sensitive probe of the internal magnetic fields than is possible using magnetometer measurements.

Chapter 4

Superconducting and Normal-State Properties of Cubic Noncentrosymmetric Re_6Zr

4.1 Introduction

Research has recently been focussed on the Re-based α-Mn family of intermetallic superconductors due to the detection of time-reversal symmetry break in several Re_6T (where T = transition metals) compounds [6, 7, 115, 8]. In this chapter we will focus our discussion on the characterisation of the superconducting and normal-state properties of polycrystalline Re_6Zr which crystallises in a noncentrosymmetric cubic structure with the space group $I\bar{4}3m$, as seen in Fig. 4.1. The first report of superconductivity in these compounds was made 1961 but the lack of inversion symmetry in the crystal structure was not noted by the authors [58, 57]. Here, we present a comprehensive characterisation of the normal and superconducting states of this intermetallic compound through studies by magnetisation, electronic transport, and heat capacity. We estimate several normal-state parameters of Re_6Zr such as the electronic specific heat contribution γ_n, residual resistivity ρ_0, and the hyperfine contribution to the specific heat. Using the electronic-transport and heat capacity measurements, we estimate the Debye temperature by using the parallel-resistor model, the Debye lattice contribution to the specific heat at low temperature, and the Debye-Einstein model. Several superconducting parameters, including the lower and upper critical fields H_{c1} and H_{c2}, the coherence length ξ_{GL}, and the penetration

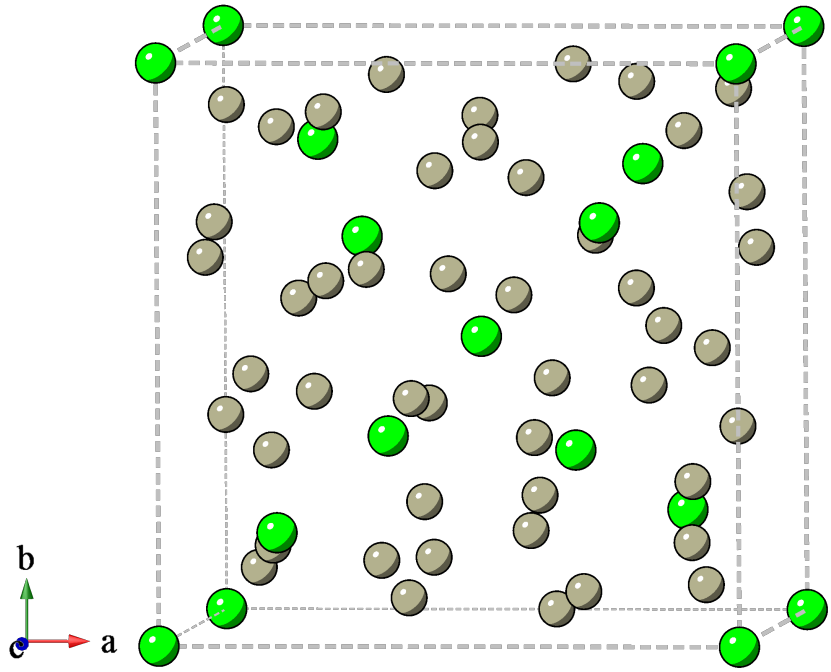

Figure 4.1: Crystal structure of Re_6Zr with a noncentrosymmetric cubic structure containing 58 atoms. The Re atoms are shown in grey and the Zr are shown in green.

depth λ_{GL} are estimated. The specific heat jump $\Delta C/\gamma_n T_c$, the superconducting gap $\Delta_0/k_B T_c$, and the temperature dependence of the specific heat at low-temperature suggest that Re_6Zr is an isotropic, fully gapped s-wave superconductor with enhanced electron-phonon coupling. We also present evidence of unusual flux pinning not normally seen in low-T_c systems.

4.1.1 Sample Preparation and Structural Analysis

Polycrystalline samples of Re_6Zr were produced by arch-melting stoichiometric amounts of the base elements together. The buttons were flipped and remelted several times to ensure sample homogeneity. The buttons where wrapped in tantalum foil, inserted inside an evacuated quartz tube and annealed at 900 °C for 9 days. The structure of Re_6Zr was checked by powder neutron diffraction measurements. These measurements were carried out using the General materials Diffractometer (GEM) at ISIS which uses the time of flight technique. Roughly 6 grams of sample where crushed into a fine powder and placed inside a 6 mm diameter vanadium sample holder. The sample was measured at several different temperatures between 5 K and room

Table 4.1: Crystallographic and Rietveld refinement parameters obtained from powder neutron diffraction data of Re_6Zr.

Structure			α-Mn-type cubic		
Space-group			$I\bar{4}3m$ (No. 217)		
Formula units/unit cell (Z)			58		
Lattice parameter					
a(Å)			9.707(4) (at 300K)		
V_{cell}(Å^3)			914(1)		
Atom	Wyckoff Position	Occupancy	x	y	z
Re1	2a	0.8	0	0	0
Re2	24g	1	0.09146(3)	0.09146(3)	0.28541(4)
Re3	24g	0.98(1)	0.35901(3)	0.35901(3)	0.03813(4)
Zr1	8c	1	0.31572(7)	0.31572(7)	0.31572(7)
Zr2	24g	0.014(1)	0.35901(3)	0.35901(3)	0.03813(4)

temperature. Figure 4.1 shows the data taken at room temperature. The diffraction patterns were Rietveld refined using TOPAS software which are shown by the red lines along with the difference between the data and the Rietveld refinement which are shown by the green lines below in Fig. 4.3. It was found that the patterns were largely temperature independent with a small contraction in the lattice parameter, this indicates there are no structural transitions in Re_6Zr down to 5 K as shown in Fig. 4.2. The results of the Rietveld refinement are shown in Table. 4.1.

4.1.2 Electrical Resistivity Measurements

Figure 4.4(a) shows the resistivity as a function of temperature $\rho(T)$ of a polycrystalline Re_6Zr sample from 2 to 300 K in zero field. The small value of the residual resistivity ratio, RRR $\equiv \rho(300\text{ K})/\rho(10\text{ K}) \approx 1.09$, and the high normal-state resistivity at 10 K indicate poor metallic behaviour. This is comparable to other Re compounds such as Re_6Hf with a RRR quoted from 1.08 to 1.4 [113, 114], $Re_{24}Ti_5$ with RRR ~ 1.3 [116], and $Nb_{0.18}Re_{0.82}$ with RRR ~ 1.3 [122]. A sharp, zero-field superconducting transition ($\Delta T_c = 0.20$ K) can be seen clearly in Fig. 4.4(b) at $T_c = 6.76(5)$ K. T_c is gradually suppressed with increasing applied magnetic field [see Fig. 4.4(b)] and the transition is broadened so that $\Delta T_c = 0.28$ K at 9 T.

At temperatures greater than ~ 50 K the $\rho(T)$ of Re_6Zr is seen to flatten. This characteristic is similar to that seen in many superconductors containing d-block elements including BiPd [160]. It has been proposed that in certain compounds

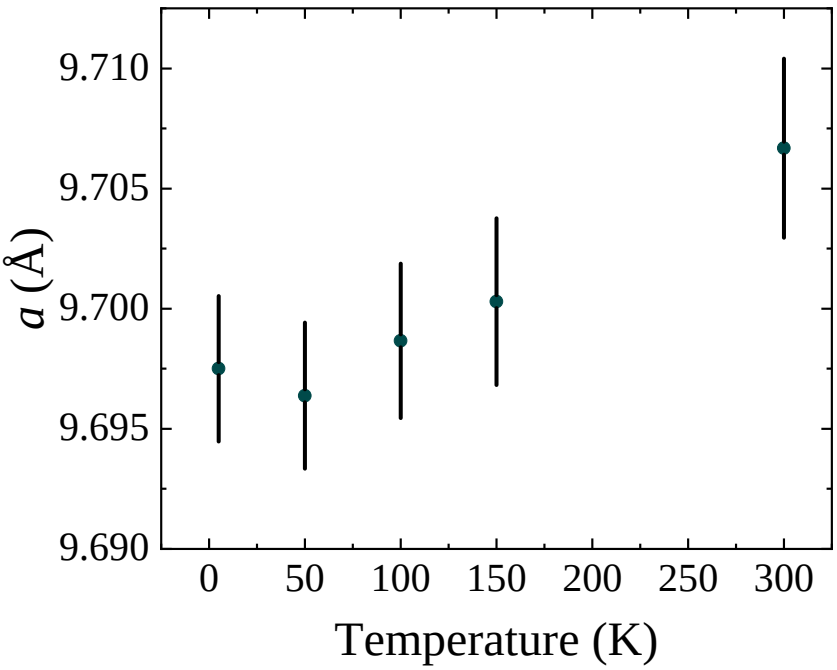

Figure 4.2: Temperature dependence of the a lattice parameter. Linearly decreases with temperature with no structural transition over the entire temperature range.

at high temperatures the resistivity saturates at a value that corresponds to the mean free path on the order of the inter-atomic spacing [161]. This idea was further developed by Wiesmann *et al.* [162] who found empirically that $\rho(T)$ could be described by the parallel-resistor model:

$$\rho(T) = \left[\frac{1}{\rho_{\text{sat}}} + \frac{1}{\rho_{\text{ideal}}(T)}\right]^{-1}, \tag{4.1a}$$

where ρ_{sat} is the saturated resistivity at high temperatures and is independent of T, and $\rho_{\text{ideal}}(T)$ is the "ideal" contribution which according to Matthiessen's rule is:

$$\rho_{\text{ideal}}(T) = \rho_{\text{ideal},0} + \rho_{\text{ideal},L}(T). \tag{4.1b}$$

Here $\rho_{\text{ideal},0}$ is the ideal temperature-independent residual resistivity and $\rho_{\text{ideal},L}(T)$ is the temperature-dependent contribution which can be expressed by the generalised Bloch-Grüneisen model [163]

$$\rho_{\text{ideal},L}(T) = C\left(\frac{T}{\Theta_{\text{R}}}\right)^{n} \times \int_0^{\Theta_{\text{R}}/T} \frac{x^n}{(e^x - 1)(1 - e^{-x})} dx, \tag{4.1c}$$

where Θ_{R} is the Debye temperature obtained from resistivity measurements, C is

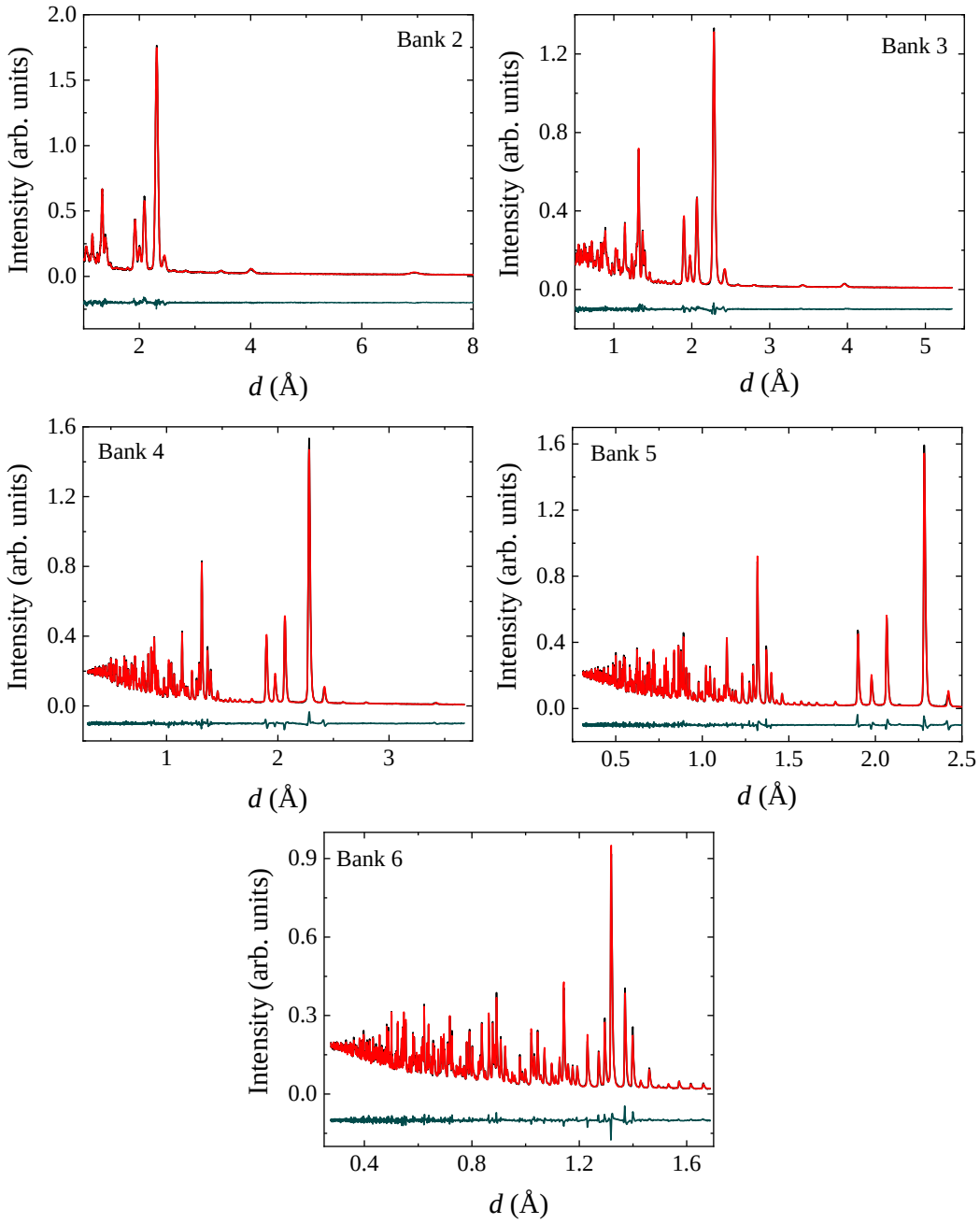

Figure 4.3: Powder neutron diffraction data of Re_6Zr taken on the GEM diffractometer at room temperature. The solid red lines show the Rietveld refinement to the data and the solid green line show the difference between the refinement and the data.

a material-dependent pre-factor and $n = 3 - 5$ depending on the nature of the carrier scattering. Fig. 4.4(c) shows the normal-state resistivity data from 10 to

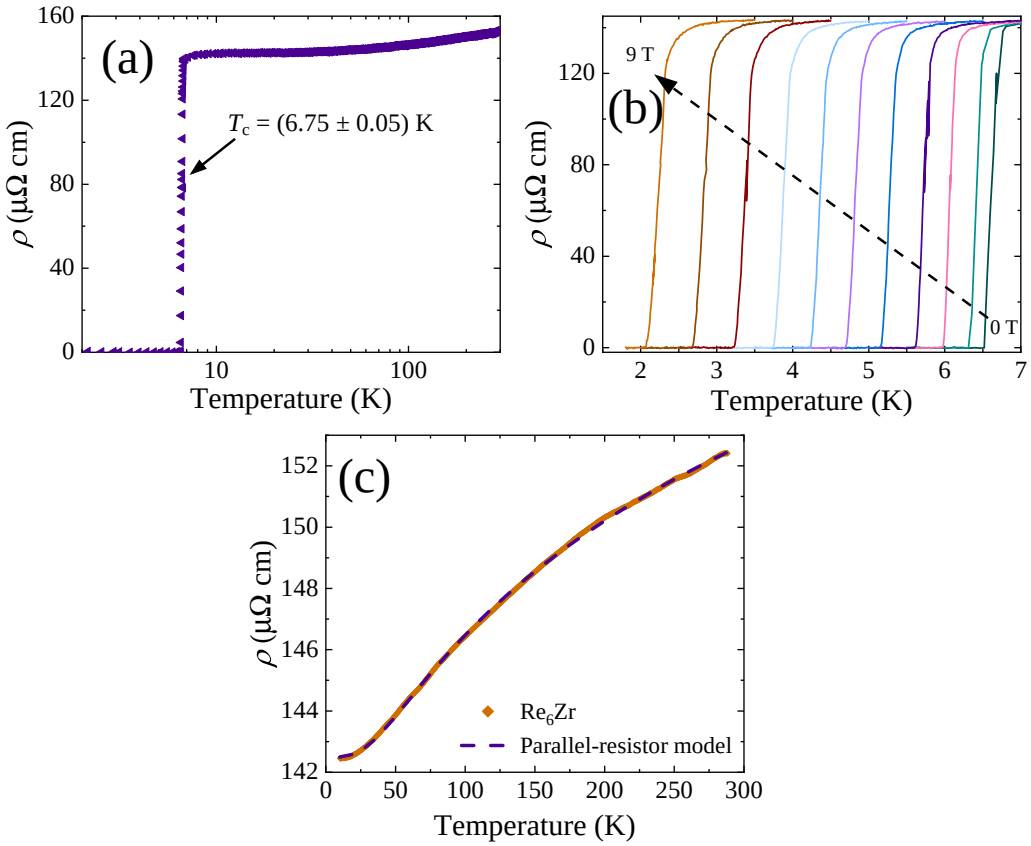

Figure 4.4: (a) Resistivity versus temperature $\rho(T)$ of Re_6Zr in the range $1.8 \leq T \leq 250$ K measured in zero applied magnetic field. The midpoint of the resistivity drop was taken as the transition temperature. (b) $\rho(T)$ below 7.5 K shows the suppression of the transition temperature under various applied fields $\mu_0 H$ from 0 to 9 T. (c) $\rho(T)$ data in the normal-state fit with the parallel-resistor model over the temperature range 10 to 290 K.

290 K fit using Eq. 4.1a. It was found that a value of $n = 3$, which takes into account Umklapp scattering between bands, achieved the best fit giving $\rho_{\text{sat}} = 167(2)$ $\mu\Omega$ cm, $C = 315(6)$ $\mu\Omega$ cm and $\Theta_{\text{R}} = 237(2)$ K. The measured residual resistivity, $\rho_0 = 142(2)$ $\mu\Omega$ cm, which is related to $\rho_{\text{ideal},0}$ and ρ_{sat} by

$$\rho_0 = \frac{\rho_{\text{ideal},0}\rho_{\text{sat}}}{\rho_{\text{ideal},0} + \rho_{\text{sat}}}, \tag{4.2}$$

is consistent with the values of the fit. This electrical resistivity data is in close agreement with that previously reported in Ref. [111].

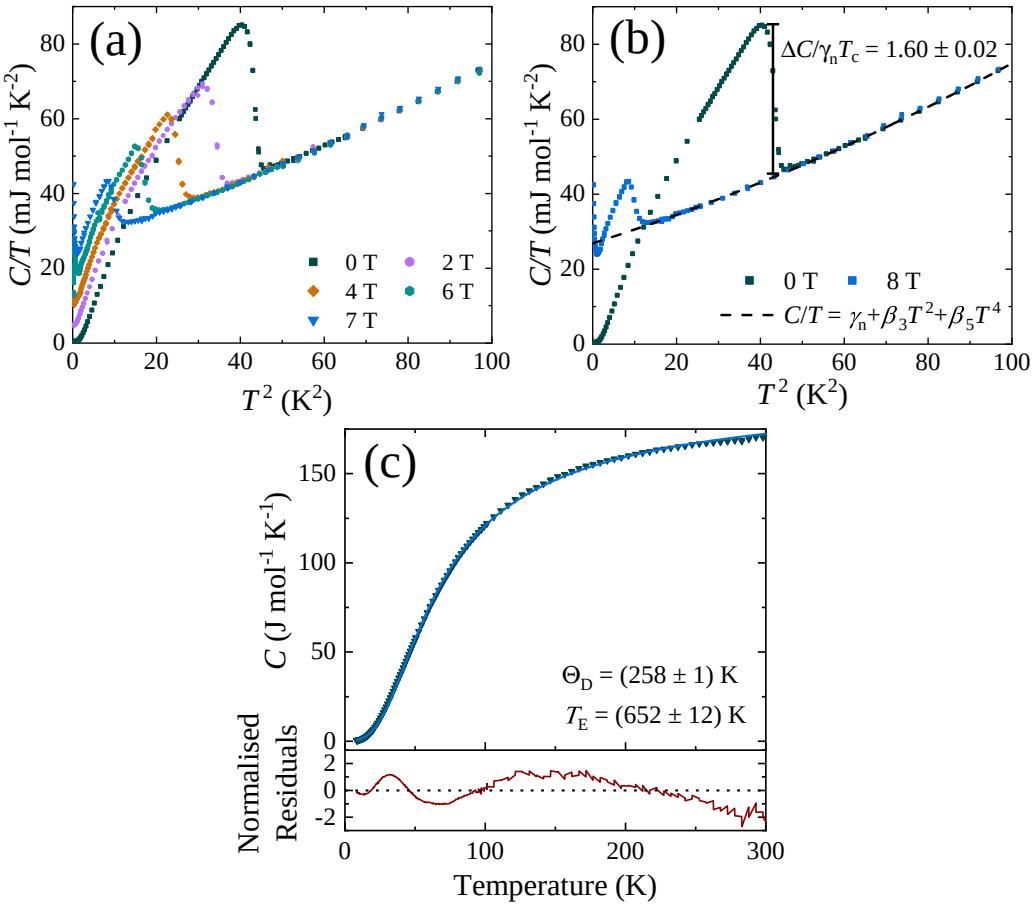

Figure 4.5: (a) C/T versus T^2 in different applied fields ($\mu_0 H$ in teslas), showing the suppression in T_c for increasing field. (b) C/T versus T^2 with $\mu_0 H = 0$ and 8 T. The line is a fit using $C/T = \gamma_n + \beta_3 T^2 + \beta_5 T^4$ for all the $C\,(T)$ data collected above $T_c\,(H)$ in the different applied fields. The normal-state electronic contribution to the specific heat $\gamma_n = 26.9(1)$ mJ/mol K^2, and the Debye temperature $\Theta_D = 338(9)$ K. (c) C versus T from 10 to 300 K. The line shows the fit using Eq. (4.5a), the Debye-Einstein function. The residual plot underneath indicates the quality of the fit using the Debye-Einstein function to the data.

4.1.3 Specific Heat Measurements

The temperature dependence of the heat capacity divided by temperature, C/T, versus T^2 from 2 to 10 K is shown in Fig. 4.5(a), where a sharp jump at 6.75(5) K indicates a bulk superconducting transition. The sharpness of this peak gives an indication of the high quality of the sample. We analysed the normal-state data

C/T versus T^2 between 4.4 and 10 K at $\mu_0 H = 0$ T using

$$C/T = \gamma_{\rm n} + \beta_3 T^2 + \beta_5 T^4, \tag{4.3}$$

where $\gamma_{\rm n}$ is the normal-state Sommerfeld electronic-heat-capacity contribution, β_3 is the Debye law lattice-heat-capacity contribution, and β_5 is from higher-order lattice contributions. A fit using Eq. (4.3) can be seen in Fig. 4.5(b) which gives $\gamma_{\rm n} = 26.9(1)$ mJ/mol K^2, $\beta_3 = 0.35(2)$ mJ/mol K^4 and $\beta_5 = 1.2(3)$ μJ/mol K^6. The Debye temperature, $\Theta_{\rm D}$, can then be calculated using

$$\Theta_{\rm D} = \left(\frac{12\pi^4 RN}{5\beta}\right)^{1/3}, \tag{4.4}$$

where R is the molar gas constant and N is the number of atoms per unit cell. Eq. 4.4 gives $\Theta_{\rm D} = 338(9)$ K which is slightly higher than the previously reported value [6].

Figure 4.5(c) shows the temperature dependence of the heat capacity up to 300 K. There is no sign of any structural phase transition, and the value of C at 300 K is 169.5 J mol^{-1} K^{-1}, which is close to classical Dulong-Petit value for Re_6Zr of 174.6 J mol^{-1} K^{-1} and is consistent with $\Theta_{\rm D} > 300$ K. We fit the normal-state data using a Debye-Einstein function. It was found that by including the additional Einstein term to the Debye model for lattice-heat-capacity the fit could be significantly improved. Figure 4.5(c) shows heat capacity data from 10 to 300 K, which was fit with [164]

$$C(T) = \gamma_{\rm n} T + n\delta C_{\rm Debye}\left(\frac{T}{\Theta_{\rm D}}\right) + n(1-\delta) C_{\rm Einstein}\left(\frac{T}{T_{\rm E}}\right), \tag{4.5a}$$

where δ is the fractional contribution of $C_{\rm Debye}$, n is the number of atoms in a formula unit (f.u.), $C_{\rm Debye}$ is given by

$$C_{\rm Debye}\left(\frac{T}{\Theta_{\rm D}}\right) = 9R\left(\frac{T}{\Theta_{\rm D}}\right)^3 \int_0^{\Theta_{\rm D}/T} \frac{x^4 e^x}{\left(e^x - 1\right)^2} dx, \tag{4.5b}$$

and $C_{\rm Einstein}$ is given by

$$C_{\rm Einstein}\left(\frac{T}{T_{\rm E}}\right) = 3R\frac{z^2 e^z}{\left(e^z - 1\right)^2}, \tag{4.5c}$$

where $z = T_{\rm E}/T$ and $T_{\rm E}$ is the Einstein temperature. The fit was performed using a fixed value $\gamma_{\rm n} = 26.9$ mJ/mol K^2 to help reduce the number of free parameters.

We obtained $\delta = 0.912(2)$, $\Theta_D = 258(1)$ K, and $T_E = 652(12)$ K. The difference between Θ_D and Θ_R is also expected due to the limitations of the parallel-resistor model.

In Fig. 4.5, at very low temperatures, an upturn in C/T appears in magnetic fields above 6 T. This anomalous contribution to the specific heat is proportional to T^{-2}, which suggests that it is due to the high-temperature tail of a nuclear Schottky anomaly. The specific heat of the measured Re_6Zr can be expressed as

$$C(T, B) = C_{el}(T, B) + C_{ph}(T) + C_{hf}(T, B), \tag{4.6}$$

where C_{el} is the electronic contribution, C_{hf} is the Schottky contribution, and C_{ph} is the phonon contribution. The high-temperature approximation of the nuclear hyperfine contribution to the specific heat was modelled by $C_{hf} = A_0 T^{-2}$, where A_0 is a field-dependent parameter. A_0 is estimated to be ~ 1.4 mJ K mol^{-1} at 8 T, which is consistent with the value previously obtained for pure rhenium [165, 166]. The results of this analysis raise a note of caution.

A hyperfine contribution to the specific heat has also been seen in other Re-based α-Mn compounds, $Nb_{0.18}Re_{0.82}$ [123] and Re_6Hf [114], as well as in pure Re [165, 166], indicating that a Schottky anomaly may always be present in Re-based superconductors at low temperatures. Mazidian *et al.* demonstrated that in order to establish the presence of point or line nodes in the superconducting gap, the heat capacity needs to be fit below $T_c/10$ [167]. Modifications by a magnetic field below T_c to both $C_{el}(T, B)$ and $C_{hf}(T, B)$ mean that a precise evaluation of the temperature dependence of the electronic specific heat and hence the gap structure in all Re-based NCS superconductors, including those with an α-Mn structure, may be challenging, as this will require an accurate evaluation of the hyperfine contribution to the specific heat.

4.1.4 Magnetisation and Lower Critical Field Measurements

Figure 4.6(a) shows the dc susceptibility data $\chi_{dc}(T)$ taken in zero-field-cooled warming (ZFCW) and field-cooled cooling (FCC) modes in an applied field of 1 mT. These data confirm that Re_6Zr is a superconductor with $T_c^{onset} = 6.70(5)$ K. The sample exhibits a full Meissner fraction for the ZFCW. There is almost no flux expulsion on re-entering the superconducting state during FCC. The strong pinning is consistent with a disordered system. Magnetisation versus field sweeps in low fields (0 to 16 mT) at several temperatures are shown in Fig. 4.6(b). The lower critical field, $H_{c1}(T)$, is determined from the first deviation from linearity of the

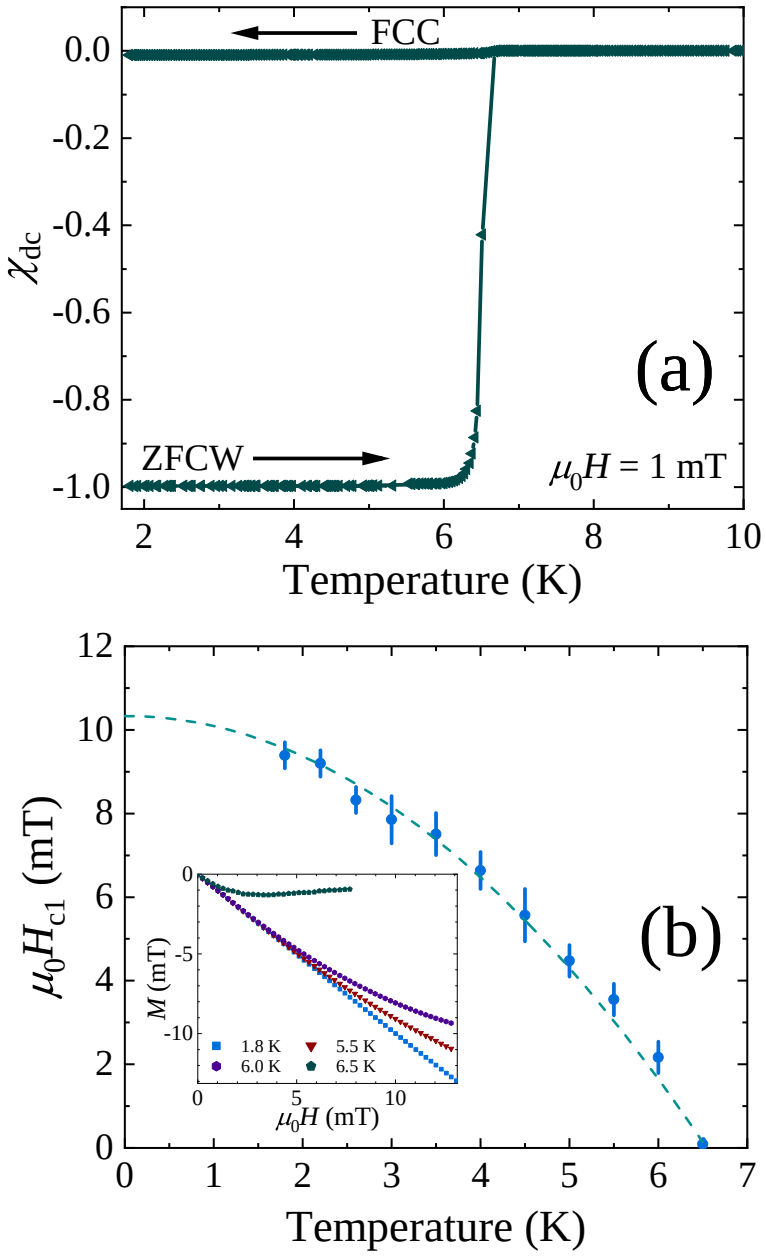

Figure 4.6: (a) Temperature dependence of the dc magnetic susceptibility $\chi_{dc}(T)$ collected in zero-field-cooled warming (ZFCW) and field-cooled cooling (FCC) modes in an applied field of $\mu_0 H = 1$ mT. (b) Lower critical field H_{c1} versus temperature for Re_6Zr. The H_{c1} values were taken as the fields at which initial magnetisation versus field data shown in Fig. 4.6(b) first deviate from linearity (as shown in the inset). The dashed line shows the fit using Eq. (4.7) giving $\mu_0 H_{c1}(0) = 10.3(1)$ mT.

initial slope as the field is increased. In Fig. 4.6(c) the resulting $H_{c1}(T)$ values are plotted against temperature. Ginzburg-Landau (GL) theory gives

$$H_{c1}(T) = H_{c1}(0)\left[1 - \left(\frac{T}{T_c}^2\right)\right]. \tag{4.7}$$

Fitting the data using Eq. (4.7), $H_{c1}(0)$ was estimated to be 10.3(1) mT.

The ac susceptibility versus temperature measurements $\chi_{ac}(T)$ shown in Fig. 4.7 confirm the superconducting transition of $T_c = 6.70(5)$ K. In dc bias fields less than $H_{c1}(0)$ the sample exhibits a full Meissner fraction. The out-of-phase component of the ac susceptibility $\chi''(T)$ contains a sharp maximum close to T_c and falls to zero for lower temperatures. This is consistent with the strong flux pinning seen in the low-field FCC $M(T)$ data. For applied fields much greater than $H_{c1}(0)$, T_c is suppressed, and a full Meissner fraction is not seen due to partial flux penetration. An anomalous dip can be seen close to T_c, suggesting flux is being reexpelled from the sample due to unusual flux dynamics. At lower temperatures, $\chi''(T)$ exhibits a broad maximum, indicating losses due to flux motion in dc applied fields $\mu_0 H \geq 2$ T.

Further evidence of unusual flux pinning in Re_6Zr can be seen in the $M(H)$ loops taken in the both the superconducting quantum interference device (SQUID) magnetometer and the VSM (see Fig. 4.8), suggesting that the observed features cannot simply be attributed to the significant movement of the sample in a magnetic field or the magnetic field sweep rate. As is evident from Fig. 4.8(a), above H_{c1}, Re_6Zr exhibits the conventional behaviour for a type-II superconductor, with a hysteresis in the magnetisation ΔM decreasing with increasing temperature and magnetic field. For applied fields close to $H_{c2}(T)$ this hysteresis ΔM disappears, and the magnetisation becomes reversible as vortices appear to become unpinned. The inset in Fig. 4.8(a) shows how this irreversibility field H_{Irr} varies with temperature. These data were collected using a plate-shaped sample with the field applied in the plane of the plate, i.e., with the demagnetisation factor of the sample minimised. By changing the sample orientation with respect to the applied field a change in vortex pinning is observed, as can be seen in Figs. 4.8(b) and 4.8(c), where the demagnetisation factor was maximised. In Figs. 4.8(b) and 4.8(c) a clear secondary maximum (fishtail) is observed. As the sample is cooled, there is a slight shift to higher magnetic field in the onset and the peak of the fishtail. This behaviour is not normally observed in low-T_c superconductors but is quite common in the high-T_c oxides and in some two-dimensional superconducting materials, indicating unconventional vortex states. The symmetry of the hysteresis in the field-increasing

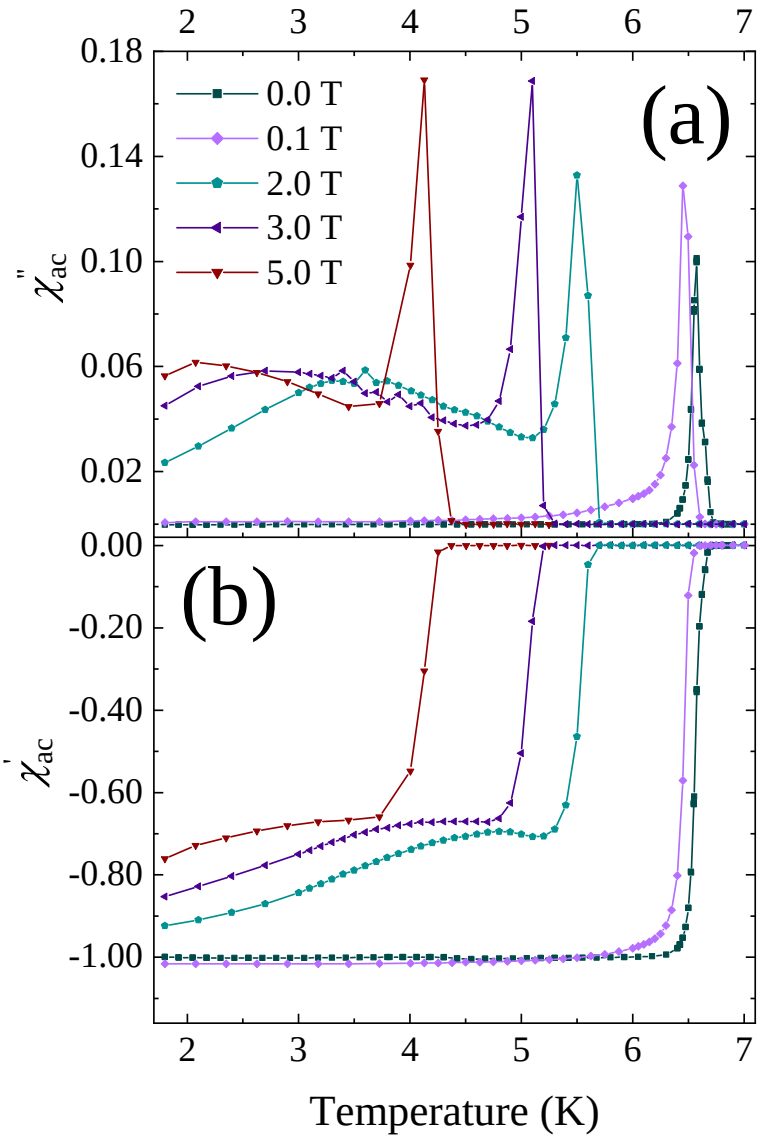

Figure 4.7: (a) Imaginary part of ac susceptibility versus temperature $\chi''(T)$ in various dc applied fields. (b) Real part of ac susceptibility versus temperature $\chi'(T)$ at various dc applied fields. In zero dc field, a sharp superconducting transition can be seen at 6.70(5) K. In fields above $H_{c1}(0)$ an anomalous dip in the magnetisation is seen close to the transition temperature.

and field-decreasing legs of the $M(H)$ curves suggests that bulk pinning rather than surface barriers may be the dominant mechanism leading to the fishtail. Assuming the superconducting critical current is proportional to ΔM, the maximum pinning force in the field of range 1 to 3 T, as reflected in the fishtail, and appears to be

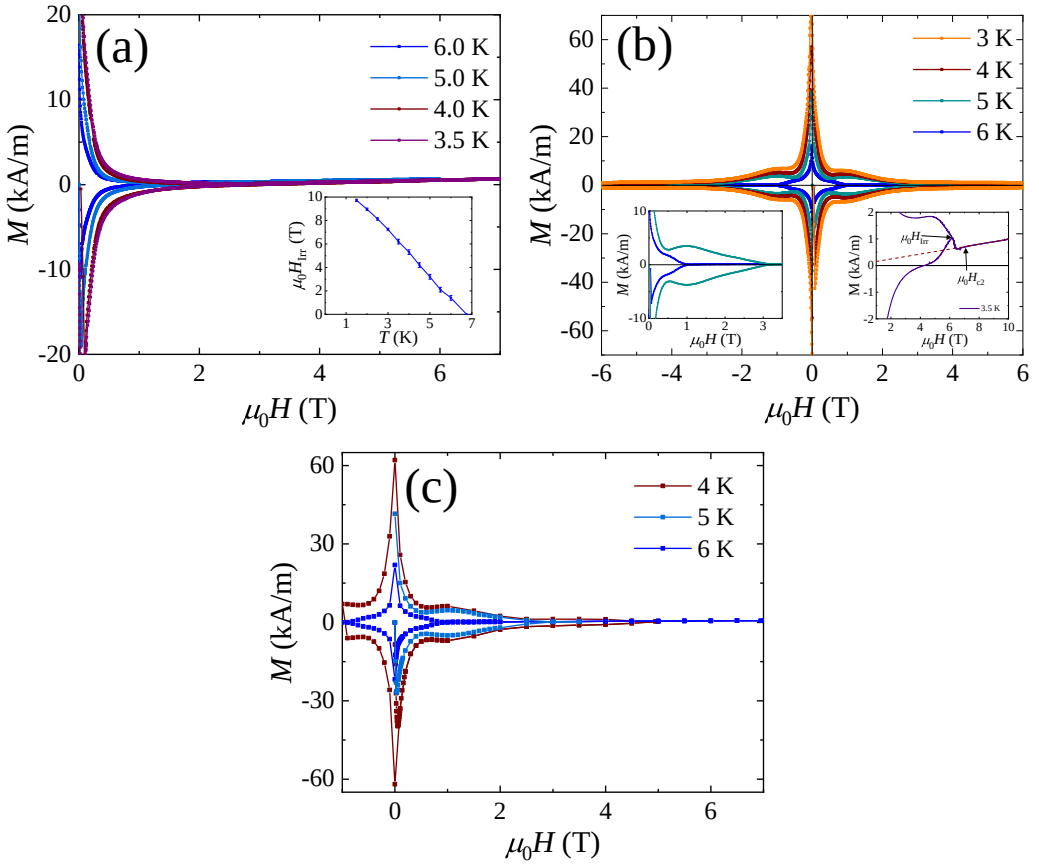

Figure 4.8: (a) Magnetisation versus magnetic field at several temperatures for Re_6Zr. The data were collected in a VSM on a plate-shaped sample with the demagnetisation factor of the sample minimised. The inset shows how H_{Irr} varies with temperature. (b) Magnetisation versus magnetic field at several temperatures collected in a vibrating sample magnetometer with the demagnetisation factor of the Re_6Zr sample maximised. A secondary maximum (fishtail) can clearly be seen in the magnetisation at around 1.25 T. The left inset shows the 5 and 6 K curves between 0 and 3.5 T. H_{Irr} and H_{c2} are indicated in the right inset showing the 3.5 K curve between 2 and 10 T. (c) Magnetisation versus magnetic field at several temperatures collected in the SQUID magnetometer. The fishtail can also be clearly seen in a magnetic field of $\sim$ 1.25 T.

almost temperature independent between 3 and 5 K. It is suggested that the unusual vortex states arise from the normal pinning centres such as grain boundaries within the sample. A detailed study on the vortex states in high-quality single crystals of Re_6Zr is needed to explore the vortex physics further.

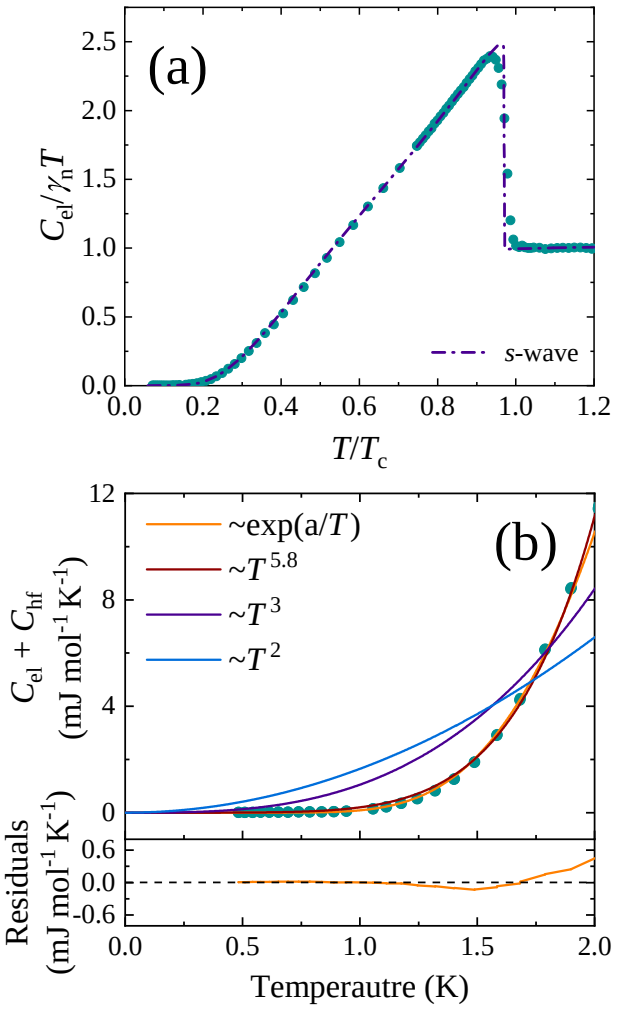

Figure 4.9: (a) Normalised electronic heat capacity versus temperature in zero field for Re_6Zr across the superconducting transition. Here C_{el} is defined as $C_{el} = C - \beta_3 T^3 - \beta_5 T^5$. The red line shows a fit across the superconducting transition for a fully gapped superconductor as described in Sec. 4.1.5. From this it can be see that the data are very well fit by the isotropic s-wave BCS model. (b) Electronic-heat-capacity C_{el} versus temperature below 2.5 K showing various power laws (anisotropic gap) and an exponential (isotropic gap) fit to the low-temperature data. The residual is shown for the exponential fit.

4.1.5 Superconducting Gap

The jump in specific heat in zero-field indicates the onset of bulk superconductivity. The transition temperature is defined as the midpoint of the transition, giving $T_c = 6.75(5)$ K. The data in Fig. 4.9(a) were fit using the BCS model of the specific

heat given in Ref. [11]. The entropy S was calculated from

$$\frac{S}{\gamma_{\rm n}T_{\rm c}} = -\frac{6}{\pi^2}\frac{\Delta_0}{k_{\rm B}T_{\rm c}}\int_0^\infty \left[f\ln f + (1-f)\ln(1-f)\right] dy, \tag{4.8}$$

where f is the Fermi-Dirac function given by $f = \left[1+\exp\left(E/k_{\rm B}T\right)\right]^{-1}$ and $E = \Delta_0\sqrt{y^2+\delta(T)^2}$, where y is the energy of the normal-state electrons and $\delta(T)$ is the temperature dependence of the superconducting gap calculated from the BCS theory. The specific heat of the superconducting state is then calculated by

$$\frac{C_{\rm sc}}{\gamma_{\rm n}T} = \frac{d(S/\gamma_{\rm n}T_{\rm c})}{dt}, \tag{4.9}$$

where $t = T/T_{\rm c}$. The superconducting gap $\Delta_0/k_{\rm B}T_{\rm c}$ was estimated to be 1.86(5), which is in agreement with Ref. 6. For conventional BCS superconductors a value of 1.76 is expected, and the larger value for Re_6Zr indicates that the electron-phonon coupling is slightly enhanced. $\Delta C/\gamma_{\rm n}T_{\rm c} = 1.60(2)$ is also larger than the 1.43 expected for conventional BCS superconductors and agrees with the values reported in Refs. [6] and [111]. A fit was also attempted using a two-gap model, but it was found that $\Delta_0/k_{\rm B}T_{\rm c}$ for the two gaps iterated to the same value, indicating that the material has a single gap.

To determine whether the superconducting gap is isotropic (exponential) or anisotropic (power law) it is necessary to determine the temperature dependence of the electronic component of the heat capacity down to low temperature, as shown in Fig. 4.9(b). Due to the difficulties in approximating the zero-field hyperfine contribution in the specific heat this contribution has also been included in Fig. 4.9(b). Figure 4.9(b) shows fits to several power laws of the form $b \times T^N$, where b is a constant. Setting $N = 2$ or 3 the fits are poor, while $N = 5.8$ gives a good fit to the data, although this provides no physical insight. The $(C_{\rm el} + C_{\rm hf})$ data are best described by an exponential temperature dependence, suggesting an isotropic fully gapped s-wave BCS superconductor. To obtain the true nature of the superconducting gap heat capacity data well below $T_{\rm c}/10$ need to be analysed [167]. From Fig. 4.9(a) it can be seen that the specific heat is rather low. A more complete understanding of the hyperfine term is required to make any further progress with this analysis. Nuclear quadrupole measurements have been performed on polycrystalline Re_6Zr along with London penetration depth measurements on single crystals of Re_6Zr both of which have report an s-wave gap structure with a moderate coupling strength providing further evidence of a conventional BCS gap symmetry [168, 169].

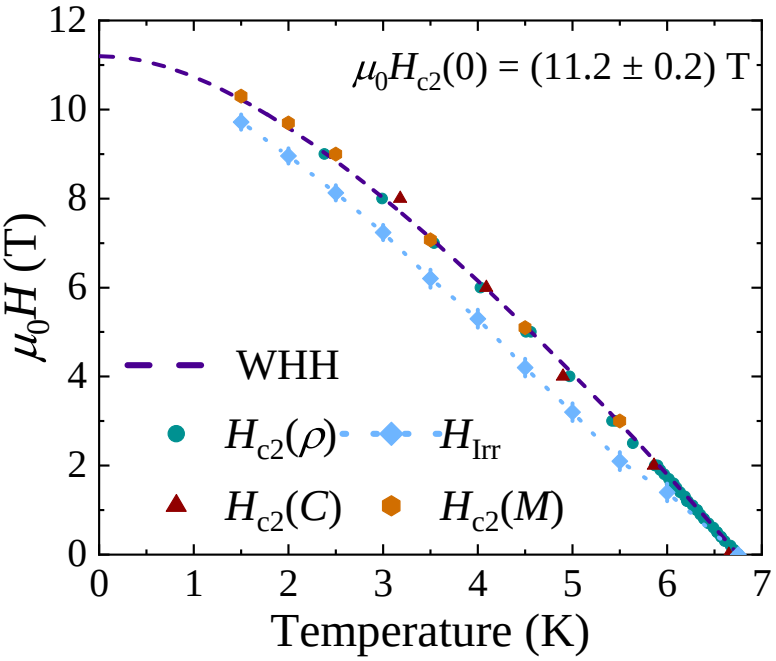

Figure 4.10: Upper critical field versus temperature of Re_6Zr determined from the electrical resistivity, heat capacity, and magnetisation data. The black curve shows the prediction for $H_{c2}(T)$ from the WHH model. For comparison $H_{Irr}(T)$ from Fig. 4.8(b) is included. $H_{Irr}(T)$ can be seen to diverge away from $H_{c2}(T)$ close to T_c and then stay a constant distant from $H_{c2}(T)$ down to 1.5 K.

4.1.6 Upper Critical Field

In order to measure the upper critical field as a function of temperature $H_{c2}(T)$, the shift in T_c in magnetic fields of up to 9 T was determined from heat capacity and resistivity data.

Figure 4.10 shows how H_{c2} varies with T. At temperatures just below T_c it is clear that H_{c2} increases linearly with decreasing T, and this indicates that the temperature dependence of H_{c2} given by the Ginzburg-Landau formula is not appropriate. Instead, the Werthamer-Helfand-Hohenberg (WHH) model was used. This allows $H_{c2}(0)$ to be calculated in terms of the spin-orbit scattering and Pauli spin paramagnetism [170] as it is expected that spin-orbit coupling may be strong

due to the presence of the rhenium. $H_{c2}(T)$ can be found by solving

$$\ln\left(\frac{1}{t}\right) = \left(\frac{1}{2} + \frac{i\lambda_{so}}{4\gamma}\right)\psi\left(\frac{1}{2} + \frac{\bar{h} + \frac{1}{2}\lambda_{so} + i\gamma}{2t}\right) + \left(\frac{1}{2} - \frac{i\lambda_{so}}{4\gamma}\right)\psi\left(\frac{1}{2} + \frac{\bar{h} + \frac{1}{2}\lambda_{so} + i\gamma}{2t}\right) - \psi\left(\frac{1}{2}\right), \quad (4.10)$$

where $t = T/T_c$, λ_{so} is the spin-orbit scattering parameter, α_M is the Maki parameter, ψ is the digamma function, $\bar{h}$ is the dimensionless form of the upper critical field given by

$$\bar{h} = \frac{4H_{c2}}{\pi^2}\left(\frac{dH_{c2}}{dT}\right)^{-1}_{t=1}, \quad (4.11)$$

and $\gamma = \sqrt{(\alpha\bar{h})^2 - (\frac{1}{2}\lambda_{so})^2}$. It is estimated that $\mu_0 H_{c2}(0) = 11.2(2)$ T, close to the value reported by Ref. [6] but below the Pauli paramagnetic limiting field $\mu_0 H_{Pauli}$ of 12.35(9) T.

The WHH expression has three variables: the Maki parameter α_M, the spin-orbit scattering parameter λ_{so}, and the gradient at T_c. In their original work [170], WHH state that α_M is not an adjustable parameter and needs to be obtained from experimental data; thus, α_M was not varied during the fitting.

The Maki parameter can be estimated experimentally by using the WHH expression

$$\alpha_M = \sqrt{2}\frac{H_{c2}^{orb}(0)}{H_{c2}^{Pauli}(0)}, \quad (4.12)$$

where H_{c2}^{orb} is the orbital limiting field given by

$$H_{c2}^{orb}(0) = -\alpha T_c \left.\frac{-dH_{c2}(T)}{dT}\right|_{T=T_c}, \quad (4.13)$$

where α is the purity factor, which for superconductors is 0.69 and 0.73 in the dirty and clean limit respectively. The initial slope $-dH_{c2}(T)/dT|_{T=T_c}$ was found to be 2.44 T/K, giving $\mu_0 H_{c2}^{orb}(0) = 11.41(5)$ T. From Eq. (4.12) we obtain $\alpha_M = 1.31$, and the relative size of the Maki parameter indicates that the Pauli limiting field is non-negligible. Fixing $\alpha_M = 1.31$ produced $\lambda_{so} = 18(5)$. It was found that this model is highly dependent on the starting values as an equally good fit, as judged by the reduced χ^2, could be obtained by allowing the Maki parameter to vary. α_M was found to drift towards zero in nearly all cases along with λ_{so}, which would also tend to zero when allowed to vary. Unsurprisingly, the initial gradient $-dH_{c2}(T)/dT|_{T=T_c}$ was found to remain constant within error.

In the first case with α_{M} fixed, the value for the spin-orbit term seems unusually large. There are several reasons why the WHH model may misrepresent what is happening in the system: (1) *Two-gap superconductor.* While the analysis of the superconducting gap was assumed to be a single gap it is possible that Re_6Zr is a two-gap superconductor where the gaps are of a similar magnitude, and this would give rise to some enhancement of H_{c2} [171]. (2) *Granularity.* The polycrystalline sample of Re_6Zr will contain grain boundaries. The upper critical field will be increased above the bulk value once the grain size becomes smaller than the coherence length [172] (the grain size is unknown, so contributions from this source are unclear). (3) *Spin-orbit coupling.* Strong spin-orbit coupling effects can yield large enhancements of H_{c2} such that the temperature dependence of H_{c2} can become linear, although in the dirty limit this enhancement should be weaker [173]. In order to obtain a more accurate value for $\mu_0 H_{c2}(0)$ high-field, low-temperature measurements of H_{c2} are needed in order to determine the form of the $\mu_0 H_{c2}(T)$ curve much closer to $T = 0$ K.

4.1.7 Properties of the Superconducting State

The results of resistivity, heat capacity, and magnetisation measurements can now be combined in order to estimate some of the important superconducting properties of Re_6Zr. The Ginzburg-Landau coherence length $\xi_{\mathrm{GL}}(0)$ can be estimated using $\mu_0 H_{c2}(0)$ from [144]

$$H_{c2}(0) = \frac{\Phi_0}{2\pi\xi_{\mathrm{GL}}^2(0)}, \tag{4.14}$$

where $\Phi_0 = 2.07 \times 10^{-15}$ Wb is the magnetic flux quantum. We calculate $\xi_{\mathrm{GL}}(0) = 5.37(9)$ nm. $\mu_0 H_{c1}(0)$ and $\xi_{\mathrm{GL}}(0)$ can be used to calculate the Ginzburg-Landau penetration depth $\lambda_{\mathrm{GL}}(0)$ from the relation

$$H_{c1}(0) = \left(\frac{\Phi_0}{4\pi\lambda_{\mathrm{GL}}^2(0)}\right) \ln\left(\frac{\lambda_{\mathrm{GL}}(0)}{\xi_{\mathrm{GL}}(0)}\right). \tag{4.15}$$

Using $\mu_0 H_{c1} = 10.3$ mT and $\xi_{\mathrm{GL}}(0) = 5.37$ nm, we calculated $\lambda_{\mathrm{GL}}(0) = 247(4)$ nm. The Ginzburg-Landau parameter can now be calculated by Eq. 2.17 which yields a value of $\kappa_{\mathrm{GL}} = 46.2(8)$. For a superconductor to be classed as a type-II superconductor $\kappa_{\mathrm{GL}} \geq \frac{1}{\sqrt{2}}$. It is clear that Re_6Zr is a strong type-II superconductor.

The thermodynamic critical field H_{c} can be calculated using $\xi_{\mathrm{GL}}(0)$ and $\lambda_{\mathrm{GL}}(0)$ using the relation

$$H_{\mathrm{c}}^{\mathrm{cal}}(0) = \frac{\Phi_0}{2\sqrt{2}\pi\xi_{\mathrm{GL}}(0)\lambda_{\mathrm{GL}}(0)}, \tag{4.16}$$

from this $H_{\rm c}^{\rm cal}(0)$ is estimated to be 175(3) mT. The thermodynamic critical field can be experimentally estimated from the difference between the free energies per unit volume of the superconducting and normal states ΔF by [144]

$$\frac{H_{\rm c}^2(T)}{8\pi} = \Delta F = \int_{T_{\rm c}}^{T}\int_{T_{\rm c}}^{T'} \frac{C_{\rm s} - C_{\rm n}}{T''} dT'' dT', \tag{4.17}$$

where $C_{\rm s}$ and $C_{\rm n}$ are the heat capacities per unit volume. From Eq. (4.17) we obtain $H_{\rm c}^{\rm exp}(0) = 130(2)$ mT.

In order to calculate the electronic mean free path and London penetration depth in Re_6Zr the Sommerfeld coefficient can be written as [174]

$$\gamma_n = \left(\frac{\pi}{3}\right)^{2/3} \frac{k_{\rm B}^2 m^* V_{\rm f.u.} n^{1/3}}{\hbar^2 N_{\rm A}}, \tag{4.18}$$

where $k_{\rm B}$ is the Boltzmann constant, $N_{\rm A}$ is the Avogadro constant, $V_{\rm f.u.}$ is the volume of a formula unit, m^* is the effective mass of quasiparticles, and n is the quasiparticle number density per unit volume. The electronic mean free path $\ell_{\rm e}$ can be estimated from the residual resistivity ρ_0 by the equation

$$\ell_{\rm e} = \frac{3\pi^2\hbar^3}{e^2\rho_0 m^{*2}\nu_{\rm F}^2}, \tag{4.19}$$

where the Fermi velocity $\nu_{\rm F}$ is related to the effective mass and the carrier density by

$$n = \frac{1}{3\pi^2}\left(\frac{m^*\nu_{\rm F}}{\hbar}\right)^3. \tag{4.20}$$

In the dirty limit the penetration depth is given by

$$\lambda_{\rm GL}(0) = \lambda_{\rm L}\left(1 + \frac{\xi_0}{\ell_{\rm e}}\right)^{1/2}, \tag{4.21}$$

where ξ_0 is the BCS coherence length and $\lambda_{\rm L}$ is the London penetration depth, which is given by

$$\lambda_{\rm L} = \left(\frac{m^*}{\mu_0 n e^2}\right)^{1/2}. \tag{4.22}$$

The Ginzburg-Landau coherence length is also affected in the dirty limit. The relationship between the BCS coherence length ξ_0 and the Ginzburg-Landau coherence $\xi_{\rm GL}$ at $T = 0$ is

$$\frac{\xi_{\rm GL}(0)}{\xi_0} = \frac{\pi}{2\sqrt{3}}\left(1 + \frac{\xi_0}{\ell_{\rm e}}\right)^{-1/2}. \tag{4.23}$$

Table 4.2: Comparison of electronic properties of Re_6Zr for $\lambda_{GL}\,(H_{c1})$ and $\lambda_{GL}\,(\mu SR)$.

Property	Units	H_{c1}	μSR
$\lambda_{GL}(0)$	(nm)	247	356
m^*/m_e		10.1(1)	12.9(2)
m^*_{band}/m_e		6.0(1)	7.7(1)
n	(10^{27}m^{-3})	15.2(2)	7.4(1)
ξ_0	(nm)	3.28(5)	3.70(5)
ℓ_e	(nm)	1.45(2)	2.36(3)
ξ_0/ℓ_e		2.25(3)	1.56(2)
λ_L	(nm)	136(2)	222(3)
ν_F	($\times$ 10^4 m/s)	8.8(1)	5.4(8)
T_F	(K)	2570(40)	1240(20)
T_c/T_F		0.0026(1)	0.0054(1)

Equations (4.18) - (4.23) form a system of four equations. To estimate the parameters m^*, n, ℓ_e, and ξ_0 this system of equations can be solved simultaneously using the values $\gamma_n = 26.9$ mJ/mol K^2, $\xi_{GL} = 5.37$ nm, and $\rho_0 = 142$ $\mu\Omega$ cm. For comparison, two values of λ_{GL} have been used; 247 nm is taken from Eq. (4.15), and 356 nm is taken from the μSR study in Ref. [6]. The results are shown in Table 4.2. From the mean free path ℓ_e calculated in Eq. (4.19) and ξ_0 calculated in Eq. (4.23), it is clear that $\xi_0 > \ell_e$, indicating that Re_6Zr is in the dirty limit. We find that these values are in close agreement with those previously reported for Re_6Zr [111].

The bare-band effective mass m^*_{band} can be related to m^*, which contains enhancements from the many-body electron-phonon interactions [175]

$$m^* = m^*_{band}\,(1 + \lambda_{el-ph})\,, \tag{4.24}$$

where λ_{el-ph} is the electron-phonon coupling constant. The electron-phonon coupling constant gives the strength of the interaction between electron and phonons in superconductors. This can be estimated from McMillan's theory [176] from Θ_D and T_c,

$$\lambda_{el-ph} = \frac{1.04 + \mu^* \ln\left(\Theta_D/1.45T_c\right)}{(1 - 0.62\mu^*)\ln\left(\Theta_D/1.45T_c\right) - 1.04}, \tag{4.25}$$

where μ^* is the repulsive screened Coulomb parameter, which can have a value between 0.1 and 0.15 but for intermetallic superconductors a value of 0.13 is typically

used. Using T_c and Θ_D taken from Fig. 4.5(b), a value of $\lambda_{el-ph} = 0.67(2)$ is obtained, suggesting this a moderately coupled superconductor. Using this value of λ_{el-ph} and Eq. (4.24) a value for m^*_{band} can be found, as seen in Table 4.2. Recently, these parameters have also been determined for the related compound Re_6Hf [113, 114]. By substituting Zr by Hf the spin-orbit coupling should be enhanced, and it was hoped that this would provide an increase in the contribution of the spin-triplet component in the superconducting ground state. From the measurements performed in Refs. [113] and [114] it is clear that Re_6Hf and Re_6Zr are very similar and that the spin-orbit-coupling strength seems to have little effect on the properties of polycrystalline samples at least. Uemura *et al.* have described a method for classifying superconductors based on the ratio of the critical temperature T_c to the effective Fermi temperature T_F [177]. The values of m^* and n can used to calculate an effective Fermi temperature for Re_6Zr using

$$k_B T_F = \frac{\hbar^2}{2m^*} \left(3\pi^2 n\right)^{2/3}, \tag{4.26}$$

and the result is presented in Table 4.2. It has been observed that the high-T_c, organic, heavy-fermion, and other unconventional superconductors lie in the range $0.01 \leq T_c/T_F \leq 0.1$ [178, 179, 177]. However, Re_6Zr lies outside of the range for unconventional superconductivity, supporting the view that the superconducting mechanism is primarily conventional.

4.2 Discussion and Summary

In summary, single-phase polycrystalline samples of Re_6Zr were prepared by the arc-melting technique. Powder neutron diffraction data confirmed the cubic, non-centrosymmetric α-Mn crystal structure and the phase purity of the samples. The normal-state and superconducting properties of Re_6Zr were studied using magnetisation, heat capacity, and resistivity measurements. We have established that Re_6Zr is a moderately coupled superconductor with a transition at $T_c = 6.75(5)$ K. In the normal-state, resistivity measurements show that Re_6Zr has poor metallic behaviour that is dominated by disorder. We showed that it is possible to fit these data with a parallel-resistor model that considers contributions in addition to the electron-phonon interactions. Specific heat measurements of the normal-state reveal no indication of any structural phase transitions down to low temperature and were fit using a simple Debye-Einstein function. The jump in specific heat at T_c is $\Delta C/\gamma_n T_c = 1.60(2)$, while $C(T)$ below T_c was fit using the BCS model, giving

$\Delta_0/k_\mathrm{B}T_\mathrm{c} = 1.86(5)$. Both values are well above those expected for a conventional BCS superconductor, suggesting the electron-phonon coupling is enhanced in this system. The mean free path ℓ_e is estimated to be 1.45(2) nm. The best approximation for $H_{c2}\,(0)$ was found using the WHH model. From $H_{c2}\,(0)$ the coherence length was calculated with $\xi_\mathrm{GL}\,(0) = 5.37(9)$ nm, confirming that $\mathrm{Re_6Zr}$ is in the dirty limit. Using the magnetisation data, it was possible to estimate $\mu_0 H_{c1}\,(0) = 10.3(1)$ mT and so calculate the penetration depth $\lambda_\mathrm{GL}\,(0) = 247(4)$ nm. The Ginzburg-Landau coefficient $\kappa_\mathrm{GL}\,(0) = 46.2(8)$ confirmed that $\mathrm{Re_6Zr}$ is a strong type-II superconductor. A summary of all the experimentally measured and estimated parameters is given in Table 4.3. From our measurements we can conclude the superconducting order parameter is well described by an isotropic gap with s-wave pairing symmetry and enhanced electron-phonon coupling, despite the observation of spontaneous magnetisation associated with time-reversal symmetry breaking being observed at temperatures below the superconducting transition in previous work [6]. This suggests $\mathrm{Re_6Zr}$ has a superconducting ground state that features a dominant s-wave component, while the exact nature of the triplet component is undetermined. The observation of time-reversal symmetry breaking in pure centrosymmetric Rhenium now indicates that this phenomena in the ReT family is not necessarily due to the noncentrosymmetric structure. Further evidence of the structure having little influence on time-reversal symmetry breaking comes from the measurements performed two compounds that are isostructural to ReT, these being $\mathrm{Mg_{10}Ir_{19}B_{16}}$ [180] and $\mathrm{Nb_{0.5}Os_{0.5}}$ [181] where time-reversal symmetry is preserved. The number and size of the spin-orbit coupling of the second element in ReT also seems to have little influence on the strength of the time-reversal symmetry breaking so what is the key component to this phenomena? In order to to investigate the superconductivity in the ReT family, further experimental work on high-quality single crystals, as well as further analysis of "clean" and "dirty" samples to examine the role grain boundaries and impurities play in determining the superconducting behaviour of ReT, is vital. Investigations into other Re-free compounds with an α-Mn structure are also of key interest.

Table 4.3: Comparison of the normal-state and superconducting properties of Re_6Zr, Re_6Hf, Re_3Ta compounds, noncentrosymmetric and centrosymmetric versions of Re_3W, Re_6Ti and $Re_{24}Ti_5$.

Property	Units	Re_6Zr (This work & [6])	Re_6Hf [113, 114, 7]	Re_3W (NCS) [121, 120]	Re_3W (CS) [121, 120]	Re_3Ta [118]	Re_6Ti [115]	$Re_{24}Ti_5$ [117, 116]
TRSB		Yes	Yes	No	No	No	Yes	Yes
T_c	(K)	6.75(5)	5.96	7.8	9.4	4.6	5.98	6.0
ρ_0	($\mu\Omega$ cm)	142(2)	106	148	135	248	–	215
Θ_D	(K)	338(9)	364	228	219	284	–	428
γ_n	(mJ/mol K^2)	26.9(1)	27.2	15.9	11.6	13.1	–	26.9
$\Delta C/\gamma_n T_c$		1.60(2)	1.53	1.57	–	–	1.58	1.4
$\Delta_0/k_B T_c$		1.86(5)	1.83	1.85	1.90	1.8	1.84	1.9
$\mu_0 H_{c1}(0)$	(mT)	10.3(1)	5.6	9.7	27.9	2.03	5.8	8.3
$\mu_0 H_{c2}(0)$	(T)	11.2(2)	12.2	12.5	14.7	7.3	–	11.2
$\mu_0 H_{c2}^{Pauli}(0)$	(T)	12.35(9)	11.1	14.5	17.4	9.03	–	11.7
$\xi_{GL}(0)$	(nm)	5.37(9)	5.2	5.13	4.73	6.7	–	5.41
$\lambda_{GL}(0)$	(nm)	247(4)	354	257	141	604	493	286
$\kappa_{GL}(0)$		46.2(8)	68	50	30	90	–	53
ℓ_e	(nm)	1.45(2)	3.4	0.27	0.24	2.33	–	29.4

Chapter 5

Hexagonal Noncentrosymmetric Superconductors La_7Pd_3 and La_7Ir_3

5.1 Introduction

The discovery of time-reversal symmetry breaking along with a isotropic s-wave gap symmetry in polycrystalline La_7Ir_3 has opened up a new family of hexagonal superconductors to investigate for more unconventional behaviour [124, 125]. Additionally time-reversal symmetry breaking has now been observed in La_7Rh_3 suggesting it is a common feature of the La_7T_3 (where T = transition metal) family similar to the Re_6X family of noncentrosymmetric superconductors [182]. The superconducting and normal-state properties have also been reported in single crystals of the noncentrosymmetric superconductor La_7Ni_3 [183]. Nakamura *et al.* report conventional BCS-like behaviour in La_7Ni_3 although no μSR results have yet been published.

La_7Ir_3 and La_7Pd_3 crystallise in the hexagonal Th_7Fe_3-type structure with the space group $P6_3mc$. Pedrazzini *et al.* previously reported some of the superconducting and normal-state properties of La_7Pd_3 as well as other members of this family of superconductors, however, no significance was drawn to the noncentrosymmetric structure that is a common features of the family [184]. In this chapter we present our detailed characterisation of the normal-state and superconducting properties of La_7Pd_3 using magnetisation, heat capacity and resistivity measurements. μSR data will then be presented showing a conventional s-wave superconducting gap symmetry before finally presenting evidence of time-reversal symmetry breaking in La_7Pd_3. We also present single crystal synthesis of La_7Ir_3 and the characterisation

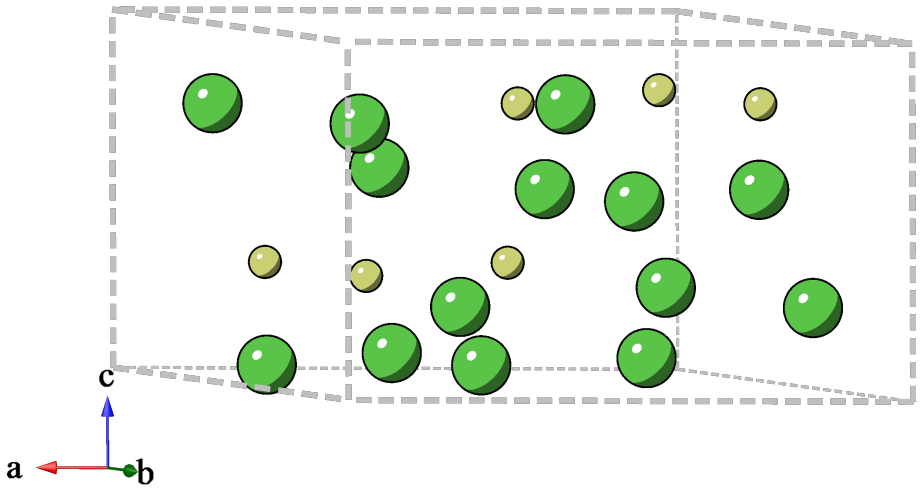

Figure 5.1: La_7Pd_3 and La_7Ir_3 crystallise in the hexagonal Th_7Fe_3-type structure with the space group $P6_3mc$. The La atoms are shown in Green and Pd/Ir atoms are shown in yellow.

of these crystals by magnetisation, resistivity and heat capacity measurements. Single crystals of La_7Ir_3 provide an excellent opportunity to look for any anisotropic behaviour that may explain the unusual superconducting properties previously report in polycrystalline samples. Finally the results of both La_7Pd_3 and La_7Ir_3 will then be compared and discussed with those of La_7T_3 family.

5.2 Time-Reversal Symmetry Breaking in Polycrystalline La_7Pd_3

In this section the synthesis and characterisation of polycrystalline samples of La_7Pd_3. Superconductivity in La_7Pd_3 was first reported in Ref. [184] where a $T_c = 1.48$ K was observed. Here we give detailed characterisation of the superconducting and normal-state properties of La_7Pd_3. We also present evidence of time-reversal symmetry breaking in La_7Pd_3 from zero-field μSR measurements.

5.2.1 Sample Preparation

Several polycrystalline samples of La_7Pd_3 were prepared by arc melting stoichiometric quantities of La (3N) and Pd (3N) in an arc furnace under an argon atmosphere on a water-cooled copper hearth. The sample buttons were melted and flipped several times to ensure phase homogeneity. The observed weight loss during the melting

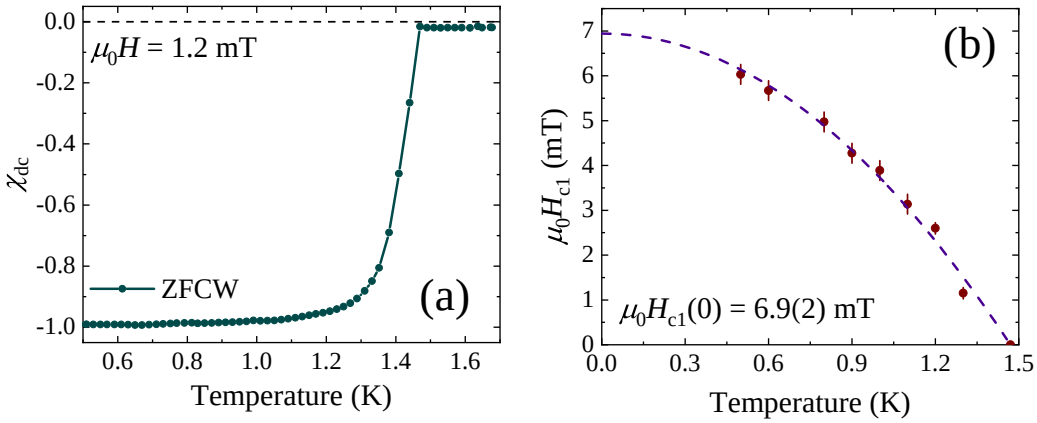

Figure 5.2: (a) Zero-field-cooled temperature dependence of the dc magnetic susceptibility $\chi_{\rm dc}$ for La_7Pd_3 measured in an applied magnetic field 1.2 mT showing a superconducting onset temperature $T_{\rm c}^{\rm onset} = 1.46(5)$ K. (b) Lower critical field $H_{\rm c1}$ versus temperature for La_7Pd_3. The dashed line show the fit to the data from Eq. (4.7) which gives $\mu_0 H_{\rm c1}\,(0) = 6.9(2)$ mT.

was negligible. The sample buttons were then sealed in an evacuated quartz tube, and annealed for 5 days at 500 °C. The material is air sensitive and was noticed to rapidly develop a orange surface discolouration if exposed to air. The sample was stored in a glove-box under an argon atmosphere.

5.2.2 Magnetisation and Electrical Resistivity Measurements

To confirm bulk superconductivity in La_7Pd_3 magnetisation as a function of temperature was measured in an applied field of 1.2 mT between 0.5 and 1.7 K as shown in Fig. 5.2(a). A rectangular sample of La_7Pd_3 was cut from the sample button to allow for the demagnetisation factor to be well defined [151]. Below 1.4 K a sharp change in the gradient of the magnetisation is observed and between 0.5 and 1.1 K a full Meissner fraction ($\chi_{\rm dc} = -1$) is clearly visible indicating bulk superconductivity in La_7Pd_3 and good sample quality. The superconducting onset temperature for La_7Pd_3 was found to be $T_{\rm c}^{\rm onset} = 1.46(5)$ K. The lower critical field can be estimated by measuring the first deviation from linearity in the magnetisation versus applied field. Several magnetisation versus field loops were performed at different temperatures from 0.5 to 1.5 K in fields up to 10 mT. Figure. 5.2(b) shows the extracted lower critical field from the magnetisation versus field loops, the temperature dependence of which can be described by the Ginzburg-Landau formula, Eq. (4.7). Using the Ginzburg-Landau formula yields $\mu_0 H_{\rm c1}\,(0) = 6.9(2)$ mT for La_7Pd_3.

The normal-state resistivity of La_7Pd_3 was measured between 10 and 300 K

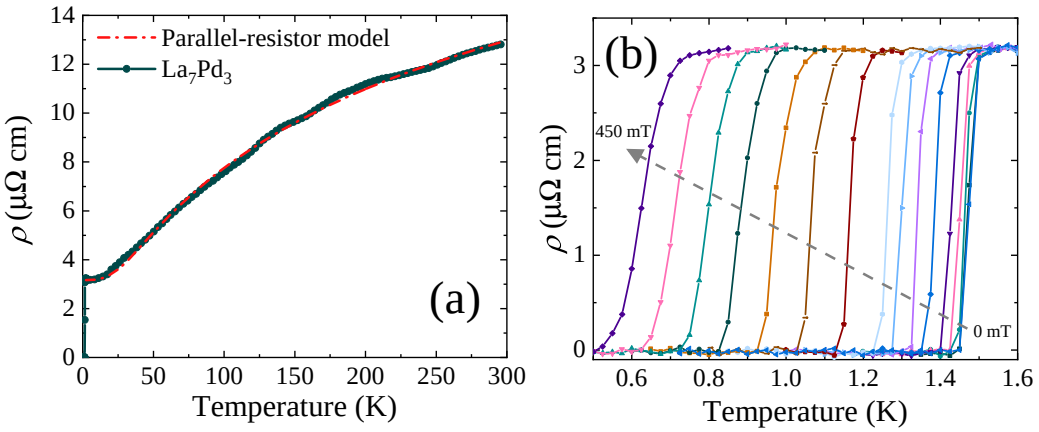

Figure 5.3: (a) Temperature dependence of the electronic resistivity of La_7Pd_3 between 1.8 and 300 K in zero applied field. The residual resistivity is measured to be $\rho_0 = 3.1(2)$ $\mu\Omega$ cm and a RRR = 4 is observed to be comparable to other members of Th_7Fe_3 family. The red dot dashed line shows the fit to the 5 to 300 K data using the parallel resistor model. (b) Suppression and broadening of the resistive superconducting transition in applied fields from 0 to 450 mT.

in zero applied field as shown in Fig. 5.3(a).The resistivity ratio is seen to be comparable to other members of the Th_7Fe_3 family with RRR = 4 for La_7Pd_3, RRR $\approx$ 2.6 for polycrystalline La_7Ir_3 [125], RRR $\approx$ 3.6 for Th_7Fe_3 [184] and RRR $\approx$ 4.3 for La_7Ni_3 [183]. The normal-state resistivity is seen to have the form typical of many intermetallic d-block superconductors which starts to saturate at higher temperatures. As discussed previously in Section 4.1.2 this behaviour can be modelled using the parallel resistor model using Eqs. (4.1a) - (4.1c). The parallel resistor model provides a good fit to the data giving the following fit parameters $\rho_{sat} = 22.0(3)$ $\mu\Omega$ cm, $C = 33.7(17)$ $\mu\Omega$ cm and $\Theta_R = 179(5)$ K when the residual resistivity is fixed at $\rho_0 = 3.1(2)$ $\mu\Omega$ cm. Further evidence of superconductivity in La_7Pd_3 is provided by low-temperature resistivity measurements where a sharp superconducting transition is seen at $T_c = 1.47(5)$ K with a width of $\Delta T = 0.05$ K in zero-applied field as shown in Fig. 5.3(b). The suppression of the superconducting transition temperature for different magnetic fields can also be seen in Fig. 5.3(b) the mid-points of these transitions can be extracted to give upper critical field values which will be discussed later. The superconducting transition is also seen to broaden to $\Delta T = 0.23(1)$ K at 450 mT.

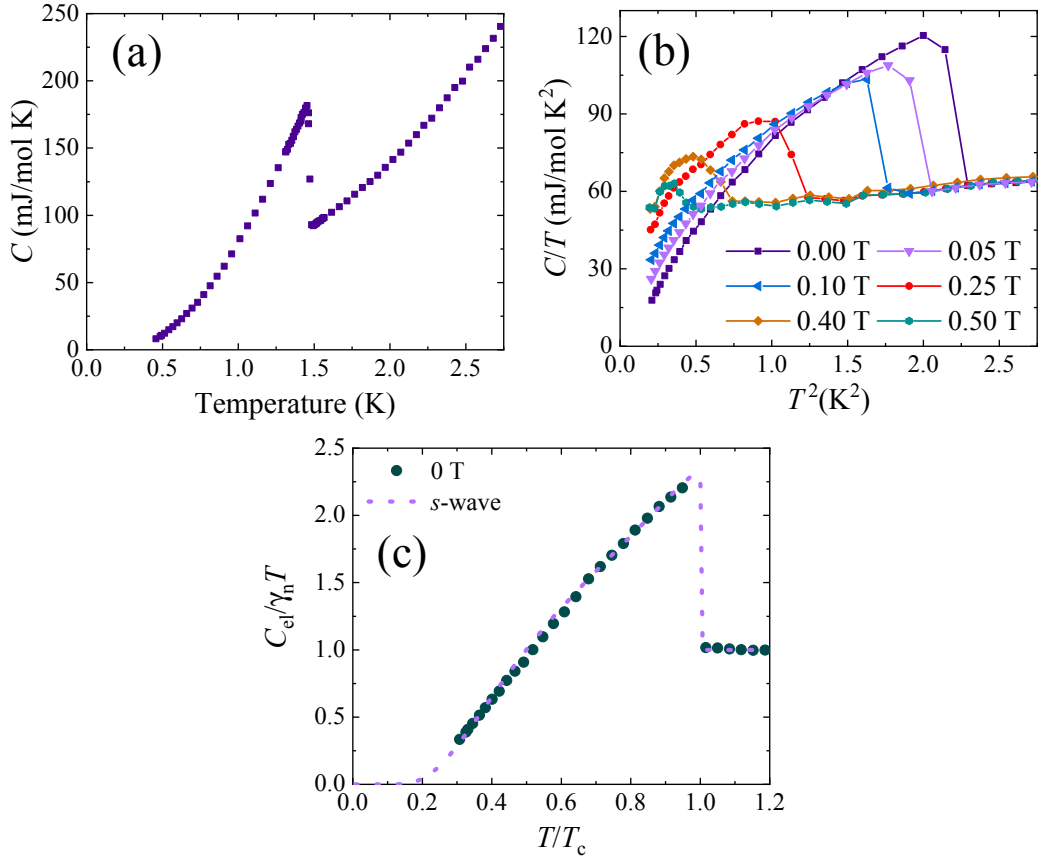

Figure 5.4: (a) Temperature dependence of the zero-field heat capacity data for La_7Pd_3 between 0.45 and 2.75 K showing a superconducting transition at T_c = 1.45(5) K. The shape of the C versus T is indicative of a typical type-II superconductor. By fitting Eq. (4.3) to the data above T_c the normal-state contribution to the heat capacity was calculated γ_n = 50.17(16) mJ/mol K^2. (b) C/T versus T^2 data showing the suppression and broadening of the superconducting transition when the applied field is increased from 0 to 450 mT. (c) Normalised electronic heat capacity $C_{el}/\gamma_n T$ versus normalised temperature T/T_c in zero applied field. The dotted line shows the fit to the data for an isotropic s-wave gap as described in Section 4.1.5.

5.2.3 Specific Heat Measurements

The temperature dependence of the heat capacity in La_7Pd_3 between 0.45 and 2.75 K can be seen in Fig. 5.4(a). A sharp anomalous jump in the heat capacity is seen at 1.45(5) K indicating the onset of bulk superconductivity in La_7Pd_3. The superconducting transition is typical of that seen in type-II superconductors indicating the La_7Pd_3 is a type-II superconductor. The normal-state heat capacity $T > 1.45$ K can can be used used to extract a value for the Sommerfeld coefficient γ_n using Eq. (4.3).

Using this equation the following values are obtained $\gamma_n = 50.17(16)$ mJ/mol K^2 and $\beta_3 = 4.86(4)$ mJ/mol K^4. The Debye temperature can now be calculated using Eq. (4.4) giving $\Theta_D = 159(2)$ K. The large γ_n is quite unusual, with the value for La_7Pd_3 surpassing some heavy fermion superconductors such as $CeCoGe_3$ ($\gamma_n = 32$ mJ/mol K^2) [74]. This suggests that there is an enhanced density of states at the Fermi surface for La_7Pd_3. This value of γ_n is consistent with that seen in other La_7X_3 [184, 125, 182, 183] compounds suggesting that this enhancement is a common feature of this family of superconductors. The field dependence of the superconducting transition for heat capacity can be seen in Fig. 5.4(b) where the transition is seen to be suppressed and broadened with increasing magnetic field. The midpoint of the superconducting anomaly for each of the fields can be used to map out the upper critical field which is discussed later in this chapter.

The superconducting heat capacity in zero applied field can be used to look for evidence of unusual superconducting order parameter by using the method described in Section 4.1.5. Figure 5.4 shows that an isotropic *s*-wave gap can be fit to the normalised electronic heat capacity data. The data and the fit are in good agreement indicating that the superconducting gap is largely *s*-wave in nature. A value of $\Delta_0/k_BT_c = 1.67$ (1) is obtained for La_7Pd_3, this value is less than the expected 1.76 indicating a slightly diminished electron-phonon coupling strength.

5.2.4 Upper Critical Field

Upper critical field values for La_7Pd_3 can be estimated by extracting the temperature and field values for the midpoint of the superconducting transition in the resistivity data [see Fig. 5.3(b)] and the midpoint of the superconducting anomaly in the heat capacity data [see Fig. 5.4(b)]. Figure 5.5 shows the upper critical field values as a function of temperature it can be seen that the resistivity values curve upwards near T_c. This behaviour is similar to the Ginzburg-Landau phenomenological model for upper critical fields. A good fit to the resistivity data can be obtained by fitting the Ginzburg-Landau model

$$H_{c2}(T) = H_{c2}(0)\frac{\left[1-(T/T_c)^2\right]}{\left[1+(T/T_c)^2\right]} \tag{5.1}$$

giving an estimated upper critical field value $\mu_0 H_{c2} = 652(5)$ mT.

It is anticipated that due to lanthanum and palladium being the constituent elements there would be a significant spin-orbit coupling contribution to the underlying physics of the superconducting state in La_7Pd_3. As previously discussed in

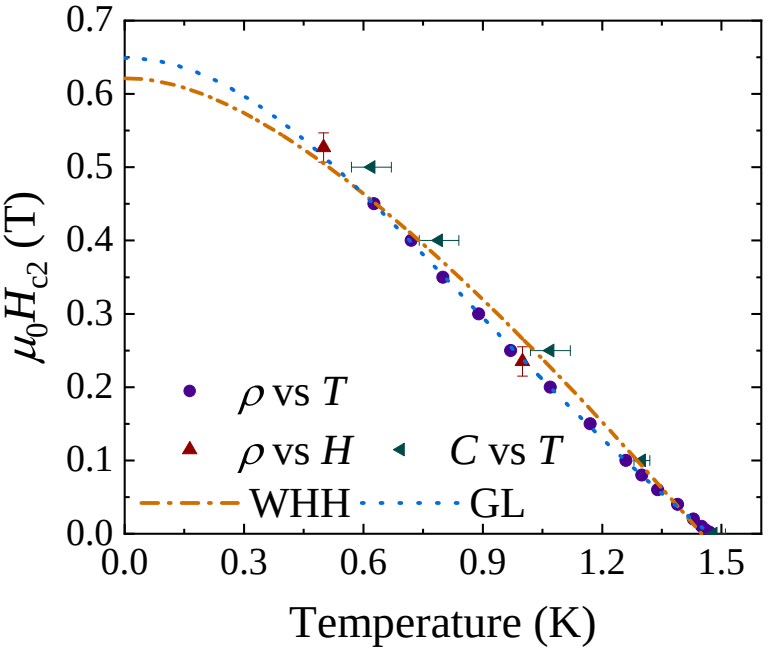

Figure 5.5: Temperature dependence of the upper critical field for La_7Pd_3. The transition temperatures were extracted from the midpoint of the anomaly in $C(T)$ and the midpoint of the resistive transition. The dashed-dotted and dotted line show the expected $\mu_0 H_{c2}$ from the WHH and GL models, respectively.

Section 4.1.6 the WHH model allows for the inclusion of small spin-orbit coupling in the upper critical field calculations. A fit to the upper critical field was attempted using the WHH model as shown by the orange dot-dashed line in Fig. 5.5 giving a slight smaller $\mu_0 H_{c2} = 620(3)$ mT. However, this model is unable to capture the curvature of the upper critical field values.

5.2.5 μSR Measurements

The macroscopic superconducting state of La_7Pd_3 was probed using magnetisation, resistivity and heat capacity however in superconductors the microscopic magnetic environment formed by the vortex lattice can provide an essential insight into the superconducting state. As previously discussed in Section 3.9 positive muons are an excellent probe of the local magnetic environment when implanted into a superconductor. The superconducting state of La_7Pd_3 has been investigated using transverse, longitudinal and zero-field μSR.

Transverse-field μSR was performed on La_7Pd_3 in applied fields above the

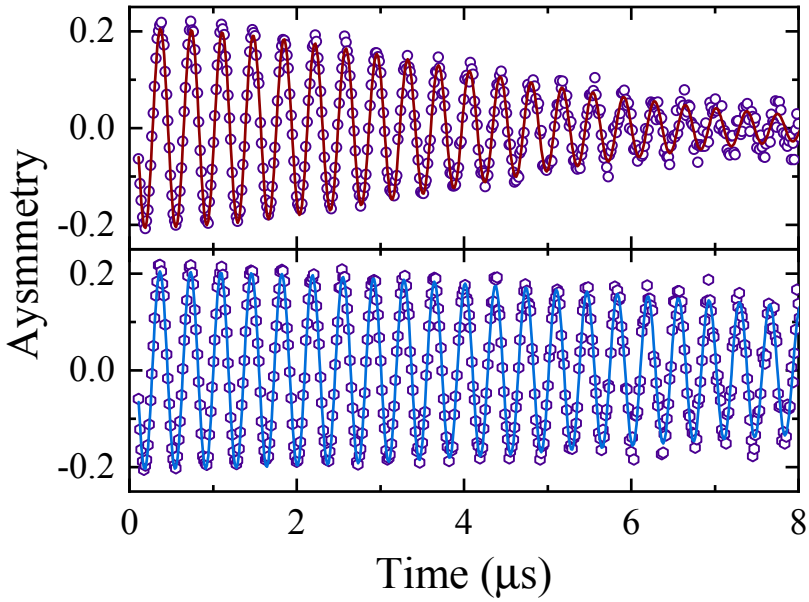

Figure 5.6: Transverse-field μSR spectra for La_7Pd_3 collected at 100 mK (top) and 2.25 K (bottom) in an applied magnetic field of 20 mT. The solid lines are fits to data using Eq. (5.2). Below the superconducting transition temperature the field distribution of the FLL causes the spectra to be significantly depolarised. Above the superconducting transition temperature the randomly oriented array of nuclear magnetic moments continue to depolarise the muons but at a reduced rate.

lower critical field ranging from 10 to 50 mT to ensure that the sample was in the mixed-state. Transverse-field spectra were collected at temperatures between 0.1 to 2.75 K. In order to produce the most stable flux line lattice possible, the sample was field cooled before starting the measurements. Figure 5.6 shows an example of the asymmetry in the superconducting and normal-state at 0.1 and 2.75 K respectively. In superconducting state the asymmetry can be seen to depolarise more quickly this is due to the effects of the flux line lattice on the muon. A small amount of depolarisation is visible in the normal-state due to nuclear magnetic moments of the sample. The oscillatory signal of the muon spectra can be fit using a Gaussian relaxation function coupled with two sinusoidal terms, one for the sample and one for the silver plate:

$$G_{\mathrm{TF}(t)} = A_1 \exp\left(-\frac{\sigma^2 t^2}{2}\right) \cos\left(\gamma_\mu B_1 t + \phi\right) + A_2 \cos\left(\gamma_\mu B_2 t + \phi\right). \qquad (5.2)$$

Here A_1 and A_2 are the sample and background asymmetries, B_1 and B_2 are the average fields in the superconductor and silver plate, ϕ is the shared phase offset,

$\gamma_\mu/2\pi = 133.5$ MHz T^{-1} is the muon gyromagnetic ratio and σ is total the depolarisation rate. By fitting Eq. (5.2) to all field and temperature spectra σ can be plotted as function of temperature as shown in Fig. 5.7(a). The total depolarisation rate is related to the depolarisation due to the flux line lattice(σ_{FLL}) and depolarisation due to the nuclear moments σ_{N} by the following equation

$$\sigma^2 = \sigma_{\mathrm{FLL}}^2 + \sigma_{\mathrm{N}}^2. \tag{5.3}$$

The nuclear depolarisation rate is found to remain constant over all temperatures at $\sigma_{\mathrm{N}} = 0.162\ \mu\mathrm{s}^{-1}$. Due to the low upper critical field compared to the applied field used in these measurements σ_{FLL} has a large field dependence. This is due to the shrinking of the intervortex distances inside the flux line lattice. The effect of the vortex cores and the expected field dependence of the second moment of the field distribution have been calculated using different models. From calculations based on the Ginzburg-Landau model the field dependence of σ_{FLL} can be described using

$$\sigma_{\mathrm{FLL}}\left[\mu\mathrm{s}^{-1}\right] = 4.854 \times 10^4 \left(1-h\right) \times \{1 + 1.21\left(1-\sqrt{h}\right)^3\}\lambda^{-2}\left[\mathrm{nm}^2\right] \tag{5.4}$$

where $h = H/H_{\mathrm{c2}}$ is the reduced field and λ^{-2} is the inverse squared penetration depth. By taking isothermal cuts of Fig. 5.7(a) as denoted by the dashed line Eq. (5.4) can then be fit to the data, as shown in Fig. 5.7(b), and the inverse squared penetration depth can be extracted. The temperature dependence of λ^{-2} can be seen in Fig. 5.7(b). The superconducting gap of La_7Pd_3can be analysed from λ^{-2}. In the clean limit the magnetic penetration depth of La_7Pd_3 can be modelled using the following

$$\frac{\lambda^{-2}\left(T\right)}{\lambda^{-2}\left(0\right)} = 1 + 2\int_{\Delta(T)}^{\infty}\left(\frac{\partial f}{\partial E}\right)\frac{EdE}{\sqrt{E^2-\Delta^2\left(T\right)}}, \tag{5.5}$$

where $f = \left[1+\exp\left(E/k_{\mathrm{B}}T\right)\right]^{-1}$ is the Fermi function and the temperature dependence of the gap for an isotropic s-wave model is $\Delta\left(T\right) = \Delta_0\delta\left(T/T_{\mathrm{c}}\right)$. Here Δ_0 is the magnitude of the superconducting gap at zero kelvin and the temperature dependence of the gap can be approximated by

$$\delta\left(T/T_{\mathrm{c}}\right) = \tanh\{1.82\left[1.018\left(T_{\mathrm{c}}/T-1\right)\right]^{0.51}\}. \tag{5.6}$$

The fit produced by this model is shown by the dashed line in Fig 5.7(c). The value of $\Delta_0 = 0.30(4)$ was obtained, giving $\Delta_0/k_{\mathrm{B}}T_{\mathrm{c}} = 2.40(13)$ which is above the BCS value of 1.76 indicating that electron-phonon coupling is enhanced in La_7Pd_3

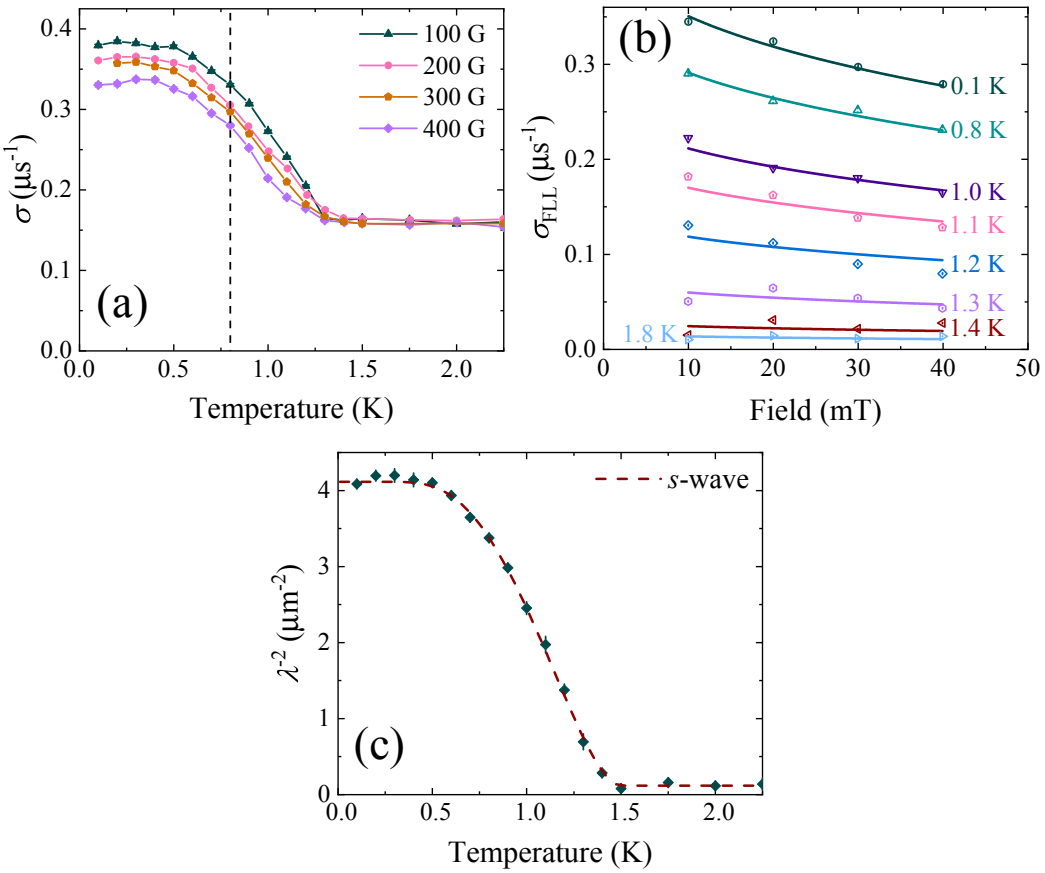

Figure 5.7: (a) Temperature dependence of the total spin depolarisation for La_7Pd_3 collected in fields between 10 and 50 mT. Isothermal cuts (represented by dashed line) are used to calculate the field dependence of σ in La_7Pd_3. (b) Field dependence of the muon spin relaxation due to the flux line lattice at several different temperatures. The solid lines are fits to the data using Eq. (5.4). (c) Temperature dependence of the the superfluid density. The dashed line is a fit to the data using Eq. (5.5).

although this contradicts with the value determined by heat capacity measurements. The penetration depth at zero kelvin was calculated to be $\lambda(0) = 495(4)$ nm.

Longitudinal-field and zero-field measurements were performed on La_7Pd_3 which can be seen in Fig. 5.8(a) to look for evidence of time-reversal symmetry breaking in the superconducting state. The asymmetry above (2.75 K) and below (0.1 K) the superconducting transition in zero-field mode are shown in Fig. 5.8(a). Here it can be seen that there is a shift between the spectra indicating the presence of small internal magnetic fields in the superconducting state. The absence of an oscillatory signal rules out the possibility of there being magnetic impurities in

the sample. Since there is a lack of atomic moments it can be assumed that this behaviour comes from the presence of static randomly orientated nuclear moments. These nuclear moments can be modelled by the Kubo-Toyabe model

$$G_{\mathrm{KT}}(t) = \frac{1}{3} + \frac{2}{3}\left(1 - \sigma_{\mathrm{ZF}}^2 t^2\right) \exp\left(-\frac{\sigma_{\mathrm{ZF}}^2 t^2}{2}\right), \tag{5.7}$$

where σ_{ZF} measures the width of the nuclear dipolar field experienced by the muons. The asymmetry above and below the superconducting transition can be modelled by

$$G(t) = A_0 G_{\mathrm{KT}}(t) \exp(-\Lambda t) + A_{\mathrm{bg}}, \tag{5.8}$$

where A_0 and A_{bg} are the sample and background asymmetries, respectively, and Λ measures the electronic relaxation rate. The sample and background asymmetries were found to be constant across all temperatures. σ_{ZF} was found to linearly decrease for increasing temperatures from 0.1 to 2.75 K [see Fig. 5.8(c)] while Λ was found to be constant above the superconducting transition with a increase slightly below the transition at $T \approx 1.4$ K [see Fig. 5.8(b)].

To eliminate any possibility of the relaxation coming from spin fluctuations due to a quantum critical point a small longitudinal field of 5 mT was applied, as shown by the purple data points in Fig. 5.8(a). The complete decoupling of the muons indicates that the spontaneous magnetic fields are static or at least quasi-static over the lifetime of the muon. While normally the evidence presented above would be taken as an observation of broken time-reversal symmetry in La_7Pd_3 the fact that the increase in the Λ-channel is below the superconducting transition temperature raises concerns as to the origin of the phenomena. The behaviour is also seen in both La_7Ir_3 [124] and La_7Rh_3 [182] though neither author comments on this. Potential sources for these behaviour are discussed at the end of the chapter.

5.2.6 Properties of the Superconducting State

Using the results of the magnetisation, resistivity, heat capacity and muon measurements several superconducting properties of La_7Pd_3 can be evaluated. Following the same calculations described in Section 4.1.7 the upper critical field can be used to estimate the Ginzburg-Landau coherence length $\xi_{\mathrm{GL}}(0) = 23.1(5)$ nm and the Ginzburg-Landau penetration depth can be estimated from the lower critical field with $\lambda_{\mathrm{GL}}(0) = 235$ nm. $\lambda_{\mathrm{GL}}(0)$ as calculated from the lower critical field is significantly lower than measurement by μSR this is however expected as the method for calculating this parameter from magnetisation is expected to overestimate the value

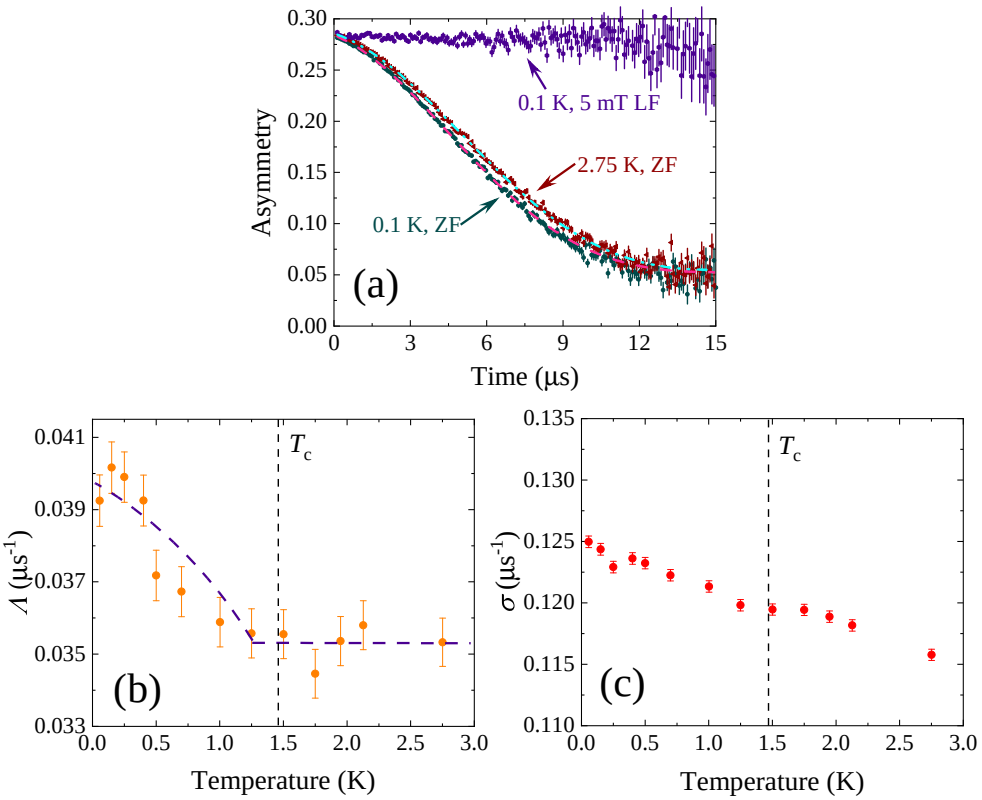

Figure 5.8: (a) ZF μSR spectra collected at 0.1 (green) and 2.75 K (red), the data is fit using the Gaussian Kubo-Toyabe model (dashed lines). (b) Temperature dependence of the electronic relaxation rate Λ can be seen to increase below 1.3 K which close to T_c.(c) Temperature dependence of the nuclear relaxation rate σ shows no change at T_c.

of the lower critical field. The value obtained from μSR will be used for further calculations. The Ginzburg-Landau parameter is calculated to be $\kappa_{GL} = 21.4$ indicating that La_7Pd_3 is a type-II superconductor. The parameters m^*, n, ℓ_e and ξ_0 can be calculated using the series of four equations Eqs.(4.18) - (4.23), the results are shown in Table 5.1. The ratio of ξ_0/ℓ_e indicates whether the La_7Pd_3 is in the dirty ($\xi_0/\ell_e \gg 1$) or clean ($\xi_0/\ell_e \ll 1$) limit. From Table 5.1, $\xi_0/\ell_e = 0.08(3)$ puts La_7Pd_3 in the clean limit due to its long scattering length and short coherence length. Finally the electron-phonon coupling constant and the Fermi temperature can be estimated using Eq. (4.25) and Eq. (4.26) giving $\lambda_{el-ph} = 0.55$ and $T_F = 387$ K. The ratio of the superconducting transition and the Fermi temperature T_c/T_F allows us to use the Uemura classification for La_7Pd_3. It can be seen that La_7Pd_3 lies outside of the region for unconventional superconductivity according the Uemura classifica-

Table 5.1: Superconducting properties of La_7Pd_3.

Property	Units	
$\lambda_{GL}(0)$	(nm)	495
m^*/m_e		14.6(1)
n	($10^{27}m^{-3}$)	1.54(2)
ξ_0	(nm)	24.4(5)
ℓ_e	(nm)	301(2)
ξ_0/ℓ_e		0.08(3)
λ_L	(nm)	516(2)
T_F	(K)	387(40)
T_c/T_F		0.004(1)

tion ($0.01 \leq T_c/T_F \leq 0.1$) however the value is of the same order of magnitude as Re_6Zr.

5.3 Growth and Characterisation of Single Crystals of La_7Ir_3

La_7Ir_3 has been of much interest to the research community since time-reversal symmetry breaking was reported in polycrystalline samples [124]. More recently evidence for conventional superconductivity in La_7Ir_3 was reported by Li *et al.* [125]. In this section we discuss the synthesis and characterisation of single crystal of La_7Ir_3. The synthesis of single crystals of La_7Ir_3 allows for any anisotropy in the superconductor to be explored to search for more conclusive evidence of exotic superconductivity.

5.3.1 Sample Preparation and Structural Analysis

Single crystals of La_7Ir_3 were grown using the Czochralski process using a radio frequency furnace where 20 g of material was prepared. More information on the Czochralski process can be found in Section 3.1.2. Figure 5.9(a) shows the pulled growth of La_7Ir_3, the growth was seen to tarnish quickly indicating that the sample is are air sensitive. Laue x-ray diffraction was used to confirm the quality and to orientate the crystals of La_7Ir_3. Single crystals of La_7Ir_3 were orientated along the $[10\bar{1}0]$ and the [0001] directions. An example of a Laue diffraction pattern for

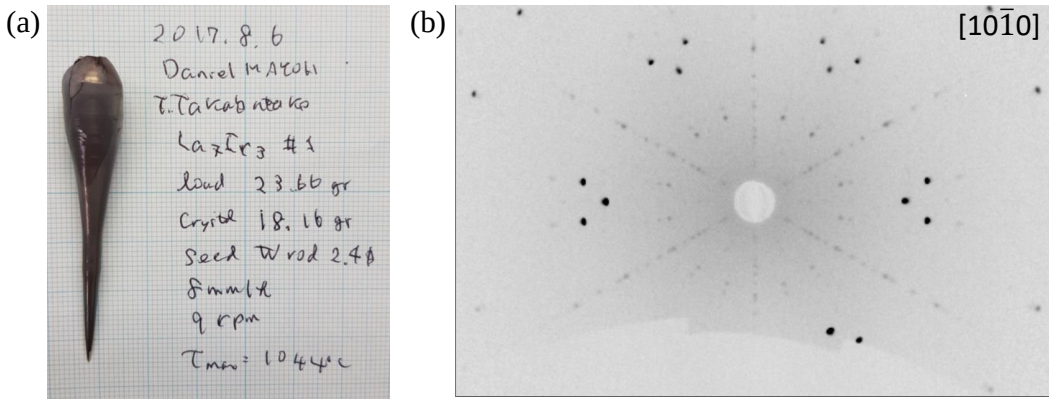

Figure 5.9: (a) Pulled growth of La_7Ir_3 by the Czochralski process. (b) Laue x-ray diffraction pattern of La_7Ir_3 orientated along the [10$\bar{1}$0].

La_7Ir_3 is shown Fig. 5.9. Powder x-ray diffraction was performed using the Bruker D5005 diffractometer with a sample vacuum chamber equipped to reduce oxidation of the La_7Ir_3 powder. The results of the powder x-ray diffraction can be seen in Fig. 5.10. The pattern was phase matched with the space group $P6_3mc$, where the lattice parameters were calculated to be $a = b = 10.243(8)$ Å and $c = 6.475(6)$ Å which is in strong agreement with previous reports [125, 185]. No impurities can be seen within the resolution limit of the instrument. EDX was used to confirm the stoichiometry and elementary variations across the single crystals of La_7Ir_3as shown in Fig. 5.11. The stoichiometry of La_7Ir_3 was measured across the bulk and at six sites. The bulk stoichiometry was measured to be 70.5% La and 29.5% Ir. Measurements of the individual sites of the sample show a stable stoichiometry across the sample. The largest variation of 1% increase in La is shown at spectrum 9 with a stoichiometry 71.2% La and 28.8% Ir. These results taken together with the sharp Laue diffraction and powder x-ray diffraction are indicative of high quality single crystals.

5.3.2 Magnetisation and Electrical Resistivity Measurements

Single crystals of La_7Ir_3 were initially characterised using magnetisation along two crystal directions to investigate if there are any anisotropy in the superconducting state. The temperature dependence of the magnetic susceptibility along the [0001] and [10$\bar{1}$0] are shown in fig. 5.12(a). The samples were measured in ZFCW and FCC mode between 1.8 and 2.8 K in an applied field of 1 mT. The onset of superconductivity is observed at $T_c^{onset} = 2.41(5)$ K, this is higher than the $T_c = 2.25(5)$ K which has previously reported in polycrystalline samples of La_7Ir_3 [124, 125]. A

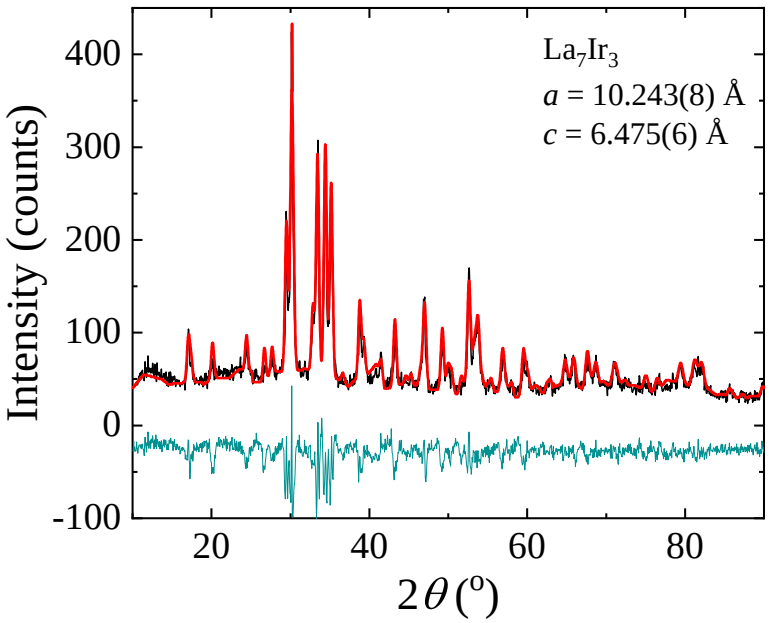

Figure 5.10: Powder x-ray diffraction of crushed single crystals of La_7Ir_3 measured using the Bruker D5005 diffractometer. The black line shows the captured x-ray pattern, the red line shows the phase match fit to the diffraction pattern and the green line shows the difference between the fit and the data.

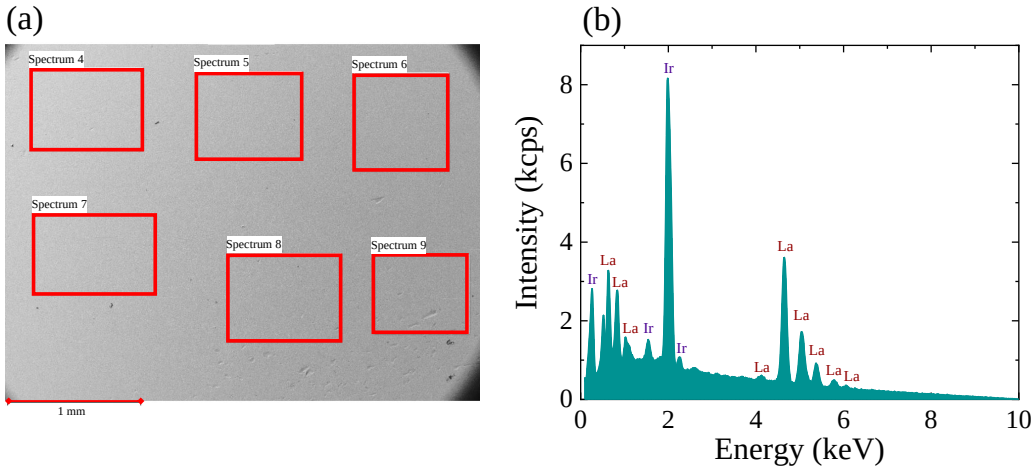

Figure 5.11: (a) Scanning electron microscope image of the surface of a single crystal of La_7Ir_3. EDX spectra were collected across the bulk of the La_7Ir_3 sample as well as the six marked sites to check for local variance in elemental stoichiometry. (b) Bulk EDX spectrum of La_7Ir_3 where the size and relative energies of the peaks indicate the elemental composition of the sample. The bulk stoichiometry was measured to be 70.5% La and 29.5% Ir.

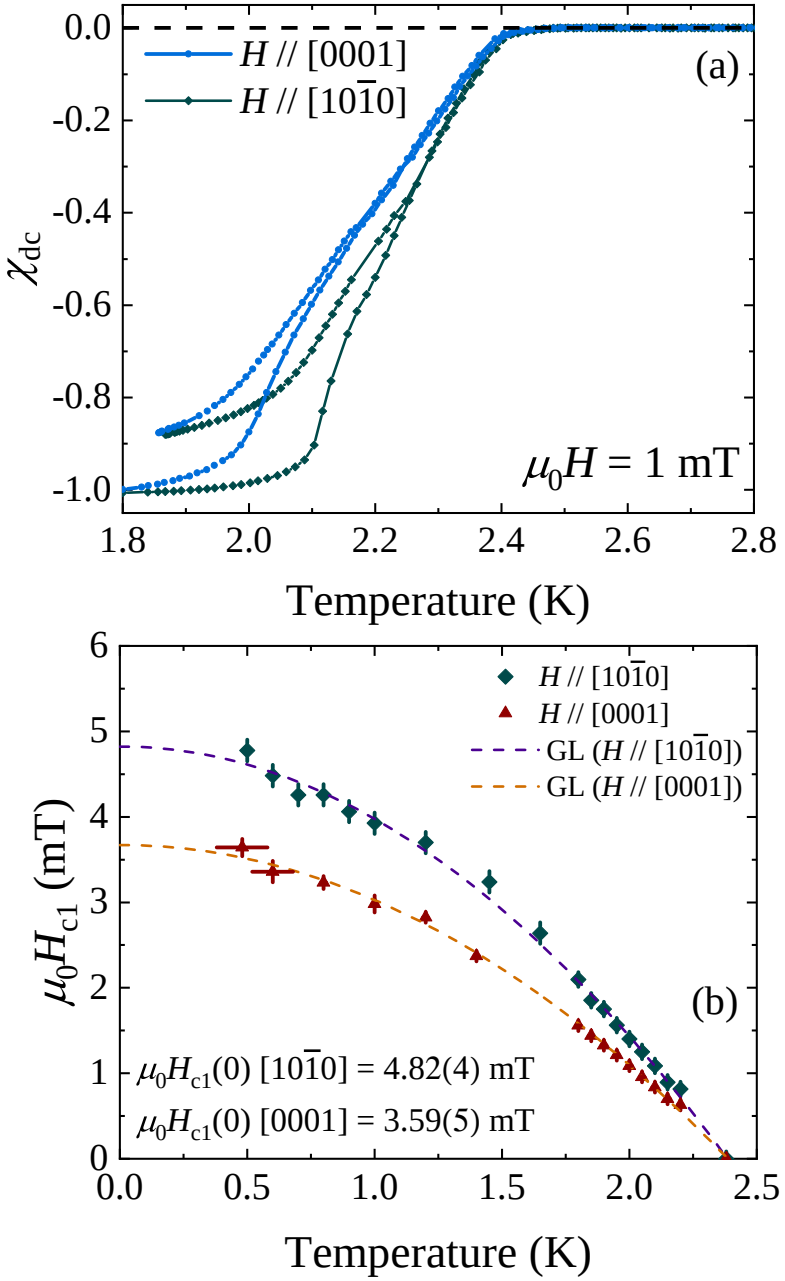

Figure 5.12: (a) Temperature dependence of the magnetic susceptibility for La_7Ir_3 with an applied magnetic field of 1 mT along the [0001] (blue) and [10$\bar{1}$0] (green) directions. The samples were measured in ZFCW and FCC mode. (b) Lower critical field as a function of temperature from [0001] (red) and [10$\bar{1}$0] (green) crystal directions. The dashed lines show fits to the data using the Ginzburg-Landau equation [see Eq. (4.7)].

full Meissner fraction of $\chi_{\rm dc} = -1$ is observed in the superconducting state indicating bulk superconductivity in single crystals of La_7Ir_3 in both crystallographic directions. When the sample is cooled in field a significant fraction of the field is re-excluded with $\chi_{\rm dc} = -0.9$ in both directions. There is a noticeable offset between the crystal directions suggesting a possible anisotropy in the critical field values. The lower critical field for both the [0001] and [10$\bar{1}$0] crystal directions was investigated using magnetisation versus applied field. By looking for the first deviation from linearity in the magnetisation versus field the lower critical field values can be extracted. Figure 5.12(b) shows lower critical field values for two crystal field directions. The lower critical field values for the two field directions have been fit by the Ginzburg-Landau model given in Eq. (4.7) giving $\mu_0 H_{\rm c1}(0) = 4.82(4)$ mT along the [10$\bar{1}$0] direction and $\mu_0 H_{\rm c1}(0) = 3.59(5)$ mT along the [0001].

The electrical resistivity of La_7Ir_3 was investigated in the normal and superconducting state. The temperature dependence of the electrical resistivity from 1.8 to 300 K with the current applied along the [01$\bar{1}$0] crystal direction can be seen in Fig. 5.13(a). The shape of the electrical resistivity in the normal-state is seen to be convex which is unusual for La-based superconductors. This shape has been previously report by Li *et al.* [125] in polycrystalline La_7Ir_3 and by Nakamura *et al.* [183] in single crystals of La_7Ni_3. A similar curvature is also seen in other noncentrosymmetric superconductors such as Re_6Zr as discussed in Section 4.1.2. The normal-state resistivity can be fit by the parallel resistor model [described in Section 4.1.2] which is shown in Fig. 5.13(b). Using Eqs. (4.1a) - (4.1c) the parallel resistor model gives $\rho_{\rm sat} = 2.31(1)$ $\mu\Omega$ cm, $C = 13.96(6)$ $\mu\Omega$ cm and $\Theta_{\rm R} = 154.7(4)$ K when the residual resistivity is fixed at $\rho_0 = 0.680(1)$ $\mu\Omega$ cm for La_7Ir_3. In single crystals of La_7Ir_3 the residual resistivity ratio is 4 which is larger than the value reported for a polycrystalline sample of La_7Ir_3 where RRR = 2.6 [125]. This is expected as there will be less disorder in the single crystal samples of La_7Ir_3.

Figure 5.13(c) shows how the superconducting transition for La_7Ir_3 is suppressed and broadened for applied fields from 0 to 2 T. In zero applied field a sharp superconducting transition ($\Delta T = 0.07$ K) is seen at $T_{\rm c} = 2.38(5)$ K, in 1.7 T a much broader transition ($\Delta T = 0.7$ K) is observed at $T_{\rm c} = 0.89(5)$ K. The mid points of the superconducting transition can be extracted to plot how the upper critical field behaves as a function of temperature which will be discussed in a later section.

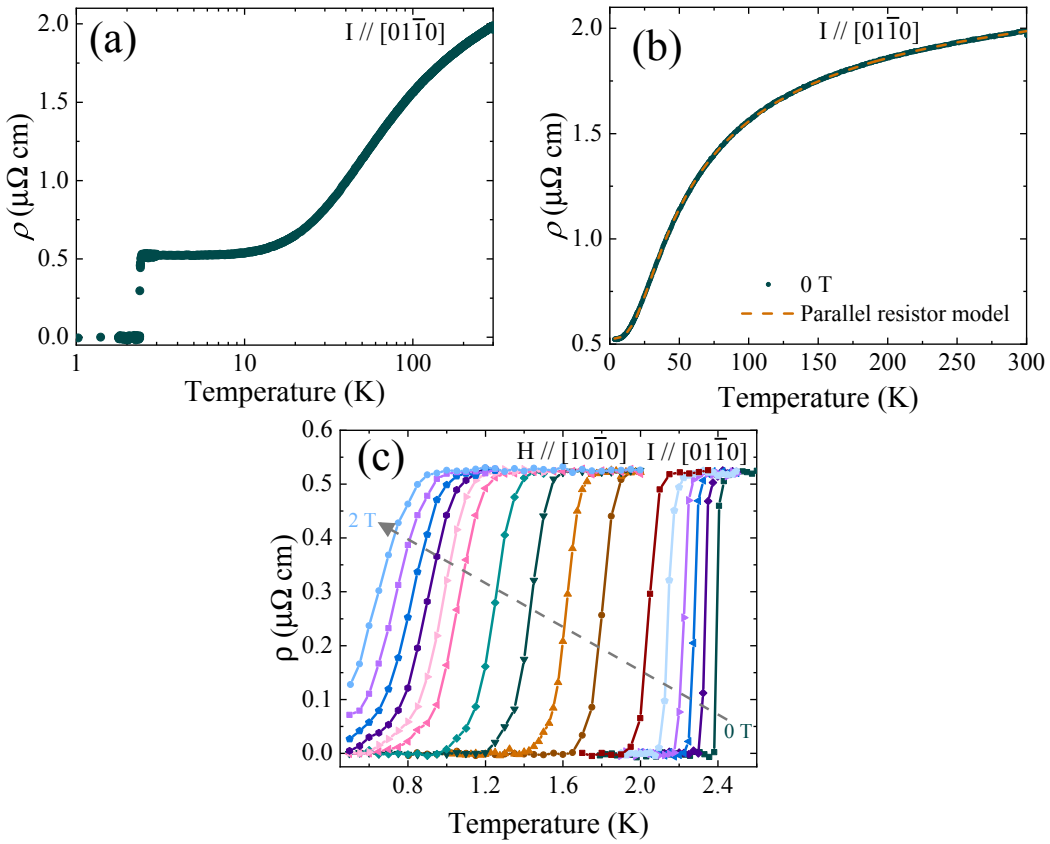

Figure 5.13: (a) Temperature dependence of superconducting and normal-state resistivity for La_7Ir_3 between 1.8 and 300 K with the current applied along the [01$\bar{1}$0] crystal orientation. La_7Ir_3 has a superconducting transition at $T_c = 2.38(5)$ K. (b) Normal-state resistivity of La_7Ir_3 fit using the parallel resistor model as described Section 4.1.2. (c) Electrical resistivity versus temperature for applied fields between 0 and 2 T. The field was applied along the [10$\bar{1}$0] direction and the current was applied along the [01$\bar{1}$0] direction. The superconducting transition is seen to be suppressed and broadened for increasing fields.

5.3.3 Specific Heat Measurements

In order to explore the symmetry of the superconducting gap in single crystals of La_7Ir_3 the heat capacity was measured. The temperature dependence of the heat capacity divided by temperature is shown in Fig. 5.14(a) where a sharp superconducting transition is observed at $T_c = 2.39(5)$ K. The heat capacity above the superconducting transition in Fig. 5.14(a) can be fit using Eq. (4.3) to obtain the Sommerfeld coefficient and Debye temperature for the normal-state. The fit to the data using Eq. (4.3) gives $\gamma_n = 49.6(5)$ mJ/mol K^2 and $\Theta_D = 163(2)$ K. These values are in close agreement with those reported by in polycrystalline La_7Ir_3 [125].

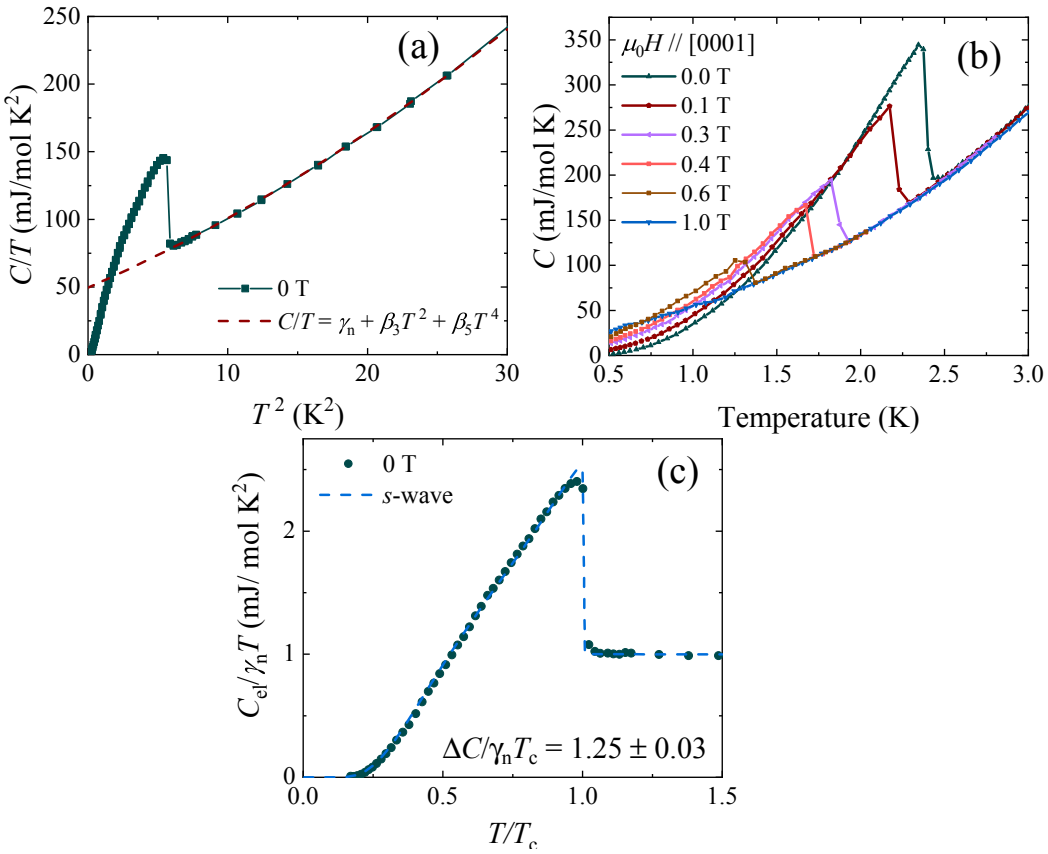

Figure 5.14: (a) Temperature dependence of the heat capacity divided by the temperature squared for La_7Ir_3. The dashed line shows a fit to the normal-state data using Eq. (4.3). (b) Heat capacity versus temperature in various fields from 0 to 1 T applied along the [0001]. A sharp superconducting transition is observed at $T_c = 2.39(5)$ K in zero applied field. (c) Normalised temperature dependence of the zero-field normalised electronic specific for La_7Ir_3. The data is found to be fit well by an s-wave model with a superconducting gap ratio of $\Delta_0/k_BT_c = 1.80(4)$.

The heat capacity as a function of temperature for various applied field between 0 and 1 T along the [0001] crystal direction is shown in Fig. 5.14(b). The superconducting transition is seen to be suppressed and marginally broadened for increasing field, the mid point of these superconducting transitions can be extracted to plot the temperature dependence of the upper critical field as discussed in the next section.

Below the superconducting transition the temperature dependence of the heat capacity can be fit to investigate the symmetry of the superconducting gap. Figure 5.14(c) show the electronic heat capacity divided by γ_n and the temperature C_{el}/γ_nT versus the normalised temperature T/T_c. As described in Section 4.1.5 the

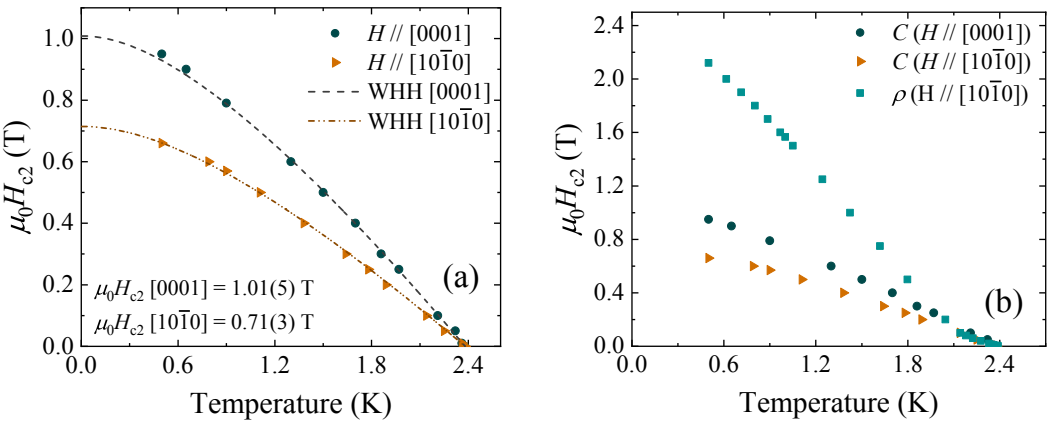

Figure 5.15: (a) Temperature dependence of the upper critical determined from the midpoint of the superconducting transition in heat capacity measurements with the applied field along two different crystal orientation in La_7Ir_3. The dashed and dashed dotted lines show fits from the WHH model giving $\mu_0 H_{c2}(0) = 1.01(5)$ T along the [0001] direction and $\mu_0 H_{c2}(0) = 0.71(3)$ T along the [10$\bar{1}$0] direction (b) Temperature dependence of the upper critical and the surface critical field. Surface critical field points are taken from the midpoint of the superconducting transition for the resistivity measurements.

superconducting gap can be fit using Eq. (4.8) and Eq. (4.9). The s-wave model shows good agreement giving a superconducting gap value of $\Delta_0 = 0.369(8)$ meV which gives $\Delta_0/k_B T_c = 1.80(4)$. This value is marginally larger than the BCS value of 1.76 indicating a small enhancement of the electron-phonon coupling. While the value of $\Delta C/\gamma_n T_c = 1.25(3)$ is smaller than the expected BCS value of 1.43 which may suggest anisotropy in the superconducting gap. These values do appear to contradict each other as they are both indicators of the electron-phonon coupling strength. The small $\Delta C/\gamma_n T_c$ comes about due to the large γ_n and the small ΔC. Where as the the large $\Delta_0/k_B T_c$ come about due to Δ_0 which is a more direct measurement of the superconducting gap.

5.3.4 Upper Critical Field and Surface Critical Field

Upper critical field values were extracted from the midpoint of the superconducting transition for heat capacity measurements where the field was applied along [0001] [see Fig. 5.14(b)] and [10$\bar{1}$0] crystal direction in La_7Ir_3. Figure 5.15 shows the temperature dependence of the upper critical field along the two crystal directions. Fits to both crystal directions were done using the WHH model as described in Section 4.1.6.

When the magnetic field is applied along the [10$\bar{1}$0] the gradient near T_c

is determined to be $dH_{c2}(T)/dT|_{T=T_c} = -0.445(5)$ T/K using Eq. (4.13) the orbital critical field can be evaluated $H_{c2}^{orb} = 0.73(1)$ T. The Maki parameter can then be calculated using Eq. (4.12) giving $\alpha_M = 0.247(3)$. In the WHH model T_c, $dH_{c2}(T)/dT|_{T=T_c}$ and α_M are all held constant during the fitting with only λ_{so} allowed to vary. Following this procedure produces the fit as shown by the dot-dashed line in Fig. 5.15(a). It is found that $\lambda_{so} \to 0$ and the upper critical field is evaluated at $T = 0$ K gives $\mu_0 H_{c2}(0) = 0.71(3)$ T. In the [0001] crystal direction the gradient near T_c is determined to be $dH_{c2}(T)/dT|_{T=T_c} = -0.620(10)$ and using Eq. (4.13) the orbital critical field can be evaluated $H_{c2}^{orb} = 1.08(2)$ T. The Maki parameter can then be calculated using Eq. (4.12) giving $\alpha_M = 0.345(5)$. The WHH model can be fit well to the data as shown by the dashed line in Fig. 5.15(a). It is found that $\lambda_{so} \to 0$ and the upper critical field is evaluated at $T = 0$ K gives $\mu_0 H_{c2}(0) = 1.01(5)$ T.

The upper critical field was also measured by electrical resistivity measurements. By taking the midpoint of the superconducting transition in Fig. 5.13(c) the following upper critical field points can be added to our phase diagram to produce Fig. 5.15(b). Interestingly the heat capacity and resistivity measurement are in agreement until ~ 2 K before the resistivity diverges substantially with $\mu_0 H_{c2}(0)$ almost $\times 2.5$ larger which would agree with previous polycrystalline measurements of the upper critical field using resistivity [125]. Due to the nature of electrical resistivity measurements it can be much more versatile in finding small channels of superconductivity across the sample either through surface or granular effects. However, heat capacity only measures bulk superconductivity.

5.3.5 Properties of the Superconducting State

Finally several superconducting properties of La_7Ir_3 along the two crystal directions can be evaluated, the results of which are summarised in Table 5.2. Following the process and the system of equations described in Section 4.1.7 the quantities $\lambda_{GL}(0)$, $\xi_{GL}(0)$, κ_{GL}, ξ_0, ℓ_e and λ_L are calculated. As shown in Table 5.2 La_7Ir_3 is a type-II superconductor in the clean limit. The thermodynamic critical field was estimated using Eq. (4.16) and the values for $\lambda_{GL}(0)$ and $\xi_{GL}(0)$ which gives $\mu_0 H_c(0) \approx 35$ mT for both crystal directions. The electron-phonon coupling constant can also be estimated using Eq. (4.25) and Θ_D which gives $\lambda_{el-ph} = 0.616$.

Table 5.2: Superconducting properties of La_7Ir_3.

		La_7Ir_3 Crystal Directions	
Property	Units	$[10\bar{1}0]$	[0001]
$\mu_0 H_{c1}(0)$	(mT)	4.82(4)	3.59(5)
$\mu_0 H_{c2}(0)$	(T)	0.71(3)	1.01(5)
$\mu_0 H_c(0)$	(mT)	35.9(14)	35.5(18)
$\lambda_{GL}(0)$	(nm)	301(12)	364(18)
$\xi_{GL}(0)$	(nm)	21.6(9)	18.1(9)
κ_{GL}		13.9(6)	20.1(9)
ξ_0	(nm)	21.3(9)	18.5(8)
ℓ_e	(nm)	87(4)	108(5)
ξ_0/ℓ_e		0.245(10)	0.169(8)
λ_L	(nm)	270(12)	337(15)

5.4 Discussion and Summary

In summary, we investigated the superconducting properties of polycrystalline La_7Pd_3 and single crystals of La_7Ir_3. The superconducting properties of both La_7Pd_3 and La_7Ir_3 are summarised in Table 5.3. Magnetisation, heat capacity, resistivity and μSR measurements have revealed that La_7Pd_3 is type-II superconductor in the clean limit. Heat capacity and transverse-field μSR measurements indicated the superconducting order parameter is dominated by BCS-like s-wave component. The upper critical field of La_7Pd_3 is well fit by the Ginzburg-Landau phenomenological model which provides further evidence of conventional superconducting behaviour. However, longitudinal and zero-field μSR measurements show an increase in the Λ-channel of the Gaussian Kubo-Toyabe model below $T = 1.4$ K. This is taken as evidence of time-reversal symmetry breaking due to the lack of long-range order in the sample and the presence of static or quasi-static spins over the lifetime of the muon. However, the Λ-channel starting to increase below the superconducting transition temperature raises concerns about the true origin of the phenomena. Multigap behaviour would allow for a lack of alignment with the superconducting transition since one gap could open up where time-reversal symmetry is preserved before a second gap opens with time-reversal symmetry breaking. No evidence for multigap superconductivity has been seen in either the heat capacity and TF-μSR. Although, as previously discussed if $\mathbf{d}(\mathbf{k})$ in Eq. (2.25a) it can prove experimentally difficult to differentiate the admixture from that of a conventional s-wave pairing.

An increase in the Λ-channel is seen in Sr_2RuO_4 [186], $LaNiC_2$ [104], Zr_3Ir [187] and SrPtAs [188] where this phenomena is also reported as time-reversal symmetry breaking. Collectively time-reversal symmetry breaking has now been observed in three members of the La_7X_3 family; La_7Ir_3 [124], La_7Rh_3 [182] and now La_7Pd_3 where an increase in Λ of a similar magnitude 0.0005 - 0.001 μs^{-1}. σ_{ZF} is also observed to increase linearly in these compounds with a magnitude between 0.006 - 0.011 μs^{-1}. The $\Delta\Lambda$ and $\Delta\sigma_{ZF}$ values for each compound are listed in Table 5.3. Time-reversal symmetry breaking can arise in superconductors for several reasons, not just from triplet pairing. In Sr_2RuO_4 the time-reversal symmetry breaking is thought to arise due to a degeneracy in the superconducting phase brought about by non-zero spin and orbital moments. This in turn allows for the creation of spontaneous supercurrents near to grain boundaries and impurities from inhomogeneous order parameters [186, 189, 190]. Conversely time-reversal symmetry breaking in $LaNiC_2$ is thought to arise due to hyperfine fields made by nonunitary spin triplet pairs [104]. However, unlike $LaNiC_2$ and Sr_2RuO_4 where unconventional gap structures have been observed, La_7Pd_3 and La_7Ir_3 only exhibit BCS-like *s*-wave gaps structures. It has been shown by Scheurer that it is not possible for a fully gapped superconductor that is mediated by electron-phonon interactions to break time-reversal symmetry [191]. This implies that an unconventional mechanism i.e. electron-electrons interactions must be responsible for the pairing in La_7Pd_3, La_7Ir_3 and La_7Rh_3. The detection of a single *s*-wave gap in these compounds causes concern but mixed pairing is allowed. A spin-split Fermi surface can look conventional in nature if the magnitude of the two superconducting order parameters are similar. In order to distinguish parity mixing effects it is now necessary to study single crystal of La_7Pd_3, La_7Rh_3 and La_7Ir_3. Further characterisation and time-reversal symmetry breaking investigations are required on other members of this family of superconductors. In particular a study of the centrosymmetric La_7Ru_3 will indicate whether broken inversion symmetry is necessary for time-reversal symmetry breaking in these compounds.

In this thesis we have begun to investigate single crystals of La_7Ir_3 along two different crystal directions to look for evidence of mixed pairing in the superconducting order parameter. A combination of magnetisation, resistivity and heat capacity have revealed that $La_7Ir_3$is a clean type-II superconductor. Measurements of the superconducting gap using heat capacity have observed an isotropic *s*-wave gap structure in La_7Ir_3. Heat capacity measurements have been found to show isotropic fully gapped superconductivity in other compounds where unconventional gaps have been seen through other techniques. Other measurements using muons and TDO

are necessary to corroborate the results seen through heat capacity and to explore if time-reversal symmetry breaking is preserved in single crystals of La_7Ir_3 as now the sources i.e grain boundaries of supercurrents are no longer present. An anisotropy has been observed in the lower and upper critical field of La_7Ir_3. As shown in Table 5.2 the Ginzburg-Landau penetration depth are seen to be anisotropic as a result. This in turn may lead to an anisotropy in the superfluid density. However, the small difference between the Ginzburg-Landau penetration depths may indicate that the superfluid density anisotropy are also small enough to be outside the detection limit of our current experiments. Muons spin spectroscopy and tunnel diode oscillations are a more sensitive probe of the superfluid density. The upper critical field was measured using heat capacity and resistivity measurements. At $T \approx 1.8$ K the upper critical field as determined by resistivity is seen to diverge away from those determined by heat capacity showing positive curvature close to the point of divergence. Resistivity measurements are sensitive to surface effects implying that source of the divergence comes from surface superconductivity. This is seen in other noncentrosymmetric compounds such as $LaPdSi_3$ and $LaPtSi_3$ [192].

Table 5.3: Physical properties of La_7Pd_3. The values for polycrystalline La_7Ir_3, La_7Rh_3, La_7Ni_3 and La_7Ru_3 are also given for comparison.

Property	Units	La_7Pd_3 (This work)	La_7Ir_3 (This work & [124])	La_7Rh_3 [182, 184]	La_7Ni_3 [183]	La_7Ru_3 [184]
T_c	(K)	1.46(5)	2.38(5)	2.65	2.4	1.92
$\mu_0 H_{c2}$	(T)	0.652(5)	1.01 $\parallel$ c, 0.71 $\parallel$ a	1.02	2.7	0.6
κ_{GL}		21.4	20.1 $\parallel$ c, 13.9 $\parallel$ a	22.1	–	–
$\xi_{GL}(0)$	(nm)	23.1(5)	18.1 $\parallel$ c, 21.6 $\parallel$ a	18.0	11	23.4
$\lambda_{GL}(0)$	(nm)	495(4)	364 $\parallel$ c, 301 $\parallel$ a	398	–	–
$\Delta C/\gamma_n T_c$		1.21 (1)	1.22	1.38	1.2	0.86
γ_n	(mJ/mol K^2)	50.2(2)	53.1	48	44	42
$\Delta\Lambda$	(μs^{-1})	0.005(1)	0.011 [124]	0.005	–	–
$\Delta\sigma_{ZF}$	(μs^{-1})	0.010(1)	0.011 [124]	0.006	–	–

Chapter 6

Chiral Noncentrosymmetric Superconductors $TaRh_2B_2$ and $NbRh_2B_2$

6.1 Introduction

In the preceding two chapters, the properties of cubic and hexagonally structured noncentrosymmetric compounds were discussed. The recent discovery of two new noncentrosymmetric superconductors with chiral structures, $TaRh_2B_2$ and $NbRh_2B_2$ [193] has added a new twist to an already exciting area of superconductivity research. Noncentrosymmetric superconductors with a chiral structure are rare but examples do exist. For example, $Li_2(Pd_{1-x}Pt_x)_3B$ $(0 \leq x \leq 1)$ has an antiperovskite structure, (chiral space group $P4_332$).
Li_2Pd_3B is an s-wave superconductor, while the stronger antisymmetric spin-orbit coupling in Li_2Pt_3B enhances the triplet component, producing line nodes in the gap, as revealed by the linear temperature dependence of the magnetic penetration depth $\lambda(T)$ at low T [4, 87]. Mo_3Al_2C, (chiral space group $P4_132$), is a strongly-coupled superconductor with a T_c of 9 K. NMR and electronic heat capacity data, along with a pressure enhanced T_c suggest Mo_3Al_2C has a nodal gap with singlet-triplet mixing [90, 91].

Multigap superconductivity has been reported in several classes of superconductor including the iron pnictides [194, 135, 136] and the borides including MgB_2 [195, 134, 196, 135, 197]. There are several non-chiral noncentrosymmetric superconductors that exhibit multigap behaviour. For example, Y_2C_3 is proposed to have a double-gap, each with s-wave symmetry and interband coupling. Even

in centrosymmetric materials, a combination of strong spin-orbit coupling and disorder can have profound effects on the superconducting properties. The $R_2Pd_xS_5$ ($x \leq 1$) family of materials where R = Nb or Ta with the centrosymmetric space group $C2/m$ are particularly noteworthy in this regard [198, 199, 200]. Strong SO coupling, along with Anderson localisation resulting from a level of disorder due to Pd deficiency, leads to highly anisotropic upper critical fields that in some cases far exceed the Pauli limit (e.g., $Nb_2Pd_{0.81}S_5$ $T_c \sim 6.6$ K and $H_{c2}(0)$ along the b axis of 37 T) [198].

$TaRh_2B_2$ and $NbRh_2B_2$ are both noncentrosymmetric superconductors with a chiral structure and have the potential to exhibit similar exciting physics. The first report on this material [193] shows $TaRh_2B_2$ and $NbRh_2B_2$ has a trigonal structure (space group *P31*), with a T_c of 5.8 K and 7.5 K respectively and upper critical fields that exceed the Pauli limit. In this chapter, we have used a combination of muon spectroscopy, heat capacity, magnetisation, resistivity and pressure to probe the nature of the superconducting state of $TaRh_2B_2$ and $NbRh_2B_2$. We report that $TaRh_2B_2$ and $NbRh_2B_2$ can be best described using a two-gap $(s+s)$-wave model. It is clearly demonstrated that $TaRh_2B_2$ and $NbRh_2B_2$ are type-II superconductors with upper critical fields of $\mu_0 H_{c2} = 15.2(1)$ T and $\mu_0 H_{c2} = 20.2(1)$ T that are significantly higher than previous reported [193] and well above the Pauli limit. We have also investigated if time-reversal symmetry is broken in zero-field μSR measurements.

6.2 Multigap Superconductivity in $TaRh_2B_2$

Here we discuss the first of the two compounds $TaRh_2B_2$. This first synthesis of $TaRh_2B_2$ was reported by Carnicom *et al.* [193]. They reported magnetisation, heat capacity and resistivity measurements showing that $TaRh_2B_2$ has a superconducting transition temperature of $T_c = 5.8$ K and that the upper critical field exceeds the Pauli limiting field. Here we have synthesised $TaRh_2B_2$ and characterised the material in more detail using magnetisation, heat capacity, resistivity and muon spin spectroscopy.

6.2.1 Sample Preparation and Structural Analysis

Polycrystalline samples were prepared by grinding together powders of elemental Ta (3N, 324 mesh, Alfa Aesar), Rh (3N, NewMet) and B (2N, 324 mesh, Alfa Aesar) in the ratio 1:1.9:2.1. The resulting powder is then pressed into pellets using a uniaxial press. The pellets were wrapped in tantalum foil, placed in alumina crucible

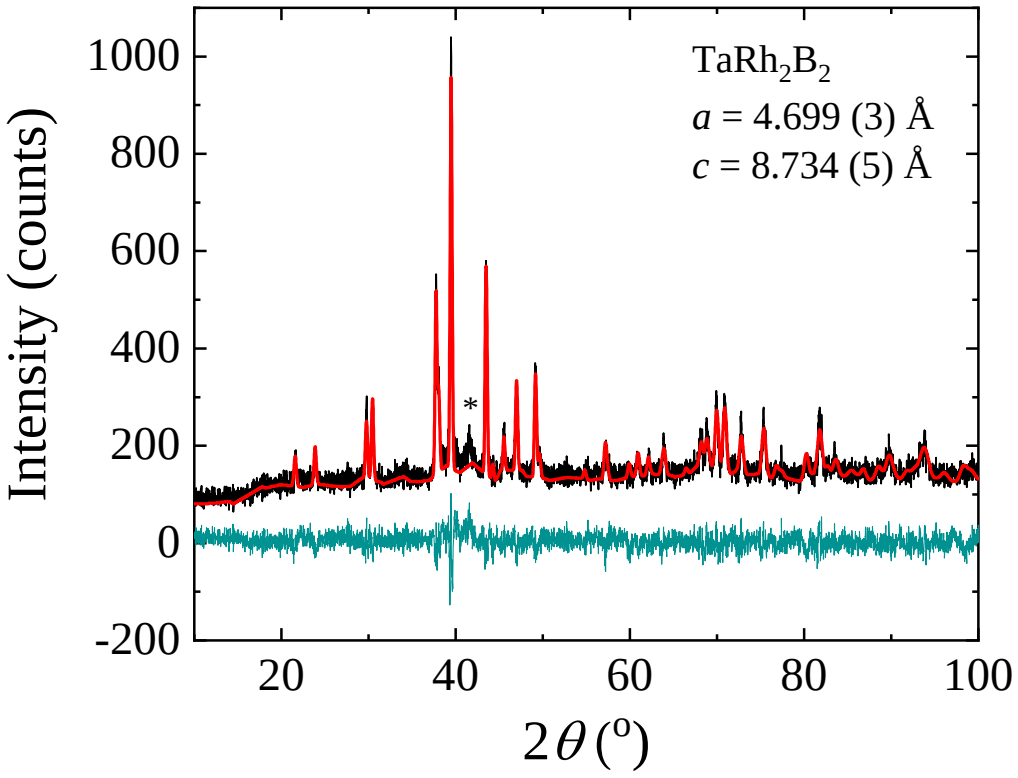

Figure 6.1: Powder x-ray diffraction data of $TaRh_2B_2$. The black line shows the captured x-ray pattern, the red line shows the phase match fit to the diffraction pattern and the green line shows the difference between the fit and the data. An unknown impurity is marked with an asterisk.

and heated at 150 °C/hour to 1200 °C, reacted for 6 hours, and then furnace cooled to room temperature, all under vacuum. Powder x-ray diffraction was performed on $TaRh_2B_2$ to check for any phase impurities in the sample. The results of the powder x-ray diffraction are shown in Fig. 6.1. The diffraction pattern was phase matched with the space group *P31*, where the lattice parameters were calculated to be $a = 4.699(3)$ Å and $c = 8.734(5)$ Å. One unknown phase impurity was found at $2\theta \approx 42$ °. Both the lattice parameters and the impurity peak are consistent with that reported in Ref. [193].

6.2.2 Magnetisation and Electrical Resistivity Measurements

The dc magnetic susceptibility, $\chi_{\rm dc}(T)$, of $TaRh_2B_2$ as a function of temperature taken in zero-field-cooled warming (ZFCW) and field-cooled cooling (FCC) modes in an applied field of 1 mT is shown in Fig. 6.2(a). These data indicate a on-

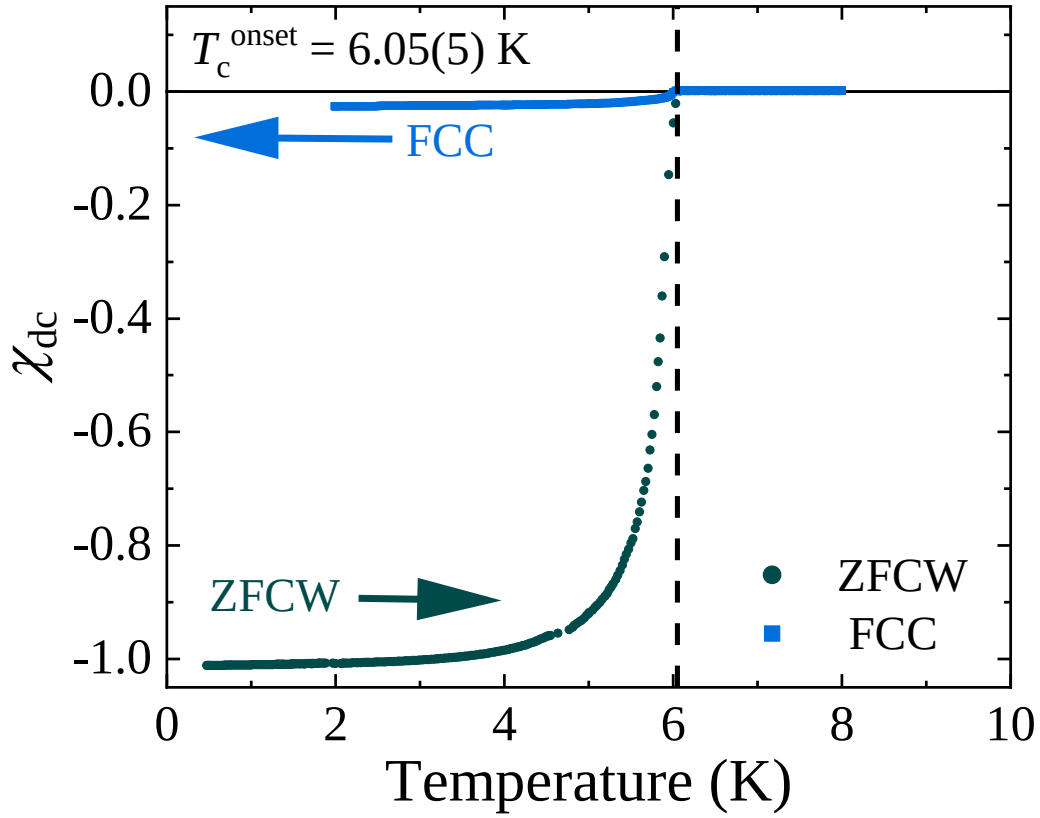

Figure 6.2: Temperature dependence of the dc magnetic susceptibility $\chi_{\mathrm{dc}}(T)$ collected in zero-field-cooled warming (ZFCW) and field-cooled cooling (FCC) mode in an applied field of $\mu_0 H = 1$ mT.

set for superconductivity in $TaRh_2B_2$ at $T_c^{\mathrm{onset}} = 6.05\,(5)$ K. The sample exhibits a full Meissner fraction, $\chi_{\mathrm{dc}}(T) = -1$, for the ZFCW data. There is some flux expulsion on re-entering the superconducting state during FCC. The behaviour is consistent with a type-II superconductor with relatively strong pinning and some disorder. There is no signature of any additional transitions (magnetic or superconducting) at very low temperature. The normal-state paramagnetic susceptibility after subtracting the contribution due to the core diamagnetism is estimated to be $\sim \chi = 2.2 \times 10^{-8}$ m^3/mol at 10 K. This value is just under half that reported for the Stoner enhanced paramagnet Pd at 20 K [201]. The susceptibility is almost temperature independent, although a small upturn on cooling just above T_c may indicate the presence of a some localised moments. Several magnetisation loops shown in Fig. 6.4 reveal $TaRh_2B_2$ exhibits the conventional behaviour of a type-II superconductor, with a hysteresis in the magnetisation, ΔM, that decreases with increasing temperature and magnetic field. This hysteresis ΔM disappears at ex-

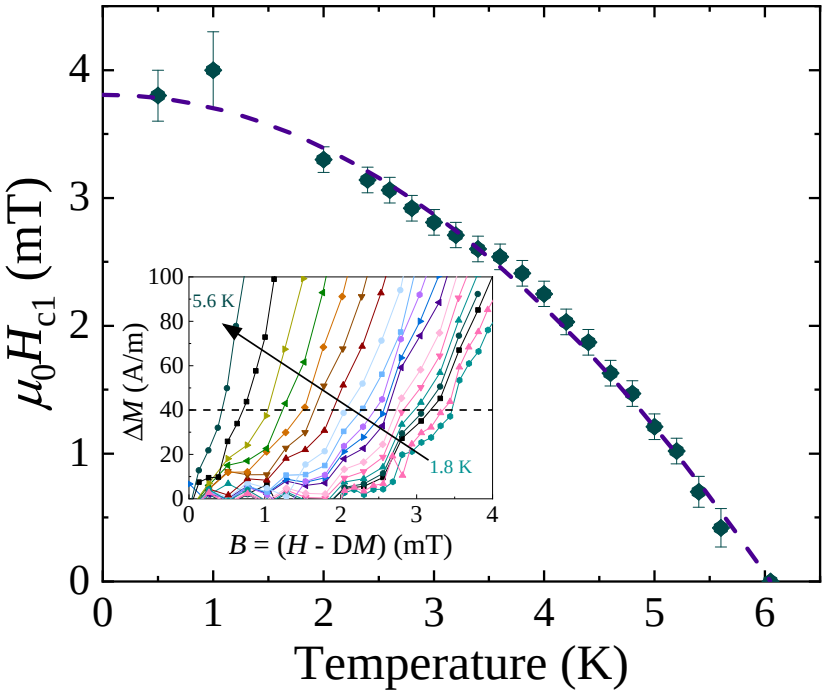

Figure 6.3: Lower critical field H_{c1} versus temperature for $TaRh_2B_2$. The H_{c1} values were taken as the fields at which magnetisation versus field data first deviate from linearity. The inset shows the demagnetisation corrected residuals for linear fit to M vs H at several temperatures. The solid line shows the fit using Eq. (4.7) giving $\mu_0 H_{c1}(0) = 3.8\,(1)$ mT.

actly $H_{c2}\,(T)$ and there is no reversible region or unusual flux dynamics. The curves are symmetric about $M = 0$. The lower critical field, $H_{c1}\,(T)$ is determined from the first deviation from linearity of the initial slope as the field is increased. Fig. 6.3 shows the resulting $H_{c1}\,(T)$ values plotted against temperature. Fitting the data using Eq. (4.7) $H_{c1}\,(0)$ is estimated to be 3.8 (1) mT. This is lower than the 9.6 mT reported in Ref. [193] due to their incorrect usage of the demagnetisation factor in their calculations.

The ac susceptibility versus temperature measurements, $\chi_{ac}\,(T)$, shown in Fig. 6.5 confirm the onset of superconductivity is at $T_{onset} = 6.05\,(5)$ K. In zero-field, the sample exhibits a full Meissner fraction. The out-of-phase component of the ac susceptibility, $\chi''(T)$, has a sharp maximum close to T_c and falls to zero for lower temperatures with a shoulder that is visible at around 5.6 K. For applied fields greater than $H_{c1}\,(0)$, T_c is suppressed and a full Meissner fraction is not seen due

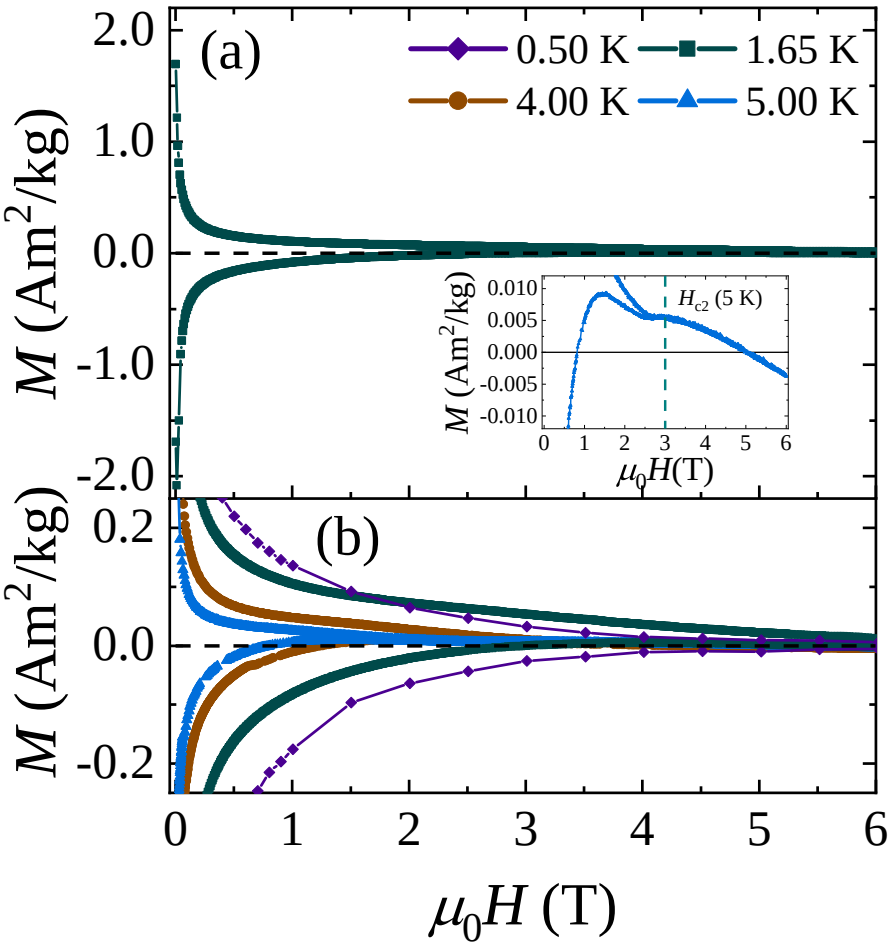

Figure 6.4: (a) Magnetisation vs magnetic field at 1.65 K for $TaRh_2B_2$ exhibits a behaviour typical for a type-II superconductor. The inset shows the $M\,(H)$ data close to the upper critical field of 3 T at 5 K. (b) Magnetisation vs magnetic field at several temperatures for $TaRh_2B_2$. The data were collected in a VSM with the demagnetisation factor of the sample minimised.

to partial flux penetration. At temperatures below $T_c\,(H)$, $\chi''(T)$ exhibits a broad maximum indicating losses due to flux motion in dc applied fields.

The temperature dependence of the resistivity, $\rho\,(T)$, from 2 to 300 K in zero magnetic field for a polycrystalline sample of $TaRh_2B_2$ is shown in Figure 6.6(a). The residual resistivity ratio, RRR $\equiv \rho(300\text{ K})/\rho(10\text{ K}) \approx 0.97$ is less than one. This along with high normal-state resistivity indicate poor metallic behaviour. Immediately below 300 K the resistivity decreases with a slope $d\rho/dT = 4.8$ $\mu\Omega$-cm/K before reaching a minimum at 150 K and then increases with decreasing temperature

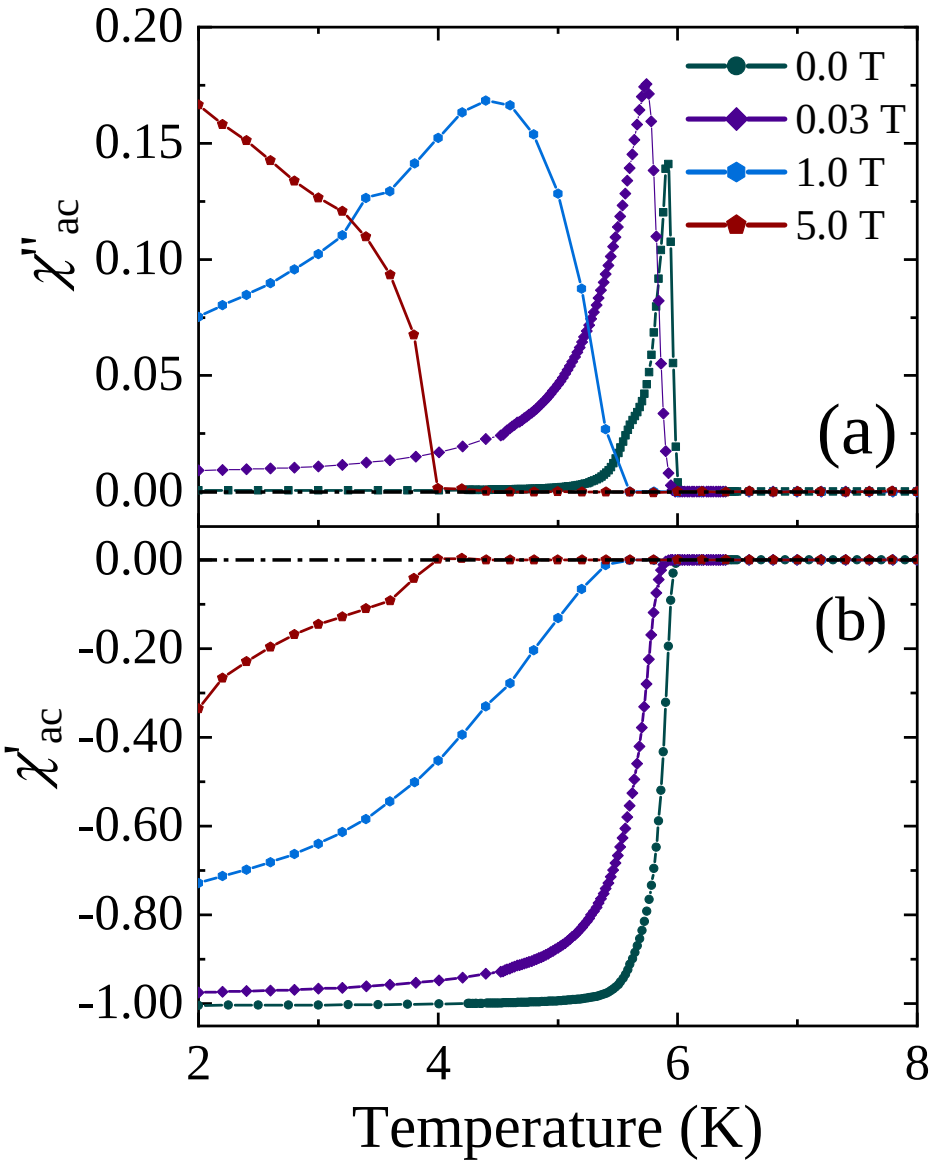

Figure 6.5: (a) Imaginary part of ac susceptibility versus temperature, $\chi''(T)$, for $TaRh_2B_2$ in various dc applied fields. (b) Real part of ac susceptibility versus temperature, $\chi'(T)$, for $TaRh_2B_2$ at various dc applied fields. In zero dc field, a sharp superconducting transition can be seen at 6.00 (5) K. In fields above $H_{c1}(0)$ the transition broadens slightly and shifts to lower T.

down to 10 K. The upturn may be due to a localisation of the charge carriers and disorder scattering [202], perhaps as a result of the small variations in the level of boron throughout the sample (although there is no evidence for variations in B content from the powder x-ray diffractogram). The polycrystalline samples have a density

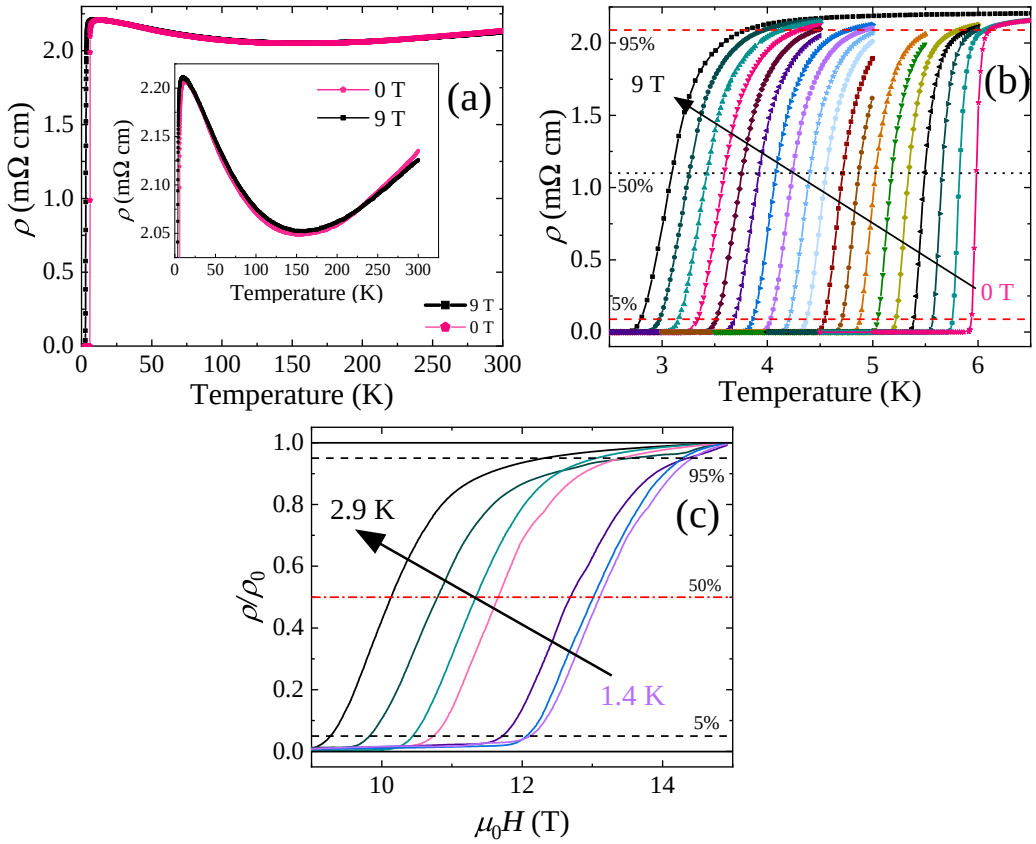

Figure 6.6: (a) Resistivity versus temperature, $\rho(T)$, of $TaRh_2B_2$ for $1.8 \leq T \leq 300$ K measured in zero applied magnetic field and a field of 9 T. The inset shows an expanded view of the normal-state resistivity. (b) $\rho(T)$ below 7.5 K shows the onset of superconductivity and the suppression of the transition temperature under various applied fields, $\mu_0 H$, from 0 to 9 T. The black (red) dashed line(s) are at 50% (95% and 5%) of the resistivity just above the superconducting transition. T_c is taken as the midpoint of the resistive transition. (c) Resistivity versus applied field, $\rho(H)$, showing the suppression of the transition at several constant temperatures down to 1.4 K.

that is around 50% of the full theoretical density of this material, so scattering from grain boundaries as well as the presence of voids will also increase the residual resistivity. The magneto-resistance at 10 K is just $\frac{\rho_{9T}-\rho_{0T}}{\rho_{0T}} \times 100\% = +0.3\%$. A sharp ($\Delta T_c = 0.10$ K), zero-field superconducting transition is seen at $T_c = 6.00\,(5)$ K [see Fig. 6.6(b)]. T_c is only gradually suppressed with increasing applied magnetic field and the transition is broadened so that $\Delta T_c = 1.0$ K at 9 T. Resistivity measurements were also performed at fixed temperature as a function of applied magnetic field up to 15 T [see Fig. 6.6(c)]. Plotting the superconducting transition tempera-

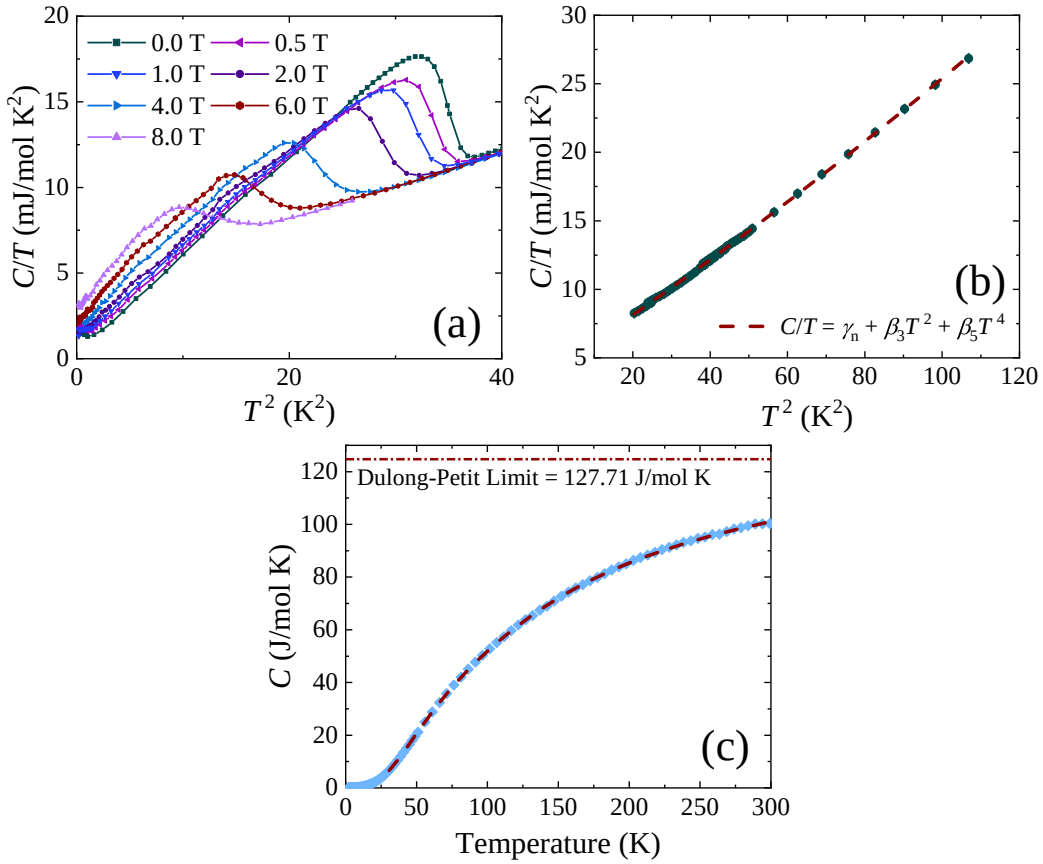

Figure 6.7: (a) $C\,(T)\,/T$ versus T^2 for $TaRh_2B_2$ in different applied fields ($\mu_0 H$ in tesla), showing the suppression in T_c for increasing field. (b) $C\,(T)\,/T$ versus T^2 with normal-state data from all the applied fields. The line is a fit using Eq. (4.3) to all the $C\,(T)$ data collected above $T_c\,(H)$ in the different applied fields. The normal-state electronic contribution to the specific heat is $\gamma_n = 4.29\,(6)$ mJ/mol K^2 and the Debye temperature is $\Theta_D = 374\,(2)$ K. (c) C versus T from 2 to 300 K. The dashed line shows the fit using Eq. (4.5a), the Debye-Einstein function.

tures at T_c^{onset} (95%), $T_c^{midpoint}$ (50%), and T_c^{zero} (5%), as a function of the applied magnetic field, H, along with H_c^{onset}, $H_c^{midpoint}$, and H_c^{zero} for the data collected while sweeping the field at fixed temperature gave three curves that show the same temperature dependence.

6.2.3 Specific Heat Measurements

Fig. 6.7(a) shows the squared temperature dependence of the heat capacity divided by temperature, $C\,(T)\,/T$, versus T^2 from 0.5 to 10 K in several fields.

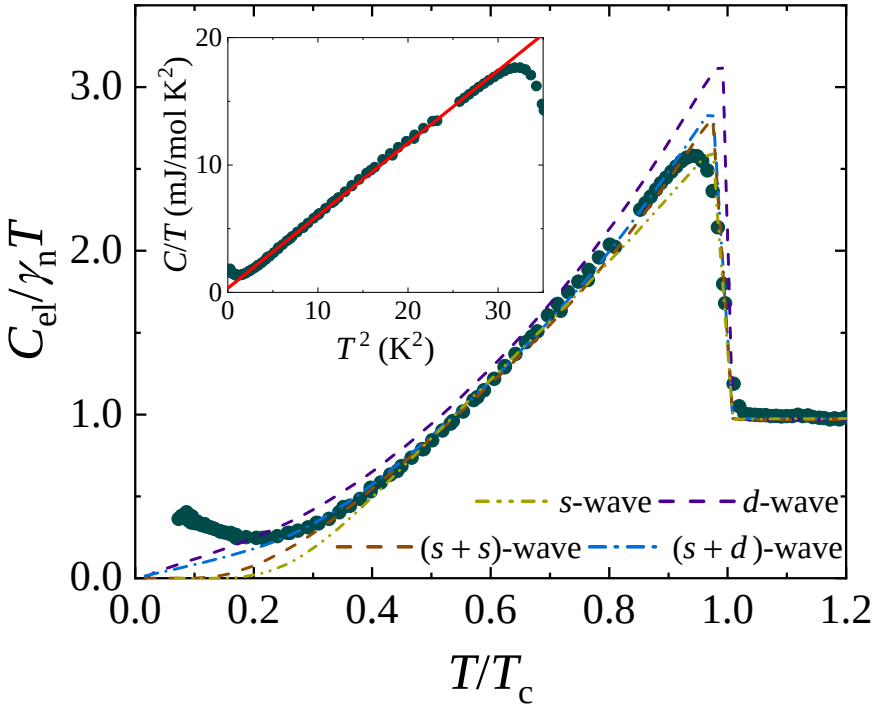

Figure 6.8: Zero-field normalised electronic specific heat of $TaRh_2B_2$ with a single-gap isotropic s-wave (yellow), a line nodal d-wave (purple), an isotropic two-gap $(s+s)$-wave (dark red) and a two-gap $(s+d)$-wave model (blue). The inset shows a linear fit to the zero-field $C\,(T)\,/T$ vs T^2 indicating a T^3 dependence to the specific heat.

The superconducting anomaly indicates the onset of bulk superconductivity in $TaRh_2B_2$. The transition temperature, $T_c = 6.00\,(5)$ K, is taken as the mid-point of the transition and in zero applied field the transition has a width $\Delta T = 0.35$ K. The normal-state heat capacity divided by the squared temperature is shown in Fig. 6.7(b). We analysed the normal-state data between 4.5 and 10 K using Eq. (4.3) giving $\gamma_n = 4.29\,(6)$ mJ/mol K^2, $\beta_3 = 0.19\,(3)$ mJ/mol K^4 and $\beta_5 = 0.24\,(3)$ μJ/mol K^6. The Debye temperature Θ_D can then be calculated using Eq. (4.4) giving $\Theta_D = 374\,(2)$ K. These values are in good agreement with the earlier report [193]. Using the values of γ_n and T_c above, the jump in specific heat at the transition temperature gives $\Delta C/\gamma_n T_c = 1.57(2)$ which is larger than the 1.43 expected from conventional BCS superconductors, suggesting the presence of a slightly enhanced electron-phonon coupling.

The temperature dependence of the heat capacity of $TaRh_2B_2$ from 300 down

to 10 K is shown in Fig. 6.7(c). There is no sign of any structural phase transition and the value of C at 300 K is 100 (2) J mol^{-1} K^{-1} which is below the classical Dulong-Petit value for $TaRh_2B_2$ of 124.65 J mol^{-1} K^{-1} and is consistent with $\Theta_D > 300$ K. We fit the normal-state data using a Debye-Einstein function. It was found that by including the additional Einstein term to the Debye model for lattice heat capacity the fit could be significantly improved. Fig. 6.7(c) shows a fit to the heat capacity data between 30 and 300 K made using Eqs. (4.5a)-(4.5c). The fit was performed using a fixed value $\gamma_n = 4.29$ mJ/mol K^2 obtained below to help reduce the number of free parameters. We obtained $\delta = 0.62\,(1)$, $\Theta_D = 301\,(2)$ K and $T_E = 790\,(30)$ K. The fit could be improved still further by adding a second Einstein term with the Einstein temperature fixed at 1400 K, but the values of δ, Θ_D, and T_E are comparable to those for the two component fit. The observation that the $C\,(T)$ data cannot be adequately described using a single Debye term, coupled with fact that the weighting of the Debye:Einstein terms in the two and three component fits is around 3:2 suggests that the vibrational modes associated with the much lighter boron atoms in $TaRh_2B_2$ differ significantly from those associated with the Ta and Rh.

The temperature dependence of the electronic specific heat, $C_{el}\,(T)$, provides important information about the nature of the superconducting gap (see Fig. 6.8). Immediately below T_c, $C_{el}\,(T)$ clearly deviates from a simple s-wave BCS-like behaviour instead exhibiting a T^3 dependence (see inset Fig. 6.8). A similar behaviour is seen in other two-gap superconductors including $Lu_2Fe_3Si_5$ [203, 204] and MgB_2 [195, 197]. In these materials, a shoulder in $C_{el}\,(T)$ is followed by a rapid fall at lower T as the second gap opens. As seen in Fig. 6.8 we observe a flattening in $C_{el}\,(T)$ in $TaRh_2B_2$ at low-temperature due to a hyperfine contribution. The temperature dependence of the electronic heat capacity C_{el} in the superconducting state was fit using the BCS and d-wave model of the specific heat discussed in Refs. [11] and [205], combined with a phenomenological two-gap model [133] that has been successfully applied to the analysis of the electronic heat of several two-gap superconductors including MgB_2 [195, 197], $Lu_2Fe_3Si_5$ [203, 204] and the noncentrosymmetric superconductor Y_2C_3 [5]. The entropy (S) was calculated from

$$\frac{S_i}{\gamma_n T_c} = -\frac{3}{\pi^3}\int_0^{2\pi}\int_0^{\infty}\left[f\ln f + (1-f)\ln(1-f)\right]dyd\phi, \tag{6.1}$$

where f is the Fermi-Dirac function given by $f = (1+\exp(E/k_BT))^{-1}$ and $E = \sqrt{y^2+\Delta_0(T,\phi)^2}$, where y is the energy of the normal-state electrons and $\delta(T)$ is the temperature and angular dependence of the superconducting gap function calculated. For s-wave superconductivity $\Delta_{0,i}\,(T,\phi) = \Delta_{0,i}\,(T)$ and for d-wave su-

perconductivity $\Delta_{0,i}(T,\phi) = \Delta_{0,i}(T)\cos(2\phi)$. The specific heat of the superconducting state is then calculated by

$$\frac{C_{\mathrm{sc},i}}{\gamma_{\mathrm{n}}T} = \frac{d(S_i/\gamma_{\mathrm{n}}T_{\mathrm{c}})}{dt}, \tag{6.2}$$

where $t = T/T_{\mathrm{c}}$. For the two-gap model the total electronic specific heat can be considered a weighted sum of each gap calculated separately given by:

$$C_{\mathrm{el}}(T) = wC_{\mathrm{sc},1}(T) + (1-w)\,C_{\mathrm{sc},2}(T). \tag{6.3}$$

The zero-field $C_{\mathrm{el}}(T)$ data to 1.5 K were fit using both a single-gap isotropic s-wave, a line nodal d-wave, a isotropic two-gap $(s+s)$-wave and a $(s+d)$-wave model [11] with the two-gap models producing a better fit to the data. The gap values for the $(s+s)$ are $\Delta_{0,1}/k_{\mathrm{B}}T_{\mathrm{c}} = 2.29(12)$, $\Delta_{0,2}/k_{\mathrm{B}}T_{\mathrm{c}} = 1.1(3)$ with weighting 4:1. The larger gap is above the BCS value of 1.76, again indicating slightly enhanced electron-phonon coupling strength.

At very low temperatures, an upturn in $C(T)/T$ appears in zero field. This upturn is also present in magnetic fields of up to 1 T but is no longer apparent in a magnetic field of 2 T. Both Ta ($\mu/\mu_{\mathrm{N}} = 2.371$) and B ($\mu_{\mathrm{ave}}/\mu_{\mathrm{N}} = 2.75$) carry a nuclear moment, and so a hyperfine contribution to the heat capacity may be expected with an associated Schottky anomaly shifting to higher T as any applied field is increased. This contribution to the specific heat may be the high-temperature tail of such a Schottky anomaly, although the nuclear moments are small, so the origin of this upturn is not clear. In order to clearly establish the presence of point or line nodes in the superconducting gap, the heat capacity needs to be fit below $T_{\mathrm{c}}/10$ [206]. This upturn in $C(T)/T$ is therefore problematic. Nevertheless, we are able to clearly establish that the electronic heat capacity of $TaRh_2B_2$ does not follow a simple BCS temperature dependence expected for a single-gap s-wave superconductor.

6.2.4 μSR Measurements

Zero-field (ZF) muon spin relaxation spectra collected at temperatures above (7 K) and below (0.3 K) T_{c} are shown in Fig. 6.9. In these experiments, any muons stopped in the silver sample holder give a time-independent background. There is no indication of a precessional signal ruling out the possibility of a large internal field and hence long-range magnetic order in $TaRh_2B_2$ down to at least 300 mK. In the absence of atomic moments, the muon spin relaxation is due to static, randomly

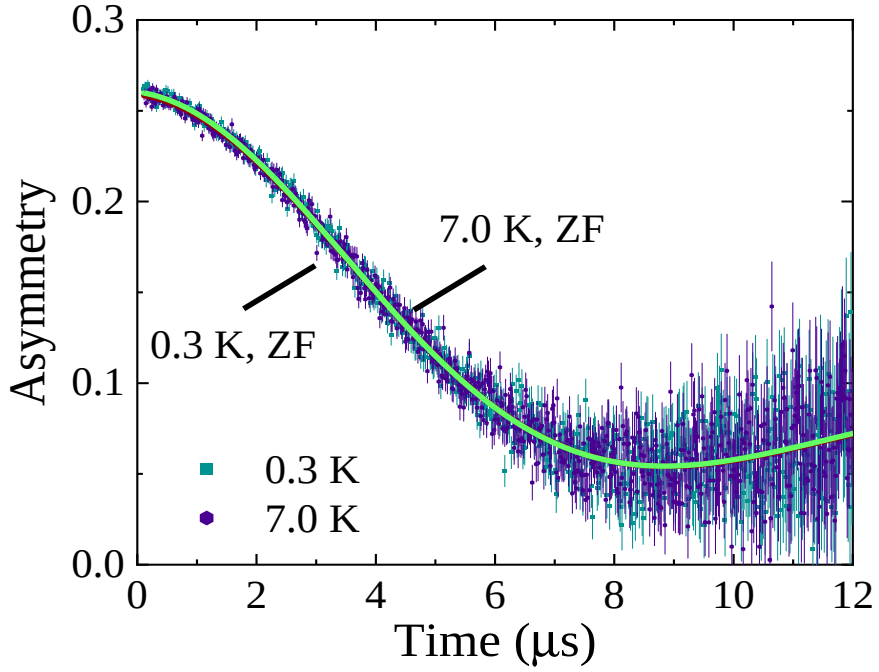

Figure 6.9: Zero-field μSR time spectra collected at 0.3 (green) and 7.0 K (purple) show time-reversal symmetry is preserved in $TaRh_2B_2$.

oriented local fields associated with the nuclear moments at the muon site. The solid lines in Fig. 6.9 are fits using Eqs. (5.7, 5.8). The fact that the spectra above and below T_c lie on top of each other confirms time-reversal symmetry is preserved in $TaRh_2B_2$ in the superconducting state.

Transverse-field μSR experiments were performed in the superconducting mixed state in applied fields of 30 and 40 mT, well above the $\mu_0 H_{c1}(0) \sim 4$ mT of $TaRh_2B_2$. In this geometry, the detectors in the spectrometer were grouped in eight blocks, each with a phase offset ϕ. In order to ensure the most uniform flux-line lattice possible, the magnetic field was applied above T_c and the sample cooled to base temperature. The data were then collected in field-cooled-warming mode. A typical TF-μSR precession signal for $TaRh_2B_2$ in 30 mT at 300 mK is shown in Fig. 6.10(a). Above T_c the signal decays with time because of the inhomogeneous field distribution of the flux-line lattice. The depolarisation above T_c is reduced but still persists due to randomly orientated nuclear magnetic moments. The TF spectra were fit using a sinusoidal oscillating function with a Gaussian relaxation with an oscillatory background term arising from the muons implanted directly into

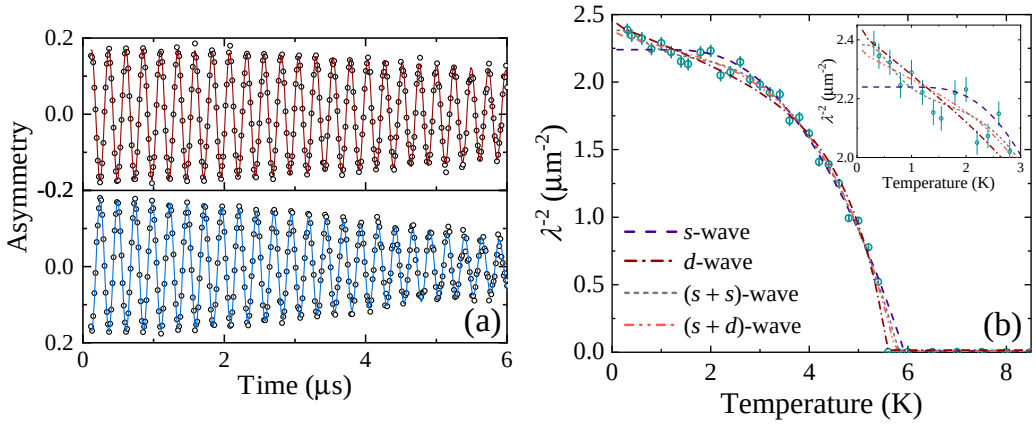

Figure 6.10: (a) Transverse field μSR time spectra for $TaRh_2B_2$ collected at 7.0 (top) and 0.3 K (bottom) in an applied field of 30 mT. The solid lines are fits using Eq. (6.4). The Gaussian decay of the oscillatory signal shows the effect of the flux-line lattice. (b) Inverse square of the London penetration depth, λ^{-2}, as a function of temperature for $TaRh_2B_2$. The lines are fits to the data using Eqs. (6.5) and (6.6) for one- and two-gap models. The inset shows the low-temperature data on an expanded scale.

the silver sample holder that do not depolarise:

$$G(t) = A_1 \exp\left(-\frac{\sigma^2 t^2}{2}\right) \cos(2\pi v_1 t + \phi) + A_2 \cos(2\pi v_2 t + \phi), \qquad (6.4)$$

where v_1 and v_2 are the frequencies of the muon precession signal and the background signal respectively, A_0 is a flat background, and σ is the Gaussian muon-spin relaxation rate. The superconducting contribution to the relaxation rate, σ_{sc}, can be calculated from $\sigma_{\rm sc} = \sqrt{(\sigma^2 - \sigma_{\rm n}^2)}$ where $\sigma_{\rm n}$ is the nuclear magnetic dipolar contribution, which is assumed to be temperature independent.

For a type-II superconductor with a large upper critical field and a hexagonal Abrikosov vortex lattice, σ_{sc} is related to the magnetic penetration depth λ by the expression $\frac{\sigma_{\rm sc}^2(T)}{\gamma_\mu^2} = 0.00371 \frac{\Phi_0^2}{\lambda^4(T)}$ where $\gamma_\mu/2\pi = 135.5$ MHz/T is the muon gyromagnetic ratio and $\Phi_0 = 2.068 \times 10^{-15}$ Wb is the magnetic-flux quantum. λ is directly related to the superfluid density from which the nature of the superconducting gap can be determined. In the clean limit, the temperature dependence of the London magnetic penetration depth, $\lambda(T)$, can be calculated using the following expression:

$$\left[\frac{\lambda^{-2}(T,\Delta_{0,i})}{\lambda^{-2}(0,\Delta_{0,i})}\right] = 1 + \frac{1}{\pi}\int_0^{2\pi}\int_{\Delta_{(T,\phi)}}^{\infty}\left(\frac{\partial f}{\partial E}\right)\frac{EdE\ d\phi}{\sqrt{E^2-\Delta_i(T,\phi)^2}}, \tag{6.5}$$

where $f = [1+\exp(E/k_BT)]^{-1}$ is the Fermi function, and the temperature and angular dependence of the gap is $\Delta(T,\phi) = \Delta_0\delta(T/T_c)\,g(\phi)$. Here $g(\phi)$ is the angular dependence of the superconducting gap function and is 1 for an s-wave gap and $|\cos(2\phi)|$ for a d-wave gap where ϕ is the azimuthal angle along the Fermi surface. $\Delta(0)$ is the gap magnitude at zero kelvin and the temperature dependence of the gap is approximated by [12] $\delta(T/T_c) = \tanh\left\{1.82\,[1.018\,(T_c/T-1)]^{0.51}\right\}$. For the multigap analysis we have used a weighted sum of the two gaps given by:

$$\left[\frac{\lambda^{-2}(T,\Delta_0)}{\lambda^{-2}(0,\Delta_0)}\right] = w\left[\frac{\lambda^{-2}(T,\Delta_{0,1})}{\lambda^{-2}(0,\Delta_{0,1})}\right] + (1-w)\left[\frac{\lambda^{-2}(T,\Delta_{0,2})}{\lambda^{-2}(0,\Delta_{0,2})}\right], \tag{6.6}$$

where w is the weighting factor. Figure 6.10(b) shows $\lambda^{-2}(T)$. We obtain good fits to the data, as measured by $\chi^2_{\rm norm}$ and the form of the normalised residual, using a two-gap $(s+s)$-wave model [see Fig. 6.10(b)]. The $\lambda^{-2}(T)$ data were also fit using a single isotropic s-wave, a d-wave, and an $(s+d)$-wave model. The parameters extracted from these fits are given in Table 6.1. There is little difference between the quality of the fits for the $(s+s)$ and $(s+d)$ models, as measured by $\chi^2_{\rm norm}$, with the $(s+s)$-wave model just preferred. Fig. 6.10(b) clearly shows that a single-gap s-wave model does not produce a good fit. The value of the larger energy gap for the $(s+s)$-wave model is $\Delta_{0,1} = 1.16(4)$ meV giving a superconducting gap ratio $\Delta_{0,1}/k_{\rm B}T_{\rm c} = 2.28(8)$, which is higher than the 1.76 expected for BCS superconductors; a further indication of the enhanced electron-phonon coupling in the superconducting state of $TaRh_2B_2$. The $(s+s)$-wave model gives a magnetic penetration depth $\lambda(0) = 648(5)$ nm, which is higher than the value calculated from magnetisation [193]. The difference between the magnetic penetration depths is due to method by which the lower critical field is approximated by magnetisation. The method used leads to an overestimation of the lower critical field which in turn leads to an underestimation of the magnetic penetration depth.

6.2.5 Upper Critical Field

The critical temperatures or upper critical fields extracted from the midpoint of the resistive transition or the anomaly in $C(T)$ at the superconducting transition are collected together in Fig 6.11. The upper critical field $\mu_0 H_{c2}(T)$ is almost

Table 6.1: Superconducting gap parameters for $TaRh_2B_2$ extracted from the fits to the penetration depth data using a BCS model in the clean limit.

Model	Units	d-wave	$(s+s)$-wave	$(s+d)$-wave
w		1	0.89(2)	0.51(2)
$\Delta_{0,1}$	(meV)	1.92(7)	1.16(4)	1.30(6)
$\Delta_{0,2}$	(meV)	-	0.14(5)	1.44(5)
$\Delta_{0,1}/k_{\mathrm{B}}T_{\mathrm{c}}$		3.78(14)	2.28(8)	2.56(11)
$\Delta_{0,2}/k_{\mathrm{B}}T_{\mathrm{c}}$		-	0.27(9)	2.83(9)
$\lambda^{-2}(0)$	(μm^{-2})	2.44(2)	2.38(2)	2.37(4)
χ^2_{norm}		1.81	1.18	1.35

linear in T at lower fields. The data deviate from the WHH model [170] at lower T and so we use a phenomenological Ginzburg-Landau expression (see Eq. 5.1) to estimate $\mu_0 H_{c2}(0) = 15.2(1)$ T, which is well above the Pauli limit of $\mu_0 H^{\mathrm{P}}[\mathrm{T}] = 1.85 \times T_{\mathrm{c}}[\mathrm{K}] = 11.1(1)$ T which is also considerably higher than the value reported by Ref. [193]. Note, however, that the $\mu_0 H_{c2}(T)$ data reported here are consistent with higher temperature data shown in Ref. [193].

In our WHH model calculations the Maki parameter was estimated experimentally by using Eq. (4.12). The initial slope $-\mathrm{d}H_{c2}(T)/\mathrm{d}T|_{T=T_{\mathrm{c}}}$ was found to be 3.1 T/K giving $\mu_0 H_{c2}^{\mathrm{orb}}(0) = 12.9(5)$ T. From Eq. (4.12) we obtain $\alpha_{\mathrm{M}} = 1.65$ and the relative size of the Maki parameter indicates that the Pauli limiting field is non-negligible. Fixing $\alpha_{\mathrm{M}} = 1.65$ produced a λ_{so} that tended to infinity and gave $\mu_0 H_{c2}(0) = 13.0(2)$ T. It was found that this model is highly dependent on the starting values as an equally good fit, as judged by the reduced χ^2, could be obtained by allowing the Maki parameter to vary. α_{M} was found to drift towards zero in nearly all cases along with λ_{so} which would also tend to zero when allowed to vary.

There are several reasons why the WHH model fails to capture the behaviour of the upper critical field in $TaRh_2B_2$. Firstly the polycrystalline sample of $TaRh_2B_2$ will contain grain boundaries. The upper critical field could be increased above the bulk value once the grain size becomes smaller than the coherence length [172], (the grain size is unknown so contributions from this source are unknown). Spin-orbit coupling effects can enhance of H_{c2} although in the dirty limit this enhancement should be weaker [173]. The presence of multiple gaps or a d-wave order parameter can lead to an increase in $\mu_0 H_{c2}$ [171]. Finally, a Stoner enhancement can lead to an increase in H_{c2} from a large paramagnetic component near T_{c} leading to an

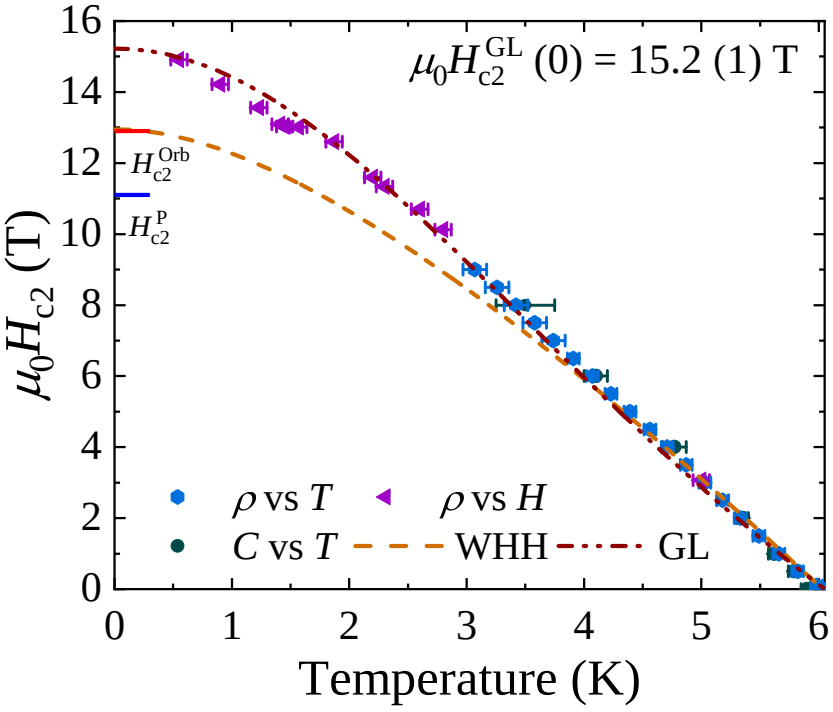

Figure 6.11: Temperature dependence of the upper critical field for $TaRh_2B_2$. Points were extracted from the midpoint (50%) of the resistive transition and the anomaly in $C\,(T)$ at the midpoint of the superconducting transition. The dashed and dashed-dotted lines show the expected $\mu_0 H_{c2}\,(T)$ from the WHH and G-L models respectively.

increased density of states near the Fermi surface.

6.2.6 Properties of the Superconducting State

The results of the characterisation measurements presented above can be combined in order to estimate some important superconducting properties of $TaRh_2B_2$. The Ginzburg-Landau coherence length $\xi_{GL}(0)$, the Ginzburg-Landua penetration depth $\lambda_{GL}\,(0)$ and Ginzburg-Landau parameter κ_{GL} can be estimated using Eqs. (2.17), (4.14), (4.15). We calculate $\xi_{GL}(0) = 4.67\,(6)$ nm, $\lambda_{GL(0)} = 444\,(5)$ nm and $\kappa_{GL} = 138\,(1)$ indicating that $TaRh_2B_2$ is a strong type-II superconductor. The thermodynamic critical field, H_c, can be calculated using Eq. (4.16) and from this $H_c\,(0)$ is estimated to be 92 (3) mT. A system of four equations can be formed using Eqs. (4.18) - (4.23) to estimate the parameters m^*, n, ℓ_e, and ξ_0. These equations

Table 6.2: Electronic properties of $TaRh_2B_2$ for λ_{GL} (H_{c1}) and λ_{GL} (μSR).

Property	Units	H_{c1}	μSR
$\lambda_{GL}(0)$	(nm)	444	648
m^*/m_e		4.31 (1)	5.66 (2)
n	$10^{27}m^{-3}$	6.2 (2)	2.7 (1)
ξ_0	(nm)	1.62 (5)	1.92 (5)
ℓ_e	(nm)	0.18 (2)	0.31 (3)
ξ_0/ℓ_e		9.06 (3)	6.2 (2)
λ_L	(nm)	140 (2)	241 (3)
T_F	(K)	–	1460(12)
T_c/T_F		–	0.0040(3)

can be solved simultaneously using the values $\gamma_n = 4.29$ mJ/mol K^2, $\xi_{GL} = 4.67$ nm, and $\rho_0 = 2.20$ mΩ cm. For comparison, two values of λ_{GL} have been used; 444 nm is taken from Eq. (4.15) and 648 nm is taken from the μSR data. The results are shown in Table 6.2. The mean free path ℓ_e can be calculated using Eq. (4.19) and ξ_0, calculated using Eq. (4.23), it is clear that $\xi_0 > \ell_e$ indicating that $TaRh_2B_2$ is in the dirty limit. We find that these values are in close agreement with those previously reported for $TaRh_2B_2$ [193].

The electron-phonon coupling constant λ_{el-ph} can be used as another estimate of the strength of the interaction between electrons and phonons in superconductors. This can be estimated from Eq. (4.25) using T_c and Θ_D taken from Fig. 6.7, a value of $\lambda_{el-ph} = 0.63\,(2)$ is obtained, suggesting this to be a moderately coupled superconductor. The results of $TaRh_2B_2$ are summarised in Table. 6.5. Where relevant the values presented are calculated from the London penetration depth measured from μSR measurements.

By calculating the Fermi temperature using Eq. (4.26) we can calculate whether $TaRh_2B_2$ is an unconventional superconductor under the Uemura classification. For $TaRh_2B_2$ $T_F = 1460(12)$ K therefore the ratio $T_c/T_F = 0.0040(3)$. This indicates that $TaRh_2B_2$ is outside of the range of unconventional superconductivity under the Uemura classification ($0.01 \leq T_c/T_F \leq 0.1$) [178, 179, 177]. However, the value is consistent with that of other noncentrosymmetric superconductors reported in this thesis.

6.3 Superconductivity and Pauli Limiting Field Violation in $NbRh_2B_2$

We will now discuss the second of the two compounds $NbRh_2B_2$. This compound was similarly first synthesised by Carnicom *et al.* [193]. They reported magnetisation, heat capacity and resistivity measurements showing that $NbRh_2B_2$ has a superconducting transition temperature of $T_c = 7.6$ K and that the upper critical field exceeds the Pauli limiting field. Here we have synthesised $NbRh_2B_2$ and characterised the material in more detail using magnetisation, heat capacity, resistivity, pressure and muon spin spectroscopy.

6.3.1 Sample Preparation and Structural Analysis

Polycrystalline samples were prepared by grinding together powders of elemental Nb (3N, 324 mesh, Alfa Aesar), Rh (3N, NewMet) and B (2N, 324 mesh, Alfa Aesar) in the ratio 1:1.9:2.1. The resulting powder is then pressed into pellets using a uniaxial press. The pellets were wrapped in tantalum foil, placed in alumina crucible and heated at 150 °C/hour to 1200 °C, reacted for 6 hours, and then furnace cooled to room temperature, all under vacuum. Powder x-ray diffraction was performed on $NbRh_2B_2$to check for phase purity and the absence of impurities as shown in Fir. 6.12. The diffraction pattern was phase matched with the space group $P3_1$ giving the lattice parameters $a = 4.7210(14)$ Å and $c = 8.729$ Å. Two unknown impurity peaks are visible in the diffraction pattern.

6.3.2 Magnetisation and Electrical Resistivity Measurements

A polycrystalline sample of $NbRh_2B_2$ was first characterised by studying the temperature dependence of the dc magnetic susceptibility $\chi_{dc}(T)$. Zero-field-cooled warming and field-cooled cooling data collected in an applied field of 1 mT are shown in Fig. 6.13(a). The onset of the superconducting state in $NbRh_2B_2$ is observed at $T_c^{onset} = 7.58(5)$ K which agrees with a previous report [193]. A full Meissner fraction is observed at 5 K in the ZFCW data indicating complete flux expulsion and bulk superconductivity in the sample. The FCC data show a small amount of flux expulsion indicating moderate to weak pinning of the magnetic field within $NbRh_2B_2$ in the superconducting state.

Figure 6.13(b) shows the lower critical field, H_{c1}, as a function of temperature. The lower critical fields were approximated by determining the point at which the $M(H)$ data first deviate from linearity ($\Delta M = 90$ A/m) in the low-field mag-

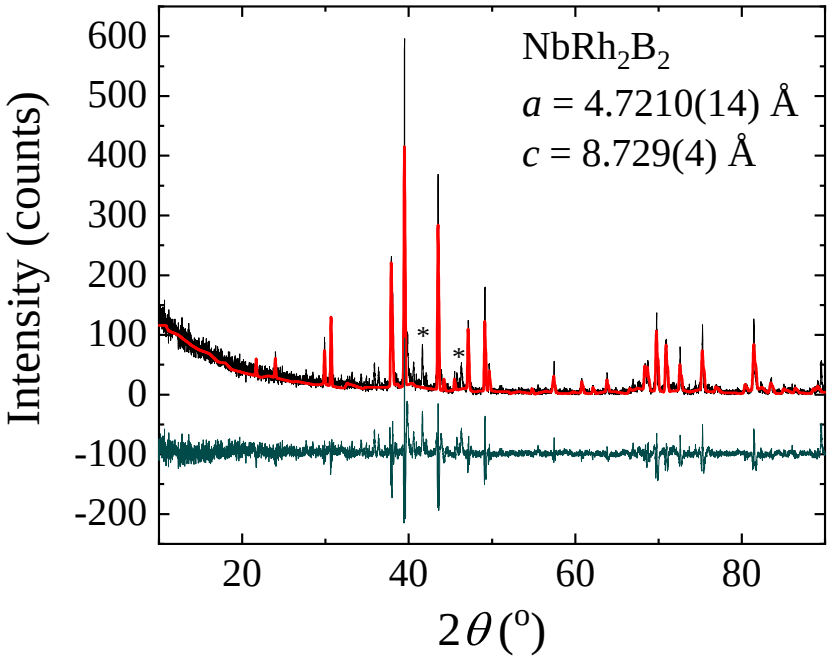

Figure 6.12: Powder x-ray diffraction of $NbRh_2B_2$. The diffraction pattern (black line) has been phase matched to the space group *P31* (red line), the difference between the two patterns is shown by the green line.

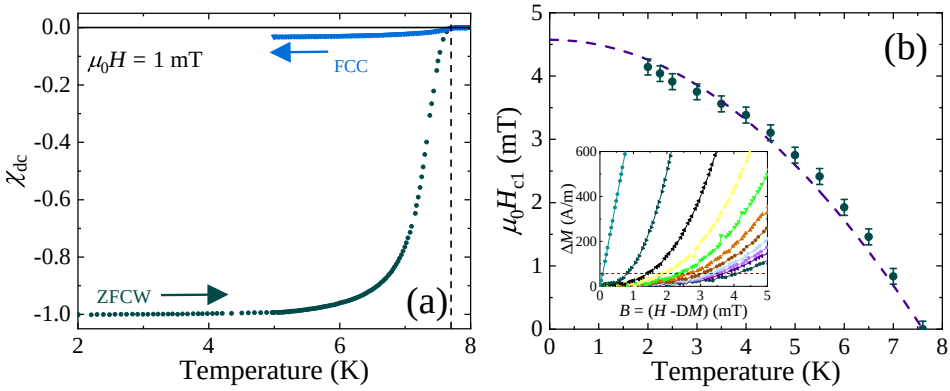

Figure 6.13: (a) Temperature dependence of the dc magnetic susceptibility $\chi_{\rm dc}\,(T)$ for $NbRh_2B_2$ collected in zero-field-cooled warming and field-cooled cooling mode in an applied field of $\mu_0 H = 1$ mT. (b) Lower critical field, $H_{\rm c1}$, versus temperature for $NbRh_2B_2$. The $H_{\rm c1}$ values were taken to be the fields at which the magnetisation versus field data first deviate from linearity. The dashed line shows the fit using Eq. (4.7) giving $\mu_0 H_{\rm c1}(0) = 4.6(1)$ mT. The inset shows the demagnetisation corrected residuals for linear fit to M versus H at several temperatures.

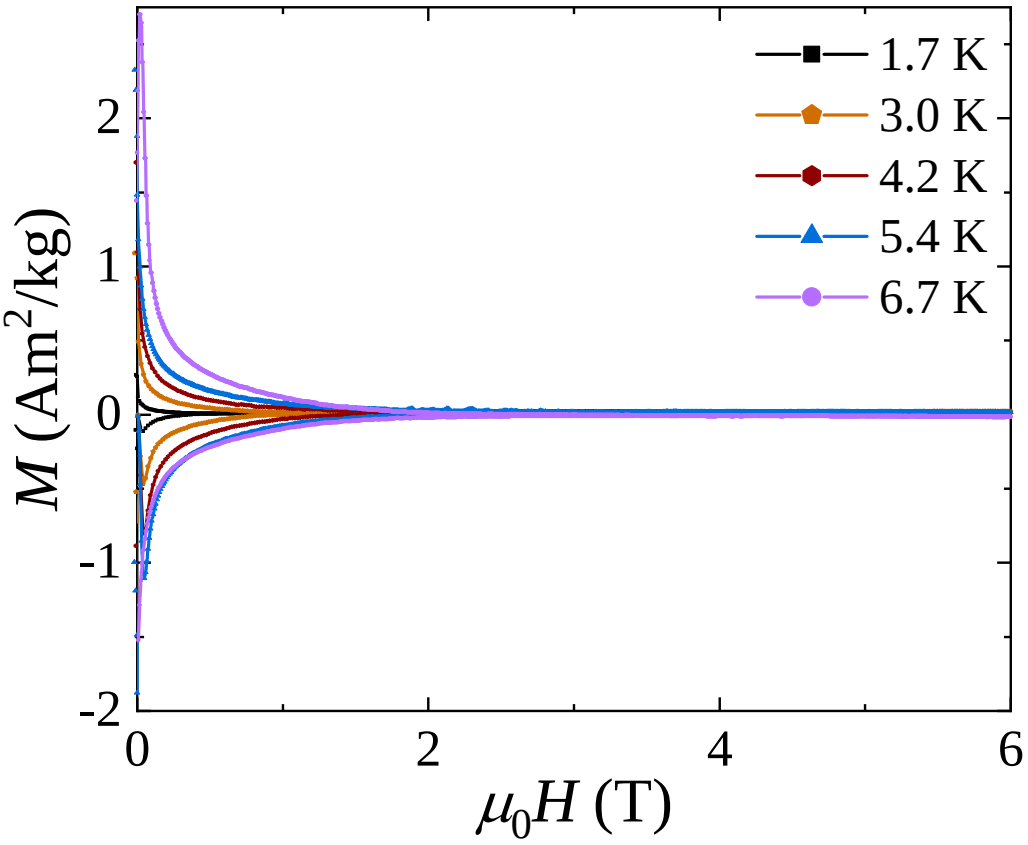

Figure 6.14: Magnetisation versus magnetic field at several temperatures for $NbRh_2B_2$ exhibits a behaviour typical for a type-II superconductor. The data were collected in a VSM with the demagnetisation factor of the sample minimised.

netisation loops at each temperature, as shown in the inset of Fig. 6.13(b). The data in Fig. 6.13(b) were fit with the Ginzburg-Landau relation using Eq. (4.7) giving a value of $\mu_0 H_{c1}(0) = 4.6(1)$ mT. This value is significantly lower than the 13.5 mT reported in Ref. [193].

The field dependence of the dc magnetisation for $NbRh_2B_2$ was measured at several temperatures between 1.7 and 6.7 K as shown in Fig. 6.14. The magnetic hysteresis loops show behaviour typical of a type-II superconductor. The $M(H)$ loops are symmetric about $M = 0$ suggesting bulk pinning plays a dominant role in determining the overall form of the $M(H)$ data. At higher fields and lower temperatures there are discontinuities in the data due to flux jumps. These flux jumps disappears at low fields and are not present in the data-set collected at 6.7 K. The hysteresis in $M(H)$ initially decreases rapidly with increasing field, before a much weaker trend is established at higher fields. The hysteresis in $M(H)$ persists

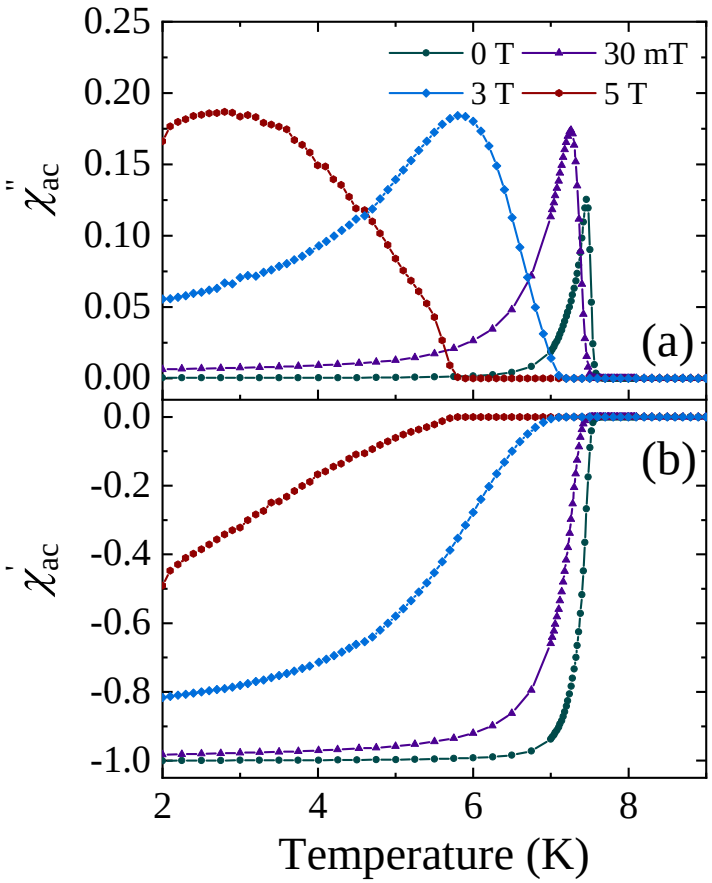

Figure 6.15: (a) Imaginary part of ac susceptibility versus temperature, $\chi''(T)$, for $NbRh_2B_2$ in various dc applied fields. (b) Real part of ac susceptibility versus temperature, $\chi'(T)$, for $NbRh_2B_2$ at various dc applied fields. In zero dc field, a sharp superconducting transition can be seen at 7.50 (5) K. In fields above H_{c1} the transition broadens slightly and shifts to lower T.

up to fields of the order of a tesla, ($\sim$ 4 T at 1.7 K), and then vanishes (below the resolution of the VSM). For higher fields the magnetisation becomes reversible. This occurs at temperatures and magnetic fields well below the $H_{c2}(T)$ values determined from the resistivity and the heat capacity measurements. The width of the magnetic hysteresis, ΔM, can be related to the critical current density, J_c, via the Bean critical state model [207]. Therefore, in the reversible regime, where the vortex lattice is free to move and can be thought of as liquid, the material may no longer carry a finite bulk supercurrent. These results support the view that this sample of $NbRh_2B_2$ exhibits moderate to weak bulk pinning of the vortex lattice.

The temperature dependence of the ac magnetic susceptibility, $\chi_{ac}(T)$, in

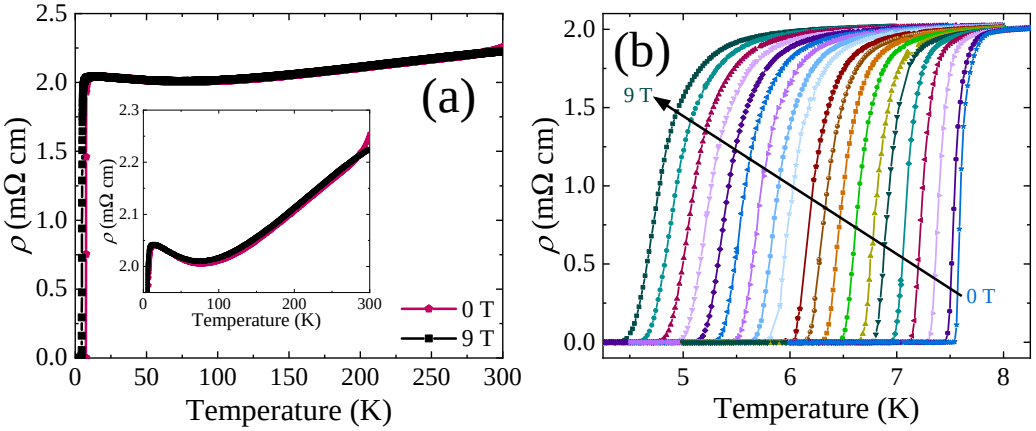

Figure 6.16: (a) Resistivity versus temperature, $\rho(T)$, of $NbRh_2B_2$ for $1.8 \leq T \leq 300$ K measured in zero applied magnetic field and a field of 9 T. The inset shows an expanded view of the normal-state resistivity. (b) $\rho(T)$ below 8.2 K shows the onset of superconductivity and the suppression of the transition temperature under various applied fields, $\mu_0 H$, from 0 to 9 T. T_c is taken as the midpoint of the resistive transition.

several dc applied fields is shown in Fig. 6.15. The data in zero dc field confirm the superconducting onset temperature of $T_c^{onset} = 7.58(5)$ K. The T_c of $NbRh_2B_2$ is only slowly suppressed in field, falling to 5.7(1) K in an dc field of $\mu_0 H = 5$ T. In zero dc field the sample exhibits a full Meissner fraction. For dc bias fields of the order of $H_{c1}(0)$ the out-of-phase component of the ac susceptibility, $\chi''(T)$, has a sharp peak close to T_c which then falls to zero at lower-temperatures, indicating that the flux lines are pinned. In higher dc fields of $\mu_0 H \geq 3$ T, a broad maximum is seen in $\chi''(T)$ typical of flux motion within the sample, and a partial flux penetration leads to a reduced Meissner fraction. Nevertheless, the in-phase component of the ac susceptibility, $\chi'(T)$, still exceeds 40% in an applied field of $\mu_0 H = 5$ T.

$NbRh_2B_2$ is a poor metal as can be seen in Fig. 6.16(a). $\rho(T)$ decreases below room temperature with a minimum in $\rho(T)$ at around 130 K. An upturn at lower T suggests the carriers then become more localised. $\rho_{300\ K}/\rho_{10\ K} = 1.09(1)$ and the resistivity at 10 K, just above T_c, is ~ 2 mΩ cm. This rather high value may be due to a combination of strong electron-phonon scattering, disorder, and poor connectivity between the grains of the polycrystalline samples. Spin-orbit scattering may also play a role. In $Ta_2Pd_xS_5$, it is suggested that strong spin-orbit scattering due to Pd deficiencies gives rise to a substantial increase in $\mu_0 H_{c2}(0)$ [199]. The behaviour of the resistive superconducting transition for increasing applied fields is shown in Fig. 6.16(b).

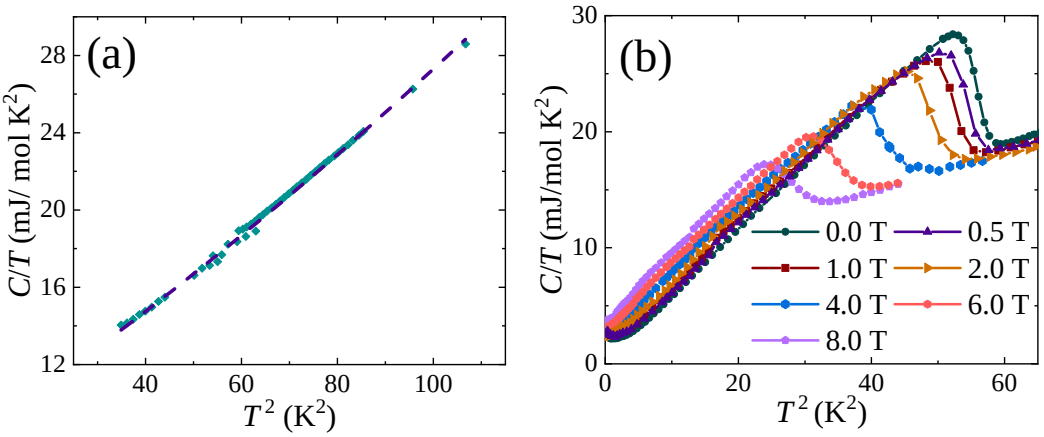

Figure 6.17: (a) $C\,(T)\,/T$ versus T^2 with normal-state data from all the applied fields. The line is a fit using Eq. (4.3) to all the $C\,(T)$ data collected above $T_{\rm c}\,(H)$ in the different applied fields. The normal-state electronic contribution to the specific heat $\gamma_{\rm n} = 7.6\,(4)$ mJ/mol K^2, and the Debye temperature $\Theta_{\rm D} = 388\,(9)$ K. (b) $C\,(T)\,/T$ versus T^2 for $NbRh_2B_2$ in different applied fields ($\mu_0 H$ in Tesla), showing the suppression in $T_{\rm c}$ for increasing field.

6.3.3 Specific Heat Measurements

Immediately above $T_{\rm c}$, the normal-state data can be used to calculate the Sommerfeld coefficient using Eq. (4.3) which gives $\gamma_{\rm n} = 7.6\,(4)$ mJ/mol K^2 for $NbRh_2B_2$, as shown in Fig. 6.17(a). Similarly $\theta_{\rm D}$ can be calculated using Eq. (4.4) giving $\theta_{\rm D} = 388\,(9)$ K. In zero-field, the onset of bulk superconductivity is indicated by an anomaly in the specific heat where the midpoint of the jump is defined as the transition temperature. For $NbRh_2B_2$, $T_{\rm c} = 7.46(5)$ K and $\Delta C/\gamma_{\rm n} T_{\rm c} = 1.69$. $\Delta C/\gamma_{\rm n} T_{\rm c}$ is larger than the 1.43 expected for a conventional BCS superconductor, again indicating moderate to strong coupling. The temperature dependence of the electronic specific heat below $T_{\rm c}/10$ can be used to establish the nature of the superconducting gap [206]. An exponential behaviour is expected for a conventional nodeless BCS gap, while a power law temperature dependence indicates that there may be nodes in the gap [91]. However, as seen in Fig. 6.18, we observe an upturn in $C_{\rm el}\,(T)\,/\gamma_{\rm n} T_{\rm n}$ in $NbRh_2B_2$ at low-temperatures. This upturn is also present in applied magnetic fields up to 1 T but is not observed at 2 T. There is no indication of any sizeable magnetic moments present in the sample from the magnetic susceptibility in the normal-state or the muon spectroscopy data so the upturn cannot be a precursor due to magnetic ordering. An upturn in the heat capacity at low-temperature may arise from a hyperfine contribution. Niobium and boron have nuclear moments of $\mu/\mu_{\rm N} = 6.17$ and $\mu/\mu_{\rm N} = 2.75$ respectively, so a Schottky anomaly shifting with ap-

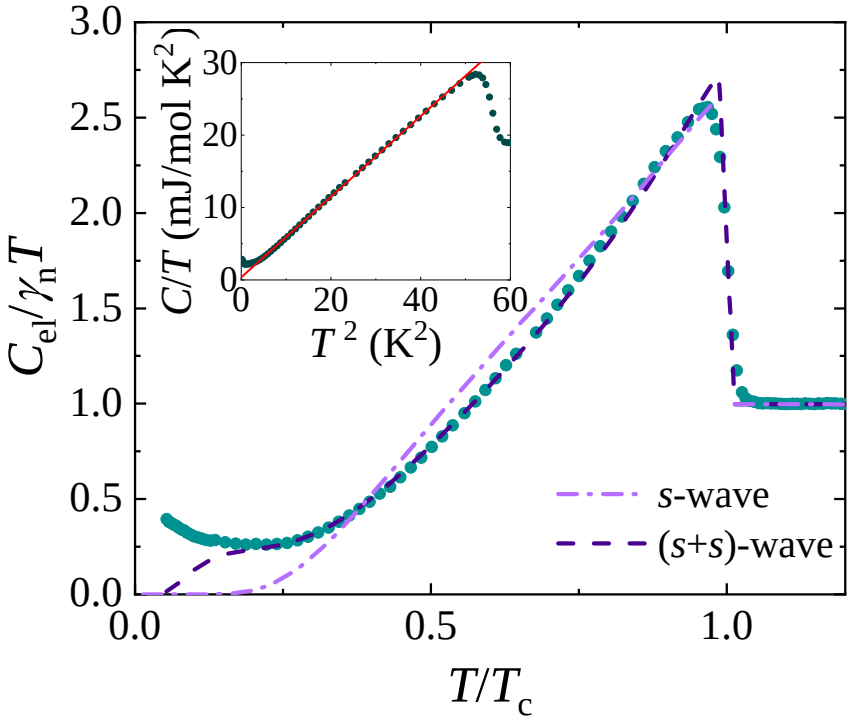

Figure 6.18: Zero-field specific heat of $NbRh_2B_2$ with the phonon contribution subtracted divided by $\gamma_n T$ where γ_n is the Sommerfeld coefficient. Fits to the data between T_c and 1.5 K are shown using a single-gap isotropic s-wave model (light purple) and an isotropic two-gap $(s+s)$-wave (purple) model. The inset shows that the zero-field specific heat has a T^3 dependence as demonstrated by the linear fit to specific heat divided by temperature as a function of T^2.

plied field may be expected. A similar feature with the same temperature and field dependence is seen in $TaRh_2B_2$ [208]. In a simple case, any hyperfine contribution to $C(T)$ is expected to follow a $1/T^2$ dependence. The contribution observed at low-temperature in Fig. 6.18 does not have this temperature dependence. It is possible to model this upturn using a simple (arbitrary) $1/T^n$ temperature dependence, but subtracting such a contribution necessarily leaves the temperature dependence of the electronic component $C_{el}(T)$ uncertain. As a result of the upturn in $C(T)/T$, it is not possible to definitively establish the nature of the superconducting gap for $NbRh_2B_2$ from heat capacity measurements. Nevertheless, the data at higher temperatures allow progress to be made. For the following analysis, the temperature region affected by the anomalous contribution is excluded. The temperature dependence of the zero-field electronic specific heat C_{el} was fit using the BCS model

of the specific heat [11] combined with a phenomenological two-gap model [133] as described above for $TaRh_2B_2$. The zero-field $C_{\rm el}(T)$ data between $T_{\rm c}$ and 1.5 K were fit using a single-gap isotropic s-wave model and an isotropic two-gap $(s+s)$-wave model. The two-gap model produces a better fit to the data (see Fig. 6.18). The gap values for the $(s+s)$ model are $\Delta_{0,1}/k_{\rm B}T_{\rm c} = 2.16(1)$, $\Delta_{0,2}/k_{\rm B}T_{\rm c} = 0.39(4)$ with $w = 0.801(3)$. The larger of the two gaps is above the expected BCS value of 1.76 for a weakly-coupled superconductor, indicating a stronger electron-phonon coupling. The observation of multigap behaviour in $NbRh_2B_2$ is consistent with previous studies of isostructural $TaRh_2B_2$ [208].

As seen in the inset of Fig. 6.18 below $T_{\rm c}$, $C_{\rm el}(T)$ deviates from an s-wave BCS-like behaviour and instead exhibits a T^3 dependence, suggesting the presence of a node in the gap or multigap behaviour. This behaviour is also observed in other noncentrosymmetric two-gap superconductors including $TaRh_2B_2$ [208] and Mo_3Al_2C [90, 91], as well as several well-studied centrosymmetric superconducting materials such as $Lu_2Fe_3Si_5$ [203, 204] and MgB_2 [195]. This power law dependence and the multigap fit of the heat capacity in the superconducting state are reasonably consistent with the values obtained for the two-gap fit to the muon spectroscopy data, but at odds with the nodeless s-wave superconducting ordering parameter as will be discussed in Section 6.3.4. The anomalous low-temperature contribution to the heat capacity, therefore, leaves open the question of the precise nature of the superconducting order parameter in $NbRh_2B_2$.

6.3.4 μSR Measurements

In order to measure the structure of the superconducting gap in $NbRh_2B_2$ transverse-field μSR experiments were performed in applied fields of 18 and 30 mT, well above the $\mu_0 H_{\rm c1}(0) \sim 4.6$ mT to ensure the sample is in the superconducting mixed state. The detectors in the spectrometer were grouped in eight blocks, each with a phase offset ϕ, and the data were collected in field-cooled-warming (FCW) mode to ensure the most uniform flux-line lattice possible. Examples of the TF-μSR precession signals above and below $T_{\rm c}$ are shown in Fig. 6.19(a). As described previously for $TaRh_2B_2$ the superfluid density of $NbRh_2B_2$ can be obtained from the Gaussian relaxation seen by the TF spectra. The superfluid density is directly related to magnetic penetration depth so can be used to determine the superconducting gap structure in $NbRh_2B_2$. In the clean limit, the temperature dependence of the magnetic penetration depth $\lambda(T)$ can be calculated using Eq. (6.5). Multigap analysis was performed using a weighted sum of two superconducting gaps [see Eq. (6.6)]. The temperature dependence of the inverse penetration depth squared $\lambda^{-2}(T)$ is

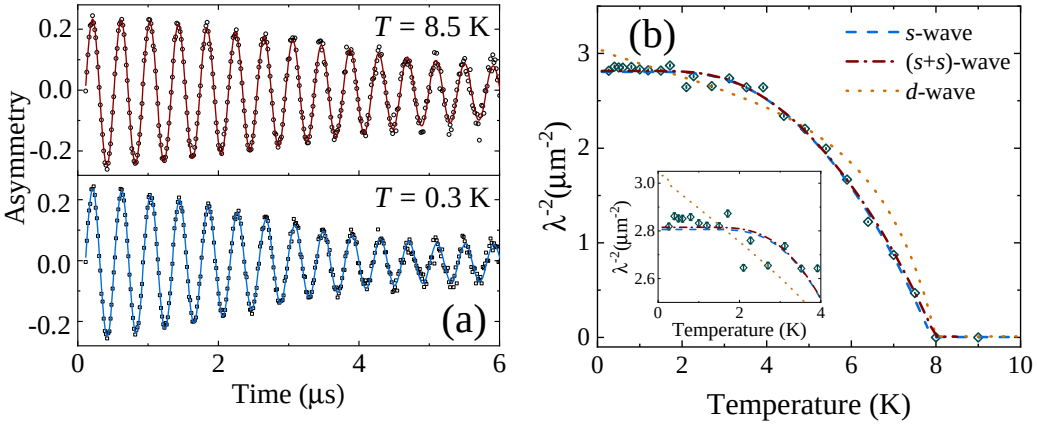

Figure 6.19: (a) Transverse field μSR time spectra for $NbRh_2B_2$ collected at 8.5 (top) and 0.3 K (bottom) in an applied field of 18 mT. The solid lines are fits using Eq. (6.4). The Gaussian decay of the oscillatory signal shows the effect of the flux-line lattice. Above T_c, the depolarisation is reduced and is due to the randomly oriented array of nuclear moments. (b) Inverse square of the London penetration depth, λ^{-2}, as a function of temperature for $NbRh_2B_2$. The lines are fits to the data using Eqs. (6.5) and (6.6) for one- and two-gap models. The inset shows the low-temperature data on an expanded scale.

Gap	$\Delta_{0,1}/k_BT_c$	$\Delta_{0,2}/k_BT_c$	w	χ^2_{norm}
s-wave	2.19(6)	-	1	1.95
$(s+s)$-wave	2.34(22)	0.85(76)	0.93(11)	1.87

Table 6.3: Superconducting gap parameters for $NbRh_2B_2$ extracted from fits to the temperature dependence of the inverse penetration depth squared $\lambda^{-2}(T)$.

shown in Fig. 6.19(b). Both an isotropic s-wave model and the isotropic two-gap $(s+s)$-wave model produce good fits to the data (see Table 6.3). Attempts were also made to fit $\lambda^{-2}(T)$ using a d-wave and an $(s+d)$-wave model. The d-wave produced a poor fit to the data and the fit using the $(s+d)$-wave model did not converge. There is little difference between the χ^2_{norm} produced by the $(s+s)$- and s-wave models, although on this basis alone the $(s+s)$-wave model would be slightly preferred. However, the uncertainty associated with both the magnitude of the smaller gap and the weighting, w, leaves open both possibilities.

The value of $\Delta_0/k_BT_c = 2.19(6)$ for the s-wave model, and the $\Delta_{0,1}/k_BT_c = 2.34(22)$ for the two-gap model, exceed the value expected for a Bardeen-Cooper-Schrieffer (BCS) superconductor, $\Delta_{BCS}/k_BT_c = 1.76$ which suggests that there is an enhancement in the electron-phonon coupling. The magnetic penetration depth given by the s-wave model is $\lambda(0) = 595(5)$ nm. This value is significantly larger

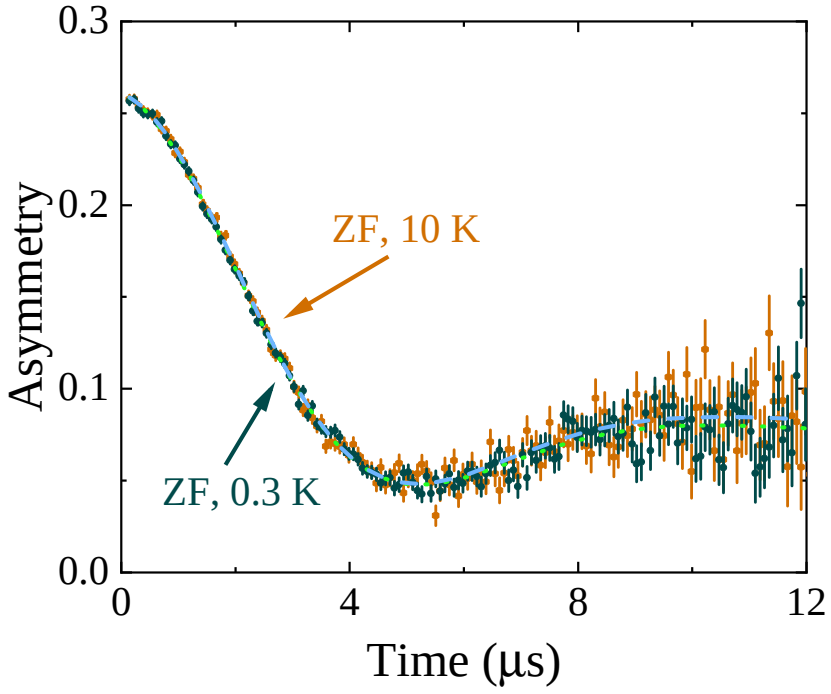

Figure 6.20: Zero-field μSR spectra of $NbRh_2B_2$ above (10 K) and below (0.3 K) the superconducting transition. No measurable difference in the relaxation of the asymmetry between the two spectra indicates that time-reversal symmetry is preserved in $NbRh_2B_2$. The dotted and dashed line shows the fit to the two spectra using a Gaussian Kubo-Toyabe function.

than the $\lambda(0)$ calculated from magnetisation measurements in Ref. [193], where $\lambda(0) = 219(7)$ nm.

In order to investigate whether time-reversal symmetry is broken in $NbRh_2B_2$, zero-field (ZF) muon spin relaxation spectra were collected in the normal and superconducting state. Figure 6.20 shows the two spectra have a Kubo-Toyabe-like form [see Eqs. (5.7, 5.8)] with no measurable difference between the two data sets, indicating that time-reversal symmetry is preserved in $NbRh_2B_2$. The absence of any oscillatory component or loss of initial asymmetry in the zero-field μSR spectra shows that no magnetic ordering takes place in $NbRh_2B_2$ down to 300 mK.

6.3.5 Pressure Measurements

The change in T_c with hydrostatic pressure is shown in Fig. 6.21. The shift in the transition temperature was determined from magnetisation versus temperature data collected in an applied field of 1 mT. T_c was estimated by extrapolating the superconducting response at the transition slope and taking the intersection with a line

drawn from the normal-state susceptibility at higher temperature. The superconducting transition decreases sharply as the initial pressure is applied before decreasing more slowly thereafter. A linear fit to the data gives $\mathrm{d}T_{\mathrm{c}/\mathrm{d}P} = -0.40(4)$ K/GPa. The width of the transition is not seen to broaden noticeably across the available pressure range. A decrease in T_{c} with pressure is typical for simple BCS superconductors, including the elements [209]. The $\mathrm{d}T_{\mathrm{c}}/\mathrm{d}P$ for $NbRh_2B_2$ is the same order of magnitude as that seen in pure Nb [$-0.28\,(2)$ K/GPa], Ta [$-0.26\,(1)$ K/GPa], and V [$-0.49\,(5)$ K/GPa] which are all transition metals with very similar isothermal compressibility. The $\mathrm{d}T_{\mathrm{c}}/\mathrm{d}P$ normalised to T_{c} is also very close to the value of $\mathrm{d}T_{\mathrm{c}}/\mathrm{d}P = -2.14\,(6)$ K/GPa observed for the two-band boride superconductor MgB_2. Variations in T_{c} with pressure are typically driven by changes in the Debye temperature or the density of states close to the Fermi energy [209]. Measurements of resistivity under pressure would help to determine the change in θ_{D} with pressure, while detailed calculations of the band structure may shed more light on the role played by changes in $N\,(E_{\mathrm{F}})$. Other noncentrosymmetric superconductors also exhibit a decrease in T_{c} with pressure. For example, La_7Ir_3 exhibits a $\mathrm{d}T_{\mathrm{c}}/\mathrm{d}P = -0.15$ K/GPa [125]. As noted above, the T_{c} of Mo_3Al_2C increases non-monotonically with $\mathrm{d}T_{\mathrm{c}}/\mathrm{d}P = +0.28(2)$ K/GPa close to T_{c} [91]. The more conventional behaviour seen in $NbRh_2B_2$ suggests that the superconducting gap is dominated by an s-wave component.

6.3.6 Upper Critical Field

The upper critical field as function of temperature, $\mu_0 H_{\mathrm{c}2}\,(T)$, in $NbRh_2B_2$ was obtained by measuring T_{c} from heat capacity up to 8 T [see Fig. 6.17(a)], and resistivity up to 17 T, [see Fig. 6.16(b)].

The temperature dependence of $\mu_0 H_{\mathrm{c}2}$ determined from the resistivity and heat capacity data is almost linear up to 9 T as shown in Fig. 6.22. $\mu_0 H_{\mathrm{c}2}\,(T)$ with a linear temperature dependence is often fit using the Werthamer-Helfand-Hohenberg model, which allows $\mu_0 H_{\mathrm{c}2}\,(T)$ to be calculated taking into account both spin-orbit scattering and Pauli spin paramagnetism [170]. Niobium and rhodium are both heavier elements where spin-orbit coupling may be expected to be significant and therefore to have an influence on the value of $\mu_0 H_{\mathrm{c}2}$. Initially α_{M} was estimated using Eq. (4.12) to be ~ 1.8, but in the subsequent fits of the WHH model both α_{M} and λ_{so} were allowed to vary and this resulted in $\alpha_{\mathrm{M}} \to 0$ and values for $\lambda_{\mathrm{so}} >> 1$, well above those expected for the WHH formalism [170, 210]. The fit using Eq. (4.10), shown with the dot-dash line, produces the maximum value for the upper critical field, $\mu_0 H_{\mathrm{c}2}^{\mathrm{orb}}\,(0) \approx 17$ T that is consistent with the gradient of the data, $dH_{\mathrm{c}2}\,(T)\,/dT$,

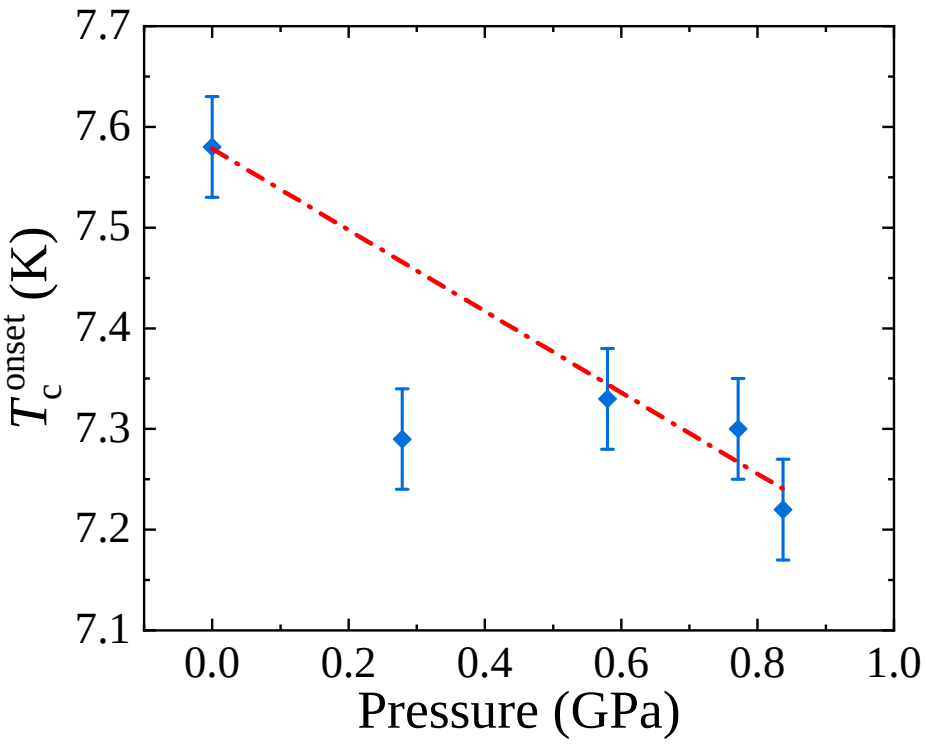

Figure 6.21: Pressure versus transition temperature for $NbRh_2B_2$. A small decrease in the transition temperature can be seen for increasing pressure.

close to T_c. This value for $H_{c2}(T)$ is comparable to that reported in Ref. [193] and well above the Pauli paramagnetic limiting field of 13.9 (2) T. However, the data clearly deviate from the WHH model at lower T and do not provide a satisfactory description of the data. We have also used the phenomenological Ginzburg-Landau expression (see Eq. 5.1) to estimate $\mu_0 H_{c2}(0) = 20.2(2)$ T, but this is clearly higher than the value that would be estimated from a visual inspection of the $H_{c2}(T)$ data. Neither model can fully explain the temperature dependence of the upper critical field of $NbRh_2B_2$ suggesting that it is necessary to consider two-band effects to describe the behaviour. A model proposed by Gurevich that considers intra- and inter-band scattering has been used to successfully describe the T dependence of H_{c2} of several two-band superconductors [171]. The model includes several free parameters, so any meaningful consideration of $H_{c2}(T)$ for $NbRh_2B_2$ within this framework requires a more complete knowledge of the intra- and inter-band scattering. Such an analysis needs single crystals. While multigap behaviour may explain why the upper critical field of $NbRh_2B_2$ exceeds the Pauli limit, it is known that strong pinning and energy gaps larger than the BCS value can also be responsible for

increasing the Pauli limiting field [210, 211]. The magnetisation and susceptibility data, however, indicate the pinning is rather weak in $NbRh_2B_2$. The magnitude of the superconducting energy gap is larger than the BCS value, but an enhancement of this kind can only increase the Pauli limit by around 30% [210].

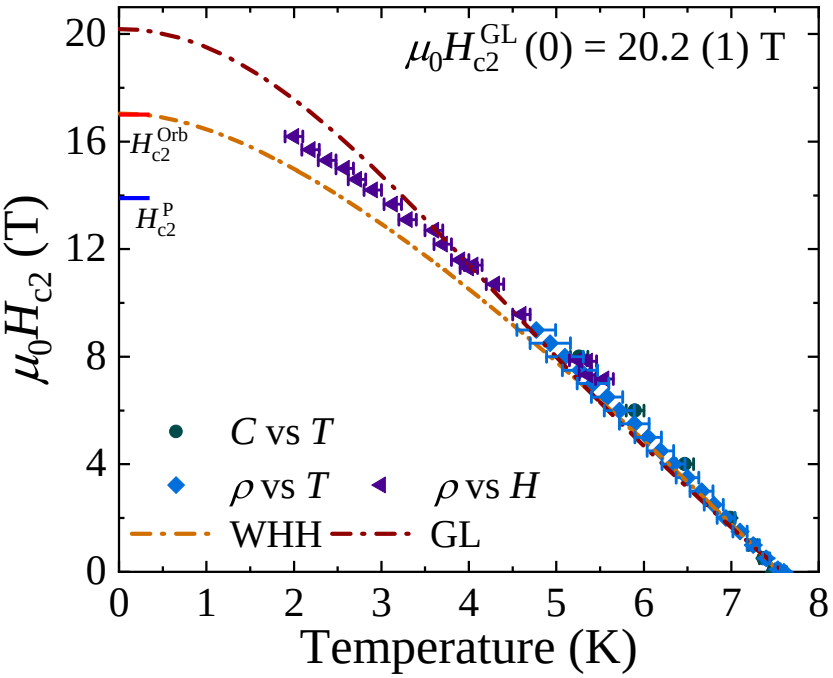

Figure 6.22: Upper critical field as a function of temperature for $NbRh_2B_2$ where the $H_{c2}(T)$ points were extracted from the T_c in heat capacity and electrical resistivity as a function temperature and field. Fits using the WHH and GL models are shown by the dashed and the dashed-dotted lines respectively.

6.3.7 Properties of the Superconducting State

As previously described in Section 4.1.7 the results of the characterisation measurements presented above can be combined in order to estimate some of the important superconducting properties of $NbRh_2B_2$ which are displayed in Table 6.4. The electron-phonon coupling constant λ_{el-ph} can be estimated from Eq. (4.25) giving a value of $\lambda_{el-ph} = 0.67\,(2)$. This suggests that $NbRh_2B_2$ is a moderately coupled superconductor. By calculating the Fermi temperature T_F it can be seen the that $NbRh_2B_2$ is outside of the Uemera classification for unconventional superconductivity.

Table 6.4: Electronic properties of $NbRh_2B_2$ for $\lambda_{GL}(H_{c1})$ and $\lambda_{GL}(\mu SR)$.

Property	Units	H_{c1}	μSR
$\lambda_{GL}(0)$	(nm)	409 (5)	595 (7)
m^*/m_e		5.86 (8)	7.69 (1)
n	($10^{27}m^{-3}$)	11.3 (1)	5.03 (5)
ξ_0	(nm)	1.32 (2)	1.55 (2)
ℓ_e	(nm)	0.13 (1)	0.22 (3)
ξ_0/ℓ_e		10.5 (1)	7.21 (8)
λ_L	(nm)	121 (2)	208 (2)
T_F	(K)	–	1610(20)
T_c/T_F		–	0.0046(5)

6.4 Discussion and Summary

Muon spectroscopy, heat capacity, and resistivity measurements have been carried out on the new chiral noncentrosymmetric superconductor $TaRh_2B_2$. We show $TaRh_2B_2$ is a bulk type II superconductor with a $T_c = 6.00(5)$ K driven by moderate electron-phonon coupling. Zero-field μSR shows time-reversal symmetry is preserved in the superconducting state. Our results clearly show strong evidence for multigap superconductivity in $TaRh_2B_2$. The temperature dependence of both the electronic heat capacity and the penetration depth, extracted from TF μSR data, reveal this multigap nature, with either an isotropic $(s+s)$-wave or an $(s+d)$-wave order parameter. For both models, the value of the larger gap $\Delta_{0,1}/k_BT_c$ extracted from the μSR and heat capacity data is higher than the BCS value of 1.76.

We determine a number of other important superconducting parameters for this new noncentrosymmetric superconductor with a chiral structure. In particular, we show that the upper critical field $\mu_0 H_{c2}(0)$ exceeds the Pauli limit. There are several potential sources for the suppression of paramagnetic pair breaking. Any triplet superconducting component should be robust to paramagnetic pair breaking [60, 59], but $TaRh_2B_2$ appears to be a superconductor in the dirty limit with considerable localisation of the carriers and perhaps some disorder due to variations in the stoichiometry. This is likely to suppress any triplet component that may be present. Strong-coupling can increase $H_{c2}(0)$. The fit to the $C_{el}(T)$ below T_c as well the jump in heat capacity at T_c suggest the coupling is only moderately enhanced, however, multigap behaviour can sometimes reduce the jump at T_c [204, 197]. Spin-

orbit scattering associated with the presence of heavier elements Ta and Rh could help to increase $H_{c2}(0)$ in $TaRh_2B_2$ (cf. $Ta_2Pd_xS_5$ and related $R_2Pd_xS_5$ materials [198, 199]). $H_{c2}(0)$ can also be increased by a Stoner enhancement [212]. The observed multigap nature of the superconductivity is also likely to play an important role in augmenting the upper critical field [171].

We have investigated the superconducting properties of the chiral noncentrosymmetric superconductor $NbRh_2B_2$ using a combination of μSR, magnetisation, pressure, heat capacity, and resistivity measurements. We have shown that $NbRh_2B_2$ is a bulk type-II superconductor with a superconducting transition at 7.46(5) K that is mediated by moderate electron-phonon coupling. The temperature dependence of the penetration depth measured by TF μSR indicates that $NbRh_2B_2$ has a superconducting gap that can be fit by both an s-wave or an $(s+s)$-wave model. The magnetic penetration depth is $\lambda(0) = 595(5)$ nm. The superconducting gap measured by heat capacity data, although convoluted with an anomalous low-temperature contribution, strongly indicates a multigap $(s+s)$-wave dependency with a conventional s-wave model providing a poor fit to the data. The decrease in T_c with pressure suggests that the superconducting gap is dominated by an s-wave component. We have also shown that the upper critical field of $NbRh_2B_2$ at low temperatures is not adequately described by either the WHH or GL models and that a two-band formalism may be required to more fully account for the $\mu_0 H_{c2}(0)$ behaviour. Strong spin-orbit scattering may also play an important role in the physics of $NbRh_2B_2$ and more complete knowledge of the intra- and inter-band scattering, including scattering due to non-magnetic defects, is required to complete such an analysis. To gain a deeper understanding of the enhancement in $\mu_0 H_{c2}(0)$ and the nature of superconducting gap in $NbRh_2B_2$ (and $TaRh_2B_2$), high-quality single crystals are urgently required. Tunnel-diode oscillator measurements of the penetration depth may also help shed light on the form of the superconducting gap in this interesting new family of superconductors.

A summary of the key superconducting and normal-state properties of $TaRh_2B_2$ and $NbRh_2B_2$ can be seen in Table 6.5. High-quality single crystals are urgently required to further investigate the superconducting order parameter of $TaRh_2B_2$ and $NbRh_2B_2$ and to confirm the mechanism allowing for a Pauli-limit violation in this compound. Further investigations of the superfluid density in $TaRh_2B_2$ and $NbRh_2B_2$ that are not sensitive to the effects of hyperfine contributions are required to understand the nature of the superconducting gap.

Table 6.5: Comparison of the normal-state and superconducting properties of $TaRh_2B_2$ and $NbRh_2B_2$.

Property	Units	$TaRh_2B_2$	$NbRh_2B_2$
T_c	(K)	6.00 (5)	7.46 (5)
ρ_0	(mΩ cm)	2.20 (1)	2.00 (1)
γ_n	(mJ/mol K^2)	4.29 (6)	7.6 (4)
β_3	(mJ/mol K^4)	0.187 (3)	0.166 (3)
β_5	(μJ/mol K^6)	0.24 (3)	0.12 (3)
λ_{el-ph}		0.63 (2)	0.67 (3)
Θ_D	(K)	374 (2)	373 (2)
$\mu_0 H_{c1}(0)$	(mT)	3.8 (1)	4.57 (6)
$\mu_0 H_{c2}(0)$	(T)	15.2 (1)	18.5 (5)
$\mu_0 H_c(0)$	(mT)	77 (3)	97 (1)
$\mu_0 H_{c2}^{orb}(0)$	(T)	12.9 (1)	17.1 (1)
$\mu_0 H_{c2}^{P}(0)$	(T)	11.1 (1)	13.9 (1)
$\xi_{GL}(0)$	(nm)	4.67 (6)	4.05 (2)
$\lambda_{GL}(0)$	(nm)	648 (4)	595 (7)
$\kappa_{GL}(0)$		138 (1)	147 (2)

Chapter 7

Summary and Conclusions

Detailed research into noncentrosymmetric superconductors began with the discovery of $CePt_3Si$ and the heavy fermion noncentrosymmetric superconductors. With the lack of inversion symmetry in these compounds meaning that the Cooper pairs may no longer form either singlet or triplet pairs but rather an admixture has led to the experimental detection of many unconventional superconducting properties. It has proved difficult to disentangle the strong correlations in these materials from the expected behaviour due to the broken inversion symmetry. Weakly correlated noncentrosymmetric superconductors allow for the isolation of these behaviours. In this thesis we have studied Re_6Zr, La_7Pd_3, La_7Ir_3, $TaRh_2B_2$ and $NbRh_2B_2$ all of which are weakly correlated noncentrosymmetric superconductors. The detection of time-reversal symmetry breaking in polycrystalline samples of Re_6Zr and La_7Ir_3 has prompted further study of the normal-state and superconducting properties of these materials. The growth of single crystals of these materials has proved essential to determine if any anisotropic behaviour exists. In this work we have also synthesised and characterised several new noncentrosymmetric superconducting compounds with an aim to find exotic behaviours. We have focussed on studying the nature of the superconducting gap in these materials by heat capacity and muon spin spectroscopy experiments. By exploring, both experimentally and theoretically, the large phase space of noncentrosymmetric superconductors a broader understanding of the underlying physics of these systems can be gained.

In chapter 4 we characterised the superconducting and normal-state properties the noncentrosymmetric compound Re_6Zr using magnetisation, heat capacity and electrical resistivity measurements. Re_6Zr forms in a cubic noncentrosymmetric α-Mn structure with space group $I\bar{4}2m$ which was confirmed using neutron diffraction. The temperature dependence of the lattice parameter indicated no structural

changes down to 5 K. Magnetisation, resistivity and heat capacity measurements all showed a sharp superconducting transition at 6.75(5) K. Normal-state electrical resistivity measurements show that Re_6Zr is a poor metal which is dominated by disorder. Heat capacity measurements performed in the normal-state also reveal no structural or magnetic phase transition down to low temperatures. Heat capacity measurements in the superconducting state in Re_6Zr were fit using the BCS model giving a superconducting gap ratio of $\Delta_0/k_BT_c = 1.86(5)$ which is higher than the BCS value. This suggests the electron-phonon coupling in Re_6Zr is moderately enhanced. Several important normal-state and superconducting parameters were calculated including the scattering length and the Ginzburg-Landau parameter which indicate that Re_6Zr lies in the dirty limit and is a strong type-II superconductor.

A significant number of other rhenium based α-Mn structured superconductors have also now been reported on. The strength of the spin-orbit coupling in these compounds has been of the most interest in understanding the underlying physics of these systems. The best compounds for this comparison are Re_6Zr and Re_6Hf [113, 114] however the normal-state and superconducting properties are consistent with each other suggesting the spin-orbit coupling strength does not play a strong role in the underlying physics. Recently the detection of time-reversal symmetry breaking in pure centrosymmetric rhenium [117] has brought into question the role of inversion symmetry in the physics of these systems. While this work has provided an important paving stone in helping to map out some of the experimental characteristics of these materials further work on new compounds in this structural series both rhenium-based and rhenium-free is now required to understand the importance of inversion symmetry breaking, spin-orbit coupling and disorder on these systems.

To understand the role of inversion symmetry breaking in the hexagonal non-centrosymmetric superconductor's in the La_7X family; we have researched another compound, La_7Pd_3, in this series. We have also successfully grown single crystals of La_7Ir_3 for the first time. La_7Pd_3 is a type-II superconductor with a transition temperature of $T_c = 1.46(5)$ K. Heat capacity measurements revealed BCS-like s-wave ordering parameter and modelling of the temperature dependence of the upper critical field using the Ginzburg-Landau model further suggests conventional superconducting behaviour in La_7Pd_3. Transverse-field μSR further indicated an isotopic s-wave superconducting gap. However, zero-field μSR measurements observed spontaneous magnetisation below the superconducting transition indicating the time-reversal symmetry is broken. This detection of time-reversal symmetry breaking suggests the presence of triplet pairing inside the superconductor. Collec-

tively time-reversal symmetry breaking has been seen in three members of the La_7X family; La_7Ir_3, La_7Rh_3 and now La_7Pd_3. In these compounds s-wave superconducting order parameters have been observed in both heat capacity and transverse field μSR measurements. These two results appear to be at odds with each other, however, if $\vec{d}$ in Eq. 2.25a is sufficiently small then it will become difficult to distinguish admixture behaviour from that of an s-wave superconductor. We need now require high quality single crystals to investigate whether there are any subtle anisotropies to the superconducting gap in the three compounds.

Single crystals of La_7Ir_3 were grown to investigate whether there is any anisotropy in superconducting properties of this material as polycrystalline measurements have shown only isotropic behaviour. A combination of magnetisation, resistivity and heat capacity showed that La_7Ir_3 is a clean type-II superconductor with an isotropic s-wave superconducting gap. The superconducting transition was found to be higher than previously reported in polycrystalline samples with $T_c = 2.38(5)$ K. When the samples were cooled in field through the superconducting transition it was seen to re-exclude approximately 90% of the magnetic flux. Measurements of the lower critical field showed that a field parallel to the c-axis gave $\mu_0 H_{c1} = 3.59(5)$ mT and a field parallel to the a-axis gave $\mu_0 H_{c1} = 4.82(4)$ mT. Similarly the upper critical was anisotropic in its behaviour with $\mu_0 H_{c2} = 1.01(5)$ T for $\mu_0 H \| c$ and $\mu_0 H_{c2} = 0.71(3)$ T for $\mu_0 H \| a$. The differences in values indicates the presence of an anisotropy in the superfluid density although further confirmation is needed by transverse-field μSR and tunnel-diode experiments. Zero-field μSR measurements along both the a and c-axis are necessary to establish if time-reversal symmetry breaking is still present and if it has preferred crystal direction.

Finally we investigated the role of chirality in the structure of noncentrosymmetric superconductors by investigating $TaRh_2B_2$ and $NbRh_2B_2$. Only two other noncentrosymmetric compounds Mo_3Al_2C and $Li_2(Pd_{1-x}Pt_x)_3B$ have been reported with chiral crystal structures, however, the chirality of the structure was not highlighted by these authors. Both Mo_3Al_2C and Li_2Pd_3B have been reported to have nodal superconducting gaps so chiral crystal structure may play an important role in the properties of a superconductor.

$TaRh_2B_2$ was found to be a type-II superconductor with $T_c = 6.05(5)$ K and a moderate electron-phonon coupling strength. The upper critical field of $TaRh_2B_2$ was estimated to be $\mu_0 H_{c2} = 15.2(1)$ T which exceeds the Pauli limiting field. Heat capacity and TF-μSR measurements provide strong evidence for multigap $(s+s)$-wave superconductivity in $TaRh_2B_2$ and the superconducting gap ratio of the larger gap in each measurements is larger than the expected BCS value. $NbRh_2B_2$ was

similarly found to be a type-II superconductor with a slightly higher $T_c = 7.46(5)$ K. TF μSR measurements indicated that the superconducting gap of $NbRh_2B_2$ can be fit by both an s-wave and a $(s + s)$-wave model. The temperature dependence of the heat capacity also indicates that the superconducting gap can be modelled by an $(s + s)$-wave model, however, an anomalous low-temperature contribution leaves the true nature of the superconducting gap open to speculation. Attempts to model the upper critical field of $TaRh_2B_2$ and $NbRh_2B_2$ using the WHH model showed the upper critical field exceeds the maximum value that the model can produce given the fixed initial gradients near T_c. It is speculated that the multiband WHH model could be used to model the behaviour of the upper critical field in both $TaRh_2B_2$ and $NbRh_2B_2$. To be able to fit the data using the multiband WHH model knowledge of the inter- and intra- band scattering is required to help estimate the many free parameters of this model.

Through the research efforts of the work presented in this thesis we have expanded and explored part of the large phase space that is noncentrosymmetric superconductors. We have presented a detailed characterisation of both the normal-state and superconducting properties of Re_6Zr, La_7Pd_3, La_7Ir_3, $TaRh_2B_2$ and $NbRh_2B_2$ in the effort to gain a better understanding of the conventional and unconventional behaviours of these systems.

Bibliography

[1] N. D. Mathur, F. M. Grosche, S. R. Julian, I. R. Walker, D. M. Freye, R. K. W. Haselwimmer, and G. G. Lonzarich, Nature **394**, 39 (1998).

[2] L. Taillefer, Annu. Rev. Condens. Matter Phys. **1**, 51 (2010).

[3] S. Nandi, M. G. Kim, R. M. Fernandes, D. K. Pratt, A. Thaler, N. Ni, S. L. Bud'ko, P. C. Canfield, J. Schmalian, R. J. McQueeney, and A. I. Goldman, Phys. Rev. Lett. **104**, 057006 (2010).

[4] H. Q. Yuan, D. F. Agterberg, N. Hayashi, P. Badica, D. Vandervelde, K. Togano, M. Sigrist, and M. B. Salamon, Phys. Rev. Lett. **97**, 017006 (2006).

[5] S. Kuroiwa, Y. Saura, J. Akimitsu, M. Hiraishi, M. Miyazaki, K. H. Satoh, S. Takeshita, and R. Kadono, Phys. Rev. Lett. **100**, 097002 (2008).

[6] R. P. Singh, A. D. Hillier, B. Mazidian, J. Quintanilla, J. F. Annett, D. M. Paul, G. Balakrishnan, and M. R. Lees, Phys. Rev. Lett. **112**, 107002 (2014).

[7] D. Singh, J. A. T. Barker, A. Thamizhavel, D. M. Paul, A. D. Hillier, and R. P. Singh, Phys. Rev. B **96**, 180501 (2017).

[8] T. Shang, M. Smidman, S. K. Ghosh, C. Baines, L. J. Chang, D. J. Gawryluk, J. A. T. Barker, R. P. Sing, D. M. Paul, E. Balakrishnan, Pomjakushina, M. Shi, M. Medarde, A. D. Hillier, H. Q. Yuan, J. Quintanilla, J. Mesot, and T. Shiroka, Phys. Rev. Lett **121**, 257002 (2018).

[9] A. Maisuradze, R. Khasanov, A. Shengelaya, and H. Keller, J. Phys.: Condens. Matter **21**, 075701 (2009).

[10] E. H. Brandt, Rep. Prog. Phys. **58**, 1465 (1995).

[11] B. Muhlschlegel, Z. Phys. **155**, 313 (1959).

[12] A. Carrington and F. Manzano, Physica C **385**, 205 (2003).

[13] J. W. G. Thomason, Nucl. Instrum. Methods A **917**, 61 (2018).

[14] A. C. Hannon, Nucl. Instrum. Methods A **551**, 88 (2005).

[15] D. V. Delft, Physica C **479**, 20 (2012).

[16] M. W. and R. Ochsenfeld, Naturwissenschaften **21**, 787 (1933).

[17] L. F. and H. London, Proc. Roy. Soc. (London) **A149**, 71 (1935).

[18] V. L. Ginzburg and L. D. Landau, Zh. Eksp. Teor. Fiz. **20**, 150 (1950).

[19] A. A. Abrikosov, Sov. Phys. JETP **5**, 1174 (1957).

[20] J. Bardeen, L. N. Cooper, and J. R. Schrieffer, Phys. Rev. **108**, 1175 (1957).

[21] G. K. Gaule, USAELRDL Technical Report , 2329 (1963).

[22] D. Pines, Phys. Rev. **109**, 280 (1958).

[23] V. J. Emery and A. M. Sessler, Phys. Rev. **119**, 43 (1960).

[24] D. D. Osheroff, R. C. Richardson, and D. M. Lee, Phys. Rev. Lett. **28**, 885 (1972).

[25] A. J. Leggett, Phys. Rev. Lett. **29**, 1227 (1972).

[26] R. Balian and N. R. Werthamer, Phys. Rev. **131**, 1553 (1963).

[27] P. W. Anderson and P. Morel, Phys. Rev. **123**, 1911 (1961).

[28] B. Patton and A. Zaringhalaml, Phys. Lett. A **55**, 97 (1975).

[29] J. A. Sauls and J. W. Serene, Phys. Rev. B **24**, 183 (1981).

[30] A. J. Leggett, Rev. Mod. Phys. **47**, 331 (1975).

[31] A. A. Abrikosov and L. P. Gorkov, Sov. Phys. JETP **12**, 1243 (1961).

[32] N. F. Berk and J. R. Schrieffer, Phys. Rev. Lett. **17**, 433 (1966).

[33] B. T. Matthias, C. W. Chu, E. Corenzwit, and D. Wohlleben, Proc. Natl. Acad. Sci. **64**, 459 (1969).

[34] E. Bucher, J. P. Maita, G. W. Hull, R. C. Fulton, and A. S. Cooper, Phys. Rev. B **11**, 440 (1975).

[35] F. Steglich, W. Franz, and H. Schafer, Phys. Rev. Lett. **43**, 1892 (1979).

[36] F. Steglich, P. Gegenwart, C. Geibel, R. Helfrich, P. Hellmann, M. Lang, A. Link, R. Modler, G. Sparn, N. Büttgen, and A. Loidl, Physica B **223**, 1 (1996).

[37] G. M. Luke, A. Keren, K. Kojima, L. P. Le, B. J. Sternlieb, W. D. We, Y. J. Uemura, Y. Ōnuk, and T. Komatsubara, Phys. Rev. Lett. **73**, 1853 (1994).

[38] G. R. Stewart, Rev. Mod. Phys. **56**, 755 (1984).

[39] H. R. Ott, H. Rudigier, T. M. Rice, K. Ueda, Z. Fisk, and J. L. Smith, Phys. Rev. Lett. **52**, 1915 (1984).

[40] G. P. Meisner, A. L. Giorgi, A. C. Lawson, G. R. Stewart, J. O. Willis, and J. L. Smith, Phys. Rev. Lett. **52**, 1915 (1984).

[41] C. Petrovic, P. G. Pagliuso, M. F. Hundley, M. R., J. L. Sarrao, J. D. Thompson, Z. Fisk, and P. Monthoux, J. Phys. Condens. Matter **13**, L337 (2001).

[42] G. Knebel, D. Aoki, and J. Flouquet, Physique **12**, 542 (2011).

[43] G. Hardy and J. K. Hulm, Phys. Rev. **89**, 884 (1953).

[44] J. G. Bednorz and K. A. Muller, Zeit. Phys. B **64**, 189 (1986).

[45] M. K. Wu, J. R. Ashburn, C. J. Torng, P. H. Hor, R. L. Meng, L. Gao, Z. J. Haung, Y. Q. Wang, and C. W. Chu, Phys. Rev. Lett. **58**, 908 (1987).

[46] L. Gao, Y. Y. Xue, F. Chen, Q. Xiong, R. L. Meng, D. Ramirez, C. W. Chu, J. H. Eggert, and H. K. Mao, Phys. Rev. B **50**, 4260 (1994).

[47] C. C. Tsuei and J. R. Kirtley, Rev. Mod. Phys. **72**, 969 (2000).

[48] W. Little, Phys. Rev. **134**, A1416 (1964).

[49] D. Jerome, A. Mazaud, M. Ribault, and K. Bechgaard, J. Phys. Lett. **41**, L95 (1989).

[50] A. Ardavan, S. Brown, S. Kagoshima, K. Kanoda, K. Kuroki, H. Mori, M. Ogata, S. Uji, and J. Wosnitza, J. Phys. Co. Japan **81**, 011004 (2012).

[51] Y. Takabayashi, A. Y. Ganin, P. Jeglic, D. Arcon, T. Takano, W. Iwasa, Y. Ohishi, M. Takata, N. Takeshita, K. Prassides, and M. J. Rosseinsky, Science **323**, 1585 (2009).

[52] Y. Kamihara, T. Watanabe, M. Hirano, and H. Hosono, J. Am. Chem. Soc. **130**, 3296 (2008).

[53] P. Richard, K. Nakayama, T. Sato, M. Neupane, Y.-M. Xu, G. F. Bowen, J. H. ane Chen, J. L. Luo, N. L. Wang, X. Dai, Z. Fang, H. Ding, and T. Takahashi, Phys. Rev. Lett. **104**, 137001 (2010).

[54] H. . Q. Yuan, J. Singlton, F. F. Balkirev, S. A. Baily, G. F. Chen, J. L. Luo, and N. L. Wang, Nature **457**, 565 (2009).

[55] W. Malaeb, T. Yoshida, A. Fujimori, M. Kubota, K. Ono, K. Kihou, P. M. Shirage, H. Kito, A. Iyo, H. Esaki, Y. Nakajima, T. Tamegai, and R. Arita, J. Phys. Soc. Jpn. **78**, 123706 (2009).

[56] L. Boeri, O. V. Dolgov, and A. A. Golubov, Phys. Rev. Lett. **101**, 026403 (2008).

[57] B. T. Matthias, V. B. Compton, and E. Corenzwit, J. Phys. Chem. Solids **19**, 130 (1961).

[58] R. Blaugher and J. Hulm, J. Phys. Chem. Solids **19**, 134 (1961).

[59] M. Smidman, M. B. Salamon, H. Q. Yuan, and D. F. Agterberg, Rep. Prog. Phys. **80**, 036501 (2017).

[60] E. Bauer and M. Sigrist, *Non-centrosymmetric Superconductors: Introduction and Overview* (Springer, Heidelberg, 2012).

[61] E. Bauer, G. Hilscher, H. Michor, C. Paul, E. W. Scheidt, A. Gribanov, Y. Seropegin, H. Noel, M. Sigrist, and P. Rogl, Phys. Rev. Lett. **92**, 027003 (2004).

[62] E. Bauer, G. Hilscher, H. Michor, M. Sieberer, E. Q. Scheidt, A. Gribanov, Y. Seropegin, P. Rogl, W. Y. Song, J.-G. Park, D. T. Adroja, A. Amato, M. Nicklas, G. Sparn, M. Yogi, and Y. Kitaoka, Czech. J. Phys. **54**, 401 (2004).

[63] N. Metoki, K. Kaneko, T. D. Matsuda, A. Galatanu, T. Takeuchi, S. Hashimoto, T. Udea, R. Settai, Y. Ōnuki, and N. Bernhoeft, J. Phys.: Condens. Matter **16**, L207 (2004).

[64] T. Takeuchi, S. Hashimoto, T. Yasuda, H. Shishido, T. Ueda, M. Yamada, Y. Obiraki, M. Shiimoto, H. Kohara, and T. Yamamoto, J. Phys.: Condens. Matter **16**, L333 (2004).

[65] A. Amato, E. Bauer, and C. Baines, Phys. Rev. B **71**, 092501 (2005).

[66] T. Takeuchi, T. Yasuda, M. Tsujino, H. Shishido, R. Settai, H. Harima, and Y. Ōnuki, J. Phys. Soc. Jpn **76**, 014702 (2007).

[67] I. Bonalde, R. L. Ribeiro, W. Brämer-Escamilla, C. Rojas, E. Bauer, A. Prokofiev, Y. Haga, T. Yasuda, and Y. Ōnuki, New J. Phys. **11**, 055054 (2009).

[68] K. Izawa, Y. Kasahara, Y. Matsuda, K. Behnia, T. Yasuda, R. Settai, and Y. Ōnuki, Phys. Rev. Lett. **94**, 197002 (2005).

[69] M. Yogi, H. Mukuda, Y. Kitaoka, S. Hashimoto, T. Yasuda, R. Settai, T. D. Matsuda, Y. Haga, Y. Ōnuki, P. Rogl, and E. Bauer, J. Phys. Soc. Jpn **75**, 013709 (2006).

[70] N. Kimura, K. Ito, K. Saitoh, Y. Umeda, H. Aoki, and T. Terashima, Phys. Rev. Lett. **95**, 247004 (2005).

[71] Y. Muro, D. Eom, N. Takeda, and M. Ishikawa, J. Phys. Soc. Jpn **67**, 3601 (1998).

[72] N. Kimura, K. Ito, H. Aoki, S. Uji, and T. Terashima, Phys. Rev. Lett. **98**, 197001 (2007).

[73] I. Sugitani, Y. Okuda, H. Shishido, T. Yamada, A. Thamizhavel, E. Yamamoto, T. D. Matsuda, Y. Haga, T. Takeuchi, S. Rikio, and Y. Ōnuki, J. Phys. Soc. Jpn **75**, 043703 (2005).

[74] R. Settai, I. Sugitani, Y. Okuda, A. Thamizhavel, M. Nakashima, Y. Ōnuki, and H. Harima, J. Magn. Magn. Mater. **310**, 844 (2007).

[75] F. Honda, I. Bonalde, S. Yoshiuchi, Y. Hirose, T. Nakamura, K. Shimizu, S. Settai, and Y. Ōnuki, Physica C **470**, S543 (2010).

[76] N. Tateiwa, Y. Haga, T. D. Matsuda, S. Ikeda, E. Yamamoto, Y. Okuda, S. Miyauchi, and Y. Ōnuki, Physica C **470**, S543 (2007).

[77] T. Kawai, H. Muranaka, M.-A. Measson, T. Shimoda, Y. Doi, T. D. Matsuda, Y. Haga, G. Knebel, G. Lapertot, D. Aoki, J. FLouquet, T. Takeuchi, R. Settai, and Y. Ōnuki, J. Phys. Soc. Jpn **77**, 064716 (2008).

[78] T. Kawai, Y. Okuda, H. Shishido, A. Thamizhavel, T. D. Matsuda, Y. Haga, M. Nkashima, T. Takeuchi, M. Hedo, Y. Uwatoko, R. Settai, and Y. Ōnuki, J. Phys. Soc. Jpn **76**, 014710 (2007).

[79] J. Katagawa, Y. Muro, N. Takeda, and M. Ishikawa, J. Phys. Soc. Jpn **66**, 2163 (1997).

[80] T. Akazawa, H. Hidaka, T. Fujiwara, T. C. Kobayashi, E. Yamamoto, Y. Haga, R. Settai, and Y. Ōnuki, J. Phys.: Condens. Matter **16**, L29 (2004).

[81] S. Fujimoto, J. Phys. Soc. Jpn **75**, 083704 (2006).

[82] S. Fujimoto, J. Phys. Soc. Jpn **76**, 051008 (2007).

[83] K. Togano, P. Badica, Y. Nakamori, S. Orimo, H. Takeya, and K. Hirata, Phys. Rev. Lett. **93**, 247004 (2004).

[84] P. Badica, T. Kondo, and K. Togano, J. Phys. Soc. Jpn **74**, 1014 (2005).

[85] H. Takeya, K. Hirata, K. Yamaura, K. Togano, M. El Massalami, R. Rapp, F. A. Chaves, and B. Ouladdiaf, Phys. Rev. B **72**, 104506 (2007).

[86] H. Takeya, M. ElMassalami, S. Kasahara, and K. Hirata, Phys. Rev. B **76**, 104506 (2007).

[87] M. Nishiyama, Y. Inada, and G.-Q. Zheng, Phys. Rev. Lett. **98**, 047002 (2007).

[88] S. P. Mukherjee and T. Takimoto, Phys. Rev. B **86**, 134526 (2012).

[89] L. E. Toth and J. Zbasnik, J.: Act Met. **16**, 117 (1968).

[90] A. B. Karki, Y. M. Xiong, I. Vekhter, D. Browne, P. W. Adams, D. P. Young, K. R. Thomas, J. Y. Chan, H. Kim, and R. Prozorov, Phys. Rev. B **82**, 064512 (2010).

[91] E. Bauer, G. Rogl, X.-Q. Chen, R. T. Khan, H. Michor, G. Hilscher, E. Royanian, K. Kumagai, D. Z. Li, Y. Y. Li, R. Podloucky, and P. Rogl, Phys. Rev. B **82**, 064511 (2010).

[92] M. C. Krupka, A. L. Giorgi, N. H. Krikorian, and E. G. Szklarz, J. Less Common Met. **17**, 91 (1969).

[93] A. Simon and T. Gulden, Z. Anorg. Allg. Chem. **630**, 2191 (2004).

[94] G. Amano, S. Akutagawa, T. Muranaka, Y. Zenitani, and J. Akimitsu, J. Phys. Soc. Jpn **73**, 530 (2004).

[95] T. Nakane, T. Mochiku, H. Kito, J. Itoh, M. Nagao, H. Kumakura, and Y. Takano, Appl. Phys. Lett. **84**, 2859 (2004).

[96] J. Chen, M. B. Salamon, S. Akutagawa, J. Akimitsu, J. Singleton, J. L. Zhang, L. Jiao, and H. Q. Yuan, Phys. Rev. B **83**, 144529 (2011).

[97] S. Akutagawa and J. Akimitsu, J. Phys. Soc. Jpn **76**, 024713 (2007).

[98] A. Harada, S. Akutagawa, Y. Miyamichi, H. Mukuda, Y. Kitaoka, and J. Akimitsu, J. Phys. Soc. Jpn **76**, 023704 (2007).

[99] H. Q. Yuan, J. Chen, J. Singleton, S. Akutagawa, and J. Skimitsu, Phys. Chem. Solids **72**, 577 (2011).

[100] S. Kadono, M. Hiraishi, M. Miyazaki, K. H. Satoh, S. Takeshita, S. Kuroiwa, S. Saura, and J. Akimitsu, Physica B **404**, 737 (2009).

[101] K. Sugawara, T. Sato, S. Souma, T. Takahashi, and A. Ochiai, Phys. Rev. B **76**, 132512 (2007).

[102] J. S. Kim, W. Xie, R. K. Kremer, V. Babizhetskyy, O. Jepsen, A. Simon, K. S. Ahn, B. Raquet, H. Rakoto, J.-M. Broto, and B. Ouladdiaf, Phys. Rev. B **76**, 014516 (2007).

[103] S. J. Blundell, Contemp. Phys. **40**, 175 (1999).

[104] A. D. Hillier, J. Quintanilla, and R. Cywinski, Phys. Rev. Lett. **102**, 117007 (2009).

[105] W. H. Lee, H. K. Zeng, Y. D. Yao, and Y. Y. Chen, Physica C **266**, 138 (1996).

[106] V. K. Pecharsky, L. L. Miller, and K. A. Gschneidner, Phys. Rev. B **58**, 497 (1998).

[107] J. Chen, L. Jiao, J. L. Zhang, Y. Chen, M. Nicklas, F. Steglich, and H. Q. Yuan, New J. Phys. **15**, 053005 (2013).

[108] I. Bonalde, R. L. Ribeiro, K. J. Syu, H. H. Sung, and W. H. Lee, New J. Phys. **13**, 123022 (2011).

[109] J. Quintanilla, A. D. Hillier, J. F. Annett, and R. Cywinski, Phys. Rev. B **82**, 174511 (2010).

[110] A. D. Hillier, J. Quintanilla, B. Mazidian, J. F. Annett, and R. Cywinski, Phys. Rev. Lett. **109**, 097001 (2012).

[111] M. A. Khan, A. B. Karki, T. Samanta, D. Browne, S. Stadler, I. Vekhter, A. Pandey, P. W. Adams, D. P. Young, S. Teknowijoyo, K. Cho, R. Prozorov, and D. E. Graf, Phys. Rev. B **94**, 144515 (2016).

[112] D. A. Mayoh, J. A. T. Barker, R. P. Singh, G. Balakrishnan, D. M. Paul, and M. R. Lees, Phys. Rev. B **96**, 064521 (2017).

[113] D. Singh, A. D. Hillier, A. Thamizhavel, and R. P. Singh, Phys. Rev. B **94**, 054515 (2016).

[114] B. Chen, Y. Guo, H. Wang, Q. Su, Q. Mao, J. Du, Y. Zhou, J. Yang, and M. Fang, Phys. Rev. B **94**, 024518 (2016).

[115] D. Singh, K. P. Sajilesh, J. A. T. Barker, D. M. Paul, A. D. Hillier, and R. P. Singh, Phys. Rev. B **97**, 100505 (2018).

[116] C. S. Lue, H. F. Liu, C. N. Kuo, P. S. Shih, J.-Y. Lin, Y. K. Kuo, M. W. Chu, T.-L. Hung, and Y. Y. Chen, Supercond. Sci. Technol. **26**, 055011 (2013).

[117] T. Shang, G. M. Pang, C. Baines, W. B. Jiang, W. Xie, A. Wang, M. Medarde, E. Omjakushina, M. Shi, J. Mesot, H. Q. Yuan, and T. Shiroka, Phys. Rev. B **97**, 020502 (2018).

[118] J. A. T. Barker, B. D. Breen, R. Hamson, A. D. Hillier, M. R. Lees, G. Balakrishnan, D. M. Paul, and R. P. Singh, Phys. Rev. B **97**, 100505 (2018).

[119] Y. L. Zuev, V. A. Kuznetsova, M. Vannette, M. V. Lobanov, D. K. Christen, and J. R. Thompson, Phys. Rev. B **76**, 132508 (2007).

[120] P. K. Biswas, M. R. Lees, A. D. Hillier, R. I. Smith, W. G. Marshall, and D. M. Paul, Phys. Rev. B **84**, 184529 (2011).

[121] P. K. Biswas, A. D. Hillier, M. R. Lees, and D. M. Paul, Phys. Rev. B **85**, 134505 (2012).

[122] A. B. Karki, Y. M. Xiong, N. Haldolaarachchige, S. Stadler, I. Vekhter, P. W. Adams, D. P. Young, W. A. Phelan, and J. Y. Chan, Phys. Rev. B **83**, 144525 (2011).

[123] J. Chen, L. Jiao, J. L. Zhang, Y. Chen, L. Yang, M. Nicklas, F. Steglich, and H. Q. Yuan, Phys. Rev. B **88**, 144510 (2013).

[124] J. A. T. Barker, D. Singh, A. Thamizhavel, A. D. Hillier, M. R. Lees, G. Balakrishnan, D. M. Paul, and R. P. Singh, Phys. Rev. Lett. **115**, 267001 (2015).

[125] B. Li, C. Q. Xu, W. Zhou, W. H. Jiao, R. Sankar, F. M. Zhang, H. H. Hou, X. F. Jiang, B. Qian, B. Chen, B. F. Bangura, and X. Xu, Sci. Rep. **8**, 651 (2017).

[126] M. Tinkham, *Introduction to Superconductivity* (McGraw-Hill, New York, 1975).

[127] C. J. Gorter and H. B. G. Casimir, Physica **1**, 306 (1934).

[128] M. Cyrot and D. Pavuna, *Introduction to Superconductivity and High-T_c Materials* (World Scientific Publishing, Singapore, 2010).

[129] W. M. Kleiner, L. H. Roth, and S. H. Autler, Phys. Rev. A **133**, 1226 (1964).

[130] J. Bardeen, L. N. Cooper, and J. R. Schrieffer, Phys. Rev. **106**, 162 (1957).

[131] J. R. Waldram, *Superconductivity of Metals and Cuperates* (Institute of Physics Publishing, Bristol, 1996).

[132] H. Suhl, B. T. Matthias, and L. R. Walker, Phys. Rev. Lett. **3**, 552 (1959).

[133] F. Bouquet, Y. Wang, R. A. Fisher, D. G. Hinks, J. D. Jorgensen, A. Junod, and N. E. Phillips, EPL (Europhysics Letters) **56**, 856 (2001).

[134] A. Y. Liu, I. I. Mazin, and J. Kortus, Phys. Rev. Lett. **87**, 087005 (2001).

[135] R. Khasanov and Z. Guguchia, Supercond. Sci. Tech **28**, 034003 (2015).

[136] Q. Si, R. Yu, and E. Abrahams, Nat. Rev. Mater. **1**, 16017 (2016).

[137] P. Monthoux, D. Pines, and G. G. Lonzarich, Nature **450**, 1177 (2007).

[138] M. Sigrist, AIP Conf. Proc. **789**, 165 (2005).

[139] A. P. Mackenzie and Y. Maeno, Physica B **280**, 2148 (2000).

[140] C. Kallin and J. Berlinsky, Rep. Prog. Phys. **79**, 054502 (2016).

[141] M. Sigrist, AIP Conf. Proc. **1162**, 55 (2009).

[142] M. Sigrist, S. Agterberg, P. Frigeri, N. Hayashi, R. Kaur, A. Koga, I. Milat, K. Wakabayashi, and Y. Yanase, J. Magn. Magn. Mater. **310**, 536 (2007).

[143] P. A. Frigeri, D. F. Agterberg, I. Milat, and M. Sigrist, Eur. Phys. B **54**, 435 (2006).

[144] C. P. Poole, A. F. Horacio, and J. C. Richard, *Superconductivity* (Academic Press, London, 1995).

[145] G. Danaraj, K. Byrappa, V. Prasad, and M. Dudley, *Springer Handbook of Crystal Growth* (Springer-Verlag, Heidelberg, 2010).

[146] R. Jenkins and R. Snyder, *Introduction to X-ray Powder Diffractometry* (J. Wiley & Sons, Inc, New York, 1996).

[147] E. J. Mittemeijer and U. Welzel, *Modern Diffraction Methods* (Wiley-VCH Verlag & Co, KGaA, Weinheim, Germany, 1996).

[148] C. Marin and R. Diéguez, *Orienatation of Single Crystals by Back-Reflection Laue Pattern Simulation* (World Scientific, Singapore, 1999).

[149] D. C. Bell and A. J. Garratt-Reed, *Energy Dispersive X-ray Analysis in the Electron Microscope* (BIOS Scientific Publisher Ltd., Oxford, UK, 2003).

[150] *Quantum Design Magnetic Properties Measurement System: Hardware Manual* (2000).

[151] A. Aharoni, J. Appl. Phys. **83**, 3432 (1998).

[152] J. C. Lashley, M. F. Hundley, A. Migliori, J. L. Sarrao, P. G. Pagliuso, T. W. Darling, M. Jamie, J. C. Cooley, W. L. Hults, L. Morales, D. J. Thoma, J. L. Smith, J. Boerio-Goates, B. F. Woodfield, G. R. Stewart, R. A. Fisher, and N. E. Phillips, Cryogenics **43**, 369 (2003).

[153] *Quantum Design Physical Properties Measurement System: Heat Capacity Operation User Manual* (2000).

[154] B. T. M. Willis and C. J. Carlile, *Experimental Neurton Scattering* (Oxford Universtiy Press, Oxford, UK, 2009).

[155] D. S. Sivia, *Elementary Scattering Theory: For X-ray and Neutron Users* (Oxford Universtiy Press, Oxford, UK, 2011).

[156] A. Amato, Rev. Mod. Phys. **69**, 1119 (1997).

[157] S. L. Lee, S. H. Kilcoyne, and R. Cywinski, *Muon Science: Muons in Physics, Chemistry and Materials* (SUSSP Publications and IOP Publishing, Bristol, 1999).

[158] A. Schenck, *Muon Spin Rotation Spectroscopy: Principles and Applications in Solid State Physics* (Adam Hilger, Bristol, 1985).

[159] A. D. Hillier and R. Cywinski, Appl. Mag. Res. **13**, 95 (1997).

[160] B. Joshi, A. Thamizhavel, and S. Ramakrishnan, Phys. Rev. B **84**, 064518 (2011).

[161] Z. Fisk and G. W. Webb, Phys. Rev. Lett **36**, 1084 (1976).

[162] H. Wiesmann, M. Gurvitch, H. Lutz, A. K. Ghosh, B. Schwarz, M. Strongin, P. B. Allen, and J. W. Halley, Phys. Rev. Lett **38**, 782 (1977).

[163] G. Grimvall, *The Electron-Phonon Interaction in Metals* (North-Holland, Amsterdam, 1981).

[164] E. S. R. Gopal, *Specific Heats at Low Temperatures* (Plenum, New York, 1966).

[165] P. H. Keesom and C. A. Bryant, Phys. Rev. Lett. **2**, 260 (1959).

[166] D. R. Smith and P. H. Keesom, Phys. Rev. B **1**, 188 (1970).

[167] B. Mazidian, J. Quintanilla, A. D. Hillier, and J. F. Annett, Phys. Rev. B **88**, 224504 (2013).

[168] K. Matano, R. Yatagai, S. Maeda, and G. Q. Zheng, Phys. Rev. B **94**, 214513 (2016).

[169] G. M. Pang, Z. Y. Nie, A. Wang, D. Singh, W. Xie, W. B. Jiang, Y. Chen, R. P. Singh, M. Smidman, and H. Q. Yuan, Phys. Rev. B **97**, 224506 (2018).

[170] N. R. Werthamer, E. Helfand, and P. C. Hohenberg, Phys. Rev. **147**, 295 (1966).

[171] A. Gurevich, Phys. Rev. B **67**, 184515 (2003).

[172] P. deGennes and M. Tinkham, Physics **1**, 107 (1964).

[173] J. P. Carbotte, Rev. Mod. Phys. **62**, 1027 (1990).

[174] C. Kittel, *Introduction to Solid State Physics*, 3rd ed. (Wiley, New York, 1967).

[175] G. Grimval, Phys. Scr. **14**, 63 (1976).

[176] W. L. McMillan, Phys. Rev. **167**, 331 (1968).

[177] Y. J. Uemura, L. P. Le, G. M. Luke, B. J. Sternlieb, W. D. Wu, J. H. Brewer, T. M. Riseman, C. L. Seaman, M. B. Maple, M. Ishikawa, D. G. Hinks, J. D. Jorgensen, G. Saito, and H. Yamochi, Phys. Rev. Lett **66**, 2665 (1991).

[178] Y. J. Uemura, V. J. Emery, A. R. Moodenbaugh, M. Suenaga, D. C. Johnston, A. J. Jacobson, J. T. Lewandowski, J. H. Brewer, R. F. Kiefl, S. R. Kreitzman, G. M. Luke, T. Riseman, C. E. Stronach, W. J. Kossler, J. R. Kempton, X. H. Yu, D. Opie, and H. E. Schone, Phys. Rev. B **38**, 909 (1988).

[179] Y. J. Uemura, G. M. Luke, B. J. Sternlieb, J. H. Brewer, J. F. Carolan, W. N. Hardy, R. Kadono, J. R. Kempton, R. F. Kiefl, S. R. Kreitzman, P. Mulhern, T. M. Riseman, D. L. Williams, B. X. Yang, S. Uchida, H. Takagi, J. Gopalakrishnan, A. W. Sleight, M. A. Subramanian, C. L. Chien, M. Z. Cieplak, G. Xiao, V. Y. Lee, B. W. Statt, C. E. Stronach, W. J. Kossler, and X. H. Yu, Phys. Rev. Lett **62**, 2317 (1989).

[180] A. A. Aczel, T. J. Williams, T. Goko, J. P. Carlo, W. Yu, Y. J. Uemura, T. Klimczuk, J. D. Thompson, R. J. Cava, and G. M. Luke, Phys. Rev. B **82**, 024520 (2010).

[181] D. Singh, J. A. T. Barker, T. Arumugam, A. D. Hillier, D. M. Paul, and R. P. Singh, J. Phys. Condens. Matter **30**, 075601 (2018).

[182] D. Singh, M. S. Scheurer, A. D. Hillier, and R. P. Singh, arxiv: , 1802.01533v3 (2018).

[183] A. Nakamura, F. Honda, Y. Homma, D. Li, K. Nishimura, M. Kakihana, M. Hedo, T. Nakama, Y. Onuki, and D. Aoki, IOP Conf. Series: J. Phys: Conf. Series **807**, 052012 (2017).

[184] P. Pedrazzini, G. Schmerber, M. Gómez Berisso, J. P. Kappler, and J. G. Serni, Physica C **336**, 10 (2000).

[185] T. H. Geballe, B. T. Matthias, V. B. Compton, E. Corenzwit, G. W. Hull, and L. D. Longinotti, Phys. Rev. **137**, A119 (1965).

[186] G. M. Luke, Y. Fudamoto, K. M. Kojima, M. I. Larkin, J. Merrin, B. Nachumi, Y. J. Uemura, Y. Maeno, Z. Q. Mao, Y. Mori, H. Nakamura, and M. Sigrist, Nature (London) **394**, 558 (1998).

[187] T. Shang, S. K. Ghosh, L.-J. Chang, C. Baines, M. K. Lee, J. Z. Zhao, J. A. T. Verezhak, D. J. Gawryluk, E. Pomjakushina, M. Shi, M. Medarde, J. Mesot, J. Quitanilla, and T. Shiroka, arxiv: , 1901.01414 (2019).

[188] P. K. Biswas, H. Leutkens, T. Neupert, S. T., C. Baines, G. Pascua, A. P. Schnyder, M. H. Fischer, J. Goryo, M. R. Lees, H. Maeter, F. Brückner, H. H. Klauss, M. Nicklas, P. J. Baker, A. D. Hillier, M. Sigrist, A. Amato, and D. Johrendt, Phys. Rev. B **87**, 180503 (2013).

[189] C. H. Choi and P. Muzikar, Phys. Rev. B **39**, 9664 (1989).

[190] Y. Aoki, A. Tsuchiya, T. Kanayama, S. R. Saha, H. Sugawara, H. Sato, W. Higemoto, A. Koda, K. Ohishi, K. Nishiyama, and R. Kadono, Phys. Rev. Lett. **91**, 067003 (2003).

[191] M. S. Scheurer, Phys. Rev. B **93**, 174509 (2016).

[192] M. Smidman, A. D. Hillier, D. T. Adroja, M. R. Lees, V. K. Anand, R. P. Singh, R. I. Smith, D. M. Paul, and G. Balakrishnan, Phys. Rev. B **89**, 094509 (2014).

[193] E. M. Carnicom, W. Xie, T. Klimczuk, J. Lin, K. Gornicka, Z. Sobczak, N. P. Ong, and R. J. Cava, Science Advances **4**, eaar7969 (2018).

[194] G. R. Stewart, Rev. Mod. Phys. **83**, 1589 (2011).

[195] F. Bouquet, R. A. Fisher, N. E. Phillips, D. G. Hinks, and J. D. Jorgensen, Phys. Rev. Lett. **87**, 047001 (2001).

[196] M. Iavarone, G. Karapetrov, A. E. Koshelev, W. K. Kwok, G. W. Crabtree, D. G. Hinks, W. N. Kang, E.-M. Choi, H. J. Kim, H.-J. Kim, and S. I. Lee, Phys. Rev. Lett. **89**, 187002 (2002).

[197] M. Zehetmayer, Supercond. Sci. Tech. **26**, 043001 (2013).

[198] Q. Zhang, G. Li, D. Rhodes, A. Kiswandhi, T. Besara, B. Zeng, J. Sun, T. Siegrist, M. D. Johannes, and L. Balicas, Sci. Rep. **3**, 1446 (2013).

[199] Y. Lu, T. Takayama, A. F. Bangura, Y. Katsura, D. Hashizume, and H. Takagi, J. Phys. Soc. Japan **83**, 023702 (2014).

[200] P. K. Biswas, H. Luetkens, X. Xu, J. H. Yang, C. Baines, A. Amato, and E. Morenzoni, Phys. Rev. B **91**, 100504 (2015).

[201] F. E. Hoare, J. C. Matthews, and J. C. Walling, P. Roy. Soc. A - Math. Phy. **216**, 502 (1953).

[202] Z. Fisk and A. C. Lawson, Solid State Commun. **13**, 277 (1973).

[203] Y. Nakajima, T. Nakagawa, T. Tamegai, and H. Harima, Phys. Rev. Lett. **100**, 157001 (2008).

[204] P. K. Biswas, G. Balakrishnan, D. M. Paul, M. R. Lees, and A. D. Hillier, Phys. Rev. B **83**, 054517 (2011).

[205] O. J. Taylor, A. Carrington, and J. A. Schlueter, Phys. Rev. Lett. **99**, 057001 (2007).

[206] B. Mazidian, J. Quintanilla, A. D. Hillier, and J. F. Annett, Phys. Rev. B **88**, 224504 (2013).

[207] C. P. Bean, Rev. Mod. Phys. **36**, 31 (1964).

[208] D. A. Mayoh, A. D. Hillier, K. Götze, D. M. Paul, G. Balakrishnan, and M. R. Lees, Phys. Rev. B. **98**, 014502 (2018).

[209] R. Meservey and B. B. Schwartz, in *Superconductivity*, Vol. 1, edited by R. D. Parks (Marcel Dekker, New York, 1969) Chap. 3, and references therein.

[210] A. M. Clogston, Phys. Rev. Lett **9**, 266 (1962).

[211] T. P. Orlando, E. J. McNiff, S. Foner, and M. R. Beasley, Phys. Rev. B **19**, 4545 (1979).

[212] G. Fuchs, S.-L. Drechsler, N. Kozlova, G. Behr, A. Kohler, J. Werner, K. Nenkov, C. Hess, R. Klingeler, J. E. Hamann-Borrero, A. Kondrat, M. Grobosch, A. Narduzzo, M. Knupfer, J. Freudenberger, B. Buchner, and L. Schultz, Phys. Rev. Lett. **101**, 237003 (2008).